

Durham E-Theses

Linear generators for direct drive marine renewable energy converters

Baker, Nicholas Jon

How to cite:

Baker, Nicholas Jon (2003) *Linear generators for direct drive marine renewable energy converters*, Durham theses, Durham University. Available at Durham E-Theses Online:
<http://etheses.dur.ac.uk/696/>

Use policy

The full-text may be used and/or reproduced, and given to third parties in any format or medium, without prior permission or charge, for personal research or study, educational, or not-for-profit purposes provided that:

- a full bibliographic reference is made to the original source
- a [link](#) is made to the metadata record in Durham E-Theses
- the full-text is not changed in any way

The full-text must not be sold in any format or medium without the formal permission of the copyright holders.

Please consult the [full Durham E-Theses policy](#) for further details.

Linear Generators for Direct Drive Marine Renewable Energy Converters

Nicholas Jon Baker

School of Engineering
University of Durham

A thesis submitted in partial fulfilment of the requirements of the Council of the
University of Durham for the Degree of Doctor of Philosophy (PhD)

2003

The copyright of this thesis rests with the author.
No quotation from it should be published without
his prior written consent and information derived
from it should be acknowledged.



- 7 JUL 2003

Linear Generators for Direct Drive Marine Renewable Energy Converters

N. J. Baker

Ph.D.

2003

Abstract

This thesis is concerned with the development of linear generators for use as the power take off mechanism in marine renewable energy converters. Delivering significant power at the low velocities demanded by wave and tidal stream energy converters requires a large force, which must be reacted by an electrical machine in a direct drive system. Attention is focused on the development of two novel topology linear permanent magnet machines suitable for use in this application.

For each topology, models are presented that are capable of predicting the force characteristics and dynamic generator performance. The models, which are verified experimentally, reveal significant behavioural differences between the two topologies. The designer is thus provided with an interesting choice when considering a direct drive power take off strategy. In short, a variable reluctance machine is shown to develop a high shear force in its airgap, offering the potential of a compact generator, yet its performance is hindered by a poor power factor and the presence of significant airgap closure forces. The second machine, an air cored stator encompassing a permanent magnet translator, is shown to lend itself favourably as a generator, but only at the expense of requiring a large quantity of magnetic material and developing a significantly lower shear stress.

Mechanical issues involved in the direct integration of linear electrical machines into the marine environment are examined. Details of two existing marine renewable energy devices are used to hypothesise about the characteristics of realistic sized generators of both the topologies investigated.

Direct drive power take off is shown to represent a feasible alternative to the complex systems frequently proposed in these applications.

Declaration

I hereby declare that this thesis is a record of work undertaken by myself, that it has not been the subject of any previous application for a degree, and that all sources of information have been duly acknowledged.

© Copyright, N. J. Baker, 2003

The copyright of this thesis rests with the author. No quotation from it should be published without prior written consent and information derived from it should be acknowledged.

Acknowledgements

Firstly, I would like to thank my supervisor, Dr. M. A. Mueller for his unfailing (and often un-rewarded) support, patience and confidence during the course of this research and subsequent thesis preparation.

Technical advice was gratefully received from several technicians of the School of Engineering, University of Durham but particular thanks is due to Mr. Ted Jones and Mr. David Jones for development and manufacture of test equipment.

Initial guidance for the analysis of the tubular machine was provided by Professor E. Spooner.

Many friends made conducting a PhD bearable, with particular thanks to Paul Gordon for various bits of information and guidance, Su Roy, Jon Bennie, Jens Lamping, Sophie Bassett and Andy Dean for creating an amiable social atmosphere.

Ongoing support from my family was invaluable, particularly from my father, Dr. R. R. Baker, who generously agreed to proof read the final draft.

Financial support from EPSRC and supplemented by Newage AVK SEG made this research possible and is gratefully acknowledged.

This thesis is dedicated to my niece, Maya Frances Baker, born 28 December 2002.

Contents

Abstract.....	ii
Declaration.....	iii
Acknowledgements	iv
Contents	v
List of Figures.....	x
List of Tables.....	xvii
Nomenclature.....	xviii
Chapter 1: Introduction	1
1.1 Wave Energy	1
1.1.1 History	1
1.1.2 Cost and Environmental Impact	2
1.1.3 Resource	3
1.1.4 Formation and Description of Waves	4
1.1.5 Principles of Energy Capture From Waves	5
1.1.6 Wave Energy Converters (WECs).....	10
1.2 Tidal Stream Energy.....	15
1.2.1 Introduction	15
1.2.2 Tidal Stream Energy Converters	16
1.3 Electrical Power Take off.....	17
1.4 Aim of Thesis	18
1.5 Layout of thesis	18
Chapter 2: Power Take off Systems.....	20
2.1 Requirements of power take off system	20
2.2 Direct Mechanical Linkage	21
2.3 Pneumatic system.....	21
2.4 Hydraulic system.....	22
2.5 Direct Drive.....	25
2.5.1 Introduction	25
2.5.2 Electronic conversion for direct drive	28
2.6 Specifying a power take off system.....	29
2.6.1 Example WEC	29
2.6.2 Sizing the WEC for a given sea state.....	30
2.6.3 Concluding remarks.....	36
2.7 Discussion	36
2.8 Conclusion.....	37
Chapter 3: Linear Electrical Machines.....	38

3.1	Linear Machines	38
3.2	Conventional Topologies	39
3.2.1	Linear Induction Machine.....	39
3.2.2	Field wound synchronous machine	40
3.2.3	Permanent Magnet (PM) synchronous	41
3.3	Variable Reluctance Permanent Magnet Machines (VRPM).....	42
3.3.1	Introduction	42
3.3.2	Power Factor.....	44
3.3.3	Transverse Flux Machine (TFM).....	46
3.3.4	Vernier Hybrid Machine (VHM).....	49
3.4	Tubular Machine	51
3.4.1	Introduction	51
3.4.2	Ironless Tubular PM machine.....	52
3.5	Shear stress comparison	56
3.6	Discussion	58
3.6.1	General Structural Comparison	58
3.6.2	Suitability for Marine Renewable Energy Converters.....	58
3.6.3	Selection of machines for further development.....	59
3.7	Conclusion.....	60
Chapter 4: The Linear Vernier Hybrid Machine		61
4.1	3 kW Prototype.....	61
4.1.1	Three phase construction	61
4.1.2	Force calculation.....	62
4.1.3	Emf calculation.....	63
4.1.4	Machine Sizing	65
4.2	Finite Element Analysis	68
4.2.1	Details of the model.....	68
4.2.2	Details of the Analysis.....	70
4.2.3	Details of Results.....	71
4.2.4	Concluding Remarks	77
4.3	Utilisation of Finite Element Analysis	77
4.3.1	Force Calculations	77
4.3.2	Performance.....	86
4.3.3	Model Development	91
4.3.4	Governing Equations	95
4.3.5	Concluding Remarks	95
4.4	Verification of Models	96
4.4.1	Description of Testrig.....	96

4.4.2	Force Results	98
4.4.3	Electrical Performance Models.....	103
4.4.4	Concluding Remarks	110
4.5	Sources of Error.....	110
4.5.1	Three dimensional error.....	110
4.5.2	Error in airgap.....	111
4.6	Real Time Response of VHM	114
4.7	Alternative Configurations of VHM	120
4.8	Discussion	121
Chapter 5: The Air-Cored Tubular Machine.....		123
5.1	Design of 3 kW Prototype.....	123
5.1.1	Flux density around translator	123
5.1.2	Selection of magnet	125
5.1.3	Selection of Steel Spacer	125
5.1.4	Coil support	126
5.1.5	Translator Support	126
5.1.6	Design of Stator Coils.....	128
5.1.7	Flux Cutting Coil.....	128
5.1.8	Prototype dimensions.....	131
5.2	Finite Element Analysis of Single Three Phase Coil in Ideal Machine	131
5.2.1	Details of the model.....	131
5.2.2	Details of the Analysis.....	133
5.2.3	Details of Results.....	134
5.3	Finite Element Analysis of Actual Three Phase Machine.....	139
5.3.1	Introduction	139
5.3.2	Details of model.....	140
5.3.3	Details of Results.....	140
5.4	Utilisation of Finite Element Analysis	143
5.4.1	Force Calculations	143
5.4.2	Performance.....	146
5.5	Verification of Models	149
5.5.1	Description of Testrig.....	149
5.5.2	Electrical Performance Models.....	151
5.5.3	Concluding remarks.....	156
5.6	Sources of Error.....	156
5.7	Real Time Response.....	158
5.8	Discussion	159
5.8.1	General.....	159

5.8.2	Construction Issues.....	160
5.8.3	Radial Forces.....	160
5.8.4	Use in Marine Energy Converters.....	161
5.9	Conclusion.....	161
Chapter 6: Mechanical Integration.....		162
6.1	General Considerations.....	162
6.2	Sealing.....	163
6.3	Solid Bearings.....	164
6.3.1	Sliding Interface.....	164
6.3.2	Rolling Contact.....	165
6.4	Corrosion.....	166
6.5	VHM.....	169
6.5.1	Introduction.....	169
6.5.2	Sealing.....	170
6.5.3	Hydrostatic Lubrication.....	171
6.5.4	Support Structure.....	188
6.6	Tubular.....	190
6.6.1	Introduction.....	190
6.6.2	Sealing.....	190
6.6.3	Hydrostatic bearings.....	191
6.6.4	Support structure.....	191
6.7	Comparison of Machine Topologies.....	191
6.8	Discussion.....	195
6.9	Conclusion.....	196
Chapter 7: Proposed VHM Design for a 150 kW Tidal Energy Device.....		197
7.1	150 kW Stingray.....	197
7.2	Power Take off Mechanism.....	198
7.3	Specifying a VHM.....	201
7.4	Direct Replacement of Cylinders.....	202
7.5	Enlarged Moment Arm.....	203
7.6	Alternative Location.....	204
7.7	Integrated Design.....	206
7.8	Discussion.....	207
7.9	Conclusion.....	208
Chapter 8: Direct Drive Wave Energy Converter.....		209
8.1	Principle of Power Extraction.....	209
8.2	Prototype.....	210
8.2.1	Introduction.....	210

8.2.2	Device Characteristics	211
8.2.3	Present Power Take off.....	212
8.2.4	Energy Yield.....	213
8.3	Alternative Power Take off.....	214
8.4	Design of tubular machine	215
8.4.1	Single machine	215
8.4.2	Multiple machines	216
8.4.3	Power Conversion.....	217
8.5	Discussion	219
8.6	Conclusion.....	219
Chapter 9: Discussion, Conclusion and Recommendations.....		220
9.1	Chapter or Results Summary.....	220
9.2	Discussion	223
9.2.1	General.....	223
9.2.2	Choice of topology	224
9.2.3	Direct drive prototype.....	224
9.2.4	Electrical Machines	225
9.3	Suggestions for further work.....	226
9.4	Conclusion.....	227
Appendix A: DERIVATION OF EQUIVALENT AIRGAP		228
Appendix B: DERIVATION OF POWER FACTOR FOR VHM IN CAPACITOR ASSISTED EXCITATION.....		230
Appendix C: COEFFICIENTS FOR FOURIER SERIES APPROXIMATION OF TUBULAR MACHINE		232
Appendix D: DEFLECTION OF DISTRIBUTED BEAM		234
REFERENCES		236

List of Figures

Figure 1.1: Comparison of life cycle emissions of CO ₂ [6].....	2
Figure 1.2: Demonstration of absorbing wave energy.....	6
Figure 1.3: Plan view of a point absorber interacting with uniform wave train.....	7
Figure 1.4: The advantages of control [9].....	10
Figure 1.5: Direct drive heaving buoy.....	12
Figure 1.6: AWS.....	13
Figure 1.7: IPS buoy.....	14
Figure 1.8: Stingray tidal stream generator.....	16
Figure 1.9: Alternative power take off schemes.....	17
Figure 2.1: Pneumatic gearing in an OWC.....	22
Figure 2.2: Hydraulic power take off system.....	23
Figure 2.3: Previous direct drive proposal.....	26
Figure 2.4: Direct drive proposal with rolling magnetic field.....	27
Figure 2.5: Linear motor as part of control strategy.....	27
Figure 2.6: Direct Thrust Designs plc 500 W prototype WEC.....	28
Figure 2.7: Three phase AC/DC/AC converter.....	29
Figure 2.8: Heaving buoy with hydraulic power take off.....	30
Figure 2.9: Scatter table of wave data [56].....	31
Figure 2.10: Energy contribution from various parts of the sea.....	32
Figure 2.11: Effect of limiting amplitude of oscillation to 2 m.....	33
Figure 2.12: Effect of limiting hydraulic extension on maximum theoretical annual energy yield.....	34
Figure 3.1: Imaginary process of unrolling rotational machine to obtain linear counterpart.....	38
Figure 3.2: Linear induction machine.....	40
Figure 3.3: Conventional linear PM machine.....	41
Figure 3.4: Equivalent current sheet of a PM.....	42
Figure 3.5: Magnetic Gearing.....	43
Figure 3.6: Phasor Diagram of VRPM.....	44
Figure 3.7: Transverse Flux Machine.....	47
Figure 3.8: Equivalent circuit of TFM.....	48
Figure 3.9: Force generation in the TFM.....	49
Figure 3.10: The VHM.....	50

Figure 3.11: Flux pattern of VHM.....	50
Figure 3.12: Ironless tubular machine	52
Figure 3.13: Simplified flux flow through tubular machine.....	53
Figure 3.14: Segment of copper in magnetic field.....	54
Figure 3.15: The effect of radius on tubular machine shear stress	56
Figure 4.1: Dimensions of the VHM	62
Figure 4.2: Equivalent Circuit of VHM.....	63
Figure 4.3: Equivalent circuit for VHM with magnetic excitation only.....	64
Figure 4.4: Effect of magnet width in predicted shear stress.....	66
Figure 4.5: Example of three phase force	66
Figure 4.6: FEA mesh of VHM	69
Figure 4.7: Definition of relative position	70
Figure 4.8: B-H data for FEA	70
Figure 4.9: Variation of phase flux linkage with excitation current, no magnets.....	72
Figure 4.10: Flux plot for magnetic excitation. (A) zero position, (B) 12 mm position	73
Figure 4.11: Flux plot for the misaligned positions (A position=18 and B position=6), magnet excitation only.....	74
Figure 4.12: Predicted no load variation of flux linkage for entire phase with position	75
Figure 4.13: Flux plot with (A) +10A, (B) -10 A. Position = 0.....	76
Figure 4.14: Flux linkage map of entire phase	77
Figure 4.15: Values of static force from FEA calculated Maxwell stress	78
Figure 4.16: Attractive forces between rotor and stator	79
Figure 4.17: Comparison of normal forces for ± 15 Amps	80
Figure 4.18: Point force along stator. The stator faces correspond to 24-96 and 240-312 mm positions.....	80
Figure 4.19: Normal force on stator, $p=6$	81
Figure 4.20: Example flux linkage-mmF trajectory	82
Figure 4.21: Explanation of calculation of co-energy	82
Figure 4.22: Flux-mmF diagram for a PM	83
Figure 4.23: Divergence of operating points of PMs.....	84
Figure 4.24: Load lines of adjacent pair of magnets.....	85
Figure 4.25: Cogging force on one face of the VHM.....	85
Figure 4.26: Simple Equivalent Circuit	87

Figure 4.27: Predicted self inductance per phase for different rotor positions and coil currents.....	88
Figure 4.28: Step variable inductance equivalent circuit model.....	89
Figure 4.29: Continuous Variable Inductance Method.....	89
Figure 4.30: Lumped Reactance	90
Figure 4.31: The look up table model.....	91
Figure 4.32: Comparison of Polynomial approximation and FEA results	91
Figure 4.33: Flux position obtained with polynomial approximation	92
Figure 4.34: Emf verses time for 0.5m/s rotor velocity.....	93
Figure 4.35: Schematic diagram of program integration technique for t=0	94
Figure 4.36: The VHM testrig	96
Figure 4.37: Aspects of VHM testrig.....	96
Figure 4.38: Position of load cell.....	97
Figure 4.39: Example of experimental data, 6 Amps flowing in coils	98
Figure 4.40: Force results with 8 Amps flowing	99
Figure 4.41: Predicted and experimental force with 16 Amps flowing.....	100
Figure 4.42: Predicted and experimental force with 2 Amps flowing.....	101
Figure 4.43: Cogging force comparison	102
Figure 4.44: Experimental force results for 20 Amps	102
Figure 4.45: Open Circuit emf.....	103
Figure 4.46: Short circuit results for model A	104
Figure 4.47: Short circuit model results for model E	105
Figure 4.48: Capacitive loaded results for model A I.....	106
Figure 4.49: Differential of voltage used in model A i.....	106
Figure 4.50: Capacitive load results for model A ii.....	107
Figure 4.51: Capacitive load results for model C i.....	107
Figure 4.52: Calculated values of inductance and its differentials in model C i.....	108
Figure 4.53: Capacitive load results for model C i, settle period	108
Figure 4.54: Capacitive load results for model E i	109
Figure 4.55: Capacitive load results for E ii	109
Figure 4.56: Keeper plate of laminated stator.....	111
Figure 4.57: Source of error in airgap.....	112
Figure 4.58: The effect of alternative airgaps on effective inductance map.....	112
Figure 4.59: Effect of varying airgap on predicted voltage, C=150 μ , R =630 Ω (experiment a).....	113

Figure 4.60: Effect of varying airgap on predicted voltage, $C=100\mu$, $R=29\Omega$ (experiment b).....	113
Figure 4.61: Equivalent circuit of VHM in short circuit	114
Figure 4.62: Flux flow in VHM during short circuit	115
Figure 4.63: Phasor diagram of power factor	116
Figure 4.64: Phasor diagram of corrected power factor	117
Figure 4.65: Capacitor assisted excitation of the VHM.....	117
Figure 4.66: Flux linkages in the VHM with a capacitive load of $150\ \mu\text{F}$, resistive load of $630\ \Omega$ at a constant velocity of $0.5\ \text{m/s}$ velocity	119
Figure 4.67: Flux linkages in the VHM with a capacitive load of $150\ \mu\text{F}$, resistive load of $630\ \Omega$ at a constant velocity of $0.8\ \text{m/s}$ velocity	119
Figure 4.68: Alternative flux pattern	120
Figure 4.69: End view of four sided VHM.....	121
Figure 5.1: Equivalent circuit of radial segment.....	124
Figure 5.2: Assumed flux flow in air core machine	124
Figure 5.3: Variation of surface flux density with width of steel spacer.....	126
Figure 5.4: Equivalent circuit including leakage	127
Figure 5.5: Effect of shaft size on surface flux density	127
Figure 5.6: Derivation of flux linkage cutting coil.....	128
Figure 5.7: Dimensions of one half (8poles) of $3\ \text{kW}$ tubular machine	131
Figure 5.8: Position of coils.....	132
Figure 5.9: FEA mesh of tubular machine.....	133
Figure 5.10: Flux lines of translator	134
Figure 5.11: Flux densities moving along the translator	135
Figure 5.12: Flux densities moving away from translator.....	135
Figure 5.13: Comparison of model with 3D FEA averaged data	136
Figure 5.14: Variation of flux linkage with position for 8 coils for each of the 3 phases	137
Figure 5.15: Single coil inductances.....	138
Figure 5.16: Flux linkage map of single coil (B).....	139
Figure 5.17: Position definition for large simulation.....	140
Figure 5.18: Flux cutting entire phases.....	141
Figure 5.19: Flux plots of large FEA.....	141
Figure 5.20: Self inductance of three phases	142
Figure 5.21: Mutual inductance between three phases	142

Figure 5.22: Comparison of force calculation method	143
Figure 5.23: Calculated radial force	144
Figure 5.24: Flux plots for (A) 0, (B) +20 and (C)-20 Amp current aligned with centre of magnet	145
Figure 5.25: calculated axial force.....	146
Figure 5.26: Equivalent circuit of red phase.....	147
Figure 5.27: Fourier series approximation.....	148
Figure 5.28: Tubular machine translator.....	149
Figure 5.29: Mechanical excitation of translator	150
Figure 5.30: Photograph of prototype.....	151
Figure 5.31: Geometric picture of crank arrangement.....	151
Figure 5.32: Comparison of actual and predicted radial flux density.....	152
Figure 5.33: Comparison of measured and predicted axial flux.....	152
Figure 5.34: Comparison of experimental (V) and FEA predicted self inductance of an entire phase	153
Figure 5.35: Open circuit results for a single phase	154
Figure 5.36: Comparison predicted and experimental voltages for a 17 Ohm load	155
Figure 5.37: Varying voltage peaks.....	155
Figure 5.38: Translator entering stator	157
Figure 5.39: Effect of translator error.....	157
Figure 5.40: predicted internal emf and voltage drop at 1 m/s.....	158
Figure 6.1: Manufacturers data on wear rate of solid contact bearings []	164
Figure 6.2 Roller bearing with return path	165
Figure 6.3: Stud bearing.....	166
Figure 6.4: Standard coating for magnets (A) new, (B) after 6 weeks and (C) 2 years submersion in seawater.....	167
Figure 6.5: Alternative coatings for magnets, (i) as new, (ii) after 2 years submerged in seawater	167
Figure 6.6: Coal Tar epoxy 6 weeks after submersion	168
Figure 6.7: Coal Tar epoxy coating of magnets after 2 years submersion	168
Figure 6.8: Coal tar epoxy coating of steel section after 2 years submersion	169
Figure 6.9: Forces on VHM. (A), with translator in centre & (B). with uneven airgap	170
Figure 6.10: Filling the translator slots.....	170
Figure 6.11: Cylindrical sealing for the VHM.....	171

Figure 6.12: View from below bearing, showing assumed flow of fluid and dimensions	173
Figure 6.13: Flow control options	174
Figure 6.14: Equivalent circuit for a single pad	175
Figure 6.15: Opposed pads given a small displacement, h , from the design clearance, H	175
Figure 6.16: Equivalent circuit for opposed pad bearings	177
Figure 6.17: Dimensionless graph of relative pumping power verses relative pad size for any given stiffness	178
Figure 6.18: Pumping power for bearings designed for 100kW machine	181
Figure 6.19: Reynolds' number for flow out of bearing compared with 2000, maximum to ensure laminar flow	182
Figure 6.20: Minimum pumping power and maximum clearance of large bearings	183
Figure 6.21: Dimensions of bearings in Figure 6.20	183
Figure 6.22: Self regulating bearing, flow path	185
Figure 6.23: Self regulating bearing, pressure distribution	185
Figure 6.24: Self regulating opposed pad hydrostatic slideway	186
Figure 6.25: End effects of hydrostatic slide way	186
Figure 6.26: Lamination tolerances []	188
Figure 6.27: Welding of laboratory laminations	188
Figure 6.28: Skeletal Structure	189
Figure 6.29: Equivalent beam for a VHM	189
Figure 6.30: Side view comparisons of both 100 kW machines	194
Figure 6.31: Rendered view of both 100 kW machines	194
Figure 7.1: Photograph of 150 kW prototype shortly before deployment	198
Figure 7.2: Configuration of hydraulic cylinders	199
Figure 7.3: Moment length cylinders have on pivot arm over 2 cycles	199
Figure 7.4: Characteristics of cylinder cycle	200
Figure 7.5: Moment exerted by power take off	200
Figure 7.6: Force provided by individual cylinders	202
Figure 7.7: Comparison of proposed generator and existing cylinder	204
Figure 7.8: Force required to exert moment at different generator positions	205
Figure 7.9: Design study of generator distance from post	206
Figure 7.10: hemispherical flux machine	207
Figure 8.1: AWS during a (failed) attempt at launching	211

Figure 8.2: F_w per m wave amplitude vs. wave period.....	211
Figure 8.3: Variation of hydrodynamic damping	212
Figure 8.4: Segment of present power take off.....	212
Figure 8.5: Annual wave distribution of test site.....	213
Figure 8.6: Characteristics of unrestricted AWS.....	213
Figure 8.7: AWS force characteristics with limited amplitude and velocity.....	214
Figure 8.8: Many designs of tubular machine	216
Figure 8.9: Phasor diagram of tubular machine with resistive load	218

List of Tables

Table 1-1: Comparison of predicted costs for energy sources [5].....	3
Table 1-2: UK deep water wave energy resource which can be turned into useful energy [7].....	4
Table 2-1: Device characteristics for hydraulic ram with $A_{\max} = 4\text{m}$	34
Table 2-2: Parameters of cylinder.....	35
Table 3-1: Values used in shear stress comparison	57
Table 3-2: Results of peak shear stress comparison	57
Table 4-1: Dimensions of VHM prototype.....	68
Table 4-2: Coefficients of 4 th order flux approximation.....	91
Table 4-3: Integrals used in VHM models.....	95
Table 4-4: Experimental short circuit current results	104
Table 4-5: Short circuit results of the VHM	105
Table 4-6: Experimental results for a 630Ω resistor and $150\mu\text{F}$ capacitor.....	105
Table 4-7: Summary of VHM model results	109
Table 4-8: Comparison of experimental results for large airgap model E i	114
Table 5-1: Dimensions of tubular prototype.....	131
Table 6-1: Values used for total power comparison.....	179
Table 6-2: Material prices used in cost analysis.....	192
Table 6-3: Mass of 100 kW VHM.....	192
Table 6-4: Size of 100 kW VHM.....	192
Table 6-5: Cost of 100kW VHM.....	193
Table 6-6: Mass of 100 kW tubular machine	193
Table 6-7: Size of 100 kW tubular machine	193
Table 6-8: Cost of 100 kW tubular machine.....	193
Table 6-9: Comparison of VHM and tubular machines	193
Table 7-1: Approximate dimensions of cylinder	201
Table 7-2: Estimated mass of hydraulic system	201
Table 7-3: Linear generator for direct replacement of cylinders	202
Table 7-4: Linear generator suitable for use with enlarged moment arm.....	204
Table 8-1: Selection of tubular machines for AWS.....	217
Table 8-2: Generator characteristics of tubular machines	218
Table 8-3: Power delivered to load for alternative generators.....	218

Nomenclature

Abbreviations

AWS	=	Archimedes Wave Swing
FEA	=	Finite Element Analysis
IPS	=	Interproject Sweden
MEC	=	Marine Energy Converter
mmf	=	magneto motive force
OWC	=	Oscillating Water Column
PM	=	Permanent Magnet
RMS	=	Root Mean Square
VHM	=	Vernier Hybrid Machine
VRPM	=	Variable Reluctance Permanent-Magnet Machine
WEC	=	Wave Energy Converter

Symbols

β_g	=	damping coefficient of generator (Ns/m)
β_h	=	hydrodynamic damping coefficient of AWS (f(wave period)) (Ns/m)
ϕ	=	phase difference between internal emf and current (rads)
ϕ_m	=	flux flow due to one magnet (Wb)
ϕ	=	flux flow (Wb)
ϕ_{face}	=	flux flow through entire stator face (Wb)
λ	=	wavelength (m)
μ	=	discharge coefficient
μ_0	=	permeability of free space = $4\pi \times 10^{-7}$
μ_r	=	relative permeability
ρ	=	density (kg/m ²)
ρ_o	=	density of oil (kgm ⁻³)
ψ_I	=	flux linkage due to current (Wb-turns)
ψ_i	=	flux linkage due to current with no PMs present (Wb-turns)
ψ_M	=	flux linkage due to magnetic excitation only (Wb-turns)
ψ_{coil}	=	flux linking coil (Wb-turns)
ω	=	frequency (rs ⁻¹)
Ω	=	magnetic vector potential

Ω_m	=	magnetic vector potential of m^{th} harmonic
A_{max}	=	maximum amplitude of oscillation (m)
A	=	area of two parallel surfaces (m^2)
A	=	surface area available for heat dissipation (m^2)
a	=	constant dictating midpoint of the position-linkage curve
a_0	=	average value (used in Fourier series)
A_m	=	area of one magnet (m^2)
a_n	=	constant (used in Fourier series)
b	=	constant dictating the amplitude of the position-linkage curve
B	=	buoyancy force (N)
B	=	magnetic flux density (T)
B_g	=	flux density in airgap (T)
B_y	=	flux density in 'y' direction (T)
B_z	=	flux density in 'z' direction (T)
\hat{B}_g	=	peak flux density at surface (T)
b_n	=	constant (used in Fourier series)
B_r	=	remnant flux density in magnet (T)
B_{root}	=	flux density in root of tooth (T)
B_s	=	flux density under slot region (T)
B_t	=	flux density under the tooth (T)
C	=	constant
C	=	Capacitance (F)
C	=	coefficient of damping (Ns^{-1})
C_{AWS}	=	spring constant of AWS (N/m)
C_D	=	drag coefficient (Ns/m)
ch	=	coil height (m)
cw	=	coil width (m)
D	=	drag force (D)
E	=	Young's modulus of material (Pa)
E_{open}	=	open circuit emf (V)
f_0	=	resonant frequency (Hz)
F	=	force (N)
F	=	load capacity of single hydrostatic pad (N)
$f(\psi)$	=	value of current obtained from Look up table (A)

$f(x)$	=	periodic function
F_E	=	the exciting force on the body (N)
F_f	=	friction force (N)
F_w	=	diffraction force of the wave acting on AWS (N)
g	=	airgap (m)
g	=	acceleration due to gravity (ms^{-2})
H	=	design clearance of bearing (m)
h	=	displacement from design clearance (m)
h	=	heat transfer coefficient ($\text{Wm}^{-2}/^\circ\text{C}$)
H_c	=	Coercivity (Am^{-1})
H_f	=	friction power (W)
H_p	=	pumping power (W)
H_s	=	significant wave height (m)
I	=	current (A)
i_r	=	current in yellow phase (A)
I	=	second moment of area (m^2)
I	=	inertia (Ns^2/m)
I_{PM}	=	Equivalent current (A)
J	=	current density (A/m^2)
k	=	spring constant (N/m)
k_0	=	stiffness of opposed pads at design clearance (N/m)
K	=	electric loading (A/m)
l	=	period of function
L	=	axial length (m into plain of paper)
L	=	recess length (m)
L	=	self inductance (H)
l_g	=	length of equivalent airgap (m)
L_i	=	constant value of inductance (H)
$L_{i,p}$	=	value of inductance varying with current and position (H)
L_{pp}	=	length of parallel plates (m)
m	=	mass (kg)
M_{ry}	=	mutual inductance of red and yellow phases (H)
M_a	=	added mass (kg)
M_{fl}	=	mass of floater (kg)
n	=	number of magnets mounted on stator face

N	=	number of turns per coil
P	=	mean power (W)
P_i	=	power available at sea state i (W)
P_{loss}	=	power lost to surroundings (W)
P_R	=	recess pressure (Pa)
prob _i	=	probability of sea state i occurring
p	=	relative position of teeth and magnets (m)
P_S	=	supply pressure (Pa)
Q	=	flow rate(m ³ /s)
R	=	load resistance (Ohm) or hydraulic resistance (Pas/m ³)
r	=	radius (m)
r	=	internal resistance (Ohm)
R_0	=	outside radius of coil (m)
R_b'	=	dimensionless resistance of bearing
R_b	=	general resistance of hydrostatic bearing (Pas/m ³)
R_{bo}	=	resistance of bearing at design clearance (Pas/m ³)
R_e	=	Reynolds' number
R_E	=	External resistance across capacitor (Ohm)
R_i	=	inside radius of coil (m)
R_m	=	radius magnet (m)
R_R	=	restrictor resistance (Pas/m ³)
R_{tot}	=	total resistance of hydraulic circuit (Pas/m ³)
S	=	reluctance (A-turns/Wb)
S_g	=	reluctance of gap (A-turns/Wb)
S_m	=	reluctance of magnet (A-turns/Wb)
S_t	=	reluctance of airgap under tooth (A-turns/Wb)
T	=	time period (S)
ΔT	=	temperature rise with respect to surroundings (°C)
t_m	=	thickness of magnet (m)
v	=	velocity (m/s)
V	=	volume (m ³)
V_L	=	load voltage (V)
V_{LD}	=	voltage dropped across imaginary inductor (V)
V_m	=	voltage output of model (V)
w	=	recess width (m)

W	=	width of wave front (m)
W	=	load capacity of bearing (N)
w_m	=	width of magnet (m)
W_p	=	width pole (m)
w_s	=	width of steel (m)
x	=	distance from translator surface (m)
x	=	land width (m)
X_C	=	reactance of capacitor (Ohm)
X_L	=	reactance of inductor (Ohm)
y	=	vertical position of AWS floater (m)

Chapter

1

Introduction

As technology relentlessly progresses, our thirst for energy shows no sign of abating. Either because of a limitation of resource, or because of the impact of their exploitation, there is a desire to replace the sources of energy to which we have become accustomed since the industrial revolution with a more sustainable alternative. A renewable energy source is one which does not use up the earth's finite mineral reserve and instead uses a source which replenishes itself. Around two thirds of the earth's surface is covered in water, it is therefore logical to look here for usable energy.

The work presented here is intended to add to the increasing body of research on the subject of capturing energy from the marine resource. It focuses on the aspects associated with converting the captured energy, in the form of physical displacement, into an electrical form and therefore stops short of the development of the capture device itself and the downstream connection to the electricity grid.

In summary this thesis is concerned with the development of reciprocating generators capable of delivering the required power at the slow velocities demanded by wave energy and tidal stream power converters. Research into such generators facilitates the use of direct drive power take off, whereby the electrical machine is joined directly to the moving part of the device.

1.1 Wave Energy

1.1.1 History

The UK development programme was first started during the oil crisis in the 1970's. At this stage it was played off directly against nuclear energy, both financially and in terms of attempting to assemble single units capable of replacing a power station. In this situation nuclear power stations were deemed to be more economical, at least in the

very short term. It is noteworthy that the cost of decommissioning, long term waste storage and overall environmental impact were not costed in at this stage. The UK's 'deep-sea' research programme was hence closed in 1982 for economic reasons. Around 10 years later interest, funding and hence research in this area was rekindled. There is presently a modest number of institutions and groups conducting research internationally, and an emerging research community, e.g. [1].

After more than twenty years since the research programme was started in the UK resulting in little commercial success, wave energy could appear to be fraught with technical problems. Although this thesis does not intend to review its history in any detail, it is important to realise that the main barriers to wave energy development have not, by any means, been solely technical. A comprehensive guide to the political and financial barriers of its development is available [2]. In 2000 a technical report commissioned by the UK Department of Trade and Industry concluded that there were no insurmountable problems for the implementation of wave energy [3].

1.1.2 Cost and Environmental Impact

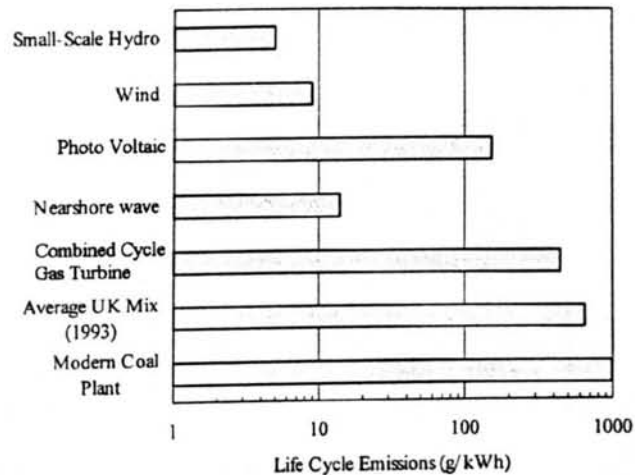


Figure 1.1: Comparison of life cycle emissions of CO₂[6]

Although waves represent a 'free' and clean source of energy, capturing this energy inevitably costs money and impacts the environment. An interesting comparison of energy sources, made more relevant by the Kyoto Protocol and so-called carbon credit scheme, is to examine the expected amount of carbon dioxide emitted to the atmosphere over the entire lifecycle of a device, divided by the expected energy yield of that device,

Figure 1.1. Noting the logarithmic scale of the diagram, the utilisation of wave energy can offer a significant reduction in life cycle emission when compared to fossil fuel generation. The device used for this comparison was the OSPREY device [4] and the emissions were primarily during material manufacture with construction, decommissioning and disposal anticipated to be an order of magnitude less.

Nuclear power stations emit zero CO₂ in use, although there will be emissions during construction and decommissioning, of which the extent of the latter is unclear.

Estimating the economic lifecycle cost of technology still at the concept stage is difficult and hence a variety of estimates have been proposed over the years. There are two main methods of cost prediction, 'engineering assessment' and 'learning curves'. The former is based on expert opinion about the potential for cost reduction over time explicitly for the application being considered and is based, for example, on closely related technology. Learning curves take a more general look at the relationship between the volume of production and the cost per unit, the trend being that the greater the cumulative production worldwide the lower the cost. A further variable is the assumptions made about financing conditions, in particular discount rates and amortisation periods, typically 8-15% and 15-20 years respectively. The general trend of these predictions over the last 20 years has been falling. A recent comparison for cost estimates, which attempts to encompass the range of predictions, is provided in Table 1-1.

Table 1-1: Comparison of predicted costs for energy sources [5]

Off shore wind	2-3 p/kWh
On shore wind	1.5-2.5 p/kWh
Wave	3-6 p/kWh
Nuclear	3-4 p/kWh
Combined cycle gas turbine	2-2.3 p/kWh
Photo Voltaic	16-10 p/kWh

Using this information, optimistic wave energy estimates put it on a similar level to nuclear energy, but more expensive than offshore wind.

1.1.3 Resource

The power contained in the world's oceans is enormous, in the region of 2 TW [6]. It is not practical, however, to consider that any great proportion of it could be harnessed. If one looks closer to home (UK) then the achievable amount of capture is still significant. Power levels of between 60 and 70 kW/metre wave front have been estimated for most suitable sites off the west coast of Scotland and Ireland. It has been

suggested that the annual average offshore wave power that is 'technically achievable' in the UK is 7-10 GW [6], of which the deep water resource is broken down as given in Table 1-2 [7]. For comparison, the present installed generating capacity in Britain is almost 80 GW.

Table 1-2: UK deep water wave energy resource which can be turned into useful energy [7]

Location	Annual energy production (TWh)
Shoreline	0.4
Nearshore	2.1
Offshore	50

1.1.4 Formation and Description of Waves

Water waves are caused by the interaction of three forces, namely wind, surface tension and gravity. Wind causes air to pass over the surface of the sea, which in turn disturbs the position of the water surface. The wave is formed as a response to this disturbance, by surface tension on the small scale and gravity when dealing with larger disturbances. As the length of time or the length of water (called fetch) over which the wind has been acting increases, so too does the height and length of the resultant wave.

Although the visible evidence of waves is on the surface there is also energy being transferred within the sea body. The particles of fluid through which the wave is travelling follow an orbital path whose amplitude decreases exponentially as depth increases. It follows that 95% of the energy contained within a wave is to be found in the region between the mean water level and a depth of one quarter the wave length.

In deep water, defined as depth greater than half a wave length, the velocity (v) of a wave is dictated by its wave length (λ), as given by equation (1.1).

$$v = \sqrt{\frac{\lambda g}{2\pi}} \quad (1.1)$$

Where g = acceleration due to gravity (ms^{-2})

In the ocean, therefore, longer waves travel faster than shorter waves. As the crest of a longer, faster, wave passes the crest of a slower wave, the amplitude of the resulting wave will be equal to the sum of the two amplitudes. The converse happens if the trough of one interferes with the peak of another. Considering the real sea state, where there are many waves of different lengths, the displacement of the surface is hence a varying frequency varying amplitude signal. These variations highlight one of the difficulties with Wave Energy Converters (WECs), namely the requirement of

adaptability to different sea states. A device which is optimised for a given amplitude and frequency must be capable of surviving in much rougher conditions if it is to have a credible lifetime. The net result is the need to over engineer structures relative to their rated capacity, a factor which increases the cost.

To calculate the mean energy contained within a given sea state it is necessary to use not the instant height of a wave but H_s , the significant wave height. This is defined as the average height of the highest third of the waves passing a site and is used in Equation (1.2) to derive power.

$$P = \frac{W\rho g^2 T H_s^2}{32\pi} \quad (1.2)$$

Where	P	=	mean power (W)
	T	=	time period (S)
	ρ	=	density $\cong 1025 \text{ kg/m}^3$ for sea water
	W	=	width of wave front (m)

The power contained within a wave is therefore proportional to its period and the square of its significant wave height.

One further description of real wave conditions is the zero upcross time, defined as the time interval between subsequent occasions when the water surface crosses the mean water height in an upward direction. It hence gives an insight to the predominant wave frequency.

These definitions may be used to further highlight the sizing difficulties for WECs. A typical site may have a most likely sea state of 0.75 m height and 6.5 seconds period, giving power levels of just 3.6 kW per metre wave front, yet a device sited there to extract this will also be expected to survive in states of 5 m height and 12 seconds period corresponding to almost 300 kW per m wave front: two orders of magnitude greater.

1.1.5 Principles of Energy Capture From Waves

1.1.5.1 Oscillating bodies

The fundamental principle behind absorbing energy from a water wave is that energy must be *removed* from that wave. It therefore follows that the resultant wave, after passing the wave energy device, is either reduced or cancelled altogether.

A WEC, or indeed any object, oscillating in water will produce waves. It is the interaction of the waves produced by the device and the original wave that gives the

resultant wave. For the device to remove energy from the wave, it is necessary for the resultant wave to be smaller than the incoming wave, and hence the two waves interfere destructively. If a device is to be a good wave absorber it must therefore inherently be a good wave maker.

A symmetrical body constrained such that it may only oscillate in one plane, either perpendicular or parallel to the water surface, is only able to absorb a maximum of 50% of the energy contained in an incident wave [8]. This is demonstrated in Figure 1.2.

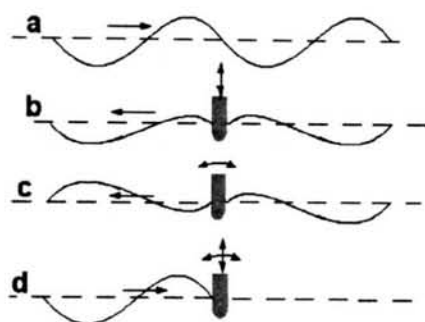


Figure 1.2: Demonstration of absorbing wave energy

The upper curve (a) represents a pure undisturbed sinusoidal wave, the ideal/theoretical sea state. In curve (b), an axisymmetric body is heaving (oscillating vertically) in otherwise undisturbed water. Similarly, curve (c) shows the same body producing axisymmetric waves by rocking.

Curve (d) shows the effects of summing the previous three curves. It hence shows the effect of a WEC being allowed to move in two degrees of freedom. The wave approaching the device is unaltered from the original wave, as the effects of the body corresponding to its degrees of freedom cancel each other out. After passing the WEC, however, these effects are summated and equal in magnitude to the original wave. Thus the theoretical ideal of 100 % energy absorption from the approaching wave by a device with two degrees of freedom is shown.

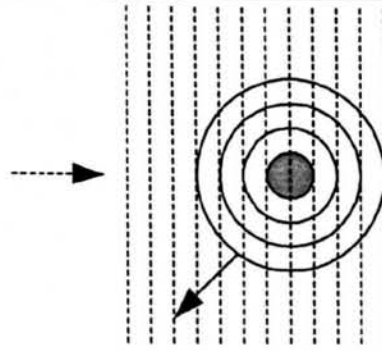


Figure 1.3: Plan view of a point absorber interacting with uniform wave train

Figure 1.3, a plan view of a symmetrical body oscillating in uniform waves, demonstrates that an oscillating point absorber affects a section of the approaching wave front greater than its width. The maximum energy which may be absorbed from an axisymmetric body equals the wave energy transported in an incident wave front of width equal to the wavelength divided by 2π [8]. This width is termed the absorption width.

1.1.5.2 Controlling a Wave Energy Converter (WEC)

Any buoyant body on the surface of a still liquid will start to oscillate and create waves if it is given an initial displacement. The equation of motion for the body given in (1.3) shows three forces acting on the body, corresponding to inertia (I), buoyancy (B) and drag (D), being equal to the radiation force required to create the waves, (F_R).

$$I\ddot{x} + D\dot{x} + Bx = F_R \quad (1.3)$$

Considering the homogeneous case, where the radiation force is set to zero, the body will behave in the familiar damped oscillatory motion common to any mass-spring-damper system as described by (1.4). A crucial characteristic of this type of system is that its natural frequency, i.e. that at which it oscillates when unconstrained, is the frequency in which it must be excited to have maximum amplitude oscillation, its resonant frequency, defined in (1.5).

$$m\ddot{x} + C\dot{x} + kx = 0 \quad (1.4)$$

Where

m	=	mass (kg)
C	=	coefficient of damping (Ns^{-1})
k	=	spring constant (Nm^{-1})

$$f_0 = \frac{1}{2\pi} \sqrt{\frac{k}{m}} \quad (1.5)$$

Where f_0 = resonant frequency (Hz)

If the body is to be used to extract power from its supporting liquid its efficiency will be a maximum when the frequency of the waves within the liquid equals the natural frequency of the floating body. In a liquid with regular sinusoidal waves the equation of motion becomes (1.6).

$$I\ddot{x} + D\dot{x} + Bx = F_R + F_E \quad (1.6)$$

Where F_E = the exciting force on the body (N)

F_E is equal to the force felt by the body held fixed in the incident waves. Furthermore it is possible to decompose F_R into its constituent parts corresponding to the added mass (M_a) and the damping (C) terms, as in (1.7).

$$-F_R = M_a(\omega)\ddot{x} + C(\omega)\dot{x} \quad (1.7)$$

Where ω = frequency (rs^{-1})

Physically, the added mass is the mass of water which must also be accelerated to allow the device to accelerate, it is hence dependant on both frequency and device topology. Substitution of (1.7) into the equation of motion, (1.6), gives (1.8)

$$(I + M_a(\omega))\ddot{x} + (D + C(\omega))\dot{x} + Bx = F_E \quad (1.8)$$

Comparison of (1.8) with (1.4) and (1.5) shows that the resonant frequency of a floating body in regular waves is given by (1.9).

$$f_0 = \frac{1}{2\pi} \sqrt{\frac{B}{I + M_a(\omega)}} \quad (1.9)$$

In order to maximise the power absorption from a variety of different frequency waves it will be necessary to alter the resonant frequency. Inspection of equation (1.9) shows that a controllable external force, provided by the power take off mechanism, either in phase with the acceleration or the displacement of the device, could be used to influence the behaviour of a WEC by altering the denominator and numerator of the right hand side respectively. The device could hence be manipulated such that it was continually in a state of resonance. Alternatively, varying the actual buoyancy of the device alters 'B' in (1.9) and would hence have an identical effect.

Many control strategies have been suggested to control WECs e.g. [9, 10, 11, 12, 13, 14], encompassing the introduction of extra forces, equipment and buoyancy alteration.

The choice of strategy depends on the permitted complexity, natural characteristics of the device and the capabilities of the power take off mechanism. The simplest to execute is known as latching and involves deliberately restraining the device at the extremities of oscillation. The release of the device is delayed until a sufficient buoyancy force has built up to ensure that the velocity and force peak at the same time.

The converse of this concept, i.e. unlatching, also exists. The device is allowed to move freely for part of the cycle and the power take off mechanism is only engaged when the device has reached the desired velocity. Unlatching is utilised when the natural period of a device is longer than the most frequent wave spectrum. Both latching and unlatching are described as discrete control functions, because they are only operable at specific points in the oscillation cycle.

In a continuous control strategy the position and velocity of a device are measured continuously and adjustments to its motion are made in real time at any instant in the device's cycle. The ultimate control system for a wave energy device which allows the theoretical maximum amount of power to be removed from a wave is known as complex conjugate control. Appropriate mathematical models exist which require future knowledge of the sea state [10] but their complexity leaves them outside the scope of this thesis. Its rationale is analogous to maximising power output of a generator by connecting a resistive load equal to that of its own internal resistance [15]. All the spring and inertia forces are manipulated to cancel each other out by continuously adjusting the damping force.

On the right hand side of (1.6) the equation of motion was split into two distinct forces, F_R and F_E , acting on the body. The radiation term F_R is primarily dependent on the geometry of the device and the velocity at which it is oscillating. In a system of more than one degree of freedom this consists of a matrix containing both real and imaginary terms, represented in the form of a complex radiation impedance matrix. The second term F_E is the force that would be required by a device to remain stationary in water with unit amplitude incident waves.

Equation (1.9) above demonstrated how these equations could be applied to a single degree of freedom device and used to calculate the frequency at which it would resonate. For more complex systems this could be done by taking the eigenvalue of the resultant force equation. A simplified version of this method approximates the eigenvalue by a causal control function, whereby prediction of the sea state is avoided [15,11].

Continuous control may require the return of energy to the sea for part of the oscillation cycle in order to keep the exciting force and body velocity in phase. The theoretical advantages of such a move are demonstrated in Figure 1.4 [9] which shows the cumulative amount of energy absorbed by a small scale wave energy converter in a 5 second period under three differing control strategies. The lower curve has no control and absorbs energy at a reasonably constant rate throughout the cycle. The middle curve, which shows a converter employing latching control, also shows a constant rate of energy accumulation, yet after 5 seconds its total yield is 4 times that of the uncontrolled oscillation.

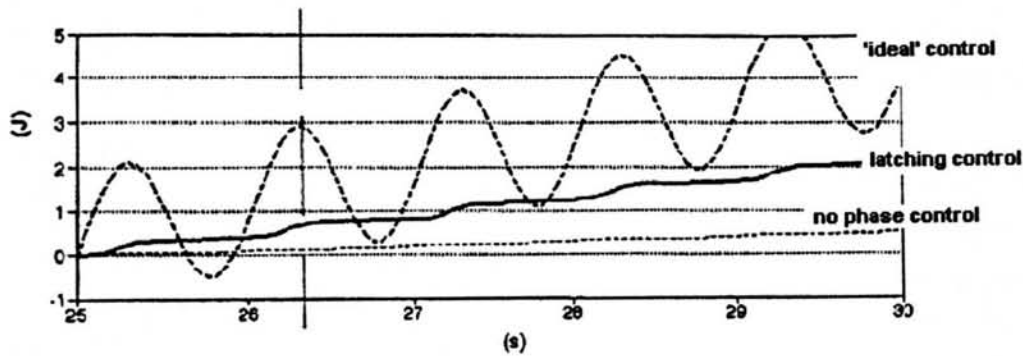


Figure 1.4: The advantages of control [9]

The upper curve, showing the energy absorbed by the device under full complex conjugate control shows some interesting features. The cumulative energy absorbed is continually oscillating, demonstrating that for part of the cycle energy is being returned to the ocean. By the end of the 5 seconds, however, the average energy removed from the sea is more than double that of the latching control and almost 10 times that of no control. The long term impact of an effective control strategy on the energy yield of a device over its lifetime is clear.

1.1.6 Wave Energy Converters (WECs)

Broadly, there are three ways of classifying a wave energy converter in terms of its position. Shoreline devices are mounted rigidly to the shore, thus ensuring simple maintenance and grid connection. The cost of land intrusion and the possibility of naturally advantageous sites being environmentally sensitive has to be considered in these schemes. Secondly there are nearshore devices, typically situated in 10-25 m depth of water. The device may be tight moored to the sea bed, either by way of pillars or tensioned cable, thus providing both stability and a datum to react force against.

Deep water or slack moored devices have no such direct contact with the seabed, and any moorings are to maintain geographical position only. It is this third category which is to be strived for. Although it presents the most technical problems it represents the largest energy resource (Table 1-2).

It is possible to group WECs according to their geometry as terminator, attenuator or point absorber, the latter of which has already been introduced. A terminator has its principal axis parallel to the incident wave crests and as such the waves are stopped as they reach the device. These devices hence tend to be quite wide, so that a large amount of the wave front will affect the device at one time. The classic example of this type of WEC and arguably the most famous of all WECs is the Edinburgh or Salter Duck [18]. This is a cam shaped floating device which is allowed to rotate about a spine. Long lines of these devices are capable of removing 100 % of the energy contained in incident waves. As a wave approaches the device the cam rocks about its axis, which is assumed to be relatively stationary. The design is such that the circular rear section does not transmit waves downstream of the device, leaving a theoretically flat water surface.

Attenuator devices have their principal axis perpendicular to the wave crests and so face the waves 'head on'. The energy is converted by relative movement of parts of the device as a wave passes underneath it. A device of this type, known as the Pelamis [16,17,19], is currently being developed for deployment off the Isle of Islay, Scotland. It is a snake like structure consisting of a number of floating segments hinged together. Power take off is in the form of hydraulic rams driven by the relative movement of the segments as a wave passes underneath.

Many other WECs have been proposed, e.g. [18, 19, 20, 21], some of which lend themselves more favourably to direct drive e.g. [22]. Good summaries covering many concepts to date are available e.g. [2, 23, 24]. Only three are presented here, the first because it is conceptually the simplest, and has been the subject of much enlightening mathematical analysis [25], the second because it has direct drive power take off and has an active research programme, and the third because its structure naturally lends itself to direct drive operation.

1.1.6.1 Heaving Buoy

A heaving buoy consists of a floating body, typically cylindrical or spherical, following the water surface in the vertical plane and reacting either against the seabed or a submerged drag plate. It may hence be a nearshore or deepwater device. As it only

has one degree of freedom, it is limited to capturing a maximum of 50% of the energy available in its absorption width.

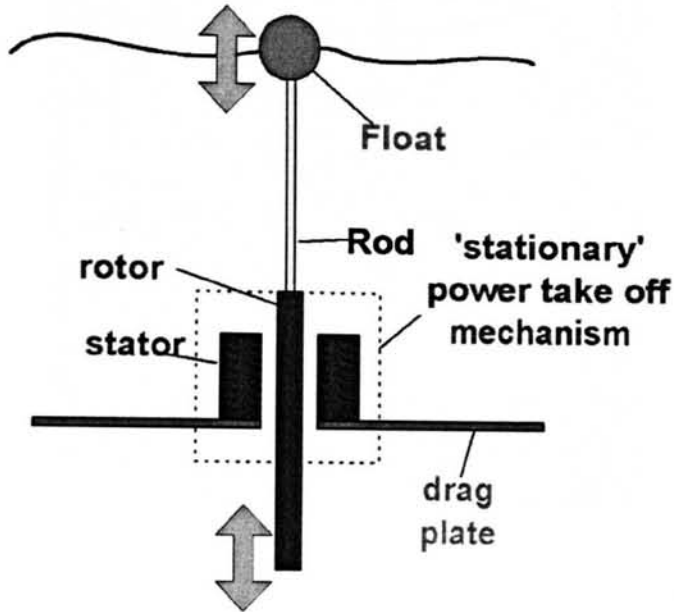


Figure 1.5: Direct drive heaving buoy

There have been many methods proposed for the power take off of this device, for example an elastomeric hose whose change in cross-sectional area with flexing is used to pump water [26]. Figure 1.5 shows the direct drive proposal, whereby the rotor of a linear generator is coupled directly to the buoy, and the stator is mounted in a submerged drag plate. Mathematical descriptions of similar two body proposals have been presented [27, 28], along with strategies for its efficient control [14]. Some characteristics of this device are explored more fully in Chapter 2.

1.1.6.2 Archimedes Wave Swing (AWS)

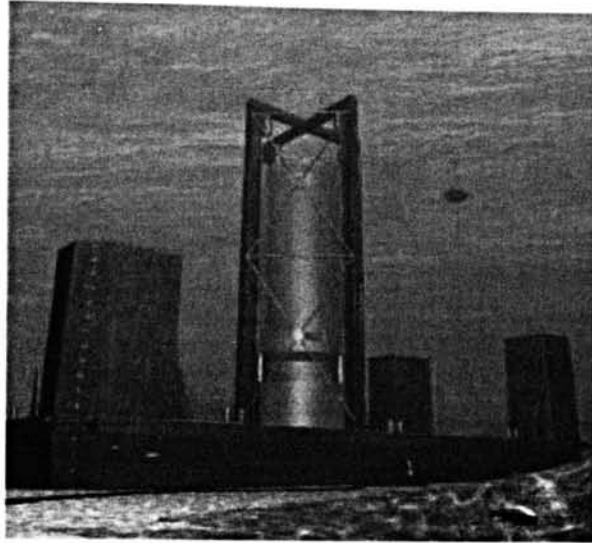


Figure 1.6: AWS

The AWS, as shown in Figure 1.6, is a nearshore device mounted on the seabed. It consists of an air filled chamber, which has the freedom to move in a vertical plane relative to its base. As a wave passes over one of these devices, the added depth of the water causes an increase in water pressure surrounding the device. The volume of air within the device is hence compressed allowing the entire hood of the device to fall. The device will rise again when a trough passes over the device, and the net result is hence slow speed reciprocating motion. A 2 MW device was due to be commissioned in September 2001 which has a 3-phase permanent magnet linear synchronous machine as the power take off mechanism [29]. Various technical problems have prevented the successful deployment of the device [30]. Details of a prototype of this device are given in Chapter 8.

1.1.6.3 Interproject Sweden (IPS) Buoy

This deep water device, also known as the mace, was first developed in Sweden in the 1980's [31], and a sloped variation has been the subject of more recent research [32, 33]. Current proposals for its development have the power take off device either as a sea water pump [34], or high pressure oil rams [35].

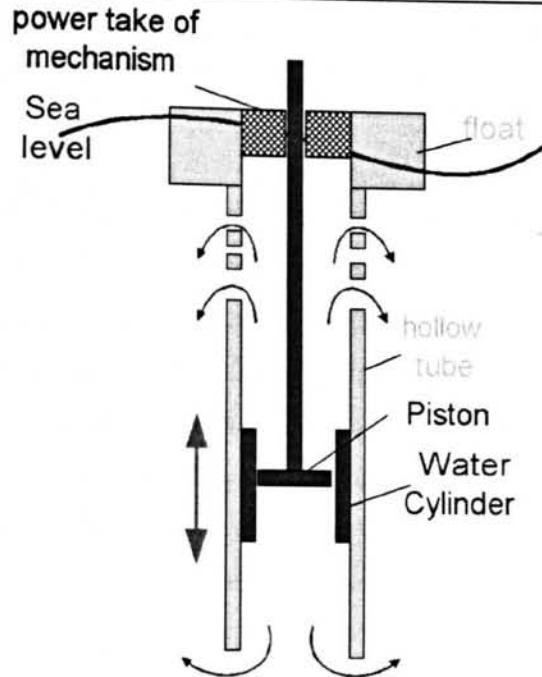


Figure 1.7: IPS buoy

Figure 1.7 shows a schematic diagram of the possible direct drive device. It shows a semi submerged float coupled to a totally submerged hollow tube, open to the sea at both ends. Part of the tube forms a cylinder enclosing a piston connected to a rod, it is relative motion between the rod and the float which forms the basis for power take off.

The enclosing cylinder prevents the water from simply slipping around the piston, effectively coupling it to the weight of the encapsulated water. The entire tube, float and cylinder will hence follow the water surface whilst the piston itself is held relatively still. If the amplitude of oscillation becomes too large, the piston will move out of the cylinder and become de-coupled from the mass of the surrounding water, thus allowing it to follow the oscillation of the tube. This feature provides built in protection against the power take off device being damaged, a function normally requiring end stops. A further advantage of this device is the possibility of running it inclined, which alters the buoyancy force and hence frequency response. It has been shown that the net effect of this is to widen the bandwidth of resonance and so shift the burden of control from the power take off mechanism to a buoyancy controller [33].

1.2 Tidal Stream Energy

1.2.1 Introduction

Previous work into the extraction and utilisation of power from tides has centred on large barrier type system, such as that frequently proposed for the Severn Estuary. In this type of scheme, water is trapped at high tide and then released through low head turbines when the tide has fallen, converting potential energy given to the water by the tides. A summary of the various methods and strategies for optimum energy extraction using this type of scheme, along with major existing and proposed sites worldwide is available [36]. In tidal stream energy projects, however, kinetic energy is extracted from the mass of water as it moves naturally between high and low tides, eliminating the need to construct barrages. Relative to both wave energy and tidal energy, tidal stream energy is quite a young technology with comparatively little research completed to date. This is due, in part, to the conclusions of a 1993 report which acknowledged the large resource available to the UK yet concluded that the cost of capture was prohibitively high, in the region of 17 – 39 p/kWh for the two most promising sites in the UK [37]. That report, funded by the Energy Technology Support Unit on behalf of the Department of Energy, led to the withdrawal of support from the UK Renewable Energy Programme for any tidal stream energy proposal. Several other independent organisations continued to be interested and research programmes continued. Their judgement was ratified by the conclusion of a more recent Department of Trade and Industry report which gave a cost estimate for the same site as 4.56 p/kWh [38]. This estimate, with an 8% discount rate over 29 years, has again renewed interest and government support from the renewable energy program for this energy source.

Based on sites with a mean spring tide greater than 2ms^{-1} , it has been estimated that 10 % of the UK's electricity capacity may be provided by expected recovery rates of energy from tidal streams [39].

This condensed form of energy is proportional to the cube of the water velocity, for example 1.89kWm^{-2} in a 1.5ms^{-1} flow. The theoretical maximum energy which can be extracted from a tidal stream is known as the Betz limit and equal to 59% of that available.

A crucial advantage of tidal stream energy over many other renewable resources is the predictable nature of its output, allowing accurate predictions of its annual yield and giving utilities ample warning of periods of low energy (i.e. neap tides).

1.2.2 Tidal Stream Energy Converters

Most forms of tidal stream energy converter to date have been analogous to wind turbines, in that they have centred around horizontal axis, multi bladed turbines, e.g. [40, 41]. As such they produce slow speed rotational motion, typically of the order of 10 rpm, which has previously demanded the utilisation of a gearbox drive train. This type of device falls outside the scope of this research, which focuses on reciprocating, primarily linear, generators. It should be noted, however, that rotary versions of the electrical machine topologies presented here would be suitable for use in these devices and hence many of the issues addressed are also relevant to this type of converter.

One device exists, however, which does require slow speed reciprocating linear power take off. The Stingray™ is a seabed-mounted device, consisting of one or more hydroplanes with variable angle of attack [42]. Figure 1.8 shows this device and the direction of tidal flow. As the angle of attack of the hydroplane is altered, so too is the resultant force on the pivot arm. The entire hydroplane and pivot arm can hence be made to oscillate about the post in a vertical plane.

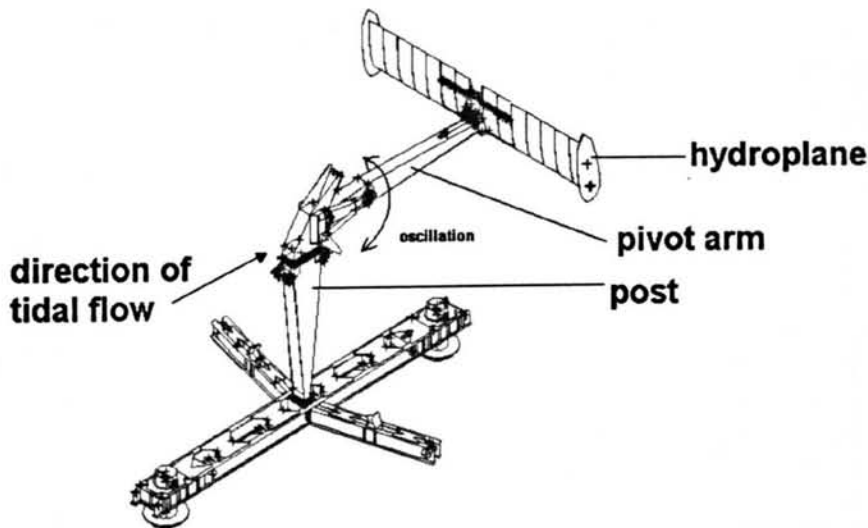


Figure 1.8: Stingray tidal stream generator

At present power take off is by way of four high pressure hydraulic cylinders mounted at the top of the post, coupled to the pivot arm. Chapter 7 explores this device and its power take off more fully.

1.3 Electrical Power Take off

Electrical machines have traditionally been designed to be driven at high speed rotary motion, typically from an internal combustion engine. This corresponds to an airgap speed within the machine of upwards of 60 m/s, allowing for easy conversion into a rapid change in flux. A typical wave energy converter, however, can expect to produce linear oscillatory motion with velocities in the region of 0.5-2m/s. Previously the trend for both wave energy and tidal energy converters has been to match the motion of the device to that required by the traditional high speed rotary electrical machines by complex systems of hydraulics, pneumatics or gearboxes. These mechanical linkages were required to rectify and step up the velocity.

A direct drive system is one where there are no intermediate mechanical systems between the primary moving element of an energy converter and the electrical machine. Directly coupling the moving element of the electrical machine to that of the energy converter in this way places special requirements on the electrical machine, in the form of slower speeds, higher forces and a variable power input not present in schemes with extra mechanical systems. It is these special requirements which have previously led the engineer to use 'off the shelf' high speed rotary electrical machines and create innovative solutions to match the required and provided motion within the energy converter. Figure 1.9 shows that these extra mechanical steps significantly increase the complexity of the overall power train.

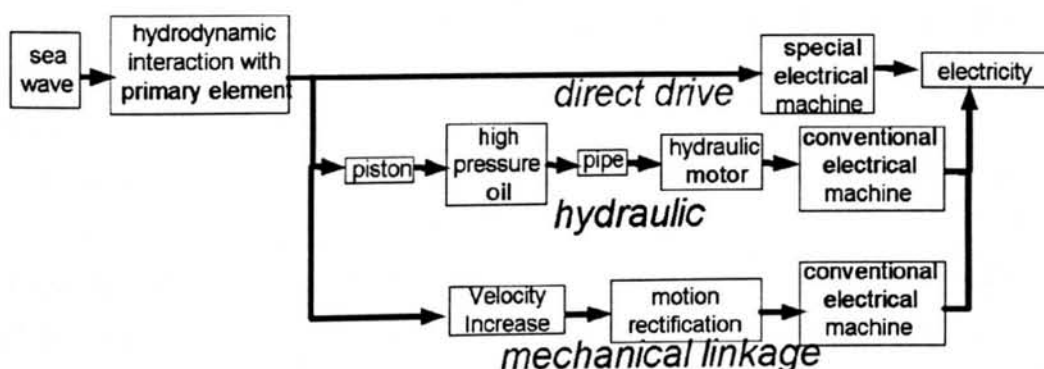


Figure 1.9: Alternative power take off schemes

Wind turbines also produce a slow speed motion, and current practice is to use a conventional high speed induction or synchronous generator, operating at 1500 rpm driven by a step up gearbox. Research in this area has allowed direct drive generators to be proposed, using electrical machines capable of running with airgap speeds of 5-6 m/s [43].

The concept of direct drive marine energy converters is hence an extension of slow speed electrical machine research. The principle was highlighted in the heaving buoy wave energy converter illustrated in Figure 1.5, where the float of the device is intended to follow the movement of the water surface. The linear generator translator is coupled directly to the float and so too follows the motion of the waves. The device is slack moored, making it appropriate to use in deep water. Energy is removed by developing a force between the moving element and the submerged drag plate, which will remain stationary or nearly stationary. As is clearly demonstrated, the direct drive system offers a very elegant method for power take off in this example, with an absolute minimum of moving parts.

1.4 Aim of Thesis

The research described in this thesis intends to enlighten the reader into the potential issues associated with the integration of linear generators into marine energy converter devices. The development of suitable electrical machines specifically for this application forms the bulk of the work, whilst some mechanical and electronic issues are highlighted and reference made to their relative importance, impact and solution.

1.5 Layout of thesis

This thesis unites a fairly diverse range of subjects separated into chapters and a brief word as to their content may prove useful to the reader. Where possible, separate chapters have been used to introduce distinct areas of research, yet some interaction and cross referencing is necessary.

The fundamentals of capture of marine renewable energy and hence the context of this research has been highlighted in this Chapter. Chapter 2 examines the variety of systems available for power conversion within marine energy converters, with particular emphasis on hydraulic systems, and hence explains the novelty of a direct drive approach.

Various topologies of linear electrical machine are introduced in Chapter 3, and some simplified comparisons made. From this, two preferred topologies are identified and investigated in significant detail in the proceeding two chapters.

Mechanical issues addressing the integration of these machines into energy converters and the main criteria upon which each electrical machine can be compared are discussed Chapter 6.

In Chapters 7 and 8 generators are proposed for use in existing wave and tidal energy converters.

The primary conclusions and author's recommendations for further work are identified in Chapter 9.

Chapter

2

Power Take off Systems

This chapter aims to demonstrate how the choice of power take off system influences the overall characteristics of a marine renewable energy device. The relative merits of alternative schemes are investigated. In particular a hydraulic system is examined in some depth, highlighting both the features of such a system and factors to be considered in the choice of power take off systems in general.

Comparison is made to current practice in offshore wind turbines, whose environment, rating and regulation is likely to be similar to that found in Marine Energy Converters (MECs).

2.1 Requirements of power take off system

The main requirements for the power take off in this kind of application are high thrusts, of the order of 10^6 N, combined with low maintenance, preferably requiring inspection of the device annually or less [3]. Ideally this would be achieved utilising a weight comparable to that of the proposed device, in order to avoid the need for extra buoyancy.

Survivability and reliability are key to the successful operation of a renewable energy generator, both in terms of time (20 years for offshore wind turbines) and response to extreme environmental events.

Electrically, the power take off mechanism must supply the grid at a constant frequency and voltage. Take for example a large wind turbine developed for offshore use whose power take off is a 6 pole doubly fed asynchronous generator, with a nominal speed of 1100 rpm and an output of 0-2750kW. The voltage has a variation of $\pm 10\%$, the frequency -5 to 3% and a power factor of 0.9 to 1 [44]. It can be envisaged that an MEC should strive to achieve a similar performance.

2.2 Direct Mechanical Linkage

The motion of an MEC can be converted to a suitable form by the use of a step up gearbox, possibly in combination with a rectifying device such as a ratchet. The introduction of a gearbox introduces extra mechanical complexity, system losses, monitoring requirements and more importantly enforces regular maintenance in terms of oil changes.

Although gearbox technology is well established, for example in the automotive industry, these are generally step down gearboxes of a smaller capacity and used intermittently. In the wind power industry, where ratios, ratings and lifetimes are likely to be similar to those required here, gearboxes have proved to be problematic, representing a considerable cost factor of a conventional wind turbine [45]. Further, the industry has been dogged by high profile cases of gearbox failure. A major wind turbine manufacturer, NEG Micon, had to replace 1250 gear boxes in 600, 700 and 750 kW machines after 150 of their gearboxes had problems [46].

The demands on a gearbox may be demonstrated by considering a 150 kW Stingray device, oscillating with a peak velocity of 2 m/s at its tip. A typical electrical generator for this rating would have a shaft diameter of the order of 70 mm and a rated speed of about 2000 rpm. If the linear speed of the hydroplane was converted directly into rotary motion using a rack and pinion arrangement, a 0.3 m diameter pinion would have a peak speed of 63 rpm. Even at the peak point in the cycle, then, a gear ratio of the order of 30 is required to match the required and available motion. Further inspection of the device implies that the long length and implicit speed reduction of the pivot arm (\cong 12m) in combination with the sinusoidal nature of its oscillation would require a gearbox with a significantly higher step up ratio and be subjected to a constantly varying load.

2.3 Pneumatic system

A typical pneumatic system for a WEC, known as an Oscillating Water Column (OWC), consists of a partially submerged air compartment with one end open to the ocean and the other open to the atmosphere. As the water level inside the chamber oscillates with incoming waves, so too must the air above it, which is hence periodically expelled to and drawn from the atmosphere. The energy in the waves is thus converted into an oscillating column of air with a velocity greater than that of the waves, Figure 2.1, which may then be converted to high speed rotary motion by an air turbine.

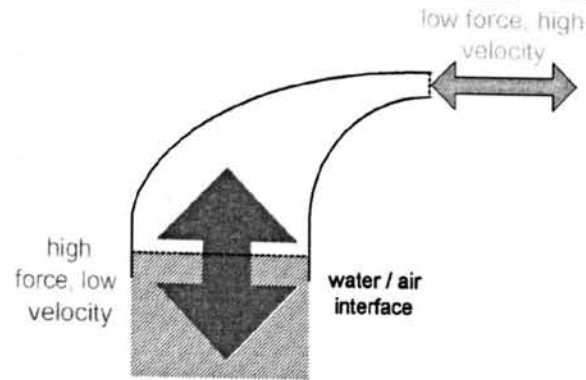


Figure 2.1: Pneumatic gearing in an OWC

In the 1970's Professor A Wells of Queens University Belfast proposed a form of self rectifying axial flow air turbine which rotates in the same direction irrespective of the direction of airflow. The Wells' Turbine became part of the standard power take off system for any OWC proposed as it provides a simple method of rectifying the movement of the air into high speed rotary motion. Further research, however, has highlighted its inherent disadvantages such as low efficiency (<40%), poor starting, high noise and high axial thrust when compared with a traditional turbine [47]. Variable pitch turbines, either externally controlled with hydraulics [48] or with self pitch control [49], have since been proposed. Both of these offset slightly the Wells' turbine disadvantages. It should be noted that the requirement for this type of unidirectional turbine technology is specific to WECs, which implies that research into efficiency improvements will only be carried out within the wave energy community.

The entire pneumatic system and turbine acts as a mechanical linkage both increasing and rectifying the motion contained within a wave. Furthermore, the resonant frequency of such a device and the power extracted from the ocean may be controlled by restricting the airflow through the turbine or by venting directly to the atmosphere.

2.4 Hydraulic system

2.4.1.1 Over view

Hydraulic systems are frequently proposed for power take off in wave energy devices and the current version of the Stingray device. Typically a hydraulic ram is used to convert the motion of the device into high pressure oil, which is then fed into a hydraulic motor driving an electrical machine. Slow speed high forces are hence converted into rotary high speed motion with a minimum onboard weight. Furthermore,

the reactive force of the rams can be controlled by the working pressure of the system. The addition of one, or possibly two, accumulators into the system allows some provision for energy storage. The system of Figure 2.2 shows a double action piston feeding into a high and low pressure accumulator. A throttling valve controls oil flow which then drives a hydraulic motor and electrical generator.

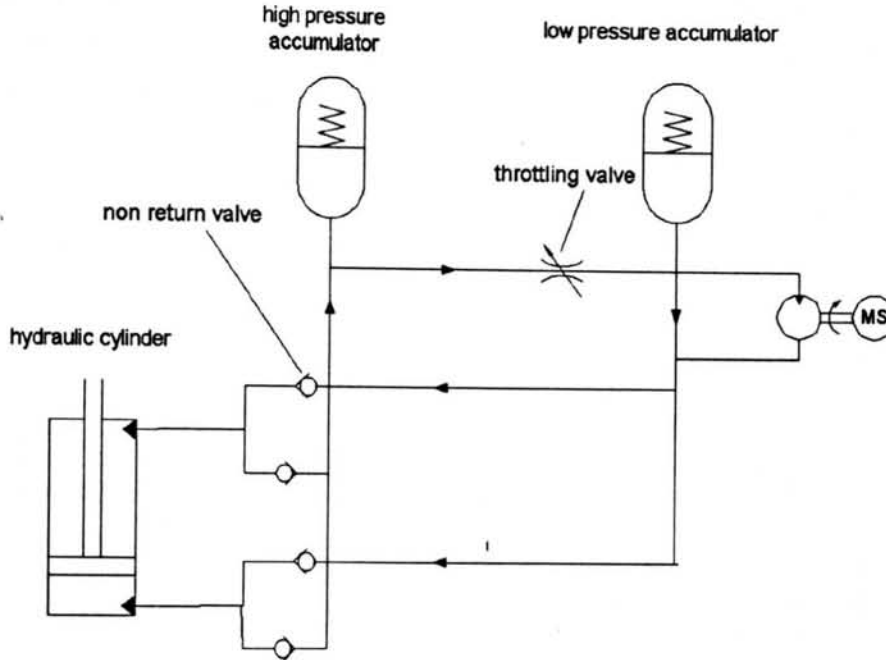


Figure 2.2: Hydraulic power take off system

Any configuration of a hydraulic power system would likely have the electrical plant close to the device, the advantage of remote shore based conversion being offset by the disadvantage of long, costly and inefficient pipe work.

Realistically, a hydraulic system is the most likely competitor to a direct drive system, because gearboxes are accepted as cumbersome and rarely proposed in WECs and the pneumatic system of an OWC is inherent in its design. As such, a typical hydraulic system is examined in further detail, and its specific parts are outlined below.

Rams

Typically used as actuators in hydraulic the industry, in this application they are used to displace the hydraulic fluid at high pressure. The dynamic seals enforce a restriction on the extraction and contraction velocity of the piston. Pressure inside the ram can be of the order of 400 Bar, allowing it to exert a very large thrust.

Accumulator

Gas-pressurised accumulators are the preferred method in the hydraulics industry for energy storage. They consist of a pressurised vessel containing hydraulic fluid and an inert pressurised gas, possibly separated by a variable membrane to avoid contamination. As more fluid is forced into the accumulator, the gas is compressed and hence the pressure of the vessel increases. If the variation in pressure due to the WEC is assumed to be sufficiently fast, and the accumulator is assumed to be a thermal insulator, the process is adiabatic and dictated by (2.1).

$$PV^\gamma = c \quad (2.1)$$

Where	P	=	pressure (Pa)
	V	=	volume (m ³)
	γ	=	1.4
	c	=	constant

Non return Valves

These are necessary to enforce the correct flow of oil around the hydraulic circuit. They will have some pressure drop, Δp , and hence power loss associated with them, the value of which may be calculated using (2.2), which assumes they may be modelled as a simple orifice of area A.

$$Q = \mu A \sqrt{2\Delta p / \rho_0} \quad (2.2)$$

Where	Q	=	flow rate (m ³ s ⁻¹)
	μ	=	discharge coefficient = 0.61 [13]
	ρ_0	=	density of oil (kgm ⁻³)

Motor

The ideal motor would have variable displacement volume and be able to work at the desired pressures and flow rates. Axial piston or wing motor appear to be suitable for this application, although the efficiency of these drops off at part load. A specific hydraulic motor suitable for this type of application has also been proposed, [50], which claims to be able to deliver varying input powers and pressures to a constant output load at high efficiencies.

2.4.1.2 Limitations of hydraulics

Hydraulic systems are expensive and designed to operate at speeds even lower than those of a typical WEC. Although the technology of hydraulics is well established, this

application is using the components in a role reversal, driven by linear motion (acting as rams not actuators) and driving rotary motion (motor not pump). As such a degree of research into their mass utilisation is still required. If oil is to be the working medium then the marine environment strictly enforces its containment to prevent contamination. This places a stringent limit on the maintenance interval in terms of moving seal life. There is a theoretical advantage in using fresh water as the medium, but leakage could then be expected to increase one thousand fold when compared to hydraulic oils, in line with the three order of magnitude decrease in viscosity.

The need for moving seals in the hydraulic rams limits the speed with which they can be operated. The maximum speed would be typically around 0.5 m/s. With the life of the seal being inversely related to the speed, distance and length of its application, it may prove desirable for the speed to be kept even lower, in the region of 0.1 m/s. An example of how hydraulic systems are the bench mark for WECs is demonstrated by a device known as the Pelamis [19] in which the designer deliberately reduces the speed of movement to those utilisable by hydraulic systems. A further example is highlighted in Chapter 7 for the design of the Stingray tidal stream device.

The requirement for non return valves, crucial to the use of accumulators, will detract slightly the efficiency of the system due to the inherent pressure drop across them.

The use of flexible hose potentially offers an attractive solution to the problem of locating the hydraulic motor and accumulators remote from the rest of the device. However, flexible hydraulic hoses do not perform well in the marine environment, especially not in comparison to electrical cable [51]. Using rigid steel pipe work clearly avoids this problem but enforces all parts of the hydraulic system to be mounted on the same platform.

Hydraulic technology is a mature technology, with a known and proven reliability. Similarly, however, the disadvantages of slow speed and low efficiency at part loads are equally proven.

2.5 Direct Drive

2.5.1 Introduction

A direct drive power take off system has the electrical generator and moving part of the device joined together with no intermediate mechanical systems. As such the resulting system is mechanically simple, with less moving parts than either a gearbox or hydraulic system.

The electrical machine is required to convert slow reciprocating motion directly into electrical power without the luxury of having the motion rectified and increased. Slow speed high power conversion inherently requires high forces to be reacted. For an electrical machine this implies the provision of a large airgap surface area. A 100 kW conventional machine with an average airgap shear stress of 20 kN/m^2 whose motion was just 1 m/s , as might be the case in a wave energy converter, would have to react a force of 100 kN , requiring an airgap area of around 5 m^2 . These large areas have dissuaded most designers from the direct drive route and imply that it may not be suitable for all MECs. Modern electrical machines, with higher shear stresses, provide the opportunity for more reasonable size machines.

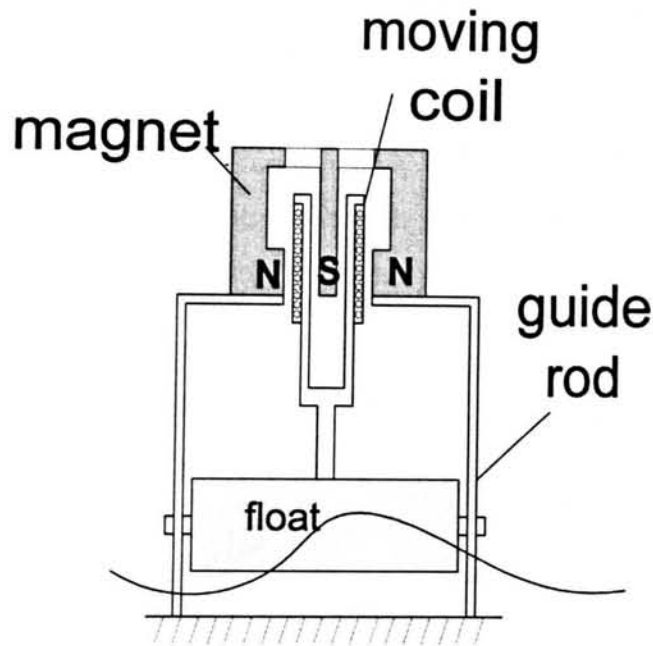


Figure 2.3: Previous direct drive proposal

The direct drive concept was first proposed in 1978 by Baz and Morcos [52], the linear version of which is shown in Figure 2.3 and its rotary counterpart in Figure 2.4. They appropriately based their design on the simple principle that electric current will be induced in a coil if it is moved relative to a magnetic field. As a wave passes through the device, the float rises, which in turn alters the position of the coils with respect to a permanent magnet. The coils experience a change in flux linkage and by Faraday's law an emf is induced. Limitations in available permanent magnet material and the utilisation of such simple electrical machine topology led the authors to conclude that the low conversion efficiency of the linear and the low speed oscillation of the rotary versions prohibited their use. The research programme hence diverted towards devices with inherent speed amplification and rectification, involving the use of a fly wheel coupled to the float via a sprocket and chain configuration.

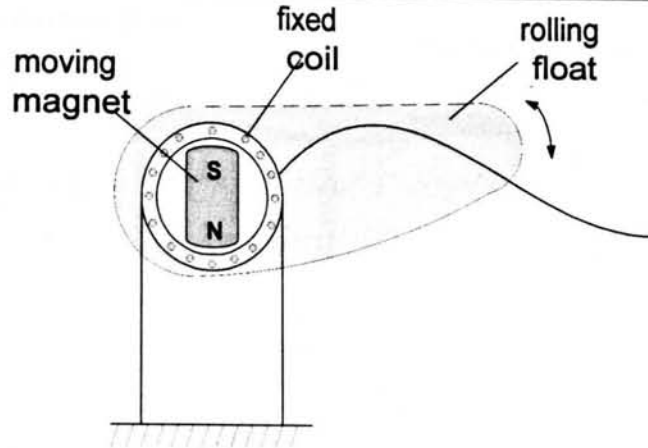


Figure 2.4: Direct drive proposal with rolling magnetic field

The use of linear permanent magnet machines directly linked to the device has been suggested more recently [53]. This system, shown in Figure 2.5, was proposed as a method of controlling the oscillation of the sea surface. It was not suggested that this device be used as the power take off mechanism however, and the linear machine was used as a control mechanism. It allowed the controller to eliminate the difference between the actual and desired chamber pressure by acting as additional damping for parts of the cycle.

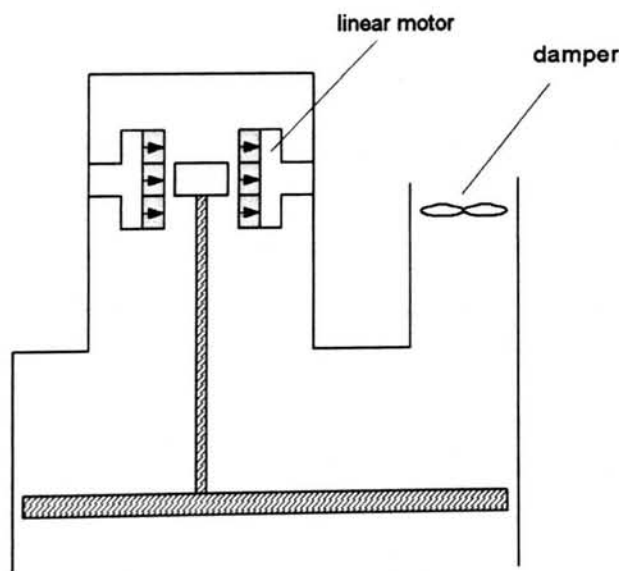


Figure 2.5: Linear motor as part of control strategy

Two groups are presently engaged in the research of direct drive as the primary source of power take off for wave energy converters, the AWS concept mentioned previously and further in Chapter 8, and a UK based company: Direct Thrust Designs plc. The latter of these have patented a tubular machine, whereby the armature winding moves relative to a permanent magnet translator, Figure 2.6 [54].

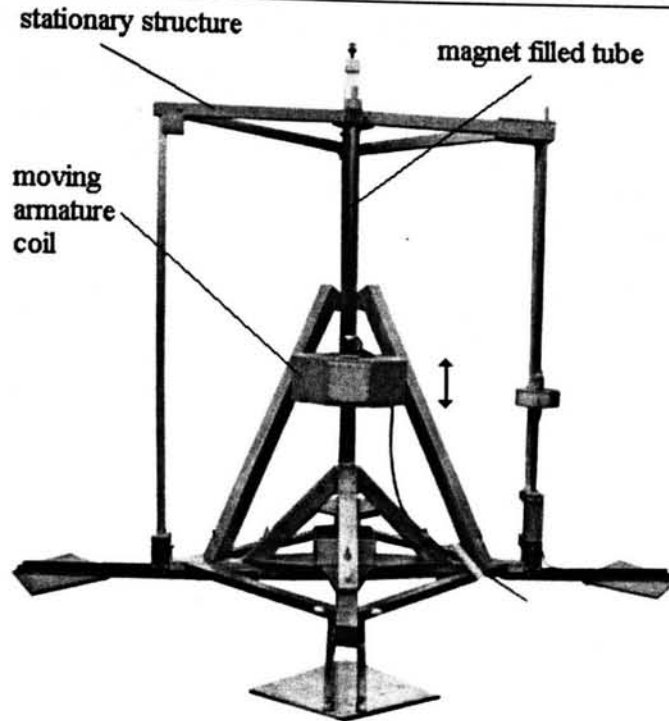


Figure 2.6: Direct Thrust Designs plc 500 W prototype WEC

2.5.2 *Electronic conversion for direct drive*

A major concern, common to all power take off strategies, is the lull in output power inherent with reciprocating motion and also the variation of net power due to atmospheric conditions. The predictable nature of tidal currents gives protection for the latter of these. Although it may be possible to operate several devices out of phase in an array and minimise the short term lull in power, some smoothing will still be necessary. Furthermore, it is advantageous to have a stand alone device with its own power smoothing, both to allow single deployment and also give protection against unit failure, i.e. preventing a fault in one device disabling an entire array. This is an area where both hydraulic power take off and, to a lesser extent, pneumatic systems, offer a reasonably simple solution, in terms of gas pressure and kinetic energy storage respectively.

In a direct drive system it is preferable if the energy can be stored in an electrical form, by means of a battery or capacitor. For a generator subject to sinusoidal motion, the RMS voltage and current are both $\sqrt{2}$ smaller than would be obtained if the velocity were constant. An energy buffer is required if there is a desire to feed the grid continuously at the average rate.

A sister project at the University of Durham intends to investigate the electronic support equipment required to facilitate direct drive power take off. For completeness a summary is contained here but the reader is directed towards [55] for more details. The

system consists of an active rectifier which converts the AC to DC, a capacitor assisted DC link and then a DC-AC converter.

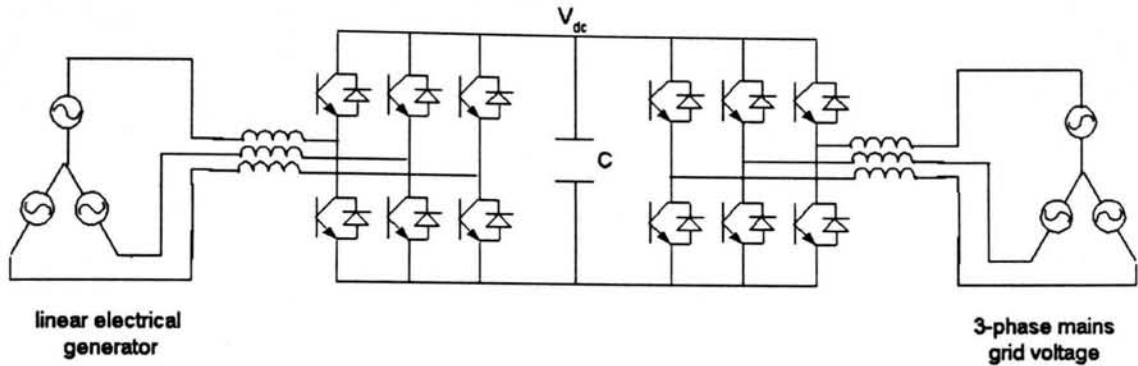


Figure 2.7: Three phase AC/DC/AC converter

Figure 2.7 shows a two stage inverter which may provide this role. On the left hand side of the diagram there are three energy sources, representing the three phases of a typical electrical machine. Each of these phases are fed into an active rectifier which will optimise the power conversion within the electrical machine. The D.C. link and capacitor have two roles. Firstly they may be used to provide reactive power to the generator, and secondly they act as an energy store to smooth power flow. The DC to AC inverter, shown on the right hand side of Figure 2.7, must provide a constant frequency constant voltage signal to the grid.

The power storage function could, in theory, be fulfilled by a battery but because of the short duration of discharge in combination with the requirement for a lack of maintenance, a capacitor is proposed here.

2.6 Specifying a power take off system

2.6.1 Example WEC

To examine the factors involved in specifying a power train, a simplified WEC is investigated. Figure 2.8 shows the simple slack moored heaving buoy introduced in Chapter 1 with hydraulic power take off. It is assumed that the elements of the hydraulic circuit will be mounted remote from the device, probably on the seabed, and that the characteristics of the device match closely those required for resonance at the predominant wave height and frequency. In so doing, the device can be modelled without the use of a control system, giving figures for a power take off system that is less device specific.

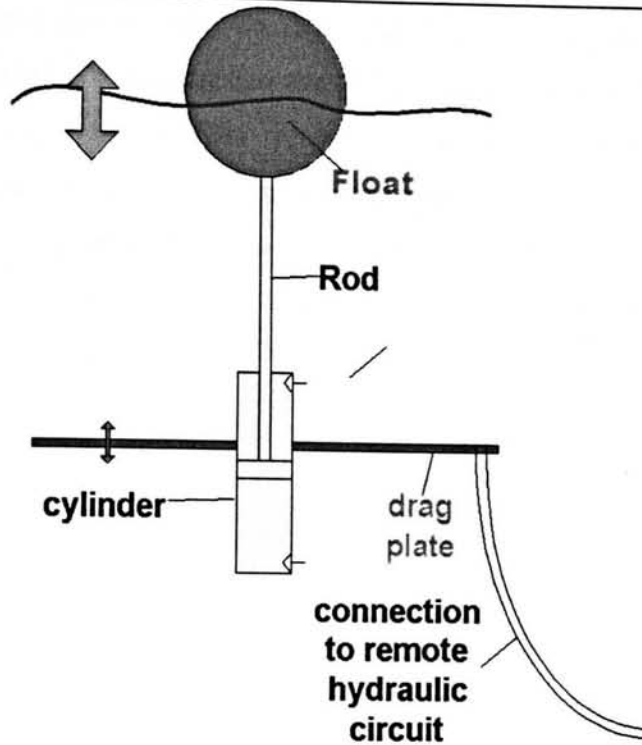


Figure 2.8: Heaving buoy with hydraulic power take off

2.6.2 Sizing the WEC for a given sea state

Wave data given in [56], cited in [57] and displayed in Figure 2.9 gives the probability of each sea state of a given point off the Norwegian coast in terms of the zero upcross time and significant wave height. If the float is assumed to follow exactly the surface of the water, these datum can be used as the basis of a simple design model. In reality, oscillation of two coupled bodies in water is mathematically more complex, e.g. [58].

Designing for the most 'likely' sea state, with a probability of 6.73 %, the significant wave height is 2m and the zero upcross time is 6 seconds. If it is assumed that the sea in this state contains waves of one frequency all in phase, a highly idealised sea state, the zero upcross time becomes the time period and hence the frequency 0.16 Hz. Using this simplification, it is possible to speculate about the component sizes for the WEC and time average energy contained in the sea. Using equation (1.2) in Chapter 1, the energy present per m wave front in this sea state is equal to 23 kW/m, the wavelength of which is 56 m. If the buoy were to act as a point absorber and remembering that this means it is capable of absorbing power equivalent to that contained in a front width equal to the wavelength divided by 2π , the total energy incident on the buoy would be equal to 204 kW. As explained in section 1.1.5.1, any WEC having only one degree of freedom will have a maximum capture efficiency of 50%, giving the maximum power

available to the buoy as 102 kW. On this assumption, one might expect a 100 kW power take off system to be making best use of the available sea and the rated output of the device in one hour to be 100 kWh. However, due to the nature of energy contained within waves, namely its increase with the square of the amplitude, the actual power which a device may capture over a 'typical' hour is 488 kWh. To obtain this value the relative probability of each sea state and the energy contained within it has been accounted for using (2.3).

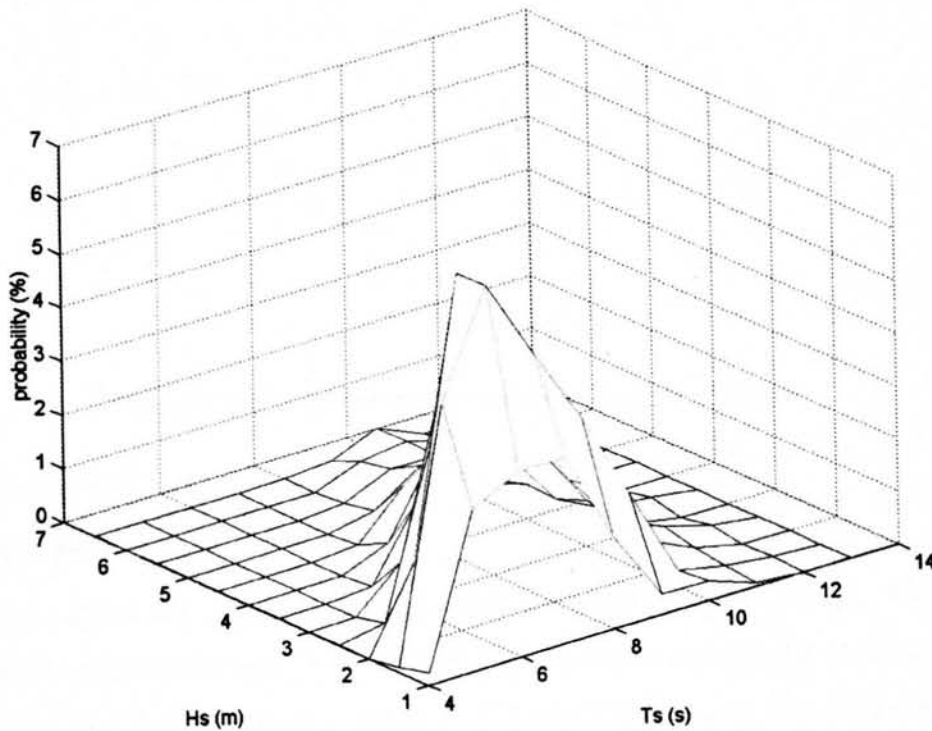


Figure 2.9: Scatter table of wave data [56]

$$P_{ave} = \frac{\sum P_i prob_i}{\sum prob_i} \quad (2.3)$$

Where P_i = power available at sea state i (W)
 $prob_i$ = probability of sea state i occurring

Still assuming the idealised sine wave which fulfils the zero upcross time and now looking at the behaviour of the device over one year allows the relative importance of each sea state to be compared, in terms of kWh Figure 2.10. Despite their rare occurrence, waves of large amplitude and time period can be seen to make a significant contribution to annual yield.

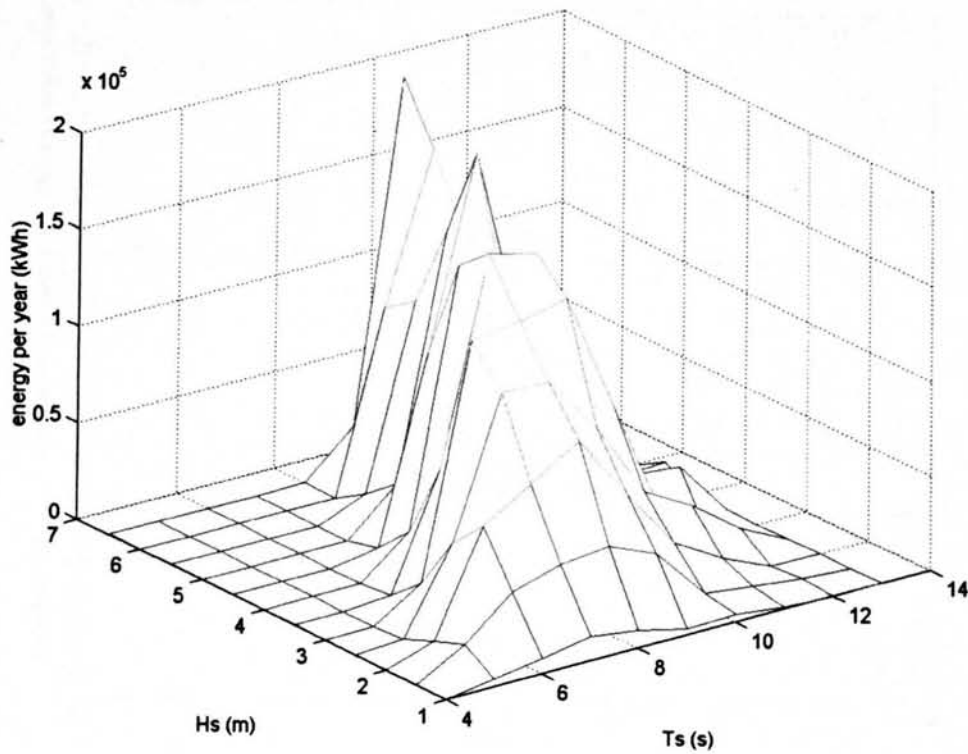


Figure 2.10: Energy contribution from various parts of the sea

2.6.2.1 Power take off

Maximum extension

Hydraulic rams have a maximum permissible extension to avoid damage. Varying the magnitude of this extension will impact on both the power yield of the device and its cost. Figure 2.10 does not show a clear cut off point, where waves above a particular amplitude no longer contribute significantly to the annual yield. It is necessary to make further assumptions about the behaviour of the buoy and sea. Stipulating that during large waves the drag plate follows the oscillation of the float when the maximum cylinder extension is reached effectively limits the amplitude of oscillation. Take for example the graphs of Figure 2.11. The upper graph shows a constant frequency sea state, with a successive amplitude of two, three and four metres. The second graph shows the displacement of a submerged plate which must always be within a 4 metre envelope of the sea surface, due to its coupling with a floating buoy. The final graph shows the extension of the hydraulic ram.

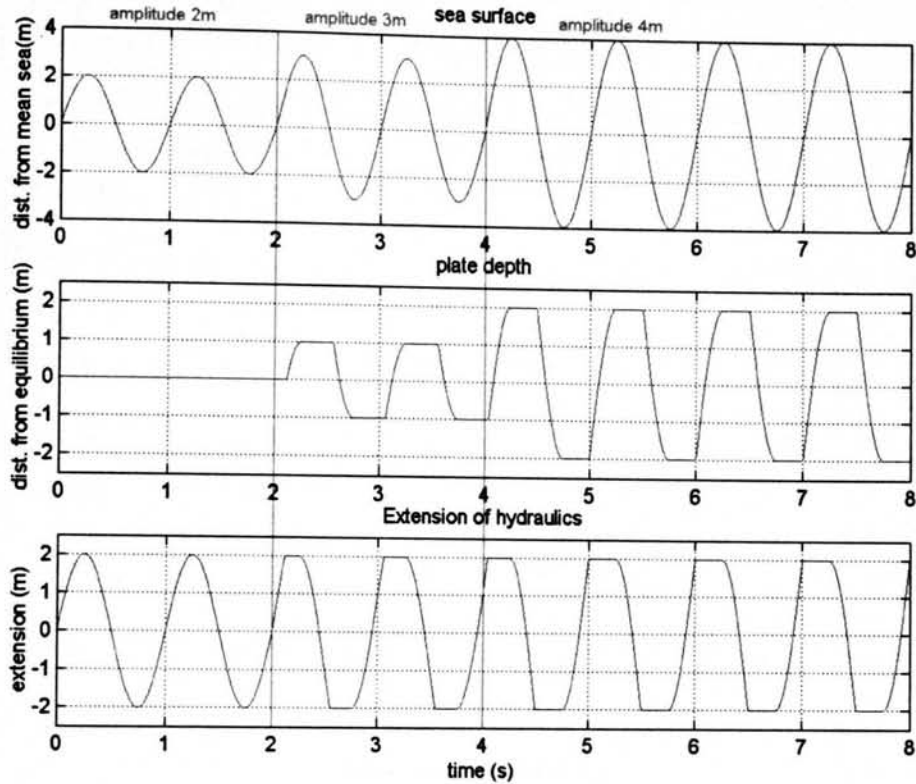


Figure 2.11: Effect of limiting amplitude of oscillation to 2 m

From these graphs it is clear that when limiting the maximum excursion of the hydraulic rams, the plate will oscillate such that the profile of the ram extension is at the same frequency as the surface but with limited amplitude. If the shape of the resultant extension graph in large waves is approximated to a sine wave, the power captured by the device can be calculated using formula (1.2). The addition of the conditional statement given in (2.4) limits the amplitude of extension to A_{max} , the size of the hydraulic ram and can be used in combination with (1.2) to calculate the power take off at any sea state.

$$\begin{aligned}
 & \text{if } H_s \leq A_{max}, H_s = H_s \\
 & \text{if } H_s > A_{max}, H_s = A_{max}
 \end{aligned}
 \tag{2.4}$$

The effect of using alternative amplitude rams on annual power yield may now be investigated, as given in Figure 2.12. Limiting the extension of the cylinder to 4 m ensures the capture of around 80 % of the available energy and gives the device characteristics shown in Table 2-1.

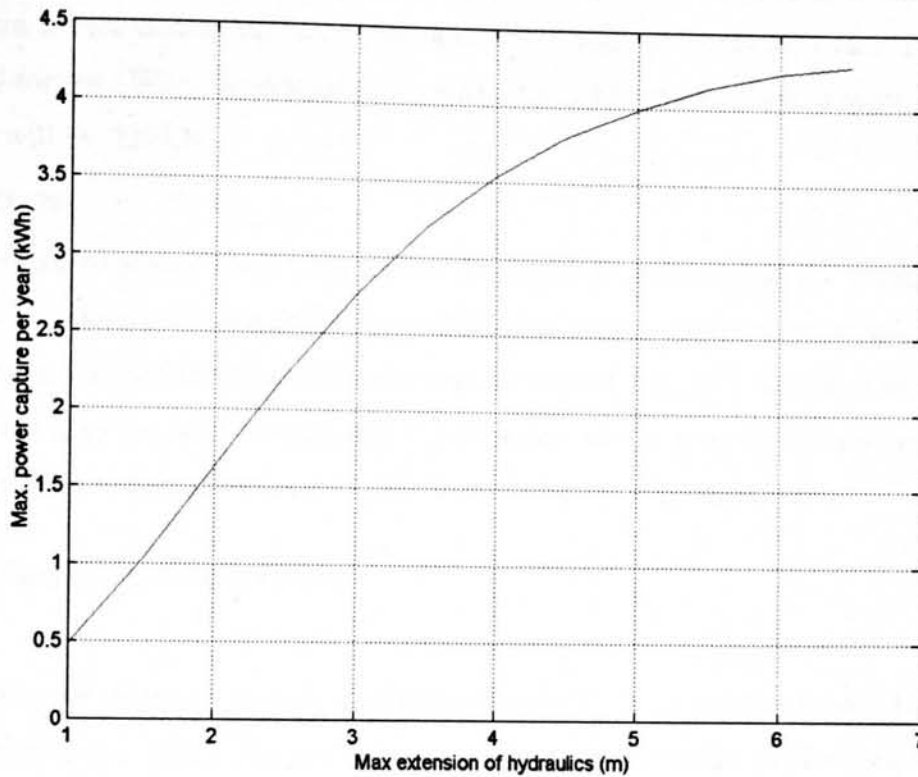


Figure 2.12: Effect of limiting hydraulic extension on maximum theoretical annual energy yield

Table 2-1: Device characteristics for hydraulic ram with $A_{max} = 4m$

	Force-peak (kN)	Velocity-peak (ms^{-1})	Power (kW)	Time period (s)
Maximum	4 430	3.1	4 290	13
Minimum	9.9	0.24	7.8	4
Average	375	0.94	403	7.29

Size of plate

The size of the plate is dictated by the drag force required for the power take off system to react against. The drag force, F_D , associated with a cylindrical plate with cross-sectional area A may be expressed as (2.5).

$$F_D = -\frac{C_D}{2} \rho A |v|v \quad (2.5)$$

- Where C_D = drag coefficient = 10 [57]
- ρ = density = 1025 kg/m^3 for sea water
- v = velocity (m/s)

From Table 2-1 the average velocity of the buoy is 0.94 m/s and the average required force is 375 kN . Specifying the area of the drag plate to give this drag force at 0.47 ms^{-1} ensures the buoy travels at least twice the speed of the cylinder and corresponds to a plate area of 360 m^2 , giving a diameter of 21m .

If the outer height of the plate is nominally taken as 0.2 m and it is made of aluminium with a density of 2700 kg/m^3 , a hollow design with only 50% material will weigh 94 tonnes. When submerged in sea water, the net buoyancy force downwards of the plate will be 220 kN.

Size of buoy

The minimum size of the floating part of the device is calculated by the required up thrust to counteract the weight of the submerged plate. In order to simplify the oscillation model and use available mathematical models, e.g. [27], the same diameter as the plate may be used. Alternatively a diameter which puts the buoy's resonant frequency close to that of the predominant wave frequency may be selected.

2.6.2.2 Specific Hydraulic System

Rams

Currently the largest commonly available cylinder [59] has a stroke of around 0.8 m. It is likely that this limit is due more to demand than any technical difficulties, so the characteristics of this cylinder are extrapolated here.

The maximum force provided by the cylinder is equal to the maximum drag provided by the plate, which itself is proportional to velocity. Assuming that the maximum velocity the plate can be expected to attain during operation is equal to half the maximum velocity of the buoy, 1.6 m/s from Table 2-1, results in a drag force of 4.7 MN. The cylinder design is hence based on a currently available cylinder with a maximum reactive force of 5118 kN [59], shown in Table 2-2.

Table 2-2: Parameters of cylinder

Maximum stroke – m	4 (extrapolated)
Average stroke – m	2.23
Outside diameter – m	0.4
Effective area push – m^2	7.312×10^{-6}
Effective area pull – m^2	2.485×10^{-6}
Max pressure - bar	700
Weight - tonnes	3.7 (extrapolated)
Max oil capacity m^3	0.3

Pressure

The force from the hydraulic piston and cylinder must be sufficient to keep the two bodies in the desired equilibrium positions. Due to the area displaced by the rod, the effective area of the piston is different depending on whether the cylinder is extending or contracting, as shown in Table 2-2. The orientation of the cylinder is such that if the smaller area is coupled to the high pressure accumulator, it is available to react against

the residual buoyancy force plus the downward force from the low pressure acting in the push side. If the low pressure accumulator is 5 Bar, then the force required to overcome the residual buoyancy of the drag plate is reacted if the high pressure accumulator is set to 100 Bar.

Accumulator

For the accumulator to provide some smoothing it must have enough capacity to smooth the power output for 30 seconds, equal to 4 average time periods. The equivalent flow into the high pressure accumulator would be equal to two pull and two push strokes during this time, 0.4 m^3 . Using (2.1), if it is specified that the high pressure accumulator must remain above 85 Bar during the loss of 0.4 m^3 , an initial gas volume of 3.2 m^3 is suitable. If the total volume of the accumulator was set at 4 m^3 this would make provision for ensuring the accumulators do not empty. A similar size can be expected for the low pressure accumulator.

2.6.3 Concluding remarks

This section has discussed the process of sizing a power take off mechanism for a WEC, highlighting its influence on the overall performance of such a device. Using the criteria for sizing the plate in section 2.6.2.1, which uses the average force on the plate at half the average velocity of the buoy gives an average power from the device of 176 kW. This value has been shown to be highly dependent on the size of drag plate and hydraulic ram chosen. In the case of extreme waves, blocking the hydraulic system will allow a maximum force of 5 MN to be reacted, with no power output.

2.7 Discussion

The low velocities of MECs require that the power take off systems deliver high thrusts at the point of contact. At delivery of energy to the grid, high frequency electrical power is required with a stable voltage rating.

Gearboxes are a conventional way of stepping up mechanical velocity, allowing high thrusts at low velocities to be converted to low thrusts at high velocities, yet they have been known to cause problems in the similar area of wind turbines.

A pneumatic system provides a simple way of stepping up the power take off velocity once it has been transferred to a column of oscillating air. The subsequent rectification and conversion into mechanical rotation either requires a Wells' turbine, with an efficiency of around 40 %, or the development of a complex system of pitch controlled turbines.

Hydraulics are the standard choice for MEC power take off system by virtue of their ability to work at high pressures and thus deliver high thrusts. Viscosity and sealing issues enforce the use of oil as the working medium. Subsequent fear of contaminating the marine environment enforces the need for complete confidence in the sealing mechanism, likely reducing usable velocities and enforcing regular checks / maintenance. An entire hydraulic power take off system comprises many moving parts to rectify and smooth the power take off, all of which are required to work with a relative reverse power flow compared to conventional hydraulic drives.

A direct drive system is simple, with an absolute minimum of moving parts and mechanical linkages. Schemes have previously been proposed and abandoned for reasons such as the large active areas required if traditional electrical machines are used. Investigation of modern machine topologies and the known limitations of other power take off mechanisms justify investigation of the direct drive concept and two other groups are known to be working in this area. Rectification and power smoothing would be purely electronic systems, removing the issues of mechanical wear. The practicalities of such a system are currently being investigated elsewhere [55].

The nature of wave distributions show the importance on the selection of power train on annual yield for a given wave energy device. The need to develop a device in tandem with its power take off system has been demonstrated.

2.8 Conclusion

Within this chapter the significance of the choice of power take off scheme on the overall characteristics of a MEC has been discussed and the steps of selecting the rating for a power take off system have been outlined.

The four forms of power train were said to be mechanical linkage, hydraulic, pneumatic, and direct drive, each of which takes the slow reciprocating motion from the device and convert it into usable energy. With the possible exception of pneumatic systems, which tend to be an inherent part of an OWC device, the power take off trains could in theory, be used in place of each other. As such, a direct drive power take off system has the ability to be applied to most MEC devices. This gives insight as to the expectations of an electrical machine proposed as direct drive power take off. The following Chapters investigate the types of electrical machine suitable for use in these applications.

Chapter

3

Linear Electrical Machines

This chapter introduces various topologies of linear electrical machine and briefly outlines both the principles and mathematics which describe their behaviour. As such it provides a platform on which they are compared. On this basis two machine topologies are selected for further investigation in the proceeding two chapters.

3.1 Linear Machines

Electrical machines are almost exclusively of a rotary configuration, primarily due to their application. Notable exceptions to this, where some research has been performed, are for transportation purposes (levitating high speed trains, 'Maglev'), projectile launchers or small biomedical actuators [60]. These are all high speed operations, with the electrical machine acting as an actuator / motor. For marine renewable applications, as demonstrated in previous chapters, the concept of a linear machine offers the opportunity to simplify the mechanics of the system if it can be used as a slow speed generator. The guiding principles for rotary and linear machines are identical, simply in a different plane of motion. As such, all equations describing a rotary machine are equally applicable to a linear machine, with the slight modification of some terms, such as torque to force. Conceptually, a linear machine can be thought of as the circumference of its rotary counterpart flattened out. Figure 3.1 shows the basic form of a linear machine being derived from its rotary counterpart.

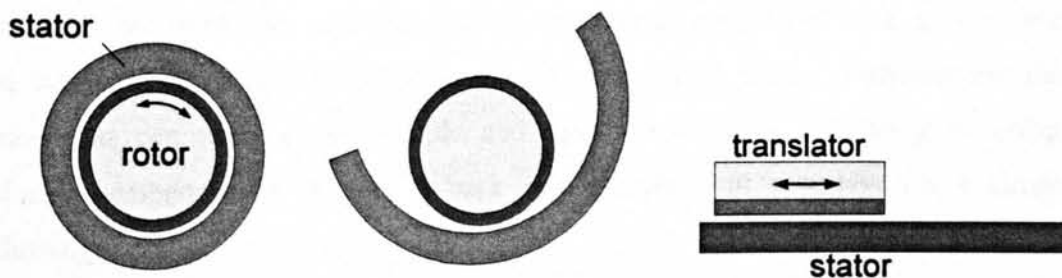


Figure 3.1: Imaginary process of unrolling rotational machine to obtain linear counterpart

The power absorbed by a linear machine is equal to the product of the reactive force it can deliver and the velocity at which it is displaced. In order to develop greater power for a given velocity, therefore, it is necessary to be able to exert a greater force. It follows that the specific shear stress, the force per unit area of the active airgap, provides a valid basis on which to assess machine topologies.

All the machines in this chapter consist of a stationary part, referred to as the stator, and a moving part, referred to either as the translator, or as with its rotary counterpart, the rotor.

3.2 Conventional Topologies

3.2.1 *Linear Induction Machine*

The induction machine is the work horse of the electric motor industry. Its robustness arises from the simple topology of its rotor, particularly in a squirrel cage motor where there is no requirement for brushes or slip rings. There is a slight preference for induction machines to be used as motors, in particular linear induction machines have previously been of primary interest for transportation actuators.

In a linear induction machine a three phase alternating current is used to excite the stator windings, which, in combination with the winding configuration, sets up a synchronous speed travelling magnetic field in the airgap region. Consequently, if the translator is not moving at synchronous speed, i.e. for all non zero-slip speeds, an emf is induced within the translator. The transition of machine operation from motor to generator occurs as the rotor speed overtakes the field speed and goes super synchronous. By feeding the stator coils through a controllable inverter any slip speed can be achieved at any rotor velocity. Controlling the output power is hence relatively simple for a variable speed input and as such the rotary version is commonly used in wind turbines.

Figure 3.2 shows a short stator type machine, where the active length is dictated by the length of the stator, the translator being as large as the anticipated amplitude. This is likely to be the preferable configuration in applications considered here, as the oversized translator is cheaper to construct than the energised stator. Furthermore, the moving part can have a very simple and light construction, consisting of either conductors embedded in slots of a back iron structure, or possibly just a single conducting sheet.

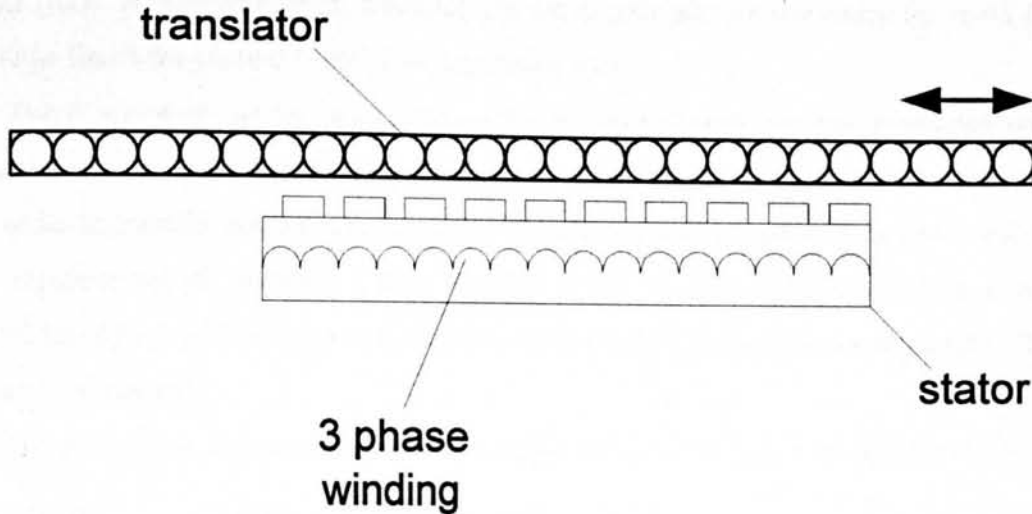


Figure 3.2: Linear induction machine

An induction generator must draw magnetising current and so requires a two way grid connection. For a linear machine, where there is likely to be a larger airgap than its rotary counterpart, the inductance and hence reactance of the excitation coil is low. Consequently a large excitation current is required and the overall efficiency of the machine is reduced.

If the peaks of electrical and magnetic loading of the machine coincide, then the peak airgap shear stress may be expressed as (3.1).

$$\hat{\sigma} = \hat{B}\hat{K} \quad (3.1)$$

Where σ = shear stress (Nm^{-2})
 B = magnetic flux density (T)
 K = electric loading (A/m)

3.2.2 Field wound synchronous machine

Synchronous machines are the primary devices used for high speed rotary power generation in the world's electric power systems today [61]. The rotor is fed with a d.c. current via brushes and slip rings and so sets up a magnetic field which follows its movement. The stator surrounds the rotor with a set of stationary coils, such that they are cut by the rotor flux pattern. Controlling the excitation currents in these machines, which are generally more efficient than induction machines, provides a way of regulating the output voltage which would otherwise be dependent on speed.

Operating as a motor for high speed transportation devices, linear synchronous machines have been shown to be more favourable than their induction equivalents, with an efficiency of 90 % when compared to 82 % and a power factor of 0.8 as opposed to

0.52 [62]. At low velocities, however, the small pole pitches necessary for rapid flux change limits the current / size of the excitation coils.

There are wear issues associated with field-wound synchronous machines when compared to induction machines. The necessity of physical contact with the translator in order to transfer magnetising current will enforce routine maintenance for inspection or replacement of brushes. The variable speed bi-directional oscillatory motion considered here will only serve to increase wear on the brushes when compared to their rotary counterpart.

The maximum shear stress is again governed by the relationship of equation (3.1).

3.2.3 Permanent Magnet (PM) synchronous

In a machine excited by PMs there is no need for the provision of field excitation, as magnetised material is used to supply pole flux as opposed to current carrying coils. A simple example of such a machine consists of surface mounted ferrous magnets mounted on an iron translator which oscillates within a cylindrical distributed three phase winding, held in place by slotted iron structure. One such machine is shown in Figure 3.3.

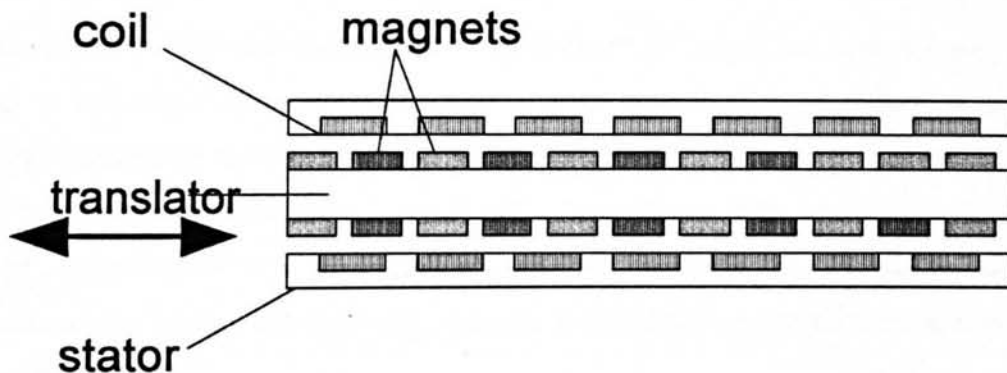


Figure 3.3: Conventional linear PM machine

As the translator moves, so too does the flux pattern resulting from the presence of magnets. An emf is hence induced in the stationary coils as the flux cutting them is changed. The flow of magnetic flux can be simplified by assuming infinitely permeable iron, in which case the total magnetomotive force (mmf) produced by a magnet is dropped across the magnetic gap length (i.e. in the airgap and within the magnet itself). The flux density in the airgap is given by equation (3.2), allowing the machine thrust on the electrical windings to be obtained by use of Lorenz's law, as expressed in equation (3.3) and per unit active area in (3.4).

$$B_g = B_r \left(\frac{t_m}{t_m + \mu_r g} \right) \quad (3.2)$$

Where	t_m	=	thickness of magnet (m)
	B_g	=	flux density in airgap (T)
	B_r	=	remnant flux density in magnet (T)
	g	=	length of airgap (m)
	μ_r	=	relative permeability (≈ 1.05 for magnetic material)

$$F = B_g IL \quad (3.3)$$

Where	F	=	force (N)
	I	=	current (A)
	L	=	length (m)

$$\hat{\sigma} = B_g K \quad (3.4)$$

3.3 Variable Reluctance Permanent Magnet Machines (VRPM)

3.3.1 Introduction

In conventional electrical machines the shear stress in the airgap has been shown to be equal to half the product of magnetic and electric loading. These quantities are limited by saturation levels in the iron and temperature levels in the copper respectively. In order to increase the shear stress available, then, it is necessary to depart from these topologies. Iron saturation is a material property and so cannot be altered, but the *equivalent* electric loading can be increased by the introduction of rare earth Permanent Magnets (PMs).

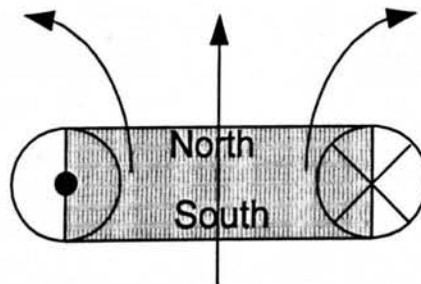


Figure 3.4: Equivalent current sheet of a PM

Figure 3.4 shows how a single permanent magnet may be modelled by two current carrying wires, producing an identical magnetic field. If these wires are thought of as

'current sheets', than the equivalent density can be greater than 900 kAm^{-1} , calculated using (3.5).

$$I_{PM} = H_c t_m = t_m \left(\frac{B_r}{\mu_0 \mu_r} \right) \quad (3.5)$$

- Where I_{PM} = equivalent current (A)
 H_c = coercivity (Am^{-1})
 μ_0 = permeability of free space = $4\pi \times 10^{-7}$

A machine which relies on a field winding for excitation is likely to be limited to around 50 kAm^{-1} , giving a shear stress an order of magnitude lower.

A slow physical velocity may be converted to a high speed flux change by a process known as magnetic gearing. Figure 3.5a shows a single stator pole, split into 3 teeth, interacting with five individual rotor poles, each a surface mounted permanent magnet. If the rotor moves by one rotor pole to the right, as in Figure 3.5b, the direction of flux flow through the pole can be seen to reverse. In non-toothed designs, the rotor would have to move a distance five times this value, Figure 3.5c and Figure 3.5d. This toothed design has therefore increased the rate of change of flux five fold. However, the rotor is only interacting with three stator poles at any one time, reducing the maximum value of flux by a factor of $3/5$ (compare 'c' and 'e'). The net magnetic gearing of the split rotor and stator poles is hence threefold.

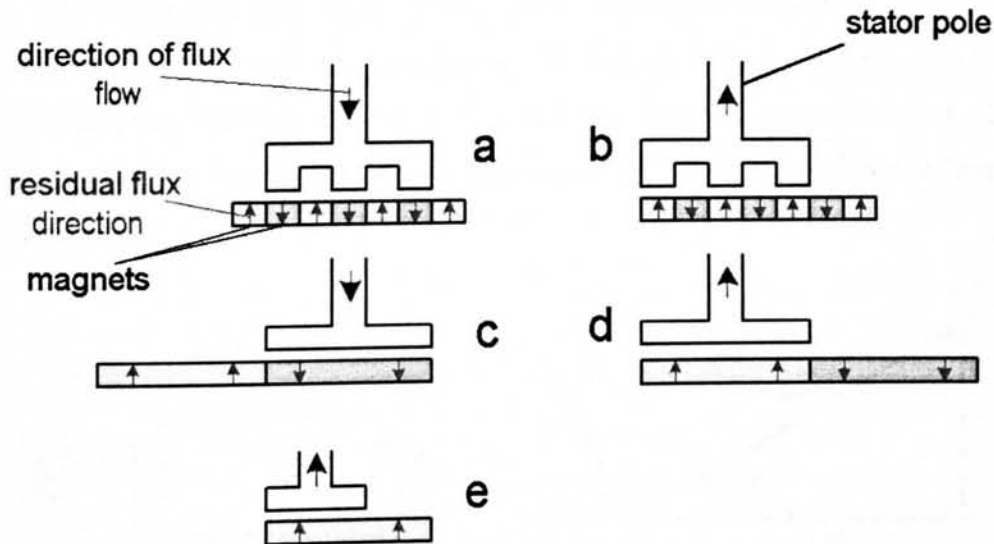


Figure 3.5: Magnetic Gearing

Recent developments have resulted in a new class of machine, known as Variable Reluctance Permanent Magnet machines (VRPM). There are many topologies of these machines [63, 64, 65, 66, 67, 68], all bound by the same principles of operation. Alternative return paths are offered to the magnetic flux through the interaction of rare

earth PMs and small pitch iron teeth. Force is developed as the path of minimum reluctance is sought. These machines are capable of shear stresses unmatched by other electrical machines, which has led to a general reduction in the size of machine. The proceeding sections detail common features associated with this family of machine plus two proposed topologies.

These advantages are further amplified if rare earth magnets are used. Neodymium Iron Boron (Nd-Fe-B) has a remnant flux density of around 1.2 T, compared with 0.4 T for ferrite magnets. Until recent years, the price of these materials has compromised the advantages they offer, yet a gradual drop in their price gives the potential for them to be economical.

3.3.2 Power Factor

3.3.2.1 The Problem

A problem common to all VRPMs is that they tend to operate at low power factors under load, values in the range of 0.35-0.55 are typical [69]. The highly effective magnetic circuit of the machine, which is key to its high shear stresses, presents this inherent disadvantage. The problem is compounded by the desire for many turns on the coil to further enhance the change in flux linkage from the slow physical velocity. The result of these factors is that current flowing within the coils produces a strong flux pattern. Any change in this current flow is hence resisted by a large change in flux flow, producing a back emf. In practice this phenomena manifests itself as a large inductance in series with the electrical machine resisting any change in current. The subsequent phase lag between emf and current results in the terminal voltage collapsing when current flows.

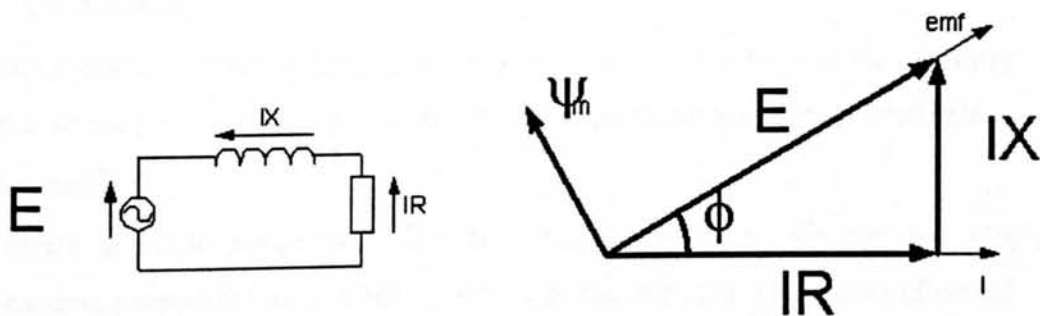


Figure 3.6: Phasor Diagram of VRPM

Consider the simple circuit and phasor diagram shown in Figure 3.6. The magnet flux, ψ_m , is pointing top left, with the subsequent emf induced in the coil lagging by 90° , pointing top right. Regarding the coil as a pure inductor and connecting it to a pure

resistor, the emf induced, E , will be dropped across the external resistance, IR , and the internal inductance, IX . The voltage across an inductor leads the current by 90° , which causes a phase difference, ϕ , between the internal emf and current. The terminal voltage is IR .

The power factor is defined as $\cos\phi$, where ϕ is found from inspection of Figure 3.6 to be equal to $\arcsin(IX/E)$. Thus the value of IX/E sets the power factor, where a value of unity is obtained when IX/E equals zero and a value tending towards zero when IX/E tends to one, i.e. when all the emf is dropped across the internal inductance. This ratio, described as the flux ratio, maybe qualitatively described as the stator flux linkage due to electric excitation only divided by that due to magnet excitation only, or ψ_I/ψ_M . A high internal power factor therefore requires either a very high flux linkage from the magnets or a very low flux linkage from the coil.

The flux due to the two sources follows the same low reluctance path, and hence gives low power factors. Furthermore, in order to exploit the effect of magnetic gearing, each of the stator magnets has oppositely polarised neighbours making a large amount of leakage and fringe flux inevitable.

Reducing the number of turns on the coils would reduce the mmf, NI , applied to the machine for a given current excitation. Less flux would cut the coil and hence the power factor would improve. This, however, would be at the expense of a lower induced emf and a lower shear stress.

The low power factor of VRPMs will hamper their useful power output. The requirements of this topology and the utilisation of magnetic gearing make it an inherent feature which must be overcome by electronic means.

3.3.2.2 The solution

In order to reduce the power factor and bring the current and voltage of the generator in phase, reactive power must be provided. Two alternative methods are detailed below.

Tuning capacitor

The effect of a low power factor may be compensated for by the addition of a parallel capacitor across the load. Chen et al. [70] demonstrated this de-tuning effect for PM machines used in wind turbines. The choice of capacitance, C , to achieve maximum power transfer is dependant on frequency, and is given by Chen et al. as (3.6).

$$C = \frac{L}{\omega^2 L^2 + R^2} \quad (3.6)$$

A fixed capacitance will only have benefits at a single resonant frequency. The electrical frequency in machines used in this application is proportional to translator velocity, which will constantly vary. Therefore, in order to benefit from assisted excitation at all frequencies, thyristor switched capacitors would have to be used. In reality there is a limit to the usefulness of this method at a large scale feeding a non constant load whilst excited at a non constant velocity.

Active rectifier

More efficient power take off can be expected with the use of an active rectifier ensuring the power flow from the generator is unidirectional. This implies that the output current wave form has the same frequency and polarity as the internal emf, forcing them to be in phase with each other and bringing the power factor up to unity, which can be achieved by an active rectifier acting as a Unity Power Factor (UPF) controller. Although power electronics is outside the scope of this thesis, in order to obtain useful power out of VRPM machines their presence must be assumed. A very brief outline of the operation of a UPF controller is hence given.

Using a search coil or a look up table, the internal emf of the generator is always known at a given current, speed and position. The maximum theoretical current may be calculated by scaling this value. The voltage difference at the terminals of each coil can then be manipulated to achieve this current. Pulse Width Modulation (PWM) with a frequency of the order of 10 kHz is used to control the terminal voltage, the characteristics of which are calculated from the difference in actual and expected coil current [55]. Work being carried out elsewhere in the School of Engineering, University of Durham, is striving to achieve this.

3.3.3 Transverse Flux Machine (TFM)

In a TFM the main flux flow is in a direction perpendicular to the direction of travel. Figure 3.7 shows three views of a linear PM excited TFM. The translator consists of surface mounted PMs in a configuration that forces the flux to vary both axially and circumferentially. There are stator coils mounted either side of the translator with a series of iron yokes channelling the flux in such a way that alternate rotor poles excite the same coil [63, 64]. The result is an inherently three dimensional flux path, and flux from all the magnets contributes to linking one or other of the coils at all times. As such

the TFM is the ultimate VRPM machine, producing very high shear stresses, values approaching 200kNm^{-2} have been reported [63].

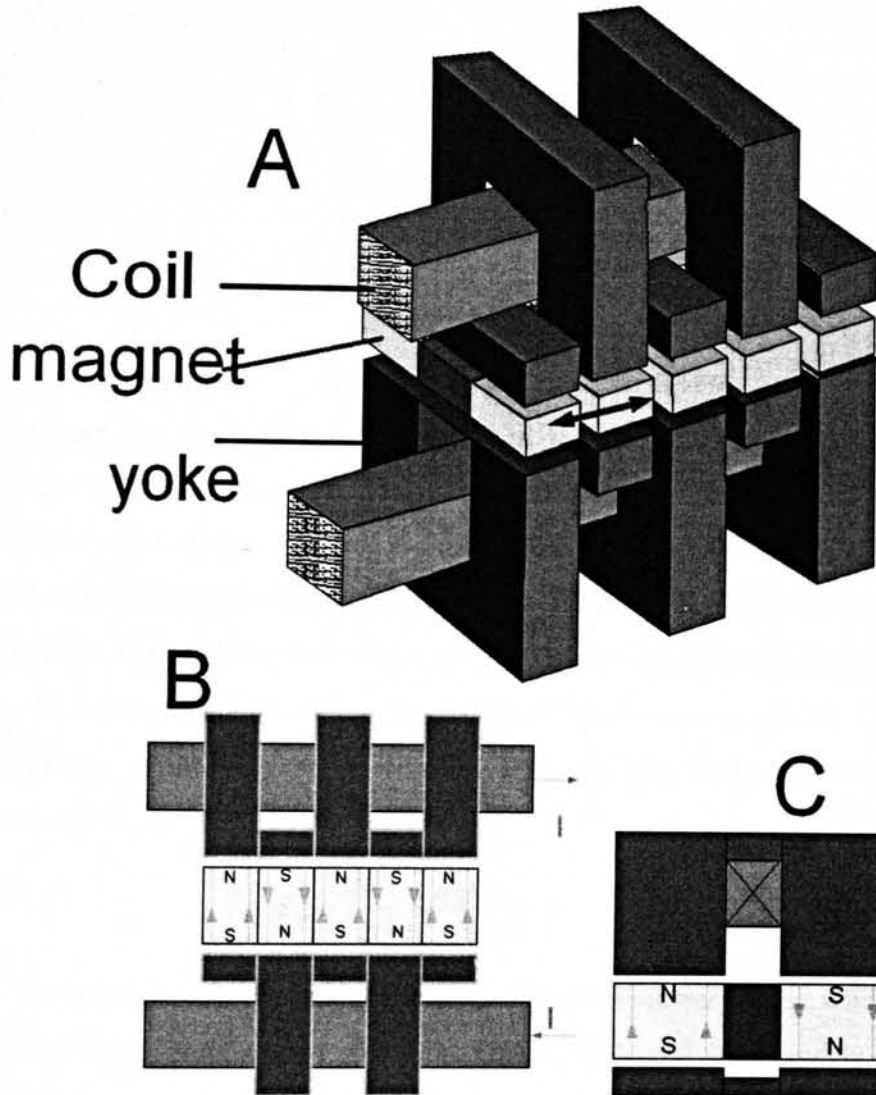


Figure 3.7: Transverse Flux Machine

The mounting of the stator yokes in combination with the three dimensional flux path present various problems with the support structure of this machine. The typical three dimensional structure does not allow the ferromagnetic elements to be laminated and the necessary small pitch often demands a large number of individual parts. Furthermore, inherent in this machine is the presence of cogging torque: the tendency of the magnets to align themselves with the path of least reluctance. It has been reported as 30 kNm^{-2} in one machine [64].

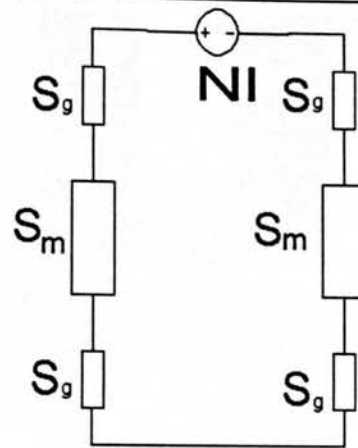


Figure 3.8: Equivalent circuit of TFM

Consider the magnetic circuit shown in Figure 3.8, where S_g and S_m are the reluctance of the gap and magnet respectively and NI is the mmf source from current in one of the coils. If the magnets in the TFM were replaced with air, and viewing the machine from the angle shown in Figure 3.7C, it can be seen that this circuit represents a simplified equivalent circuit of the machine with I amps flowing through the N coil turns. The flux density in the airgap, due to current excitation only, in a machine made of infinitely permeable iron is deduced from the equivalent circuit and given by equation (3.7).

$$B_g = \frac{NI}{2} \left(\frac{\mu_0 \mu_r}{t_m + 2g\mu_r} \right) \quad (3.7)$$

If the rotor magnets are replaced with an equivalent current sheet, when the machine is viewed from the direction shown in Figure 3.7B, and the magnets and teeth are misaligned, the force resulting in the interaction of the current sheet and the flux due to the coil current is shown in Figure 3.9.

Each of the forces will be given by equation (3.8). The resulting shear stress, incorporating one of these forces acting per rotor pitch, is given in equation (3.9).

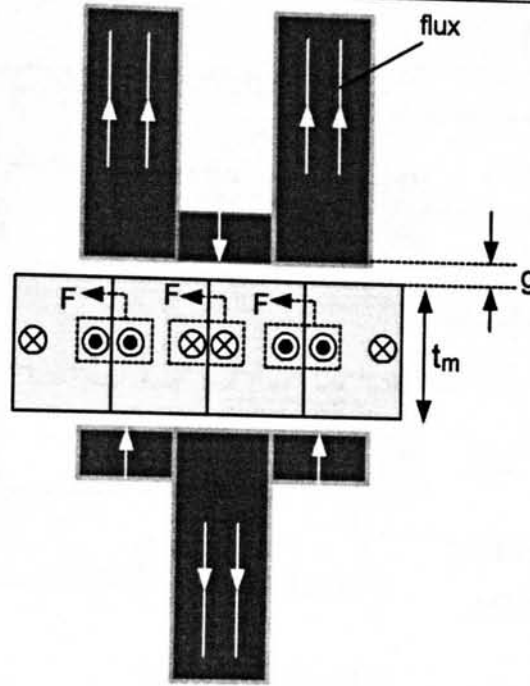


Figure 3.9: Force generation in the TFM

$$F = B_g \left(\frac{t_m B_r}{\mu_0 \mu_r} \right) L \times 2 \quad (3.8)$$

$$= \frac{N I t_m B_r L}{(t_m + 2g\mu_r)}$$

Where w_m = width of magnet (m)
 L = axial length (m into plain of paper)

$$\hat{\sigma} = \frac{2 B_g t_m B_r}{w_m \mu_0 \mu_r} \quad (3.9)$$

3.3.4 Vernier Hybrid Machine (VHM)

The VHM has a significantly more conventional machine structure, and a two dimensional flux pattern [65, 68]. Figure 3.10 shows four stator pole faces supported on two opposed C-cores each carrying two coils. The stator mounted PMs interact with the purely iron toothed rotor, in order to produce the flux path shown. This two dimensional path links all four coils, four magnets and four airgaps. A similar topology has been proposed, [66], which had the magnets on the moving part and the stator face toothed. If the rotor moved one magnet pitch, equal to half a rotor pitch, in either direction, it can be seen that the teeth would fully align with the opposite poles to those shown, and hence the flow of magnetic flux would be completely reversed.

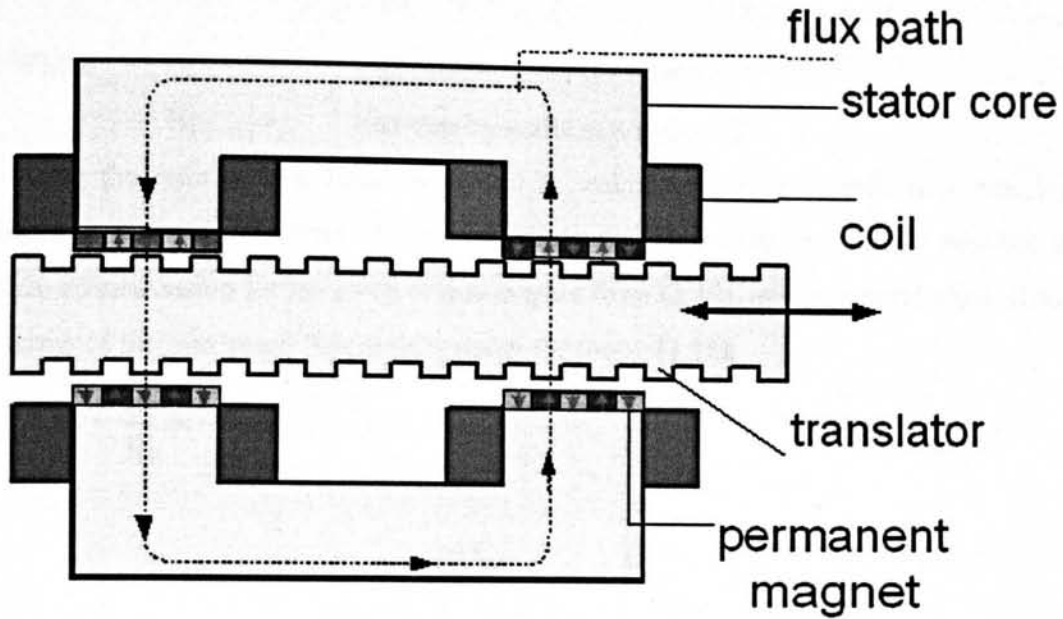


Figure 3.10: The VHM

Because of the slots in the rotor the flux density is not constant throughout the width of the airgap. The flux pattern will resemble that shown in Figure 3.11, with a higher density being observed under the tooth region than under the slot region. Due to the magnets being alternatively magnetised, the greatest force is reacted when the magnets and teeth are exactly misaligned and hence the equivalent current carrying coils are in the area of highest flux density. As shown, the flux under the slot region causes a force which opposes that under the teeth.

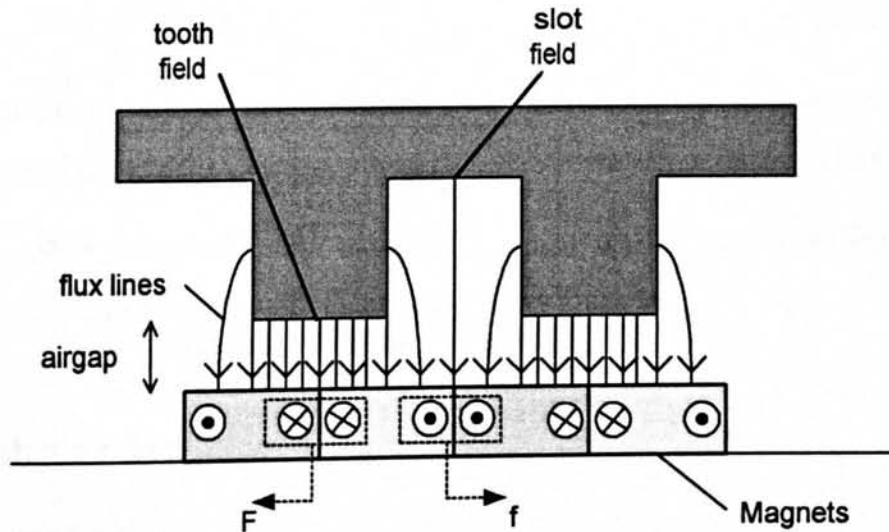


Figure 3.11: Flux pattern of VHM

The peak resultant force per tooth pitch, F_{net} , will be the difference of these opposing forces, given by (3.10).

$$F_{net} = (B_t - B_s)I_{PM}L \quad (3.10)$$

Where B_t = flux density under the tooth (T)
 B_s = flux density under slot region (T)

Using the ratio of flux densities B_t and B_s , calculated using a conformal mapping technique given in [65] and (3.11), and substituting I_{PM} from (3.5), it is possible to obtain a relationship for the force of one magnet from (3.10), or the general shear stress in terms of the maximum flux density under the tooth, (3.12).

$$\frac{B_s}{B_t} = \frac{g + t_m}{\sqrt{(g + t_m)^2 + 0.25w_m^2}} \quad (3.11)$$

$$\left. \begin{aligned} F &= t_m B_t \left(1 - \frac{g + t_m}{\sqrt{(g + t_m)^2 + 0.25w_m^2}} \right) \left(\frac{B_r}{\mu_0 \mu_r} \right) L \\ \therefore \hat{\sigma} &= \frac{t_m B_t}{w_m} \left(1 - \frac{g + t_m}{\sqrt{(g + t_m)^2 + 0.25w_m^2}} \right) \left(\frac{B_r}{\mu_0 \mu_r} \right) \end{aligned} \right\} \quad (3.12)$$

Considering slots of infinite depth, and ignoring the field driven by the magnets, all of the airgap flux would have to pass through the roots of the translator teeth. It is hence saturation of this region of steel which limits the strength of the field under the tooth. A good approximation relating the field strength under the tooth to that at the root, B_{root} , is given in (3.13) from [65].

$$B_t \approx \frac{B_t}{B_t + B_s} B_{root} \quad (3.13)$$

Substitution of (3.11) into (3.13) hence gives the relationship between flux density under the tooth, in terms of tooth geometry and the flux density at its root, (3.14).

$$B_t = \frac{B_{root}}{\left(1 + \frac{(t_m + g)}{\sqrt{(t_m + g)^2 + 0.25w_m^2}} \right)} \quad (3.14)$$

3.4 Tubular Machine

3.4.1 Introduction

All the machines considered previously have a flat cross-section. There is no physical necessity for this and conceptually linear machines can be rolled about an axis parallel to the direction of travel. The term tubular refers to the cross-sectional shape of the machine and hence covers a wide variety of possible topologies. As such a tubular

VHM is possible, yet the now three dimensional flux path and cylindrical translator would prevent the use of laminations. The TFM does not have a uniform cross-section, which prevents it being extended to a tubular machine.

The PM synchronous machine has a simple topology well suited to building a tubular equivalent. The basic layout for brushless permanent magnet tubular machines consists of a stationary copper coil surrounding a moving cylindrical rotor incorporating permanent magnets, resulting in a moving magnetic field passing through the coils. The active part of the translator consists of a series of alternate steel pole pieces and Nd-Fe-B magnets. The magnetisation of the magnets is axial and they are mounted such that the steel pieces form alternate North and South surface poles.

It is more usual for this type of machine to be used as an actuator, not a generator, and work on driving them in this mode is available [71, 72]. Research on tubular linear generators appears to be sparse.

3.4.2 Ironless Tubular PM machine

Significant structural savings can be made if the magnetic forces can be reduced or eliminated, which can be achieved by constructing a stator which contains no iron. These features are demonstrated in Figure 3.12.

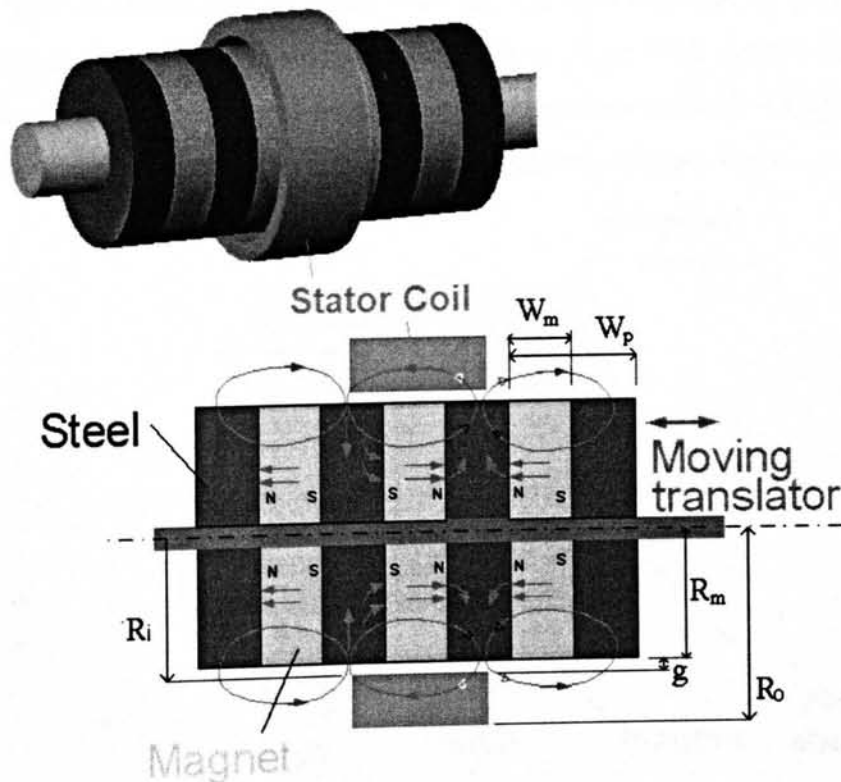


Figure 3.12: Ironless tubular machine

The translator consists of opposed axially magnetised PMs separated by steel spacers, both mounted on a non magnetic shaft. This configuration, assuming that the iron does not saturate, results in the residual rotor forces being attractive. Without the spacers, strong repellent forces would be present. Radially magnetised or surface mounted magnets may prove more attractive for large diameters, but at small scale represent a more difficult structure to manufacture.

3.4.2.1 Surface Flux Density

A similar design with an iron core has been analysed [71] and optimised [72], which provides some relevant results. Using the notations given in Figure 3.12 and assuming that the airgap, g , is a specified design parameter restricted to its minimum obtainable size, there are three dimensional ratios which may be considered: w_m/W_p , R_m/R_o and w_m/R_o . The first of these, which for a given magnet width specifies the width of steel spacer, is said to behave independently and not influence the choice for the other two [72]. The choice of W_p is, by implication, not affected by the lack of iron in the stator, which effectively sets R_o to infinity. Within this research it was concluded that the value w_m/W_p should be set for the condition of minimum torque ripple and a value of 0.6 and 0.7 was recommended [72].

For the same electrical and magnetic loadings, the ratio of thrust of a three phase machine compared to that of a two phase machine is 1.061 [72]. A 6% increase in performance can hence be expected from making a three phase machine when compared to its two phase equivalent, with an advantageous reduction in ripple force.

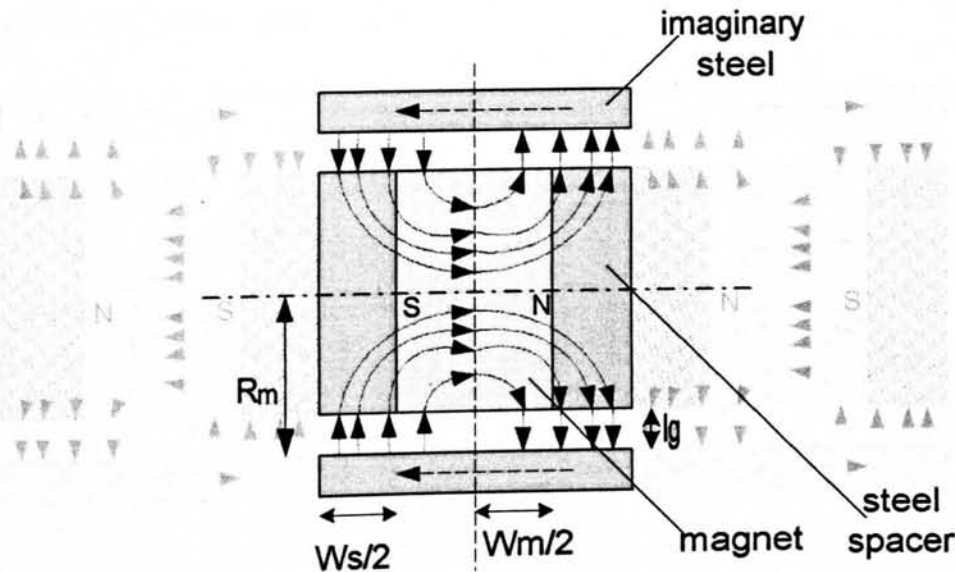


Figure 3.13: Simplified flux flow through tubular machine

Figure 3.13 shows the simplified assumed flux flow through one magnet and two separate halves of steel spacers. The section consists of two half surface poles, separated by the centre line of the magnet. The pattern is repeated to make up a series of adjacent North and South poles along the surface, the polarity of which changes at the centre line of the magnet. Included here is the presence of an imaginary steel outer sleeve, which allows the flux density at the translator surface to be calculated. The flux flow is assumed to be parallel in the airgap and flow from the translator into the surrounding air through both the magnet and steel boundaries. The length of the airgap, l_g , which gives the same reluctance as the ironless core is given by (3.15), see Appendix A.

$$l_g = \frac{w_m + w_s}{\pi} \quad (3.15)$$

In the actual airgap the flux density will rapidly reduce with distance from the surface. As a first estimate, it can be assumed that the decay of field is exponential with distance x , as shown in (3.16).

$$B_g = \hat{B}_g e^{-\frac{x}{l_g}} \quad (3.16)$$

3.4.2.2 Reactive Force

Force is developed as a result of current flowing through the coils, which are situated in the magnetic field of the stator. The direction of this force is mutually orthogonal to the current and field strength and has a magnitude of their product multiplied by the length of conductor in the field.

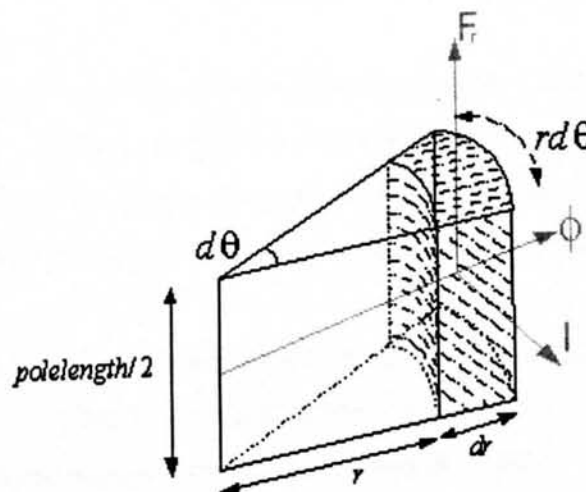


Figure 3.14: Segment of copper in magnetic field

Figure 3.14 shows a segment of the copper coil over a surface pole with the mutually orthogonal elements shown. If the segment carries a peak current density of J Amps/m² in the I direction then the force per m³ of this segment is given by (3.17).

$$F = BIL$$

$$\therefore \frac{F}{vol} = JB_g e^{\frac{-r+R_m}{l_s}} \quad (3.17)$$

The force acting on a single coil carrying a uniform current over an entire surface pole is simply the integral of this equation over the entire volume within the field. Equation (3.18) gives the force per pole assuming that the flux density above the magnet region of the translator is equal to zero.

$$F_{pole} = \int_0^{2\pi} \int_{R_i}^{R_o} \int_0^{w_s} JB_g e^{\frac{-r+R_m}{l_s}} r dz dr d\theta$$

$$= 2\pi w_s JB_g l_g e^{-\frac{g}{l_s}} \left[R_m + g + l_g - e^{-\frac{ch}{l_s}} (R_m + g + ch + l_g) \right] \quad (3.18)$$

- Where
- g = airgap (m)
 - ch = coil height (m)
 - R_i = inside radius of coil (m) = $R_m + g$
 - R_o = outside radius of coil (m) = $R_m + g + ch$, see Figure 3.12
 - R_m = radius of magnets (m)

The average shear stress developed across the pole is equal to the force developed, divided by the area of that pole, (3.19).

$$\bar{\sigma} = \frac{JB_g l_g}{R_m} \frac{w_s}{(w_m + w_s)} e^{-\frac{g}{l_s}} \left[R_m + g + l_g - e^{-\frac{ch}{l_s}} (R_m + g + ch + l_g) \right] \quad (3.19)$$

In order to compare this value with the other topologies, it is necessary to make two further assumptions. Firstly, as there is no iron in the stator, and hence no fixed boundary to the end of the airgap, an outer value for the coil has to be specified. This value is specified as twice l_g , which implies utilising almost 90% of the available flux, according to (3.16).

Secondly, the value of l_g is dependant on the pole width of the translator, nominally the width of spacer is taken to be equal to the magnet width. These two conditions combined give a general equation for the shear stress as (3.20).

$$\sigma = \frac{JB_g w_m e^{\frac{g\pi}{2w_m}}}{\pi R_m} \left(0.865(R_m + g) + 1.188 \frac{w_m}{\pi} \right) \quad (3.20)$$

3.5 Shear stress comparison

As a reference guide to the typical loading of a direct drive generator, this section compares machines capable of removing 100 kW from an element moving at 1 ms^{-1} , i.e. a machine capable of reacting 100 kN.

The three distinct topologies of machine, conventional, VRPM and tubular have been described in terms of shear stress equations within this Chapter. The constants used in their comparison are given in Table 3-1 and are dictated either by experience and general practice or justified below.

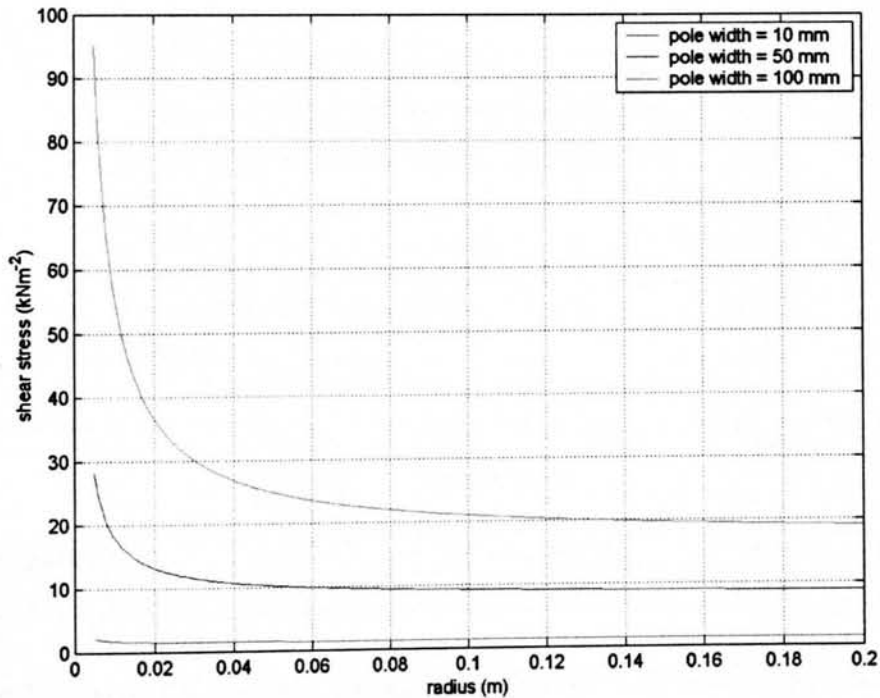


Figure 3.15: The effect of radius on tubular machine shear stress

The shear stress value for the tubular machine, (3.20), includes a term for the magnet radius R_m . There is no equivalent dimension for the other topologies, nor is there an obvious method with which to choose one. The effect of the chosen radius is demonstrated in the shear stress graph of Figure 3.15, which also includes three alternative pole widths. The theoretical shear stress of the machine is seen to be very large for machines of unrealistic dimensions. Unlike the VRPM and synchronous PM machines, the magnet width here both determines the pole width of the stator winding

and affects the shear stress. To ensure adequate space for a three phase winding, the dimensions chosen are 0.1 m radius translator with magnets of 50 mm thickness, corresponding to a pole width of a 100 mm and an average shear stress of 21 kN/m². Assuming a sinusoidal variation with position, the peak shear stress will be twice this value, 42 kN/m².

In the VHM, whose shear stress was related to the difference in flux density under the root and the tooth, the density under the tooth was calculated using (3.13) to be 1.2 T, which corresponds to the steel at the root of the tooth being saturated, 1.9 T.

In the TFM, Equation (3.7) shows that only half the mmf is dropped across each airgap, there being two such gaps in the magnetic circuit. To obtain realistic values of shear stress, the value of flux density used in the TFM is half that used in the other machines.

Table 3-1: Values used in shear stress comparison

Airgap (mm)	1
Electric Loading (kAm ⁻¹) –flat machines	50
Electric Loading (Amm ⁻²)-tubular machine	1.6
Maximum achievable airgap flux density (T)	0.8
μ_r	1.1
t_m (mm)	5
w_m (mm) –VRPM machines	12
w_m (mm) –tubular machine	50
B_r (T)	1.2

Table 3-2: Results of peak shear stress comparison

	Field-wound machines	PM machine	VHM	TFM	Ironless tubular
Shear stress (kNm ⁻²)	40	50	133	303	42
Required active area (m ²)	2.5	2	0.75	0.34	2.4

Table 3-2 shows the results of this analysis. The two VRPM machines show superior characteristics, with the TFM having over twice the shear stress of the VHM. It is important to note that the comparisons give no consideration to power factor or efficiency. Furthermore, no consideration has been given to the relative quantities of material used, in particular the rare earth used in the PMs which will significantly impact the cost of designs.

3.6 Discussion

3.6.1 General Structural Comparison

The synchronous and induction machine are both well established structures made exclusively of iron and copper, which greatly simplifies their construction and reduces cost.

The VHM uses less magnetic material than the tubular and TFM topologies because it is only required to cover the stator area. Consequently, the physical construction of translator for the VHM is considerably easier, being a purely iron structure. The TFM has an unfortunate combination of complicated rotor and stator configurations.

In the VRPM machines, a high rate of change of flux will induce eddy currents in the iron structures of the stator and translator. To reduce the associated iron losses, the path of this unwanted current is limited by using a laminated structure. Comparing the VHM and TFM, the former has just two sets of laminations to secure, one for each C-core. The TFM structure is likely to be more troublesome. Some eddy current losses may also be expected in the PMs, although the likely low frequency of operation will limit this effect.

3.6.2 Suitability for Marine Renewable Energy Converters

Other than overall size and weight, other factors influence the choice of electrical machine for this application. Focusing on wave energy converters and in particular the heaving and IPS buoys introduced in Chapter 1, the VHM and induction machine lend themselves favourable by virtue of their simple translator topology. In order to manufacture a linear machine there is a need to limit the permitted amplitude of oscillation which will, as investigated in Chapter 2, drastically influence the power rating of a WEC. The benefit of a simple translator construction is that the amplitude of oscillation may be increased with a relatively small cost and weight penalty. These two factors also provide scope for reducing or eliminating the demand on end stop devices. In both the tubular machine and the TFM, an increase in the translator has a corresponding increase in the mass of magnets required. This added cost per rotor length is likely to drive down the upper amplitude limit for which it is economical to extract power.

The requirement of transferring a current to the translator necessitates the use of slip rings for the synchronous machine. These are not favourable for the linear

configuration or oscillating motion, particularly in combination with the corroding marine environment.

A unique advantage for the tubular machine, highlighted in Chapter 6, is the availability of moving seals for members with cylindrical cross-sections. The air cored version of this, and particularly the corresponding reduction in magnetic forces, drastically simplifies the lubrication of the translator.

A notable advantage for both the electrically excited machines is the ability to de-energise the magnetic field. In the case of a malfunction, or during periods of routine maintenance, it is possible to instantly cut the output power of the machine to zero by disconnecting the field current. The equivalent for a magnet excited machine is to short its outputs, which in the case of the ironless tubular and PM synchronous machine may result in large currents. The large inductance present in the VRPM machines would act to limit the short circuit currents.

The slow velocity demands short pole pitches in order to stimulate a high rate of change of flux to induce large emfs. Any of the PM excited machines are capable of this. This advantage is likely to be slightly offset for the VRPM machines, however, which will require power electronic equipment to compensate for low power factor.

3.6.3 Selection of machines for further development

Permanent magnet excitation of electrical machines has been shown to represent significant shear stress increases when compared with electrical excitation. There are significant efficiency and maintenance savings inherent in the lack of demand for magnetising force or current carrying brushes. The TFM has the highest shear stress and so would require the smallest machine to react a given force. However, this advantage must be offset against the complex translator and stator configurations, high reported cogging torque, inherently three dimensional flux pattern and translator mounted magnets. The VHM is instead chosen.

For comparative purposes the air cored tubular machine is also selected for further analysis. Its smooth cylindrical translator makes it physically very similar to the well established technology of hydraulics and thus desirable for MECs. Furthermore, the translator flux pattern and stator air core avoid the requirement of a laminated structure to reduce eddy currents. Zero current cogging force and airgap closing force will be eliminated with the lack of stator iron and likely to remain small if a three phase concentric winding is used to carry current.

These two machines represent extremes in terms of PM usage and rotor configuration, where the VHM uses an absolute minimal amount of Nd-Fe-B yet has a non uniform cross-sectional area in the direction of motion. The relative merits of these factors provide the designer with an interesting choice when selecting a machine topology for marine renewable applications. The proceeding Chapters intend to outline the two options more fully. The details of the methodology and equations for sizing two prototypes are further derived. Both the machines are nominally rated at 3 kW at 0.5 ms^{-1} , which allows the required force, 6 kN, to be used in conjunction with maximum shear stress as the basis for size calculation. As these machines are to be used as generators, consideration is also be given to the likely magnitude of emf induced.

3.7 Conclusion

Various linear machines have been identified. The large active airgap required by field wound machines, induction and synchronous, for use in marine renewable applications has been demonstrated and used to highlight the potential advantages of using PM excited topologies. Two radically different topologies of this sort have been selected for further investigation in the proceeding Chapters.

Chapter

4

The Linear Vernier Hybrid Machine

In this Chapter the linear Vernier Hybrid Machine (VHM), introduced in the previous Chapter, is further developed and analysed. Initially a prototype is designed based on the shear stress calculations derived in that Chapter (3.12). This simple equivalent magnetic circuit method is further expanded to include predictions for the emf and dimensions of the coil, thus allowing the specification and manufacture of a 3 kW device for further investigation. A Finite Element Analysis (FEA) model is formulated and used to describe the flux flow more accurately, allowing the force and generating characteristics to be predicted using a more sophisticated model. The accuracy of these models and the FEA are then investigated by comparison to experimental results.

Thus, after experimental verification of models, they may legitimately be used to design larger machines.

4.1 3 kW Prototype

4.1.1 *Three phase construction*

For a VHM to produce a balanced three phase output each phase must be such that the relative position of its magnets and stator teeth are 120 electrical degrees out of phase. Physically this is achieved by adjacent phases being separated by a multiple of two thirds of a rotor pitch.

There are two formats of structure which will achieve this. The more traditional approach, commonly used in rotary machines, is to have the three phases interspersed with each other, allowing the flux from differing phases to share the same return path. Preliminary studies conducted using FEA revealed that this layout was inappropriate as the three phases would no longer act independently. The flux pattern of each phase would stray significantly into the path of the other phases. Modelling of such a system

would require the development of a complex set of inter-phase current and position dependent inductance equations. To avoid this a second topology of machine is used where each phase is magnetically isolated from the others, allowing them to be treated and analysed separately. Each phase core back consists of a single C-core supported independently from its neighbours, eliminating the inter-phase back iron. Adopting this modular approach provides a high degree of flexibility in the design and choice of power ratings and results in a reduction in the total amount of steel used. A diagram of one such phase is shown in Figure 4.1.

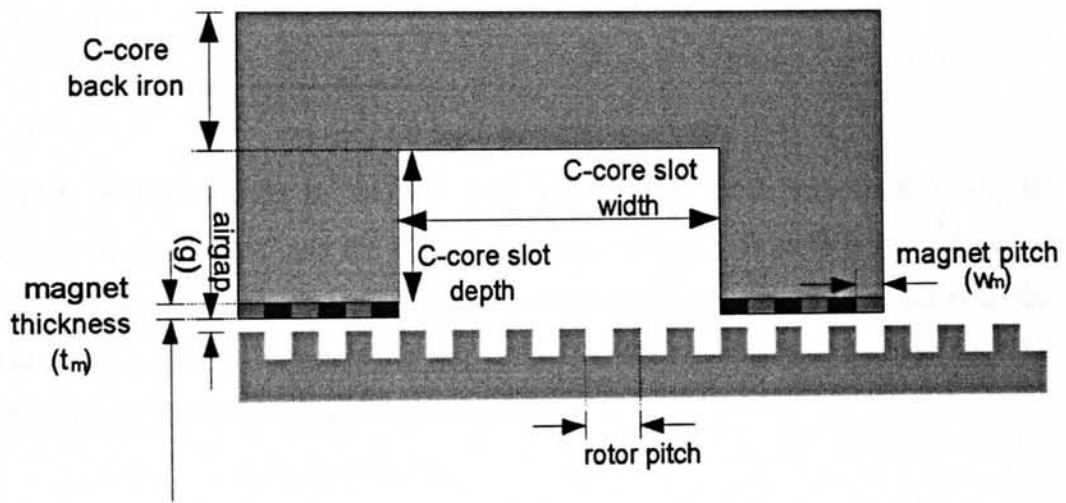


Figure 4.1: Dimensions of the VHM

4.1.2 Force calculation

The VHM may be modelled by idealising the magnetic flux pattern such that the flux density under the tooth and under the slot are constant over their length and equal to B_t and B_s respectively. The equivalent magnetic circuit of Figure 4.2 represents one quarter of the machine which would give the same value of flux as modelling all the gaps and mmf sources. This model holds true for the entire phase, where there are 4 mmf sources in series with four airgap reluctances.

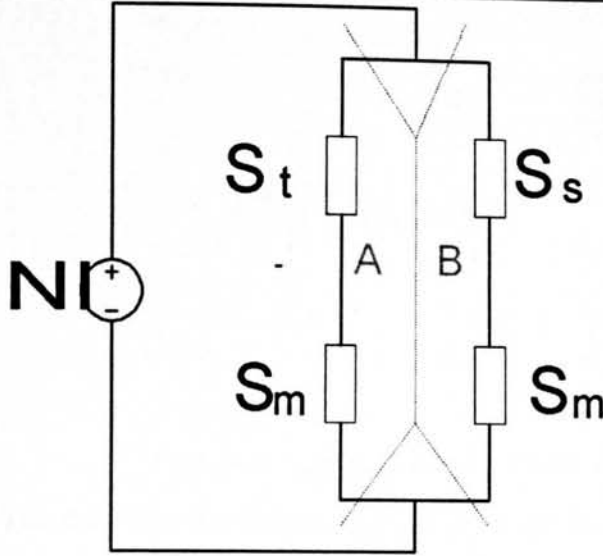


Figure 4.2: Equivalent Circuit of VHM

Branch A corresponds to the flux path through the tooth and consists of the reluctance of one magnet and the airgap under the tooth, S_t . Branch B represents the flux flow through the slot region and consists of a magnet reluctance in series with the reluctance of a slot, S_s . Considering just branch A, the reluctance is defined in (4.1), which gives the flux flow of (4.2) for each tooth.

$$\begin{aligned}
 S_A &= S_t + S_m \\
 &= \frac{g}{\mu_0 w_m L} + \frac{t_m}{\mu_r \mu_0 w_m L} \\
 &= \frac{g\mu_r + t_m}{\mu_r \mu_0 w_m L}
 \end{aligned} \tag{4.1}$$

$$\begin{aligned}
 B_A &= \frac{\phi_A}{A_m} \\
 &= \frac{1}{w_m L} \cdot \frac{NI}{S_A} \\
 &= \frac{NI\mu_0\mu_r}{(g\mu_r + t_m)}
 \end{aligned} \tag{4.2}$$

Noting that B_A is equivalent to B_t in (3.12), substitution may now be used to relate the shear stress to the excitation current.

4.1.3 Emf calculation

The emf induced in the VHM is dependent on the rate of change of flux due to magnet excitation, which means the equivalent magnetic circuit is similar to that of Figure 4.2 used to derive the shear stress, but with NI replaced with mmf from the magnets, or $H_c t_m$ (defined previously in (3.5)) as shown in Figure 4.3.

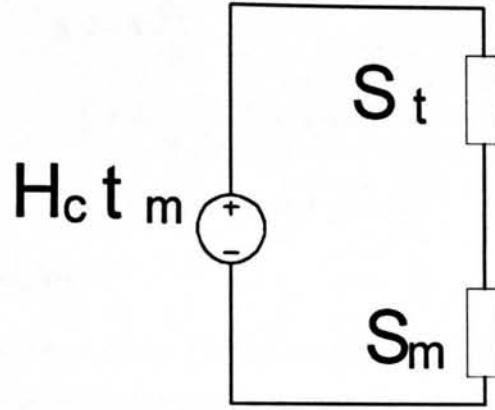


Figure 4.3: Equivalent circuit for VHM with magnetic excitation only

The flux flow due to one magnet only, ϕ_m , may now be found in a similar manner as (4.2), giving (4.3). This expression considers only the flux flowing in the tooth region and thus represents the case when the magnet and teeth are fully aligned and leakage between two adjacent magnets is ignored, a highly simplified scenario.

$$\phi_m = \frac{t_m B_r A_m}{(t_m + g \mu_r)} \quad (4.3)$$

Where A_m = area of one magnet (m^2)

If this is assumed to be the peak, $\hat{\phi}_m$, of a sinusoidal flux flow dependent on position, x , having a period of double the magnet width, then the flux flow through an entire face and its resultant emf can be expressed as (4.4).

$$\begin{aligned} \phi_{\text{face}} &= \hat{\phi}_m \frac{n}{2} \sin\left(\frac{\pi x}{w_m}\right) \\ \frac{d\phi_m}{dt} &= \hat{\phi}_m \cos\left(\frac{\pi x}{w_m}\right) \frac{\pi \dot{x}}{w_m} \frac{n}{2} \end{aligned} \quad (4.4)$$

Where n = number of magnets mounted on stator face

Combining (4.3) and (4.4) whilst remembering that $A_m = w_m L$, allows the relationship for peak emf given in (4.5) to be deduced.

$$E = -N \frac{d\phi}{dt}$$

$$\therefore \hat{E} = N \frac{t_m B_r}{(t_m + g\mu_r)} \dot{x} \pi L \frac{n}{2} \quad (4.5)$$

Where N = number of turns per coil

4.1.4 Machine Sizing

Crucial to the behaviour of the VHM is the size of the airgap, which is a result of the manufacturing and assembly process. A nominal airgap of 1mm was thought to be the minimum achievable. A convenient magnet thickness was 4 mm.

There are two factors which limit the shear stress of this machine, the heat dissipation of the coils and the saturation of the iron. The former is governed by the dimensions of the coil and is dependent on the surrounding environment whereas the latter depends on the shape and properties of the iron. Consideration of the flux flow within the machine implies that the most likely place for iron saturation will be in the root of the tooth and will hence directly affect the flux density in the airgap under the tooth, B_t . The maximum flux density achievable in mild steel is around 1.9 T (see Figure 4.8 later). Equation (4.6), a combination of (3.12) and (3.14) from Chapter 3, shows the shear stress for the VHM in terms of the translator tooth-root flux density. The behaviour of the relationship is given in Figure 4.4 which, for a density of 1.9 T, shows a clear peak for a magnet width of around 17 mm and subsequent decline with further magnet width increase.

$$\hat{\sigma} = \frac{B_r}{\mu_0 \mu_r} \frac{t_m}{w_m} \left(\frac{B_{\text{root}}}{1 + \frac{g + t_m}{\sqrt{(g + t_m)^2 + 0.25w_m^2}}} \right) \left(1 - \frac{g + t_m}{\sqrt{(g + t_m)^2 + 0.25w_m^2}} \right) \quad (4.6)$$

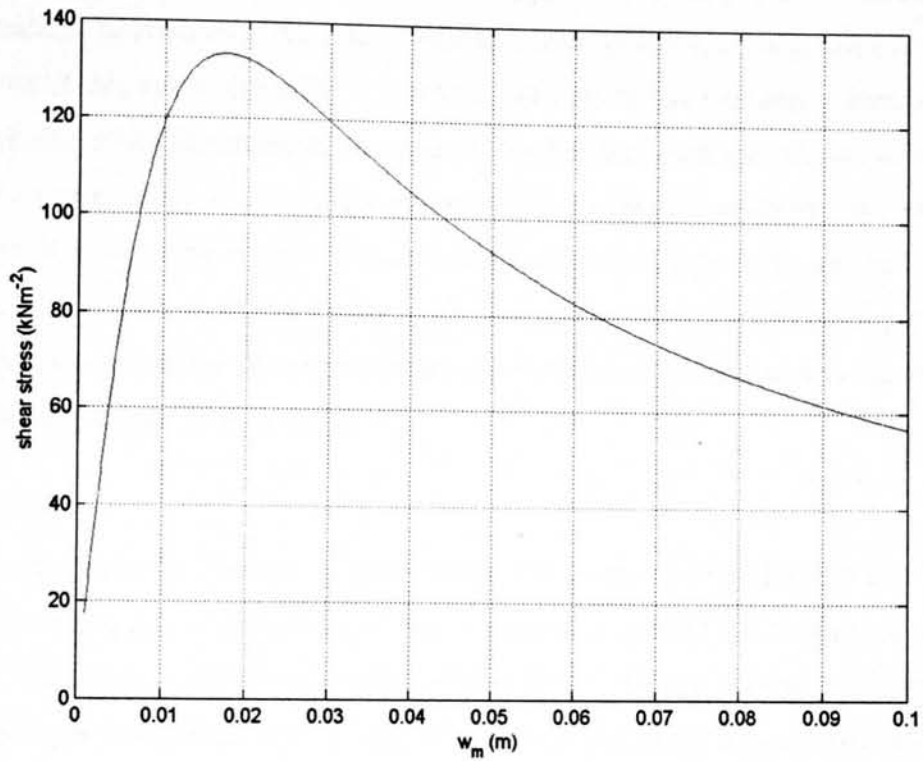


Figure 4.4: Effect of magnet width in predicted shear stress

For manufacturing and availability purposes, the value used will be 12 mm, corresponding to a predicted shear stress of approximately 126 kNm^{-2} .

Consider each phase being subjected to a sinusoidal current whilst moving at a constant velocity, the resulting three phase force reacted would be of the form given in Figure 4.5. As shown, the total contribution is equal to 1.5 times the peak of a single phase.

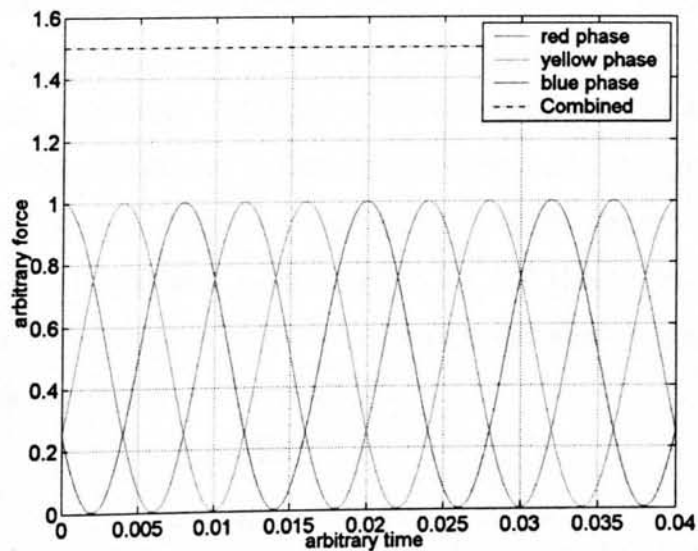


Figure 4.5: Example of three phase force

To remove 3 kW from the translator moving at 0.5 ms^{-1} requires the entire three phase machine to react an average force of 6 kN, corresponding to each phase having a peak force of this value divided by 1.5, 4 kN. Each phase has four active areas which, in combination with the predicted shear stress, implies that each area should be 0.0079 m^2 . For an axial length of 0.1 m, this corresponds to a pole face width of 0.079 m. The definition of shear stress consists of pairs of opposed forces, due to the interaction of a tooth and slot region, implying it only holds for an even number of magnets per stator pole. The closest number of magnets which gives the correct active area is therefore 6. These dimensions are given in Table 4-1

4.1.4.1 Coil

The coil affects two functions of the VHM, the product of current and number of turns gives mmf, NI, whereas the number of turns only affects the magnitude of emf induced. Substitution of the values obtained thus far into (4.5) gives the predicted open circuit emf per coil turn as 0.55 Volts. In line with the likely overestimation of this value, and the desire for a large output emf for use in the power factor correction equipment, 240 turns per coil are used, giving a 130 Volt peak output.

The dimensions of the coil depend on the current flowing within it and the allowed temperature rise due to power loss. The 'knee' of the B-H curve for iron, shown in Figure 4.8 later, is at around 1.5 T. Limiting the flux density through the tooth to this value hence ensures the iron remains unsaturated and behaves linearly. In order to have a flux density of 1.5 T within the tooth requires an mmf of 5.7×10^3 Ampere turns, according to (4.2), corresponding to 23 Amps flowing in the 240 turns. This will be the peak value of a sinusoidal current having an RMS of 16 Amps. If the instantaneous peak current density of the coil is limited to 4 Amm^{-2} , the copper wire will need a diameter of 2.7 mm. Assuming a fill factor of 40%, the coil will have a cross sectional area of 0.0034 m^2 , with dimensions of approximately 4 cm by 8 cm. The length of wire used will be around 100 m, which corresponds to a coil resistance of 0.3Ω if it is manufactured from copper with a resistivity of $1.73 \times 10^{-8} \Omega\text{m}^{-1}$. The resulting RMS power loss of 76 Watts manifests itself as a rise in temperature according to (4.7), a simplified expression of convection cooling [73].

$$P_{loss} = hA\Delta T \quad (4.7)$$

Where h = heat transfer coefficient = $60 \text{ Wm}^{-2}/^\circ\text{C}$
 ΔT = temperature rise with respect to surroundings ($^\circ\text{C}$)
 A = surface area available for heat dissipation (m^2)

Assuming that a temperature rise of the order of 60°C is acceptable, Equation (4.7) implies that a coil surface area of more than 0.02 m² with the surrounding air is desirable. Thus the outer dimensions of the 4 by 8 cm coil provide ample surface for cooling. Allowing 2 cm clearance, a 10 cm slot depth in the stator C-cores is required. The remaining prototype dimensions are as given in Table 4-1.

Table 4-1: Dimensions of VHM prototype

Magnet pitch (mm)	12
Magnet thickness (mm)	4
Airgap (mm)	1
Core length (mm)	100
Magnets per pole	6
Rotor pole pitch (mm)	24
Rotor slot depth (mm)	10
C-core slot depth (mm)	100
C-core slot width (mm)	144
Core back (mm)	50

4.2 Finite Element Analysis

The dimensions and previous descriptions of the VHM machine have been based on simplified flux flows and equivalent circuit analysis. In reality there will be significant fringing and interference effects between adjacent magnets and teeth. A detailed, more accurate, model will therefore require the use of an FEA program.

Analysis of the model will provide a visual representation of the machine behaviour, by way of flux lines. Furthermore, it will allow the development of expressions to describe the dynamic performance and static characteristics in terms of voltage induced and force reacted respectively.

4.2.1 Details of the model

The flux flow of a VHM may be assumed to be two dimensional and modelling can hence be undertaken using a two dimensional FEA program. The software used here is Vector Field's PC Opera 2 D [74]. Within this program a single phase, two pole double sided linear VHM was simulated. Each pole has six magnets attached in such a way that the flux return path passes across, not along, the axis of the translator back iron. The pattern it traces is hence symmetrical about the centreline of the translator, thus allowing the model to consist of one half of the machine, the second half being implied by a boundary condition of symmetry applied to this centreline. Flux flow is not symmetric about a plane at 90 degrees to this however, and so it is still necessary to model two poles. The basic mesh of the model is shown in Figure 4.6.

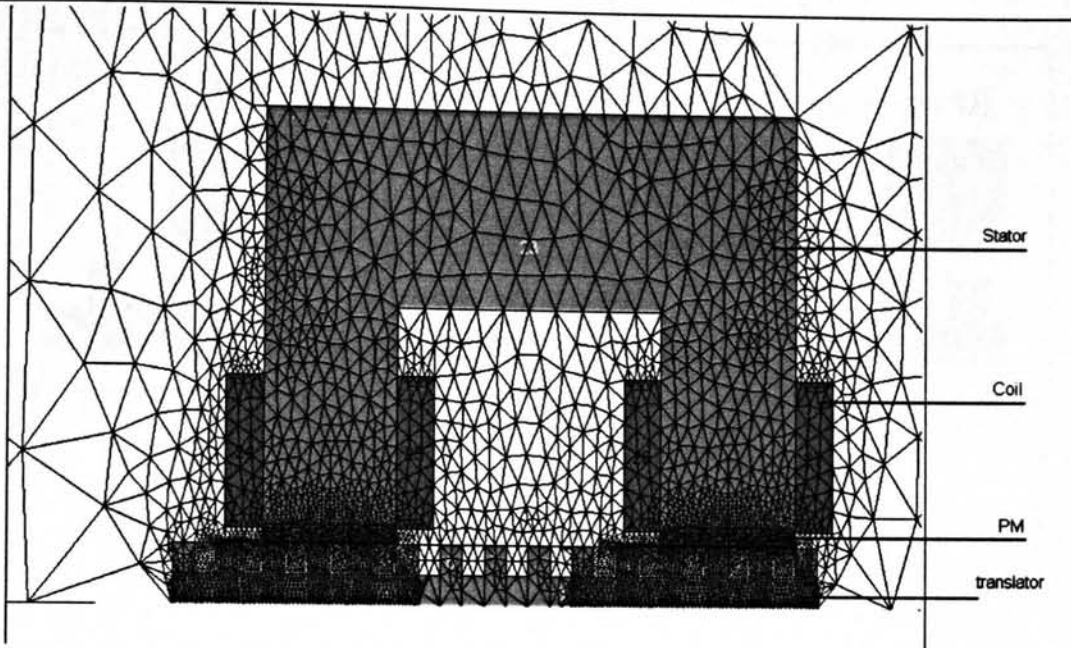


Figure 4.6: FEA mesh of VHM

The model consists of 15 000 elements of varying size, the smallest of which are within the airgap and magnetic regions. Predicting the behaviour of a variable reluctance machine using FEA generally requires the model be run at various different operating positions, typically different translator positions. In the case of the linear VHM, however, this means the model be solved at various different relative magnet and stator tooth positions. In order to maintain boundary integrity between the model regions, the smallest increment of movement is limited to the fineness of the airgap mesh. In the model presented here this is 1mm. Noting the repetitive nature of both the translator and the stator it can be seen that it is only necessary to model the movement of the rotor through the distance of the rotor pitch, or twice the magnet pitch, in order to obtain the behaviour of the machine at any subsequent position. The magnet pitch of the model was 12 mm, resulting in 24 different positions being available. In all the results quoted in this section, the relative position, p , is defined such that zero corresponds to the magnet and tooth being fully aligned, Figure 4.7.

The model is surrounded by a background region of air in order to reduce the influence of artificial boundary conditions necessary for the running of the software. To facilitate more accurate modelling, the non linearities of both the steel and magnetic materials are provided, shown in Figure 4.8.

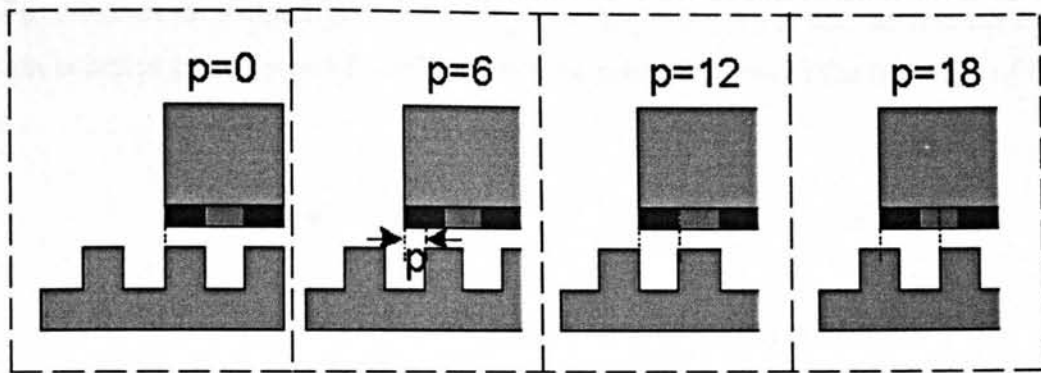


Figure 4.7: Definition of relative position

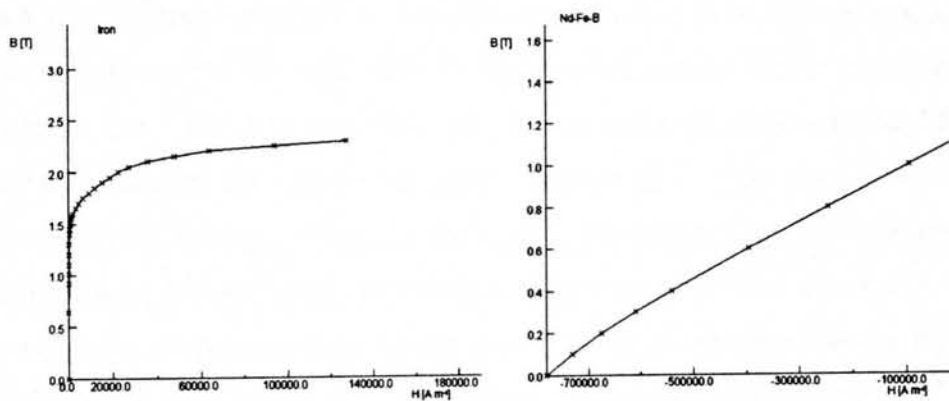


Figure 4.8: B-H data for FEA

4.2.2 Details of the Analysis

The software solves the FEA model as a non-linear magnostatic problem, it therefore does not take account of time dependent effects, such as the losses due to eddy currents. The equations solved relate the magnetic field strength, H , to the current density in the conductors, J , according to (4.8). The flux density, B , has zero divergence as in (4.9) and a magnetic vector potential, Ω , is defined as (4.10).

$$\nabla \times H = J \quad (4.8)$$

$$\nabla \cdot \tilde{B} = 0 \quad (4.9)$$

$$\tilde{B} = \nabla \times \tilde{\Omega} \quad (4.10)$$

The simulation is carried out in the x - y plane such that the magnetic vector potential, A , only exists in the z -axis, and so equation (4.10) becomes (4.11).

$$B = \frac{\partial \Omega_z}{\partial y} \underline{x} - \frac{\partial \Omega_z}{\partial x} \underline{y} \quad (4.11)$$

Where \underline{x} and \underline{y} are unity vectors in the respective directions.

For a line in the x direction, representing a surface in the x-z plane, the flux per unit length is hence given by (4.12), the difference in potential between the two ends of the line.

$$\begin{aligned}
 \phi &= \int_{z=0}^{z=l} \int_{x=a}^{x=b} B_y dx dz \\
 &= \int_{x=b}^{x=a} -\frac{d\Omega_z}{dx} dx \\
 &= \Omega_z(a) - \Omega_z(b)
 \end{aligned} \tag{4.12}$$

Generally the interaction of magnetic flux with current carrying coils is the focus of interest in an electrical machine. It is therefore important to be able to compute the total flux linkage cutting the coils and the influence of current within those coils on the magnetic flux. The former of these may be calculated by computing the difference in magnetic potential between two halves of the same coil. This gives a measure of the flux cutting the coils per metre of axial length. The coils consist of 240 turns of 2.7 mm diameter wire, but are simply modelled as solid copper regions. In order to ensure the correct value of Ampere-turns in the simulation, it is necessary to specify a current density in the nominal single coils which results in a total current one 240th that being carried in the wire.

4.2.3 Details of Results

4.2.3.1 Electrical Excitation

If the permanent magnet regions of the FEA are replaced with air regions, then it is possible to investigate the behaviour of the VHM due to armature excitation only. Figure 4.9 shows the variation of flux linking a phase of the machine with excitation plotted on the same axis as a straight line of gradient 0.425. The good agreement of the two show that, until over 15 Amps, the iron is not becoming saturated.

Investigation revealed that varying the relative position of stator and translator had negligible (<1%) effect on the total flux flow in the absence of magnetic material.

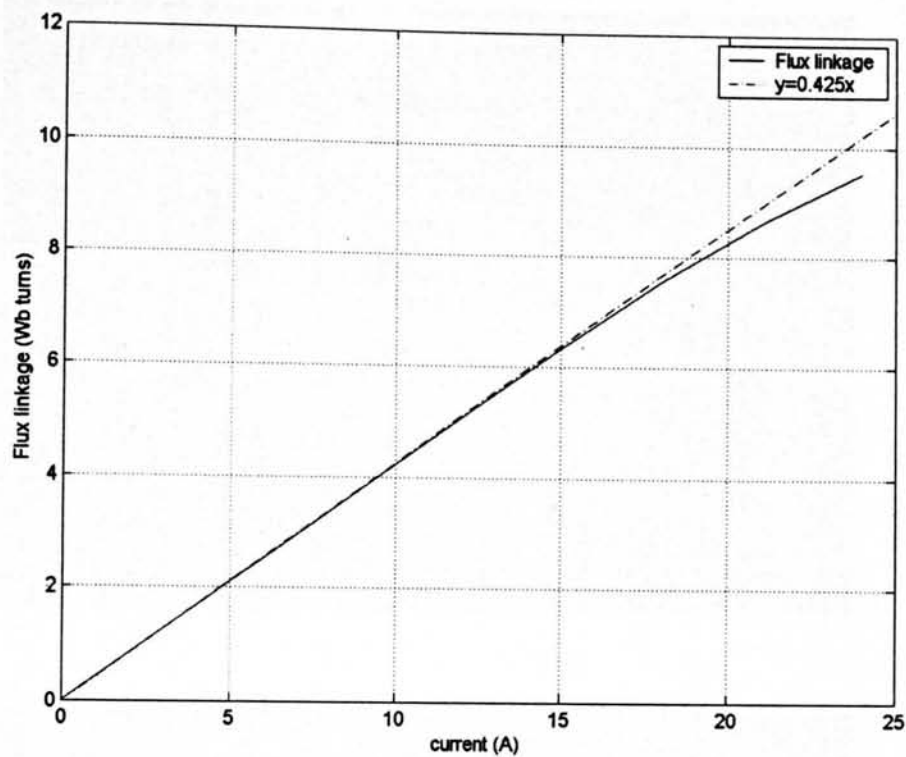


Figure 4.9: Variation of phase flux linkage with excitation current, no magnets.

4.2.3.2 Magnetic Excitation

Figure 4.10 shows the model flux plot when the rotor teeth are fully aligned with the magnets. Two return paths are visible, the leakage flux flowing between neighbouring magnets and the useful flux within the backiron linking the coils. Moving from left to right along each stator face, it is clear by inspection of Figure 4.10A that each aligned magnet contributes less to the flux linking the coils. The rightmost pair make a negligible contribution, with all the flux leaking between neighbouring magnets. With the translator displaced one magnet pitch to the right, as in Figure 4.10B, the pattern of leakage and driving magnets has reversed, with the leftmost pair making no useful contribution. By deduction it is clear that the leakage flux is most severe when the edge magnet has no tooth to channel the flux and so is forced to find a return path through its neighbouring magnet. Any even number of stator pole magnets will hence exhibit this effect. Calculation of the no load flux is therefore highly affected by the edge effects of the stator face, a factor not accounted for with the simple analysis used previously.

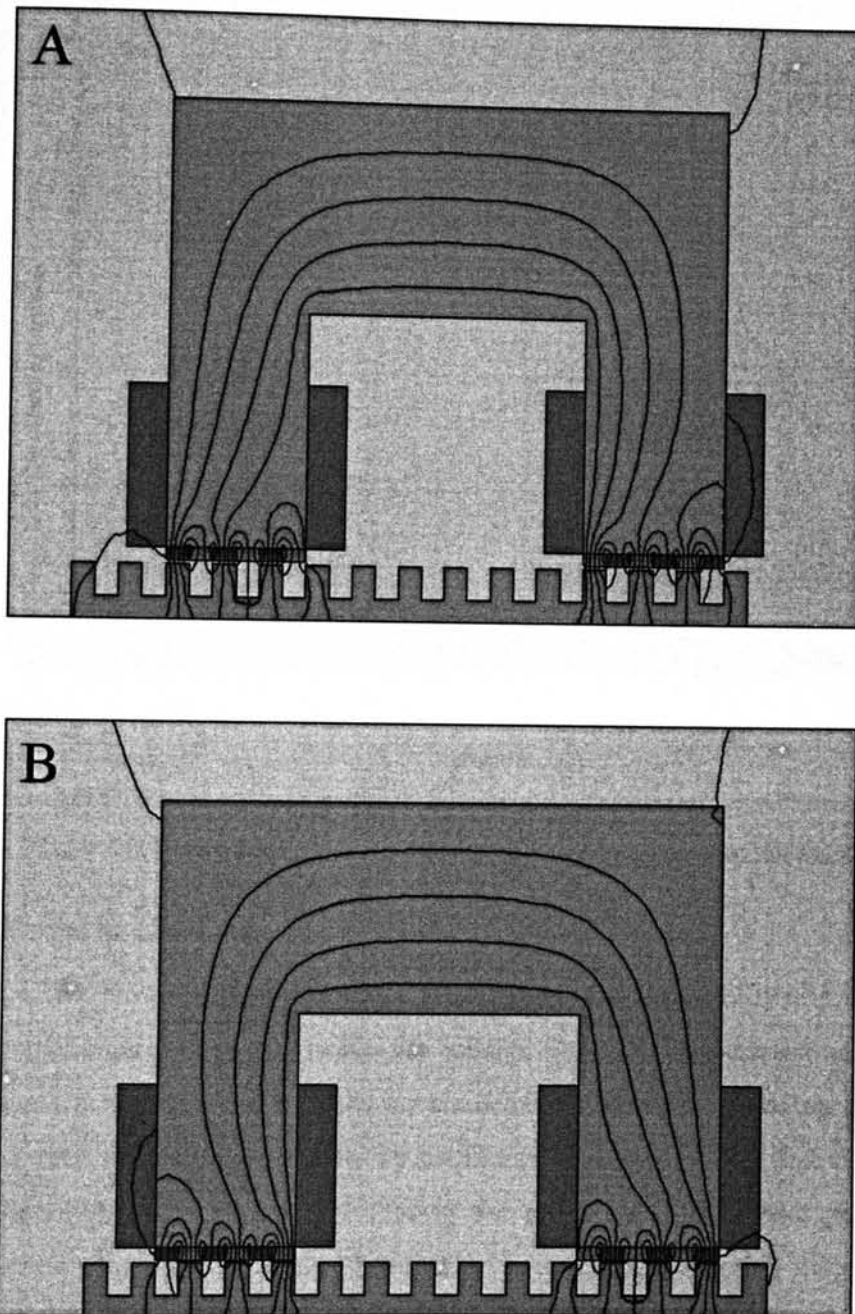


Figure 4.10: Flux plot for magnetic excitation. (A) zero position, (B) 12 mm position

The direction of flux flow is reversed in Figure 4.10A when compared with Figure 4.10B yet it is reasonable to assume the magnitude will be the same. From this it is clear that there will be a position of zero flux flow through the C-core between positions of full alignment with adjacent magnets. Figure 4.11 demonstrates that this occurs when the magnet and tooth are exactly misaligned and the flux return path is across the stator face.

The actual variation of flux linkage is cyclic over the rotor pitch and Figure 4.12 shows that it is a smooth function of relative tooth and magnet position.

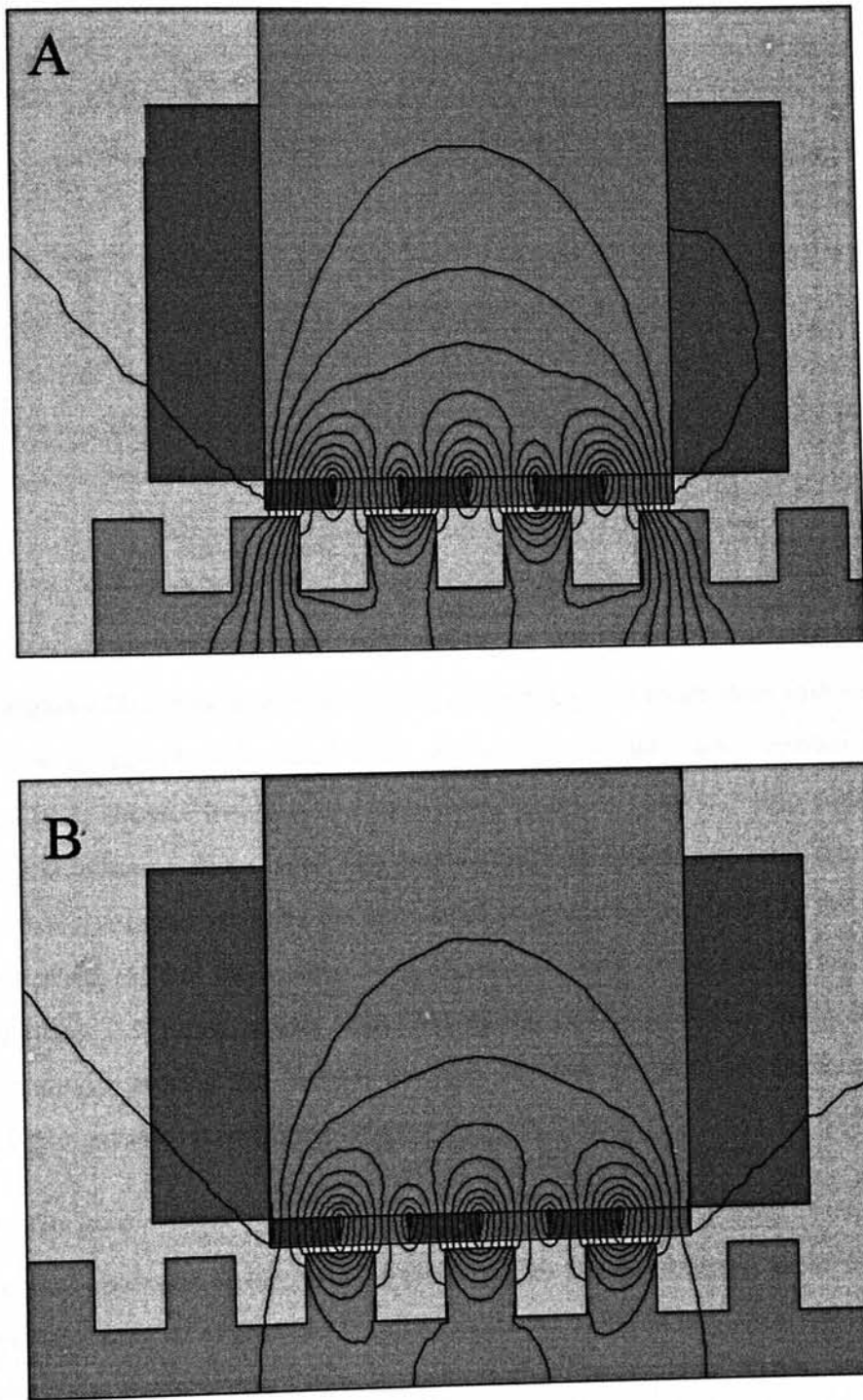


Figure 4.11: Flux plot for the misaligned positions (A position=18 and B position=6), magnet excitation only.

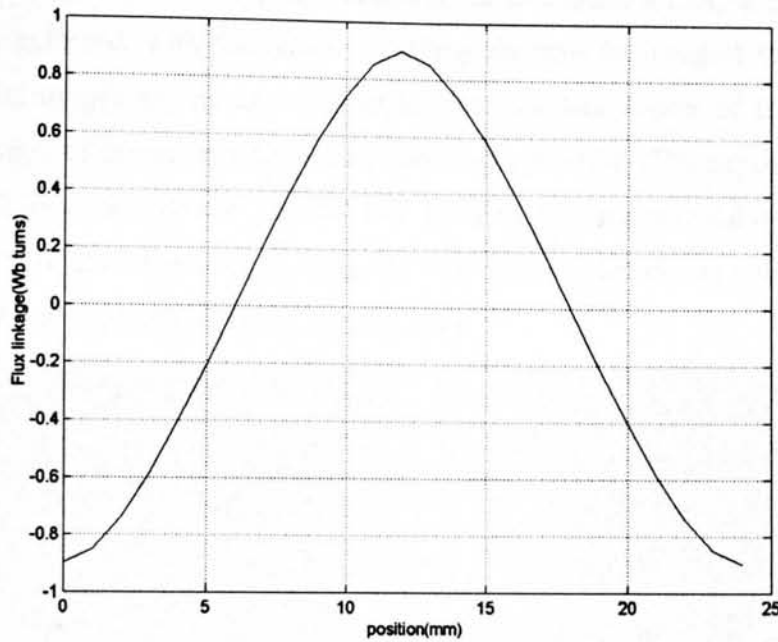


Figure 4.12: Predicted no load variation of flux linkage for entire phase with position

It is now possible to investigate the accuracy of the model used to predict the emf in Equation (4.5) above. Inserting the dimensions given in Table 4-1 into equation (4.3) predicts the value of flux due to one pair of magnets interacting with one translator tooth. Multiplying this value by the number of magnet pairs per face (3), the number of faces per phase (4) and the number of turns per coil (240) gives a peak flux linkage of 3.2 Wb turns, 3.5 times greater than that shown in Figure 4.12. Even as a rough approximation, ignoring the leakage between adjacent magnets is clearly unsuitable, further highlighted by inspection of Figure 4.10.

4.2.3.3 On load

In normal operation of the machine there will be current flowing in the coils, which will drive its own flux around the magnetic circuit in addition to that driven by the PMs. The total flux linkage may be expressed as the sum of that due to the armature excitation, ψ_I , and the original PM driven flux, ψ_{PM} , (4.13).

$$\psi = \psi_{PM} + \psi_I \quad (4.13)$$

The direction of armature excitation with respect to remnant magnet excitation will strongly affect the reluctance and hence path of flux flow in the airgap region. Figure 4.13A and B show the flux plot in this region for a 10 Amp current flowing in either direction at the same translator-stator position. At this value of current the armature excitation dominates and an even contribution from each pair of magnets implies that end effects are less pronounced with armature excitation. When the direction of current

driven flux is opposite to that of the magnets, as in Figure 4.13A, a path of high reluctance is enforced, with flux either travelling through the magnet in a direction opposite to its magnetisation, or being forced into the slot region of the translator. There is a danger of demagnetising the magnets in this position. The opposite is visible in Figure 4.13B, when almost parallel flux lines in the magnet and tooth regions demonstrate that the direction of magnetic remnance strengthens the flux flow, channelling it into the tooth region of the translator.

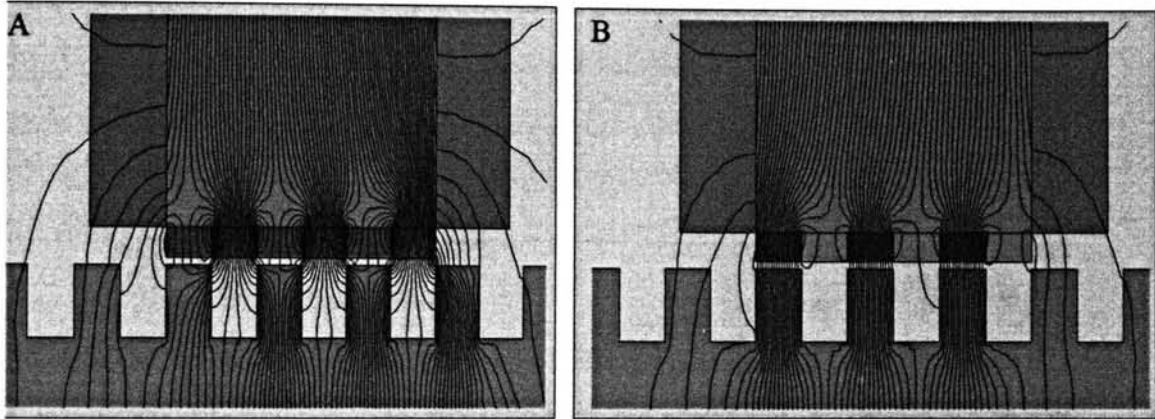


Figure 4.13: Flux plot with (A) +10A, (B) -10 A. Position = 0

Reluctance of the magnetic circuit hence varies with both position and direction of current, for example the flux linking the entire phase being 5.24 Wb turns in Figure 4.13A compared with 3.51 Wb turns in Figure 4.13B.

Flux paths have been demonstrated to be complex in this machine for both combined and magnetic only excitation. The most accurate way to model the machine is by utilising the flux-linkage map of Figure 4.14. Flux data is taken from the FEA at different coil excitations over one electrical cycle and plotted on a three dimensional flux linkage vs. position vs. current set of axes.

The symmetrical variation of flux linkage with current, present in the no load / 0 Amp condition of Figure 4.12, occurs also when the coils are carrying current. The effect of this current manifests itself in more flux being driven around the magnetic circuit and hence the entire flux vs. position curves being shifted up and down the flux axis. It is noteworthy that the plot is not symmetrical over the current range for a fixed position, for example if $p=0$ the resulting flux from a 15 Amp excitation is 7.5 Wb turns compared to -6 Wb turns for -15 A. Re-inspection of Figure 4.13 confirms that this asymmetrical affect is dependent on whether the excitation current is in the same sense as the magnetisation of the aligned magnets.

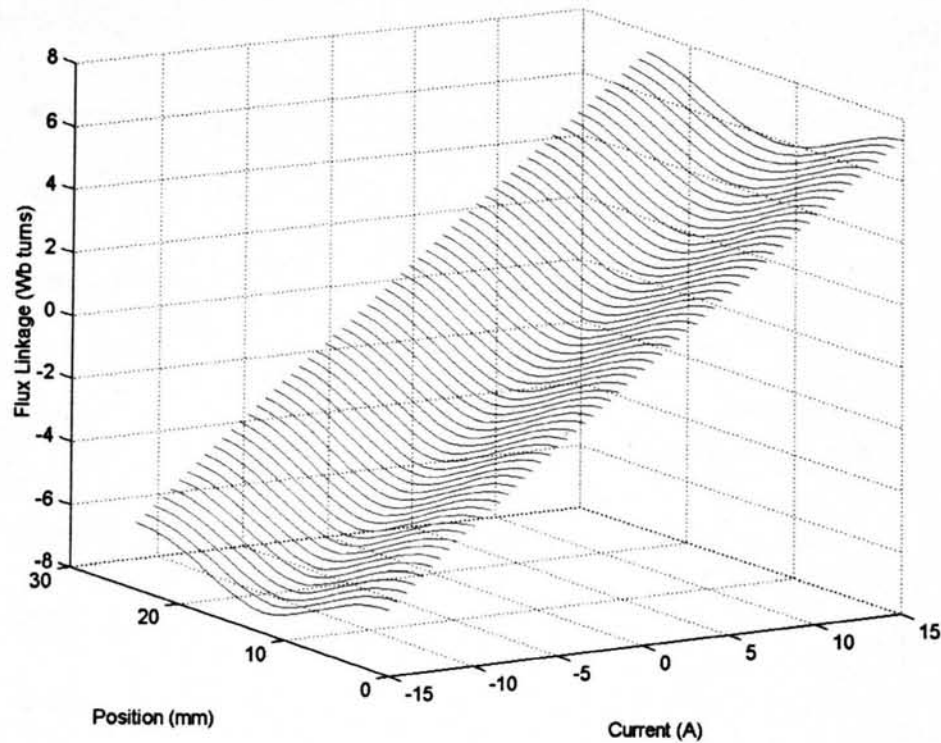


Figure 4.14: Flux linkage map of entire phase

4.2.4 Concluding Remarks

Within this section, the details of the FEA used to model the VHM prototype have been outlined and provisional comments made on the results. The flux linking the coils was found to vary over the 24 mm translator pole pitch, but leakage between adjacent magnets was such that the equivalent magnetic circuit approximation was not suitable to predict its peak value. The resultant flux pattern has been shown to consist of the interaction of two components, ψ_I and ψ_{PM} . More detailed analysis follows on how these observations and results can be used to predict the behaviour of a real machine.

4.3 Utilisation of Finite Element Analysis

4.3.1 Force Calculations

4.3.1.1 Maxwell Stress

A useful feature of using FEA is the ability to calculate the integral of the Maxwell stress tensor, which provides a simple method of calculating the magnetic forces acting on the machine [75].

Static force curves at a variety of different currents are shown in Figure 4.15. They are all cyclic over the 24 mm rotor tooth pitch. Currents of the same magnitude but

opposite direction result in curves which are reflected about the x axis, or 180° out of phase.

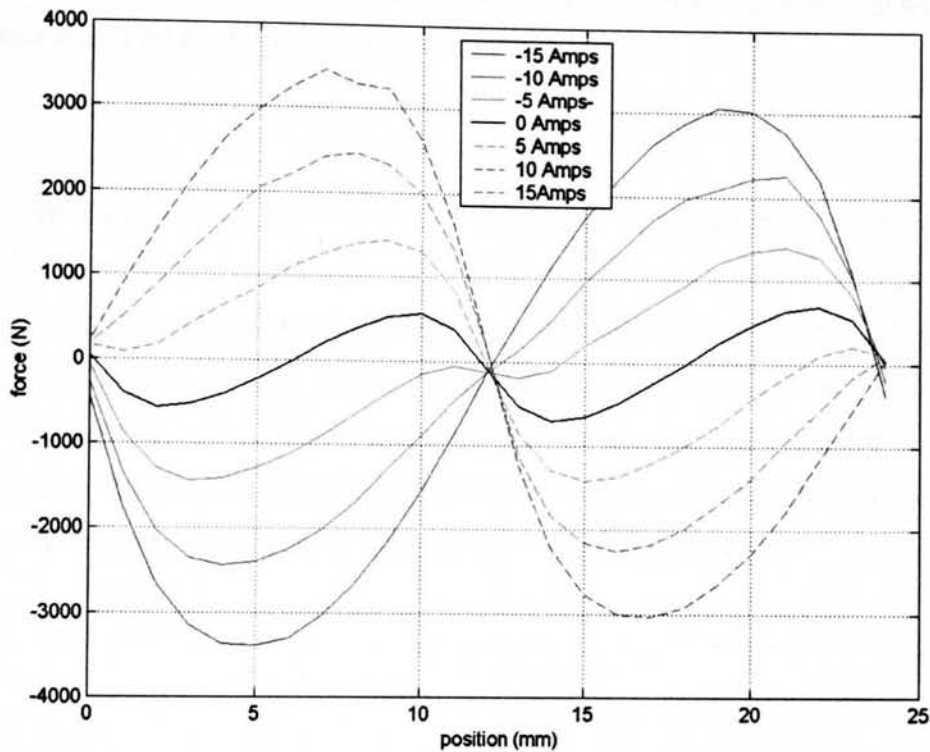


Figure 4.15: Values of static force from FEA calculated Maxwell stress

The zero current result is the cogging force, which results from the natural tendency of the teeth to align themselves with the magnets: the position of least reluctance. As the current is progressively increased in magnitude and the armature flux starts to dominate, the effect of cogging force decreases as electromagnetic force increases.

It is now possible to investigate the accuracy of the simple shear stress calculations used in the design stage. Substitution of the values given in Table 4-1 into the equation for flux density under the tooth, (4.2), with 10 Amps flowing in the coils gives 0.63 T. The force on each magnet can be found from Equation (3.12), giving 82 N, corresponding to a phase force of 2.0 kN. Inspection of Figure 4.15 shows that the FEA predicted amount for 10 Amps has two maxima, corresponding to 2.26 and 2.43 kN. The average of these two is 2.3kN, implying an error of 15 % for the simplified method.

The peak force at 15 Amps is around 3.2 kN, which over the total active area of 0.0288 m² gives a shear stress of 111 kN/m².

4.3.1.2 Normal Force

The magnetic force per unit area between two ferromagnetic surfaces is given by the relationship of (4.14), derived from the change in energy stored in the magnetic field associated with a small change in airgap size.

$$\frac{F}{A} = \frac{B^2}{2\mu_0} \quad (4.14)$$

By calculating the values of flux density at points along the airgap of the machine it is therefore possible to predict the attractive forces between the rotor and the stator. In a two sided machine with an equal airgap between each half of the stator, the net force on the rotor will be zero, it being equally attracted in two opposite directions. The forces present between the rotor and any one side of the linear machine are given in Figure 4.16. As with the tangential force above, the force is cyclic over the 24 mm pole pitch at high currents, yet cyclic over the 12 mm magnet pitch at zero current.

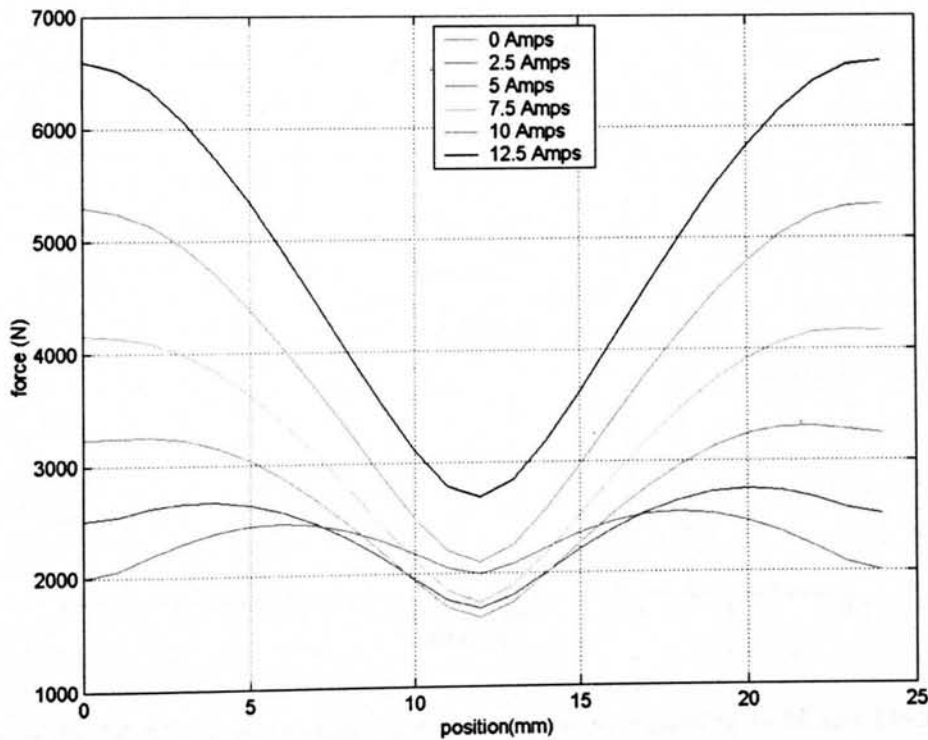


Figure 4.16: Attractive forces between rotor and stator

Figure 4.17 shows the normal force for a positive and negative 15 Amp current, demonstrating that current direction dictates the phase with respect to the position and not the amplitude. This figure demonstrates the high frequency cyclic load which the support structure has to withstand.

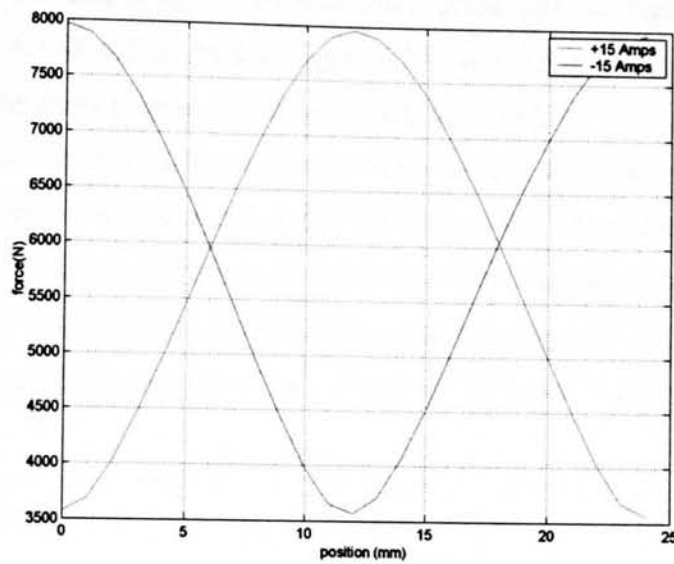


Figure 4.17: Comparison of normal forces for ± 15 Amps

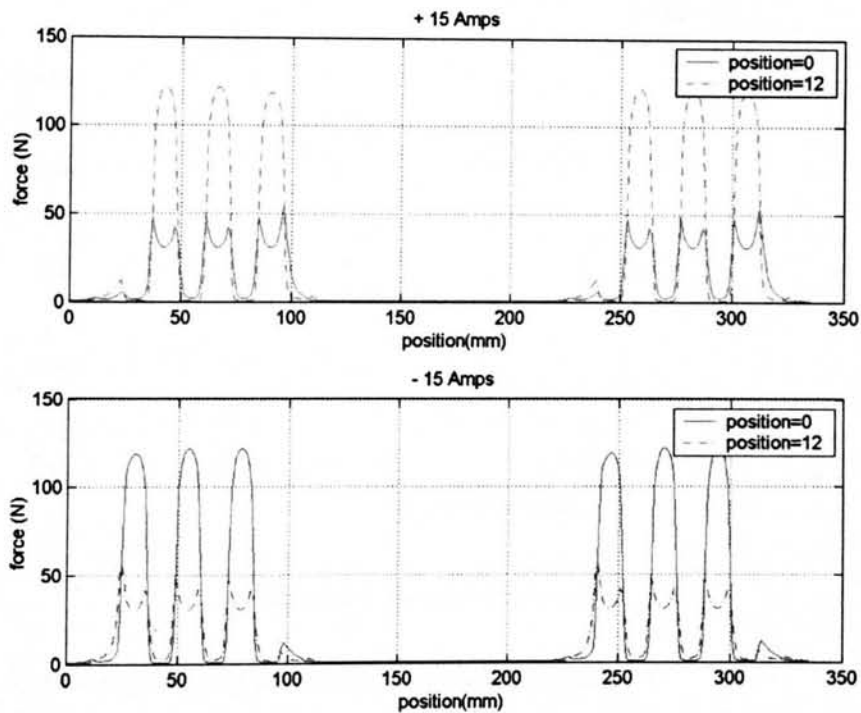


Figure 4.18: Point force along stator. The stator faces correspond to 24-96 and 240-312 mm positions.

A breakdown of the force distribution across the stator airgap for these two currents in the two alternative aligned positions is given in Figure 4.18. As expected, there is no force felt by the majority of the translator, only regions under pole face. Comparison of the upper and lower graphs reveals that the position of the force is dictated not by the location of the rotor tooth, but by that of the magnet in phase with the armature field. When the tooth region is under the in phase magnet, a large 'smooth' force is observed,

corresponding to the dashed upper and solid lower graph lines of Figure 4.18, the flux pattern of Figure 4.13B and the peak of Figure 4.17. When it is the slot region which is aligned with the in phase magnet, a smaller force is observed.

Figure 4.19 shows the variation of force with a current of 10 Amps flowing in the coils, when the rotor and stator are at the 6 mm position. It demonstrates that the attractive forces are highly dependant on the chosen size of airgap. The gradient of the force vs. gap size graph, effectively the stiffness of the magnetic attraction, increases slightly with current, from 1.49 MNm^{-1} at 5 Amps to 2.2 MNm^{-1} at 20 Amps.

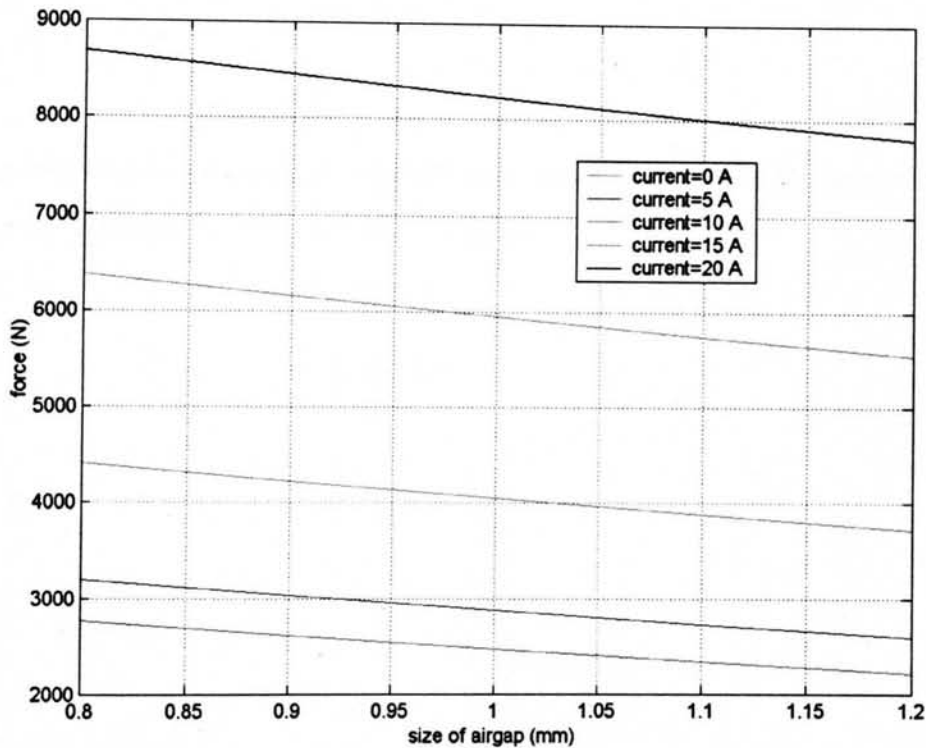


Figure 4.19: Normal force on stator, p=6

4.3.1.3 Co-Energy Model for Electromagnetic Force

Electromagnetic force in a linear machine can be calculated by determining the rate of change of co-energy with position. Using the flux linkage vs. mmf diagram as a visual tool to analyse co-energy in switched reluctance motors is well established [76] and it has recently been used to characterise a doubly salient permanent magnet motor [77]. Total mmf is obtained by the product of current flowing and number of turns for an entire phase, whereas the instantaneous flux linkage is calculated from FEA results. Both of these quantities are a function of translator position and coil current, giving a closed trajectory for each electrical cycle as shown in the typical Ψ -mmf graph of Figure 4.20.

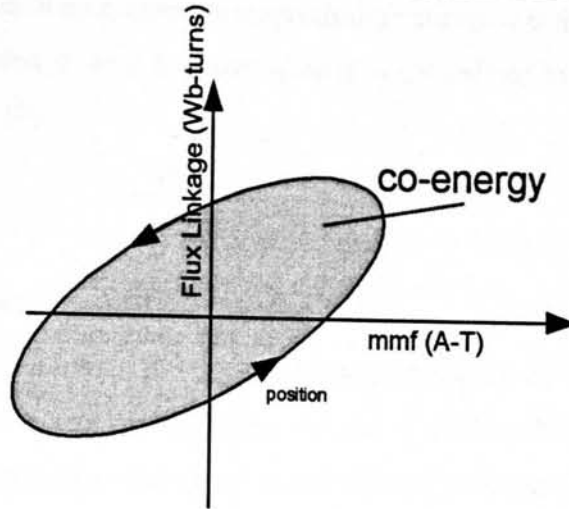


Figure 4.20: Example flux linkage-mmf trajectory

Figure 4.21A shows a typical magnetisation curve, with the field energy and co-energy, corresponding to (4.15) and (4.16) respectively, labelled.

$$W = V \int H . dB \quad (4.15)$$

$$W' = V \int B . dh \quad (4.16)$$

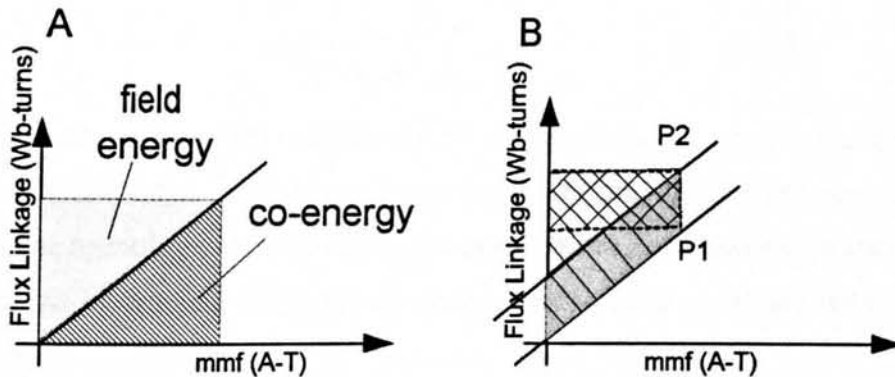


Figure 4.21: Explanation of calculation of co-energy

During the constant current operation of the VHM, the behaviour may be explained by considering the effect of moving from one magnetisation curve to another, P1 to P2 in Figure 4.21B, corresponding to moving the translator. The energy exchanged with the supply during this operation is equal to the change in field energy and represented by the crosshatched area. Stored field energy of the system has changed from the single hatched area to the light grey area. The discrepancy between the change in field energy and supply energy can be deduced to be the change in co-energy and is hence represented by the dark grey area. Expressed more concisely, the change in co-energy

is equal to the area bound by successive magnetisation curves and the x-axis of a ψ -mmf graph. The area shaded in grey in Figure 4.20 is hence related to the electromagnetic force by equation (4.17).

$$F = \frac{\partial W'(i, x)}{\partial x} \quad (4.17)$$

4.3.1.4 Demagnetisation model for Cogging Force

The above method accounts for the electromagnetic force of the VHM. At zero current there is no area swept by moving between rotor position lines on a flux linkage vs. mmf graph and hence no change in co-energy and corresponding force. Section 4.3.1.1, the calculation of force by Maxwell stress, demonstrated that significant magnetic forces are present in the absence of current. These forces result from the tendency of the translator teeth to align with the magnets and are called cogging forces. An alternative approach, which considers the co-energy stored within each magnet is required to calculate the cogging force of a VHM. To achieve this the data must be converted into the flux-mmf for a permanent magnet [78]. The flux emanating from a magnet corresponds to the mmf within that magnet according to (4.18), which describes its loading curve.

$$\text{mmf} = \frac{t_m}{\mu_0 \mu_r} \left(\frac{\phi}{A_m} - B_r \right) \quad (4.18)$$

The intersection of the load line and the de-magnetisation curve is the operating point of a magnet, which will change according to Figure 4.22. Over one cogging force cycle the operating point moves up and down the PM demagnetisation curve. The area swept out by this line represents the change in co-energy contained within the magnet [78,79].

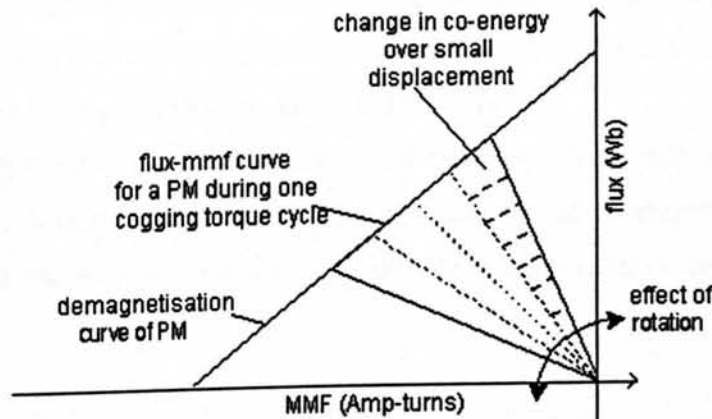


Figure 4.22: Flux-mmf diagram for a PM

This method has been applied successfully to PM machines with large magnet pole pitch. In the VHM however, the pole pitch is of the order 10 to 20 mm and magnets sit side by side. The cogging force is produced by the interaction of a tooth on the translator and a pair of magnets of opposite polarity on the stator. It is therefore necessary to consider the effect of a pair of magnets and their respective operating points.

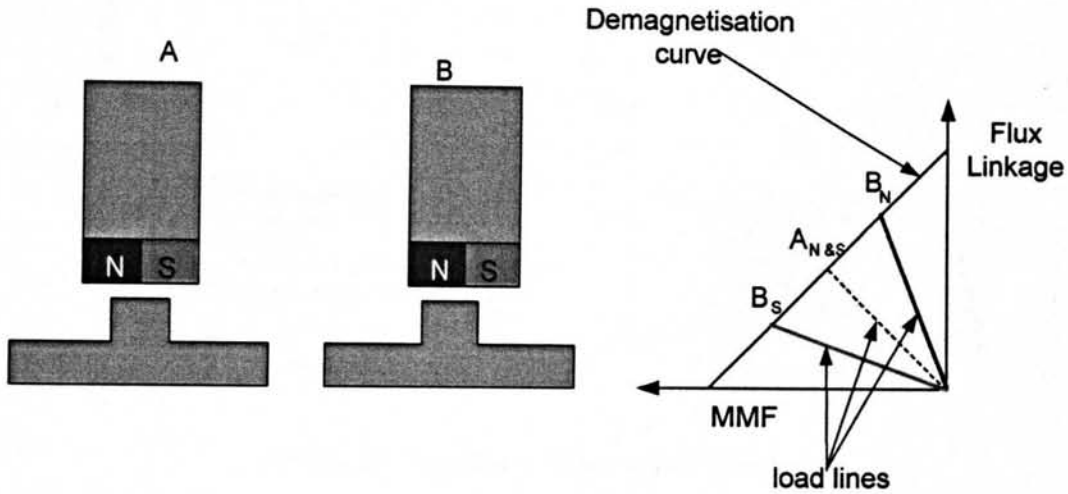


Figure 4.23: Divergence of operating points of PMs

When a rotor tooth overlaps 2 PMs equally, the unaligned position, the reluctance seen by each magnet is identical and hence the operating points coincide. As the rotor tooth moves closer to either magnet, the reluctance path of that magnet is reduced and hence more flux will flow. Figure 4.23 shows the tooth moving towards the North pole magnet and the corresponding move up the load curve. Simultaneously the reluctance path for the South pole increases, reducing the flux flow and moving it down the load line. The divergence of the operating points for the VHM is demonstrated by the FEA results shown in Figure 4.24. The area enclosed by the airgap lines for each magnet and the demagnetisation curve is equal to the co-energy, and hence the cogging force is equal to the rate of change of this co-energy with distance.

The operating points are at a maximum divergence when the translator is in the fully aligned position. The area between the two load lines and the demagnetisation curve is then equal to the total energy that has to be overcome in order to move the translator.

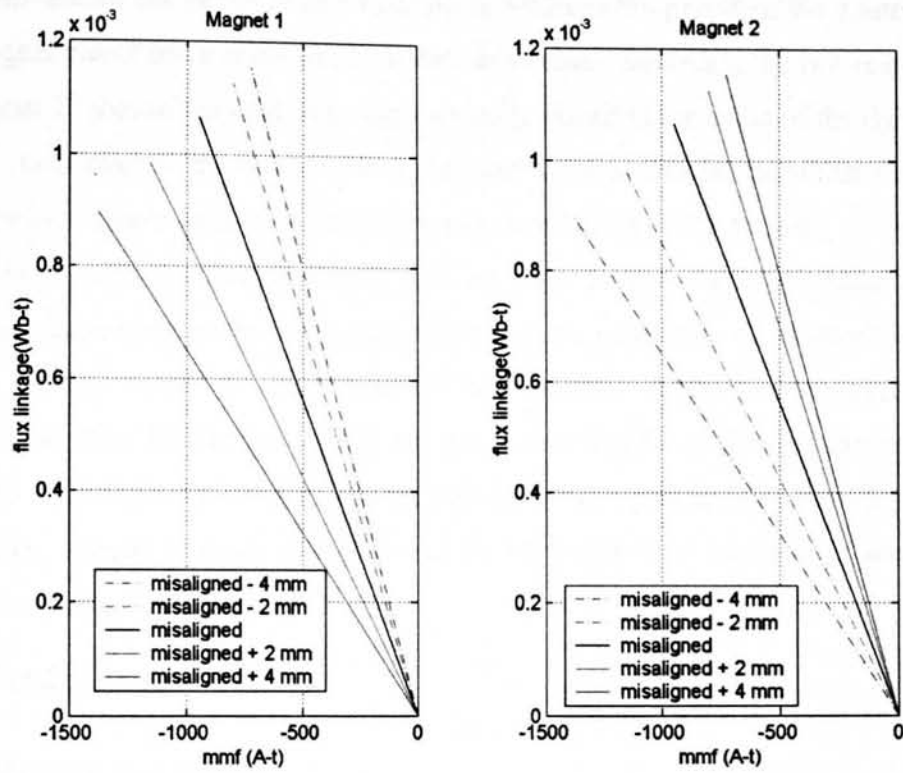


Figure 4.24: Load lines of adjacent pair of magnets

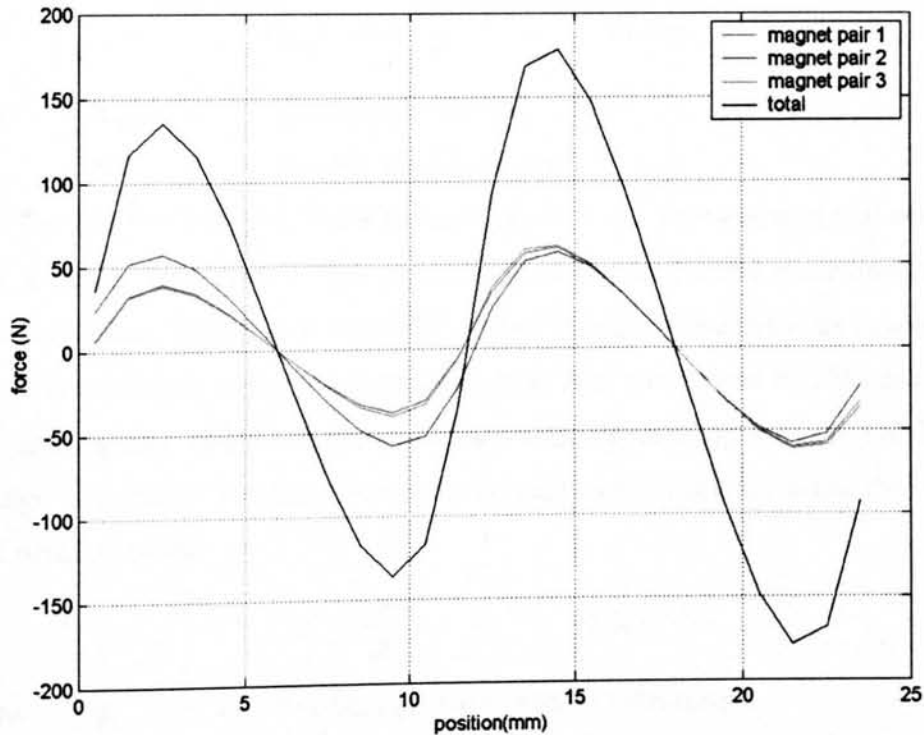


Figure 4.25: Cogging force on one face of the VHM

The cogging force calculated in this manner is shown in Figure 4.25. There are several points of interest to note from this graph, firstly that the period of the resulting

wave form is over the entire 24 mm rotor pitch, whereas the period of the contribution from magnet pair 2 has a wave length of half this value. Secondly, the two maxima in the leftmost 12 mm of the total wave form are only around $\frac{3}{4}$ the value of the right hand maxima. Inspection of the two outside magnet pairs, one and three, show that it is these magnets which do not behave uniformly over the two halves of the period.

It is clear referring back to Figure 4.11 on page 74 that there are different flux patterns corresponding to the two misaligned positions, depending on whether the edge magnets are above teeth or slot regions of the translator. In the former case, Figure 4.11A and position 18, there is a small amount of flux that flows through the translator back iron. This implies a lower reluctance path allowing a greater flux flow through the iron, which represents more energy stored in the airgap and hence a greater force required to change the position.

4.3.2 Performance

4.3.2.1 Open circuit emf

Emf is induced in the stator coils by virtue of a change in flux linking them, the magnitude and direction of which is given by Faraday's law as expressed in (4.19).

$$E_{open} = -N \frac{d\phi}{dt} \quad (4.19)$$

Where E_{open} = open circuit emf (V)
 N = number of turns on coil

In the flux plots of Figure 4.13 and equation (4.13) it was demonstrated that when the machine is run on load there is flux in the machine due to the PM excitation and the armature excitation. Substitution of (4.13) into (4.19) implies that there are two emfs to consider: the driving or open circuit emf, resulting from interaction of PMs and teeth, and an opposing emf, called inductance or back emf, representing the coil's resistance to a change in current. The latter term may be expressed in several ways, the 'purest form' of which is (4.20)

$$E = \frac{d\psi_I}{dt} \quad (4.20)$$

Where ψ_I = flux linkage due to current (Wb-turns)

The two emfs can be treated combined or as separate entities in an equivalent circuit and described by a variety of equations depending on assumptions used. A total of five alternative models are considered in the following sections, becoming progressively more complex and computer intensive. In each model the circuit equation is formulated

and then solved in the time domain with translator displacement fed in from an experimental position transducer to allow direct comparison with prototype results.

4.3.2.2 Simple Equivalent Circuit Model – Model A

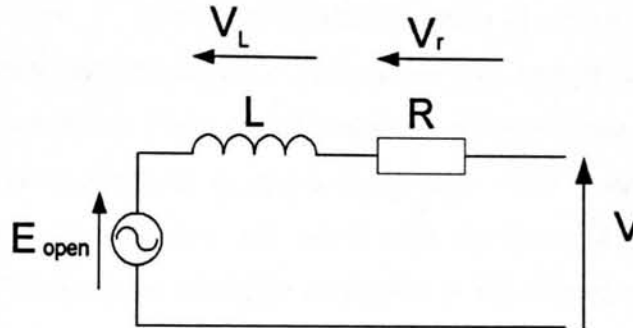


Figure 4.26: Simple Equivalent Circuit

The traditional per phase equivalent circuit for a permanent magnet synchronous machine consists of an emf source equal to the no load emf, feeding into a series reactance and resistance, as shown in Figure 4.26. Using the definition of inductance given in (4.21) substituted into (4.20) and applying Kirchoff's voltage law to the equivalent circuit gives the relationship of (4.22).

$$L_i = \frac{\Psi_i}{I} \quad (4.21)$$

Where Ψ_i = flux linkage due to current with no PMs present in FEA (Wb-turns)
 L_i = constant value of inductance (H)

$$E_{open} = V + V_L + V_r$$

$$\therefore V = E_{open} - L_i \frac{dI}{dt} - IR \quad (4.22)$$

Where the inductance is the flux flow with no PM excitation and can be deduced from the gradient of Figure 4.9, 0.425 H.

4.3.2.3 Step Variable Inductance Equivalent Circuit Model – Model B

Due to the effect of the magnets on the flux pattern, assuming that the inductance may be calculated using purely electrical excitation may have limitations. In order to account for the variation of inductance with current and relative magnet and tooth position, it has been suggested [77] that the inductance may be calculated according to (4.23).

$$L_{I,p} = \frac{\psi - \psi_{PM}}{I} \quad (4.23)$$

Where ψ = total flux linkage due to both coil and PM excitation
 ψ_{PM} = flux linkage due to PM excitation only
 $L_{I,p}$ = inductance considering effect of current and position

Figure 4.27 shows the distribution of inductance with current and rotor position calculated using this method. The value of inductance defined in this manner is greater than the electrical excitation only, L_i , and varies greatly. The 'inverse' nature of the position inductance graph across the zero current mark represents the model accounting for the direction of armature driven flux with respect to the aligned tooth magnet flux. Also highlighted in this graph are the inaccuracies of the FEA, which manifests itself as the rough nature of some of the curves, particularly at low values of current. Slight errors in these low values of flux are highlighted by division of low currents.

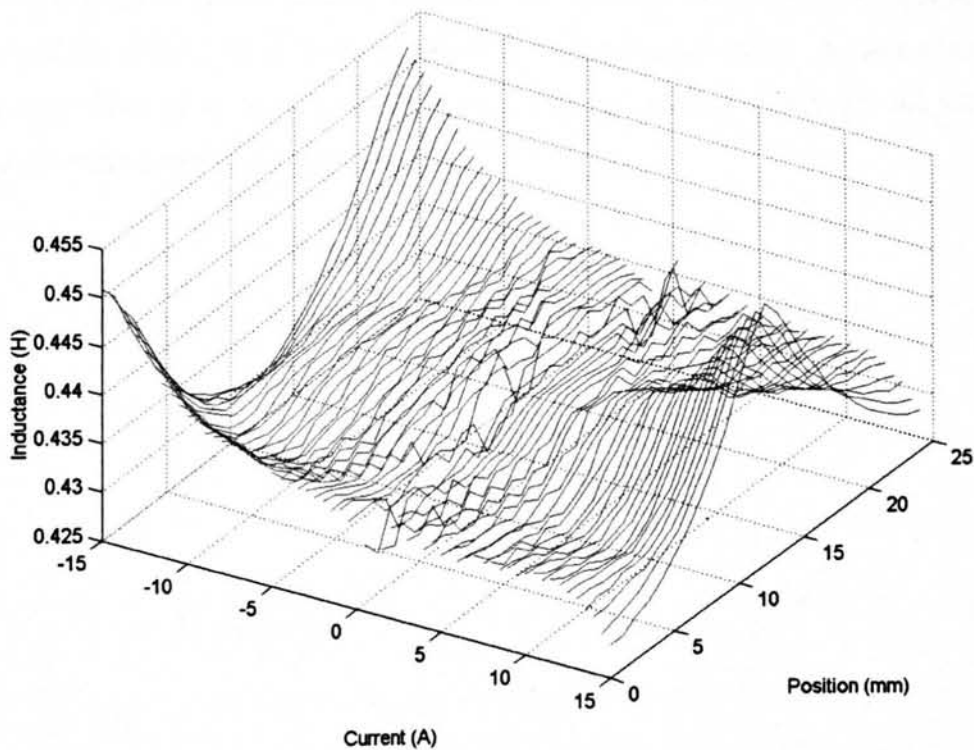


Figure 4.27: Predicted self inductance per phase for different rotor positions and coil currents

If the inductance is calculated at this value for each time step, the equivalent circuit of Figure 4.28 and its governing equation (4.24) results.

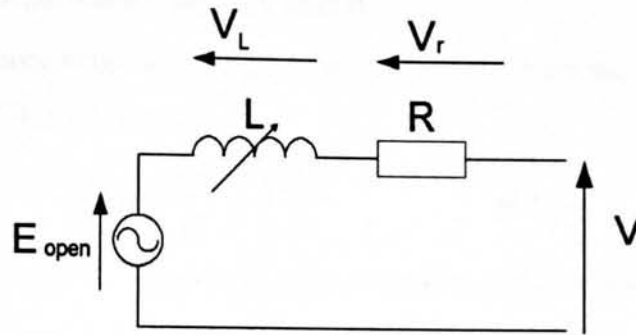


Figure 4.28: Step variable inductance equivalent circuit model

$$V = E_{open} - L_{I,p} \frac{dI}{dt} - IR \quad (4.24)$$

4.3.2.4 Continuous Variable Inductance Method – Model C

The value of inductance $L_{I,p}$ does not change significantly with low values of current (around 10%) so it can be predicted that the performance of the variable inductance model will not differ greatly from the simple fixed inductance model. A more accurate model than either of these is to restate (4.20) as (4.25), which accounts for the *rate of change* of inductance during each time step.

$$V_L = L_{I,p} \frac{dI}{dt} + I \frac{dL_{I,p}}{dt} \quad (4.25)$$

The equivalent circuit is given in Figure 4.29 and described by (4.26).

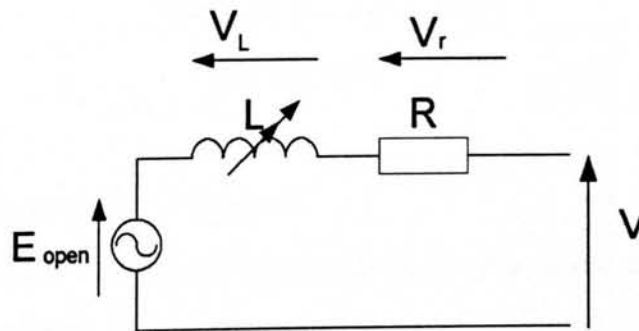


Figure 4.29: Continuous Variable Inductance Method

$$V = E_{open} - L_{I,p} \frac{dI}{dt} - I \frac{dL_{I,p}}{dt} - IR \quad (4.26)$$

Within this model, the inductance is numerically calculated by cubic spline interpolation from a look up table and its rate of change is taken as the difference in inductance value between consecutive steps, divided by the time step.

4.3.2.5 Lumped Reactance Model – Model D

The two inductance terms on the right hand side of (4.26) are the resulting terms of differentiating (4.27) in two parts.

$$V_L = \frac{d\psi_I}{dt} = \frac{d(LI)}{dt} \quad (4.27)$$

Where ψ_I = flux linkage due to electric excitation only, calculated from FEA and equation (4.13), (Wb-turns)

Within this model, the method of calculating inductance and finding its product with current is avoided by constructing a look up table for the flux flow due to current excitation only. The rate of change of this flux is the back emf accross the coil and the equivalent circuit is hence given by Figure 4.30 and described by (4.28). The latter must be integrated with respect to Ψ , not I as in the previous models.

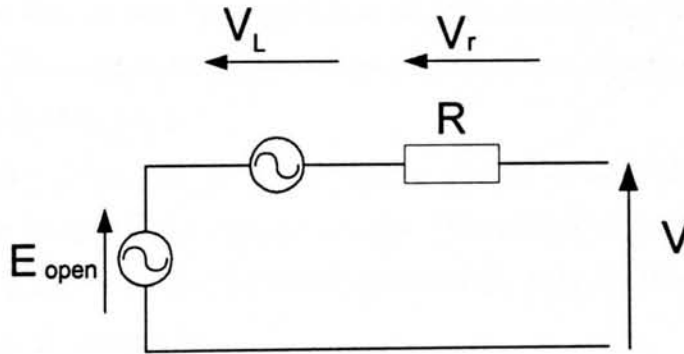


Figure 4.30: Lumped Reactance

$$V = E_{open} - \frac{d(\psi - \psi_{PM})}{dt} \quad (4.28)$$

4.3.2.6 Look Up Table of ψ -I – Model E

The unaltered ψ data is interpolated from a look up table in this model and used to calculate E, the total emf. Hence the equivalent circuit of Figure 4.31 and governing equation, (4.29), do not have separate open circuit and reactance components.

$$V = \frac{d\psi}{dt} - IR \quad (4.29)$$

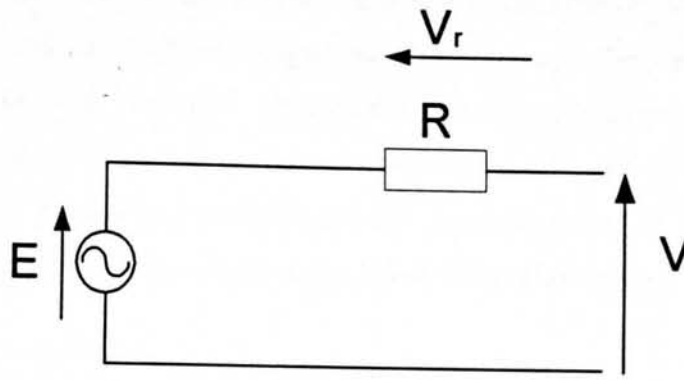


Figure 4.31: The look up table model

4.3.3 Model Development

4.3.3.1 Approximation of Flux Results for Open Circuit

To model the flux accurately at positions between consecutive 1 mm positions provided by the FEA, approximating the results to a continuous function could provide a convenient way to obtain data.

The fourth order polynomial given in (4.30), calculated using the least squares method, is shown plotted on the same axis as the FEA calculated flux in Figure 4.32. The results show good correlation and hence imply that the polynomial could be used to generate a continuous value of flux.

$$\psi = ax^4 - bx^3 + cx^2 - dx - e \quad (4.30)$$

Where the coefficients are given in Table 4-2.

Table 4-2: Coefficients of 4th order flux approximation

a	b	c	d	e
9633365136×10^5	-4.623714952×10^3	0.05757048809279	-0.05014353241196	-0.86614961061008

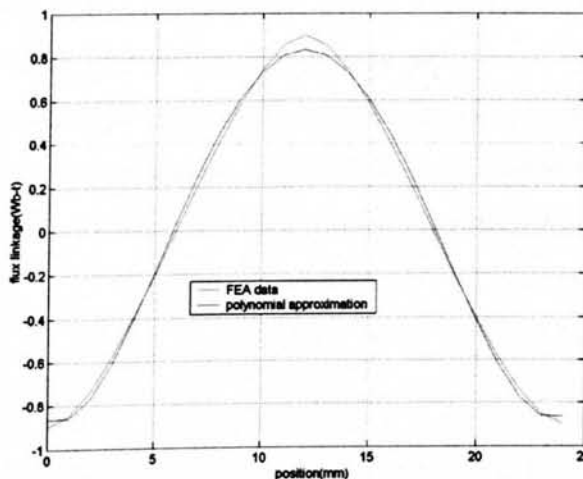


Figure 4.32: Comparison of Polynomial approximation and FEA results

The non periodic nature of this polynomial makes it necessary to convert translator displacement into relative tooth and magnet position. During a displacement of greater amplitude than the rotor tooth pitch requires the use of $p=23$ and $p=0$ in consecutive time steps. In theory these values should be smoothly separated, yet the FEA, and hence polynomial, gives a very small discrepancy between them. In Figure 4.33 this manifests itself as a small discontinuity at the trough of the flux curve.

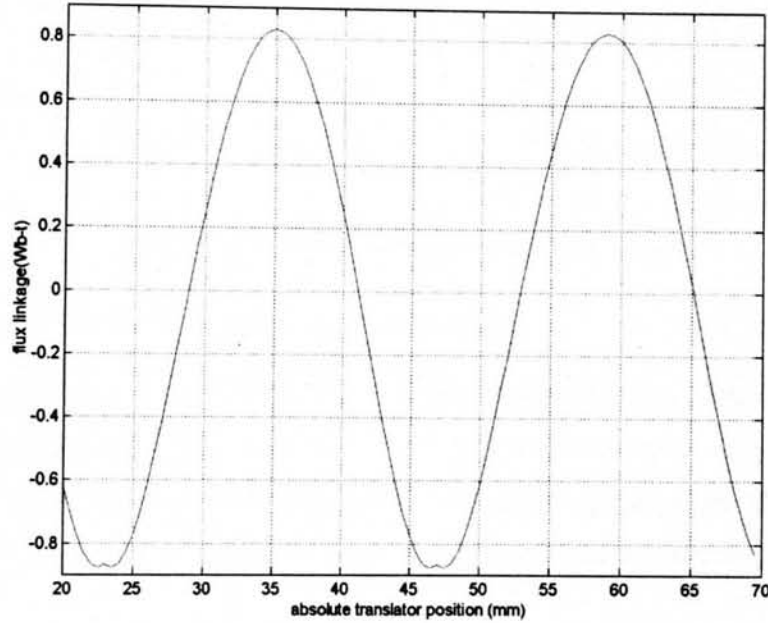


Figure 4.33: Flux position obtained with polynomial approximation

The coil emf is obtained by numerical differentiation of this signal during which this discontinuity becomes a significant spike in the results, Figure 4.34. Furthermore, if the simulation is extended to encompass inductive and capacitive elements this effect has a significant impact on the results.

Higher order polynomial approximations also exhibit this property. Polynomial substitution of the flux-position results is hence unsuitable.

An alternative approach, which has the distinct advantage of being periodic and continuously smooth, is to approximate the flux linkage to a sinusoidal function. Using an amplitude of 0.898 and a period of $\pi/24$ gives a good correlation.

4.3.3.4 First Order Modelling

During a short circuit or purely resistive load test, then the solution of all the models is a first order differential. Due to the nature of differentiation, namely that it progressively distorts a signal and amplifies errors, it is beneficial to re-state the equation as an integral. Numerical integration acts as a smoothing function, being little affected by small inaccuracies, whereas differentiation will amplify a small discrepancy by dividing it by a small increment (dt). For models A-C, the governing equations are manipulated to become expressions for the time differential of current. A fourth order Runge-Kutta routine is used to solve this. In models D and E, the expressions are functions of ψ which hence becomes the variable which must be integrated, again using the Runge-Kutta routine. Each time step of the program follows the structure shown in Figure 4.35.

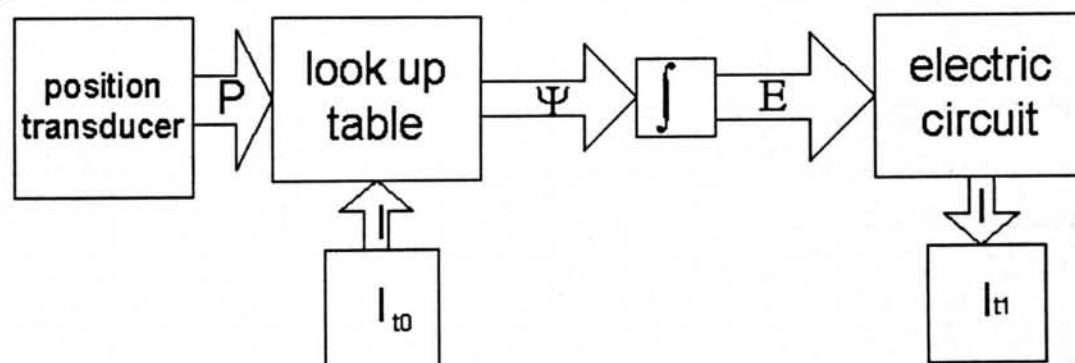


Figure 4.35: Schematic diagram of program integration technique for $t=0$

4.3.3.5 Second Order Modelling

With the introduction of capacitive elements to the external loading circuit, whereby the voltage is a function of the current integral, the guiding equations become second order. Although it is straightforward to re-arrange these into a single second order differential equation, for models A-D the presence of additional external time dependent variables (\dot{L}), or the requirement for second order time differentials ($\dot{E} = \ddot{\psi}$), may make it beneficial to express the governing equations as two independent first order equations. These two alternative methods are described below.

Runge-Kutta-Nyström – method *i*

The Runge-Kutta-Nyström algorithm [81] is a technique which generalises the standard Runge-Kutta method to solve second order differential equations. The input to the routine is a present value of the second time derivative, and the output is the value at the subsequent time step together with the value of the first time derivative. In model E

this is an elegant solution. For all other models, however, attention should be paid to the second order time differentials – see concluding remarks, Section 4.4.4.

Runge-Kutta Separate Integrals –method ii

The voltage across a capacitor is dependent on the integral of current passing into it. If the value of current is assumed to be constant for a given time step, then the governing equation remains a first order differential equation and current can be calculated using the basic Runge-Kutta technique. The current may then be integrated in a separate routine. In this method the current changes between each time step, not during. For a small time step, this should have a negligible effect.

4.3.4 Governing Equations

Equations (4.21) to (4.29) above are rearranged in Table 4-3 to the form used in the models.

Table 4-3: Integrals used in VHM models

	Short circuit / resistive loading	Capacitive loading Method i	Capacitive loading Method ii
A	$\dot{i} = \frac{E - IR}{L}$	$\ddot{i} = \frac{\dot{E}}{L} + \frac{V_c}{CR_E L} - I \frac{1}{CL} - \dot{i} \frac{R}{L}$	$\dot{i} = \frac{E}{L} + I \frac{R}{L} + \frac{\int I}{CL} - \frac{1}{CR_E L} \int V_c$
B	$\dot{i} = \frac{E - IR}{L_{1,p}}$	$\ddot{i} = \frac{\dot{E}}{L_{1,p}} + \frac{V_c}{CR_E L_{1,p}} - I \frac{1}{CL_{1,p}} - \dot{i} \frac{R}{L_{1,p}}$	$\dot{i} = \frac{E}{L_{1,p}} + I \frac{R}{L_{1,p}} + \frac{\int I}{CL_{1,p}} - \frac{1}{CR_E L_{1,p}} \int V_c$
C	$\dot{i} = \frac{E}{L_{1,p}} - \frac{I(\dot{L}_{1,p} + R)}{L_{1,p}}$	$\ddot{i} = \frac{\dot{E}}{L} + \frac{V_c}{CR_E L} - \dot{i} \left(\frac{2\dot{L} + R}{L} \right) - I \left(\frac{\dot{C} + 1}{CL} \right)$	$\dot{i} = \frac{E}{L} - I \frac{\dot{L} + R}{L} - \frac{1}{CL} \int I + \frac{1}{CR_E L} \int V_c$
D	$\dot{\psi}_1 = E - f(\psi_1)R$	$\ddot{\psi} = \dot{E} + \frac{V_c}{CR_E} - \frac{f(\psi)}{C} - Rf'(\psi)\dot{\psi}$	$\dot{\psi} = E + \frac{1}{CR_E} \int V_c - \frac{1}{C} \int I - Rf(\psi)$
E	$\dot{\psi} = Rf(\psi)$	$\ddot{\psi} = \frac{V_c}{CR_E} - Rf'(\psi)\dot{\psi} - \frac{f(\psi)}{C}$	$\dot{\psi} = \frac{1}{CR_E} \int V_c - \frac{1}{C} \int I - Rf(\psi)$

Where $f(\psi) =$ value of current obtained from Look up table

$$\frac{d}{dt}(f(\psi)) = \frac{df(\psi)}{d\psi} \frac{d\psi}{dt} = f'(\psi)\dot{\psi}$$

$$E = -\frac{d\psi_{pm}}{dt}$$

4.3.5 Concluding Remarks

Two distinct methods have been presented for predicting the useful force reacted by a VHM, utilising either the Maxwell stress or the Co-energy method. A further two methods have been outlined to calculate the airgap closing, or normal, force and the cogging force, neither of which serves useful work. Five models of increasing accuracy

and complexity for the prediction of the terminal voltage / current have been presented and, where appropriate, their development documented. Experimental verification of these predictions is now necessary.

4.4 Verification of Models

4.4.1 Description of Testrig

The VHM mounted on the testrig is shown in Figure 4.36 and labelled in Figure 4.37.

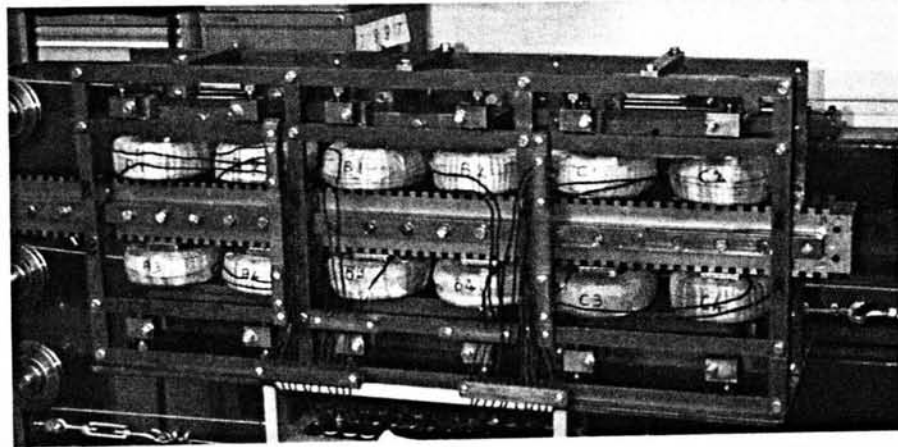


Figure 4.36: The VHM testrig

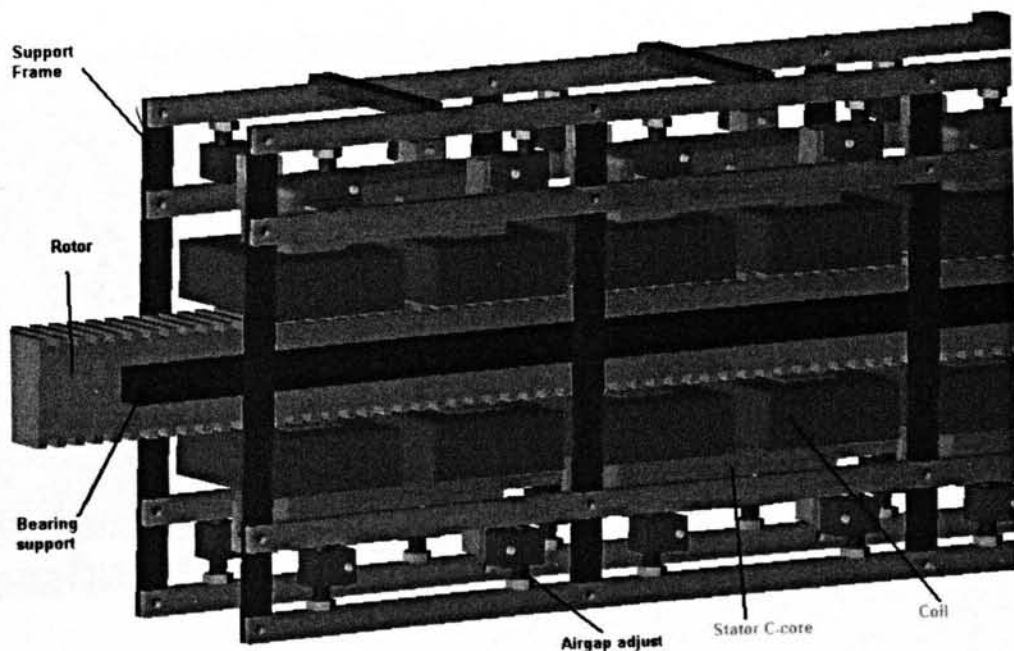


Figure 4.37: Aspects of VHM testrig

The role of the testrig is to excite the prototype in a manner analogous to that encountered in wave energy converters: linear, reciprocating and slow peak velocities.

To achieve this a conventional induction machine was coupled to a 0.1 m radius crank through a 14:1 step down gearbox. Peak speeds of less than 0.5 m/s are easily achievable.

To allow for the future expansion of the testrig and accommodate spring elements, hence simulating more closely the conditions of a wave energy converter, there is a system of steel cables and pulleys transferring the crank force to the rotor. This results in slight play between the relative position of the exciting crank and the prototype translator. In order to account for this, a displacement transducer has been mounted to the translator, allowing the exact time displacement data of the testrig to be fed into the electrical models and their performance evaluated.

Experience at the University of Durham dictates that the task of maintaining a small airgap in the presence of high magnetic forces should not be underestimated. Section 4.3.1.2, the normal force based on FEA calculation of Maxwell stress, was used to design the framework structure within which the stator cores were mounted. This framework means that the cores are essentially supported in air and are hence magnetically independent from each other and any other influence. Provision has been given, by way of in-house made screw thread adapters, for the alteration and accurate setting of the airgap.

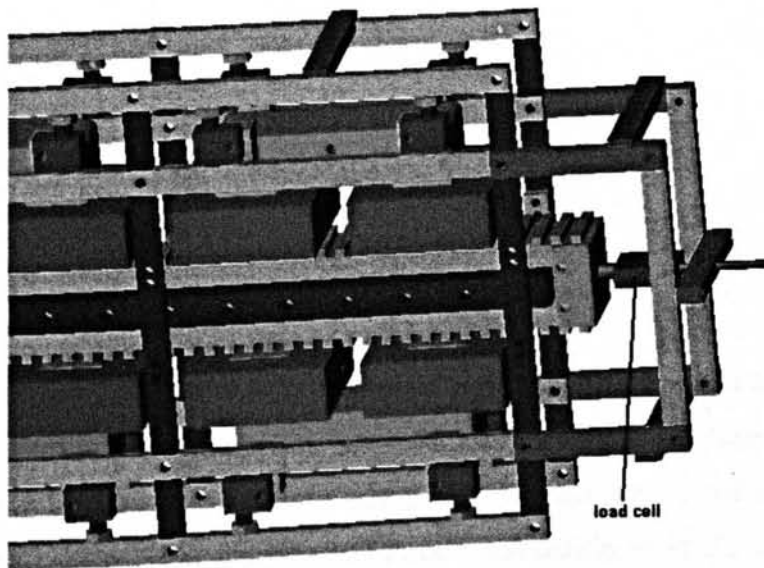


Figure 4.38: Position of load cell

The translator is supported on each side by solid steel square bars, which also act as the runners for the stud bearings mounted to the stator frame. It is thus a rigid structure which is free to move axially within the airgap.

Both the translator and the stator are made from 1 mm thick laser cut mild steel laminations, held together in compression by a series of steel bolts.

In order to measure the static force reacted by the prototype, the cables used to drive the translator were removed and replaced by a screw thread mounted load cell, Figure 4.38. The position of the rotor was selected and subsequently held in place by the cell. The cell deforms less than 0.4 mm at full load, 1000kg [82], the rotor can therefore be assumed stationary as current is altered within the coils.

4.4.2 Force Results

4.4.2.1 Smoothing of Results

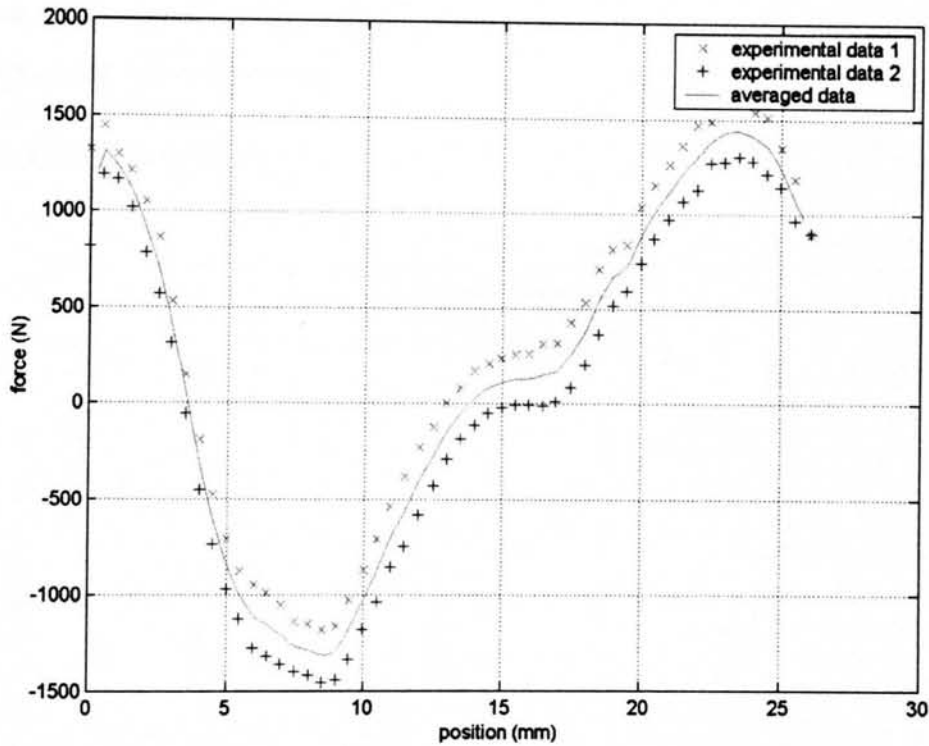


Figure 4.39: Example of experimental data, 6 Amps flowing in coils

During experimentation, the rotor was set to the necessary position by applying a force to it through the force transducer. For the position of zero magnetic force, it is clearly possible to apply a small force to the translator which, due to frictional effects of the testrig, will not result in movement. The value of force recorded by the load cell for this translator position could therefore vary, the range being from the minimum tensile force which causes displacement to its compressive counterpart. It follows that an important factor in determining the residual forces recorded in a situation such as this would be the direction in which the experiment was being performed, for example a

more likely residual force being compressive when the rotor is being pushed by the load cell. Expressed another way, the frictional effect always acts to oppose the direction of motion and is actually present throughout the experiment and not just the positions of zero magnetic force. Figure 4.39 shows a typical set of force results for a 6 Amp current flowing in the phase coils. It shows a data set corresponding to the experiment being carried out in each direction. A separate bicubic spline interpolation is used to approximate each of the 2 data sets at regular intervals along the position axis. The average value of these two interpolations is shown as the solid line in the graph and demonstrates the method employed to eliminate directional dependent friction from the results. This method of averaging is used for all the force results. At any given point, the discrepancy between the two sets of data shown is in the region of 270 N and so becomes less significant as higher currents are used to excite the phase and electromagnetic forces dominate.

4.4.2.2 Current Direction

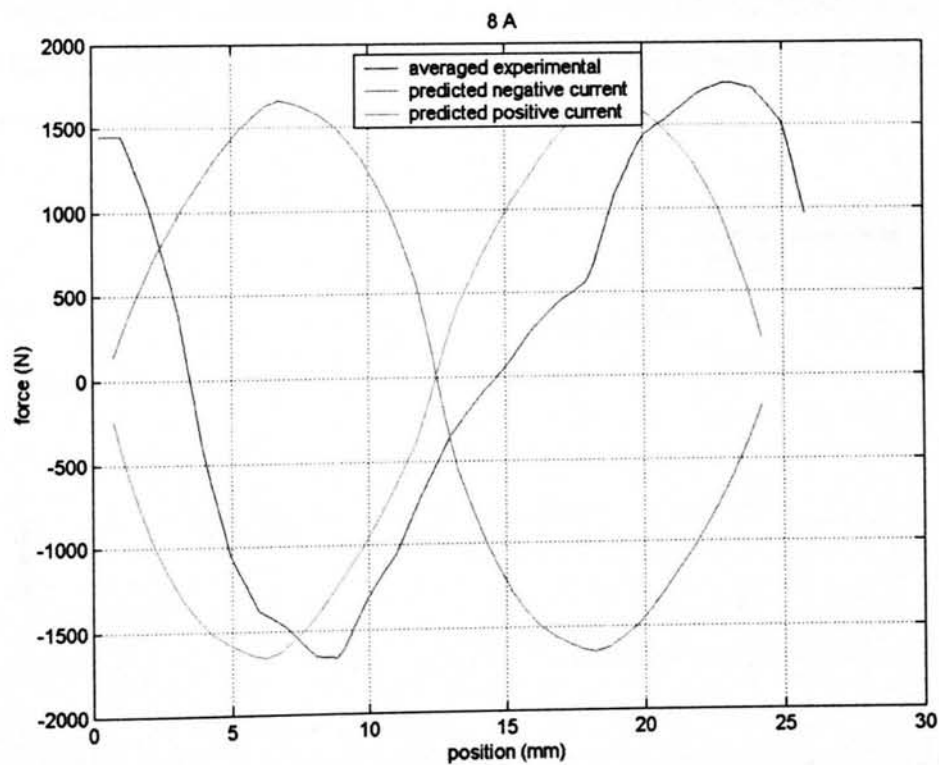


Figure 4.40: Force results with 8 Amps flowing

For any given magnitude of current, its direction has been shown to play a significant role in the magnetic flux pattern and resultant force. Figure 4.40 shows the experimental force for 8 Amps flowing, plotted on the same axis as the force predicted

by the co-energy method of Section 4.3.1.3 using a positive and negative 8 Amp current.

The two predicted force curves are 180° out of phase with each other, i.e. always in the opposite direction. The experimental force has a significant phase difference with either of those predicted, due to the arbitrary nature of the ‘zero’ position during the experiment. The aim here is to show that in analysing the force results, it is possible to ignore both the phase of the results and the direction of current in the FEA. The important feature of the curves is the shape, period and peak amplitude, the latter of which is within 5% for all the peaks shown.

There are two regions where the experimental data, despite being averaged, is not smooth, corresponding to the positions of 7 and 18 mm. It is likely that there was some debris on the bearing track at these positions, which would slightly affect the result in both directions.

4.4.2.3 High Current Co-energy Method Comparison

The comparison of experimental and co-energy method predicted force results for 16 Amps shown in Figure 4.41 shows a good correlation, with the peaks and troughs of the two curves lying within 10% of each other.

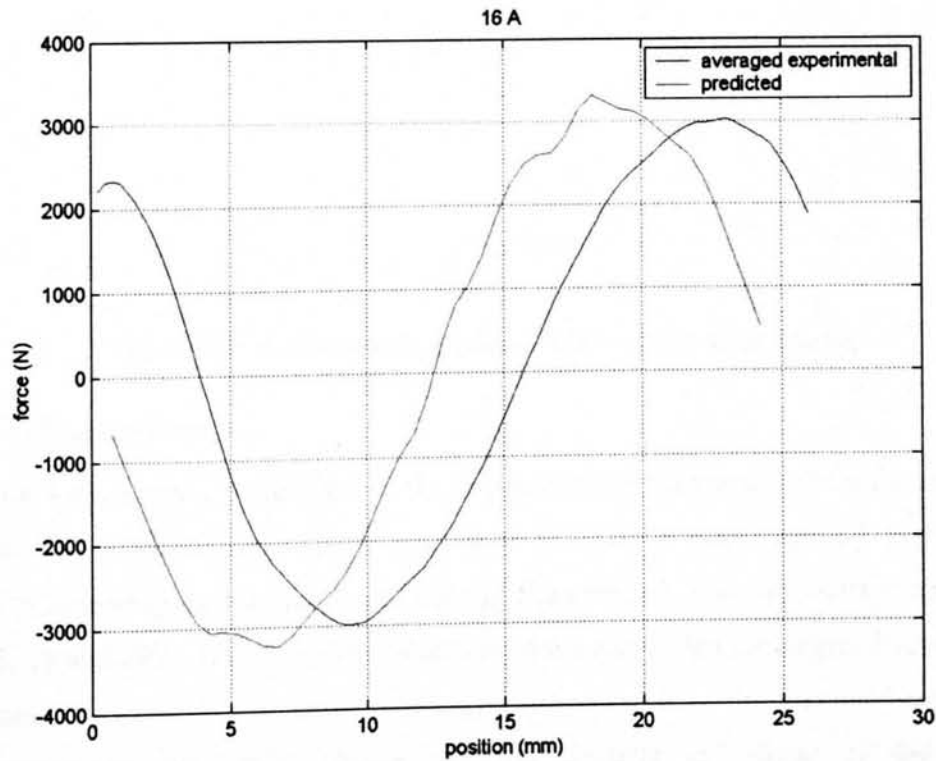


Figure 4.41: Predicted and experimental force with 16 Amps flowing

Again there are two regions where the experimental data appears slightly erratic, approximately corresponding to the positions visible in the previous experiment.

4.4.2.4 Low Current Co-energy Method Comparison

Figure 4.42 shows the 2 Amp experimental results plotted on the same axis as the co-energy predicted force results for the positive and negative current directions. The experimental results have a different shape, period and peak value to either of the predicted curves. It must be deduced, then, that this force model is not valid at low currents, where cogging force is comparable to electromagnetic force.

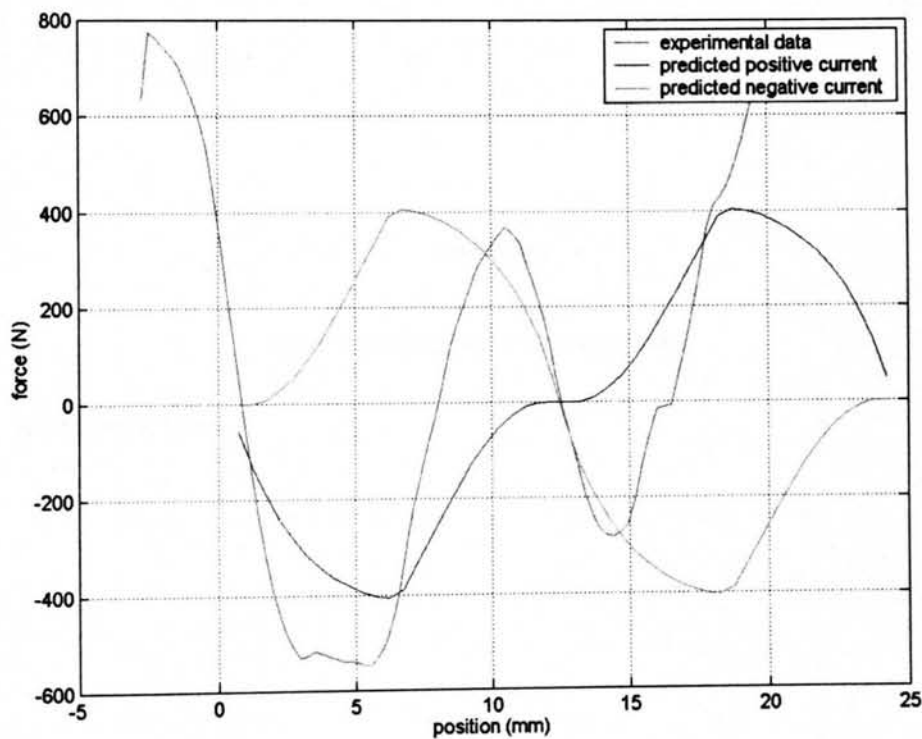


Figure 4.42: Predicted and experimental force with 2 Amps flowing

4.4.2.5 Cogging force

Figure 4.43 shows a comparison of the experimentally measured values for cogging force to that predicted using the magnet de-magnetisation curve method of Section 4.3.1.4. Comparing the turning points, starting from the left, gives percentage errors of 120, 18, 15 and 29%. It is likely, by inspection of the curve, that the largest discrepancy was caused by experimental error. Although the amplitude of the predicted results is only reasonable, the model clearly correctly predicts the shape of the force characteristic. In particular, the amplitude of the force-displacement curve can be seen to have two large peaks and two smaller ones, as discussed in 4.3.1.4, Figure 4.25.



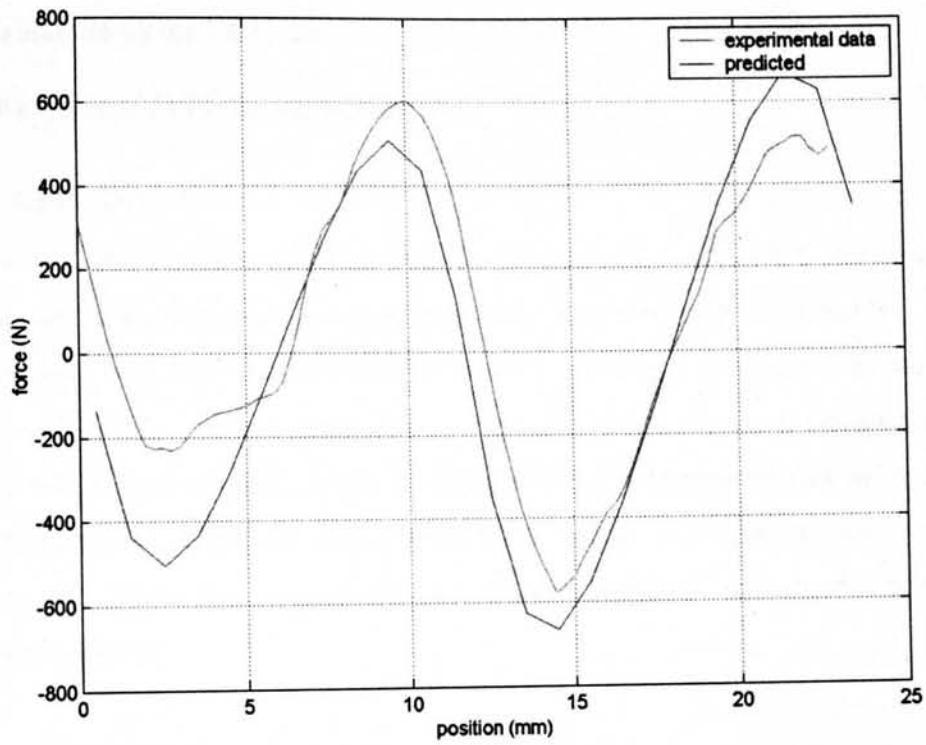


Figure 4.43: Cogging force comparison

4.4.2.6 Maximum force

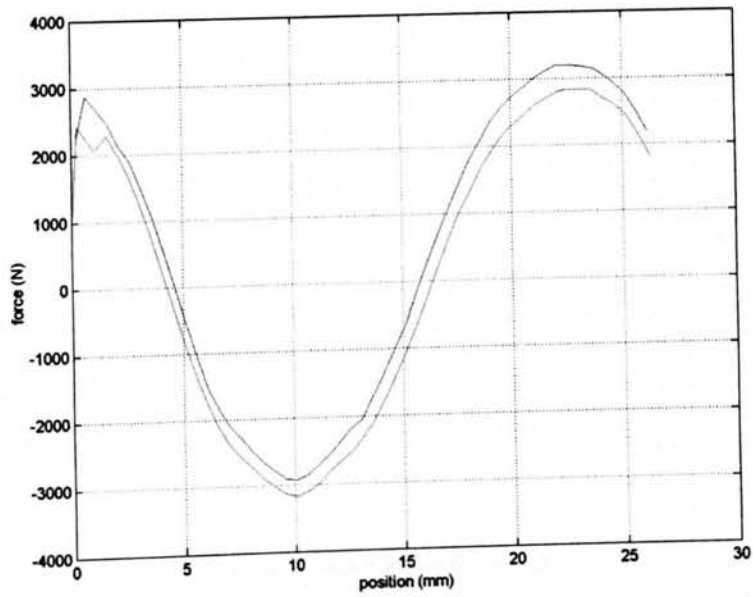


Figure 4.44: Experimental force results for 20 Amps

Figure 4.44 shows the force displacement experimental results for a phase current of 20 Amps. The average modulus of the peaks is 3.03 kN, equivalent to a shear stress

over the magnet area of 105 kNm^{-2} . The current was limited by the test equipment available and not by the VHM itself.

4.4.3 Electrical Performance Models

4.4.3.1 Open Circuit

Figure 4.45 shows the open circuit emf results predicted by the FEA plotted on the same axis as the experimentally measured results. The correlation between the two is good, although the model can over predict by up to 15 % (e.g. at time ≈ 0.8) the RMS value is within 10%. As, by definition, no current flows in an open circuit test, the predicted results were obtained simply by differentiating the predicted flux linkage time profile from the experimental time displacement results. Confidence can hence be placed in the FEA flux predictions, and their subsequent use in the proposed performance models.

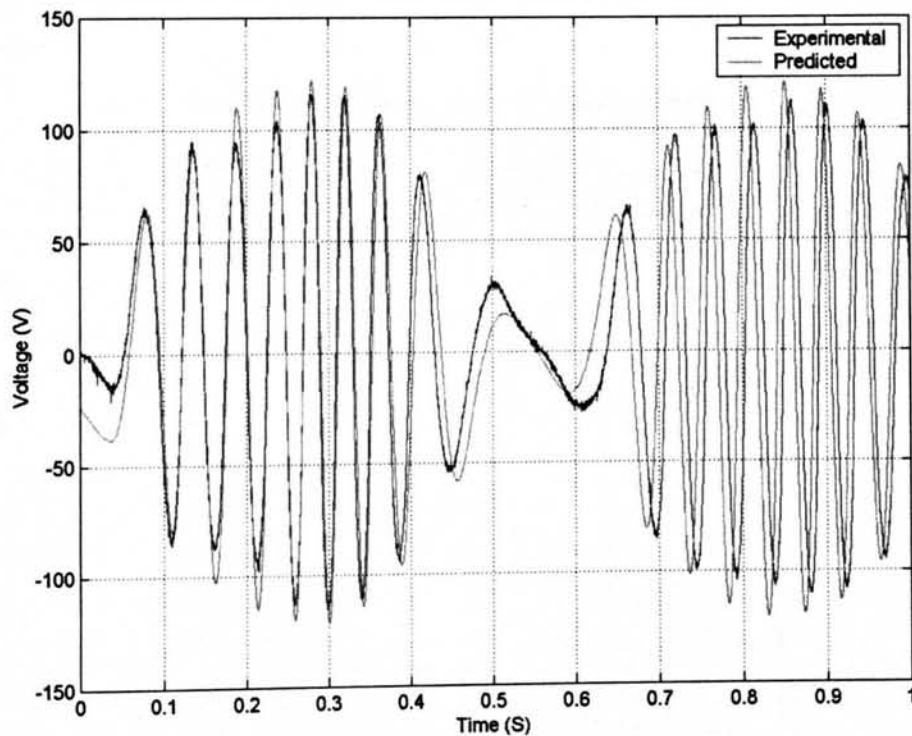


Figure 4.45: Open Circuit emf

The predicted waveform is more regular and slightly larger than the experimental results. It is likely that three dimensional end effects, not considered in the FEA, are responsible for this. Simulated results also appear to move slightly out of phase during the time period shown. The model was run with the exact analogue displacement data obtained from the transducer. Superimposed on this signal was a high frequency noise

signal, produced unavoidably from the inverter used to drive the test rig. As the displacement signal has to be differentiated into velocity, this noise becomes significant and hence requires filtering. A 200 point moving average method was used, and it is likely that this will account for the gradual loss of agreement between predicted and actual displacement results. Alternatively, a calibration error in the displacement transducer would account for the affect.

4.4.3.2 Inductance

By connecting a 50 Hz power supply of known voltage across the terminals of one phase and recording current, it is possible to calculate the reactance and hence inductance of that phase. A maximum value of 0.495 H was measured at 1.3 Amps.

4.4.3.3 Short Circuit

To investigate accuracy, all the models are run for the same displacement input, i.e. they are all compared to the same experiment, which had the characteristics given in Table 4-4.

Table 4-4: Experimental short circuit current results

Max current	1.6 Amps
Min current	-2.04 Amps
RMS current	1.08 Amps

Model A

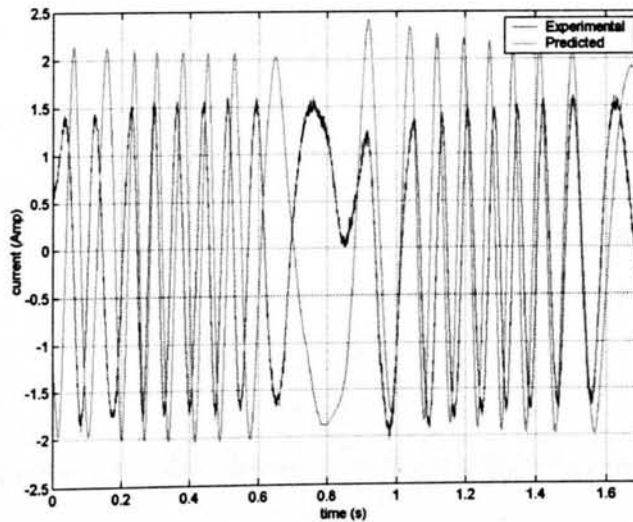


Figure 4.46: Short circuit results for model A

In each of the experiments, the equivalent predicted results and the percentage deviation from the experimental results are given in Table 4-5. Figure 4.46 and Figure

4.47 show examples of experimental compared with predictions using ‘model A’ and ‘model E’ respectively.

Model E

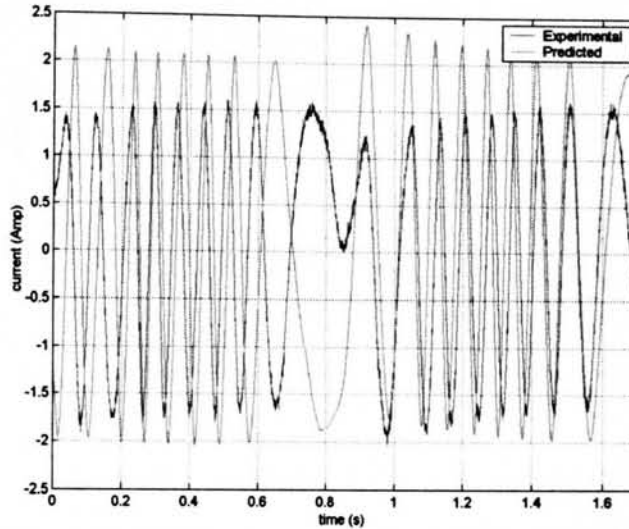


Figure 4.47: Short circuit model results for model E

Table 4-5: Short circuit results of the VHM

	A		B		C		D		E	
	Value (Amps)	Error (%)								
Max	2.44	52	2.42	51	2.44	52	2.44	52	2.43	52
Min	-2.46	20	-2.44	20	-2.46	20	-2.42	19	-2.46	20
RMS	1.40	30	1.41	31	1.40	34	1.40	30	1.40	30

Table 4-5 shows both the predicted values and their error as a percentage of the experimental value. Surprisingly, the results do not differentiate between the models.

4.4.3.4 Capacitor loading

The model results are compared with the experimental values with a 630Ω resistor in parallel with a 150μF capacitor. The experimental results are summarised in Table 4-6

Table 4-6: Experimental results for a 630Ω resistor and 150μ F capacitor

Max:	504 Volts
Min:	-472 Volts
RMS:	211 Volts

Figure 4.48 to Figure 4.55 give examples of results from ‘model A’ to ‘model E’ simulating this situation.

Model A Integration method i

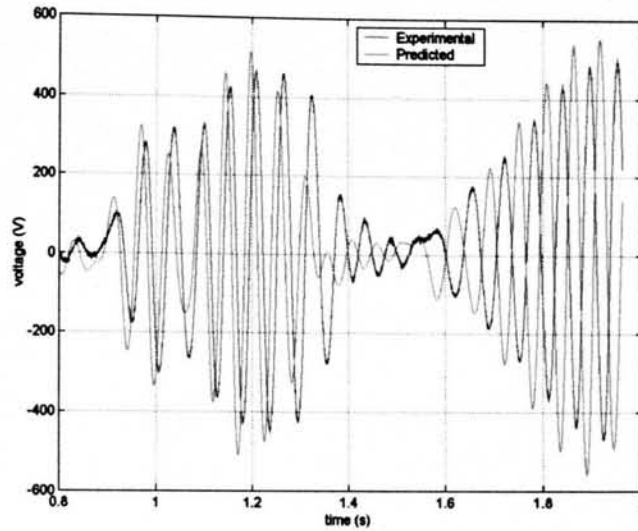


Figure 4.48: Capacitive loaded results for model A I

Figure 4.48 shows a comparison of the experimental results and the simplest of the model predictions. The agreement of the two in terms of shape is good, with the predicted waveform having a credible profile.

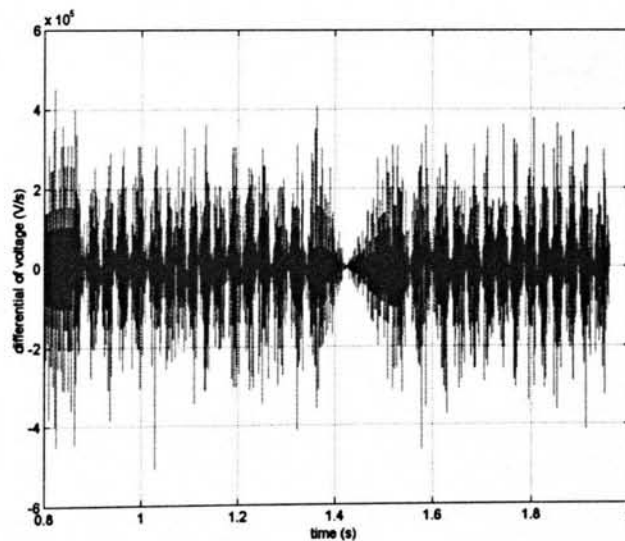


Figure 4.49: Differential of voltage used in model A i

The results of Figure 4.49 show that the derivative of voltage, which appears to be a noise signal, bears no relation to the curve expected if, for example, the flux pattern was simplified to a sine function. It is included here to demonstrate that, although the predicted voltage is acceptable, this model is not functioning properly.

Model A Integration method ii

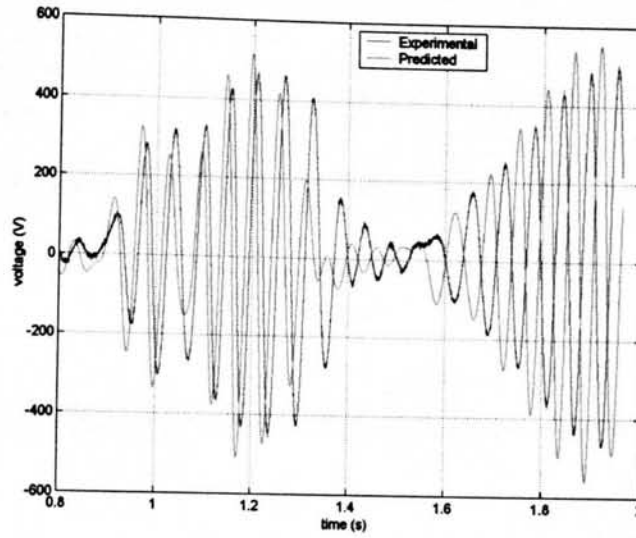


Figure 4.50: Capacitive load results for model A ii

The graph of Figure 4.50 is almost identical to that of Figure 4.48 and thus demonstrates the limited effect of integration method on overall model behaviour.

Model C Integration method i

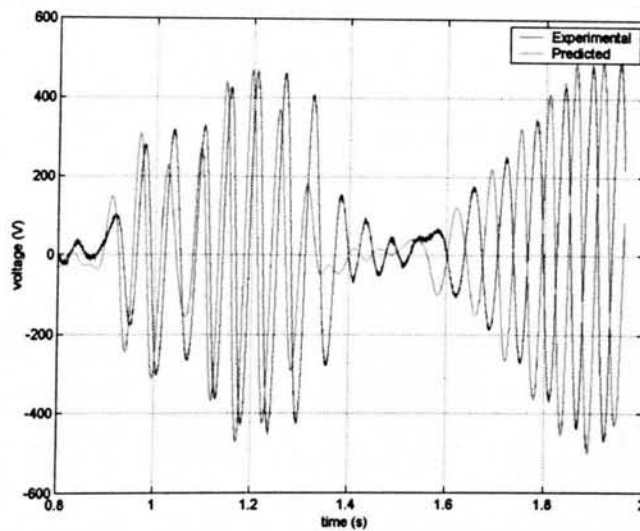


Figure 4.51: Capacitive load results for model C i

Figure 4.51 shows the results as predicted by model C i compared with the experimental. The model appears to act in a similar manner to model A. Figure 4.52 is included to further highlight the problems experienced when specifying a model that contains numerical differentiation. In this model, there is a term involving the double time differential of inductance, Table 4-3. Inspection of Figure 4.52 show how the

oscillating value of inductance is distorted through two numerical differentiation processes.

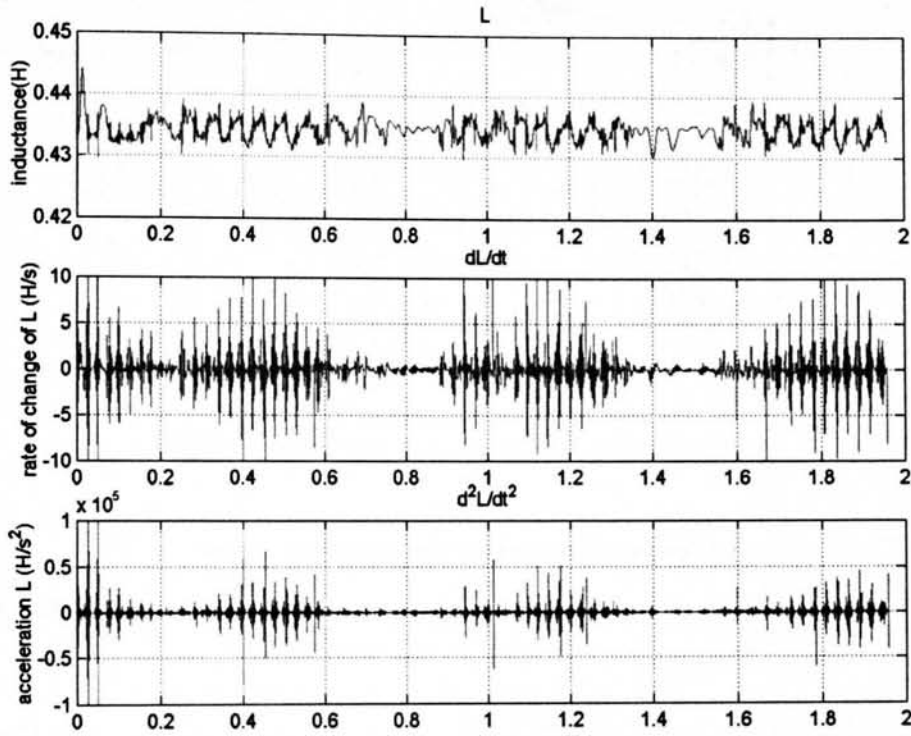


Figure 4.52: Calculated values of inductance and its differentials in model C i

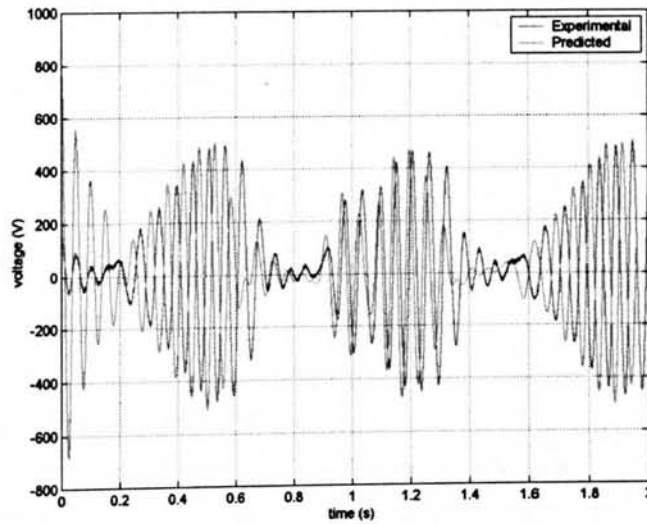


Figure 4.53: Capacitive load results for model C i, settle period

Figure 4.53 demonstrates that models require some time to settle before accurate results are obtained. For the first 0.2 seconds large amplitude voltages are predicted, until the effect of the initial conditions is replaced with the true transient response.

Model E Integration method i

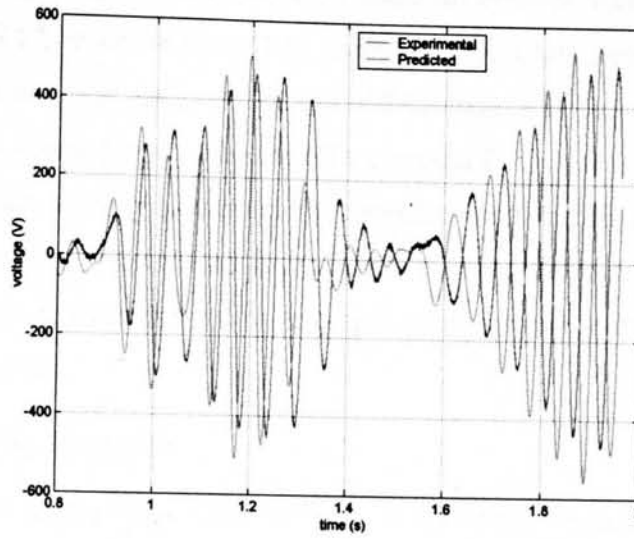


Figure 4.54: Capacitive load results for model E i

Model E Integration method ii

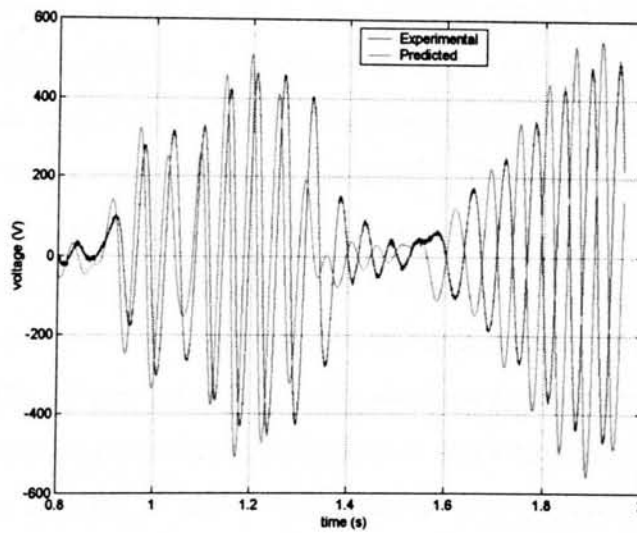


Figure 4.55: Capacitive load results for E ii

Table 4-7: Summary of VHM model results

	A.i		A.ii		B.i		B.ii		C.i		C.ii	
	Value	%	Value	%	Value	%	Value	%	Value	%	Value	%
Max	552	10	552	10	549	9	551	9	491	3	551	9
Min	-560	19	-560	19	-559	18	-560	19	-502	6	-557	18
RMS	217	3	217	3	216	2	217	3	201	5	216	2
	D.i		D.ii		E.i		E.ii					
	Value	%	Value	%	Value	%	Value	%				
Max	776	54	550	9	550	9	550	9				
Min	-760	61	-558	18	-558	18	-558	18				
RMS	332	57	216	2	216	2	216	2				

Table 4-7 compares the results of all 5 models and the two alternative methodologies for differentiation, giving an indication of the small differences between them. Figure 4.49 and Figure 4.52, however, show why some of the models cannot be functioning properly. Even though the results do little to differentiate, it is likely the model which best represents the results predicted by the FEA is model E.

The non-constant velocity prevented the capacitor and machine inductance from reaching the resonance required to drive large currents through the VHM. The relatively low resulting currents were not enough to demonstrate appreciable differences in modelling methods.

4.4.4 Concluding Remarks

Details of the prototype linear VHM designed to verify behavioural predictions given in section 4.3 above have been presented. The electromagnetic model for predicting force gave good agreement with experimental values of force at high currents, but proved unsuitable for use at low current where cogging forces are likely to dominate. The demagnetisation model for cogging force described in section 4.3.1.4, however, gave good correlation with the experimental forces at zero current. All five performance models were tested for short circuit current and for a loaded condition of a 630Ω resistor in parallel with a $150\ \mu\text{F}$ capacitor. All models were found to give similar results for the short circuit. For the capacitive loaded case, where currents were slightly higher, close inspection of the internal workings of some of the models, for example the noisy wave form of Figure 4.49, demonstrated that they were not functioning properly. Numerical differentiation does not appear to be a suitable tool in this environment and it is concluded that the more complex models using integration are using the FEA data more accurately. A closer inspection of possible sources of error in the experimental work is required to verify this. The small difference in inductance calculation used by the alternative models appears to be insignificant at the relatively small currents used here.

4.5 Sources of Error

4.5.1 Three dimensional error

All of the calculations in this Chapter have been based on the assumption that the path taken by the flux is purely two dimensional. In a manner similar to the flux straying into the slot region of the translator, it is likely that some flux fringing / leakage will occur in the third dimension, i.e. out of the plane of the paper for the flux pattern of

Figure 4.10. The primary result of such a flow is an extra return path for *current* driven flux, manifesting itself as an increase in the inductance. A lesser effect will be providing a leakage path for the *magnet* driven flux, reducing the emf induced.

In order to adequately secure the laminations in compression, a 5 mm thick steel plate was bolted to each side of the 100 mm wide stator, shown in Figure 4.56. There was no such plate on the translator, which was kept in compression by the bars mounted to act as bearing runners. The net effect is the likely encouragement of additional fringing flux and hence increase in inductance. This agrees with the experimental inductance value, given as 0.495 H in Section 4.4.3.2, being greater than the predicted values shown in Figure 4.27.

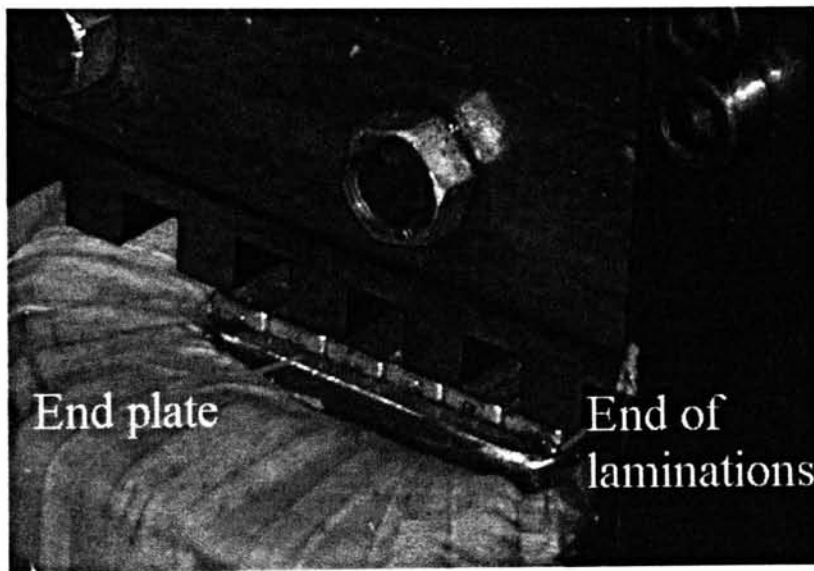


Figure 4.56: Keeper plate of laminated stator

4.5.2 Error in airgap

The size of airgap is the biggest single factor to influence the flux density in the VHM magnetic circuit. Although reasonable care was taken to set the airgap with bronze feeler gauges, human error must be accounted for. More significantly, the gauges are only used to measure and alter the clearance between the rotor teeth and the magnet surface. The mounting of the magnets onto the stator, namely with glue, has resulted in some of the magnets not sitting true to the steel. Figure 4.57 shows how a thin layer of glue may have formed between the magnet and stator, constituting an increase in the overall size of airgap.

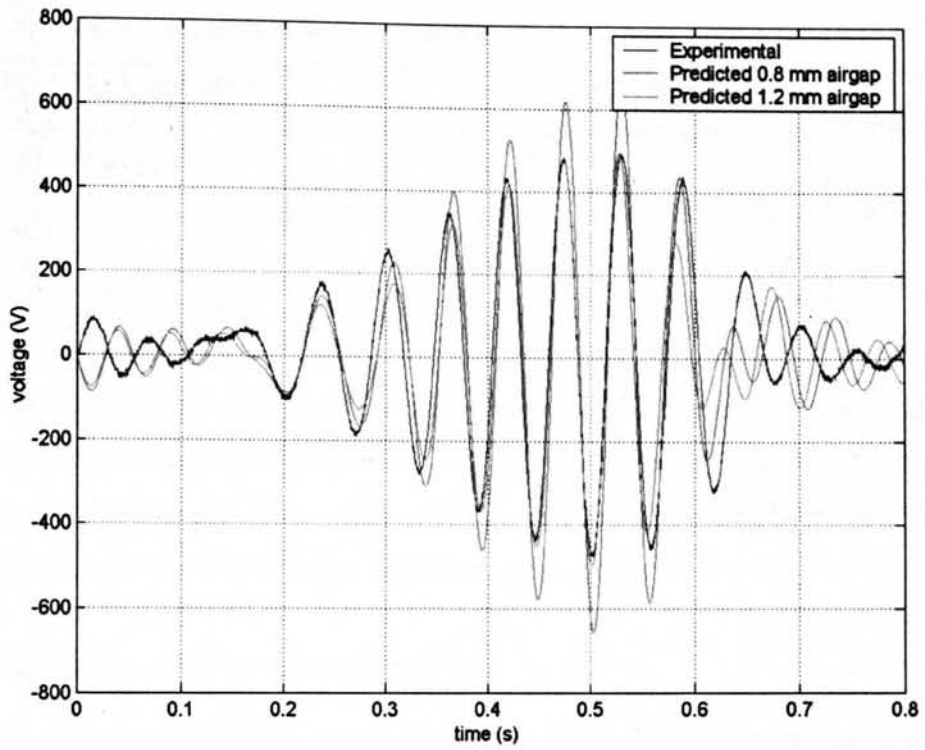


Figure 4.59: Effect of varying airgap on predicted voltage, $C=150\mu$, $R=630\Omega$ (experiment a)

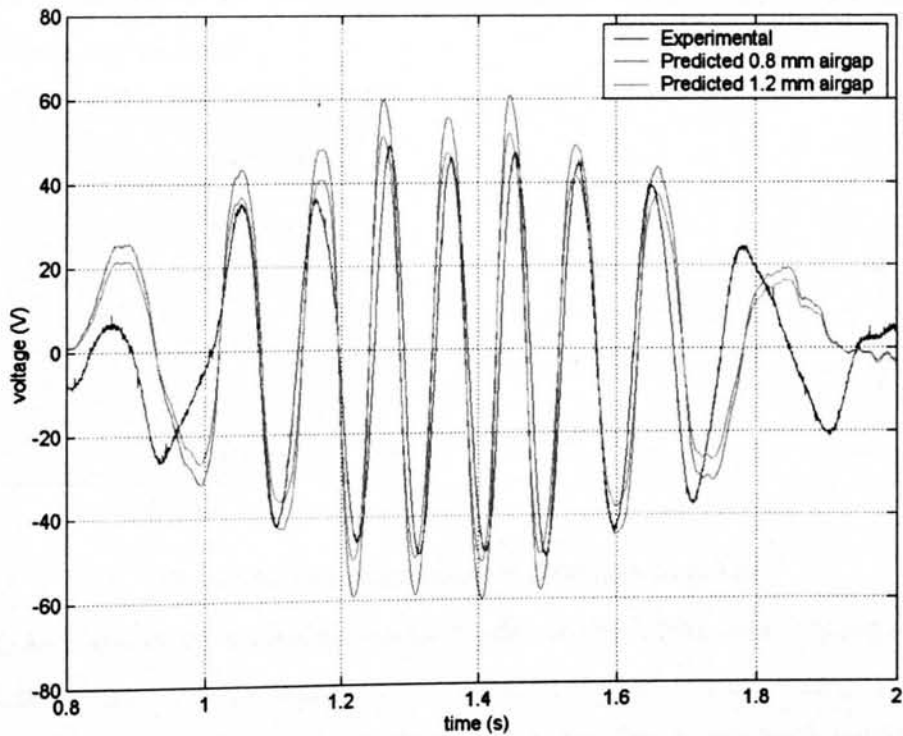


Figure 4.60: Effect of varying airgap on predicted voltage, $C=100\mu$, $R=29\Omega$ (experiment b)

Table 4-8: Comparison of experimental results for large airgap model E i

	C=150μF, R=360Ω					C=100μF, R=29Ω				
	exp. (a)	0.8 mm airgap		1.2 mm airgap		exp. (b)	0.8 mm airgap		1.2 mm airgap	
		Value	%	Value	%		Value	%	Value	%
Max	504	659	31	494	1.98	51.6	61.8	19	52.6	1.96
Min	-476	-655	38	-499	4.83	-51.2	-62.7	22	-53.3	4.14
RMS	207	241	17	184	11	26.24	32.7	240	27.5	4.94

The error is significantly reduced for the 1.2 mm airgap. Although greater confidence can be placed in the models when examining these results, it is inaccurate to assume that the prototype had an effective airgap of this value. It is the author's opinion that the three dimensional effect, which will also be affected by the airgap, is still most significant, as indicated by the reasonable open circuit prediction.

4.6 Real Time Response of VHM

With the ability to predict the dynamic response of the VHM in generator mode, it is now possible to examine the difficulties in extracting power. It has previously been demonstrated that the machine has a large inductance ($\approx 0.5H$). With a time domain model the instantaneous values of phase flux linkage, current and theoretical open circuit emf can be recorded.

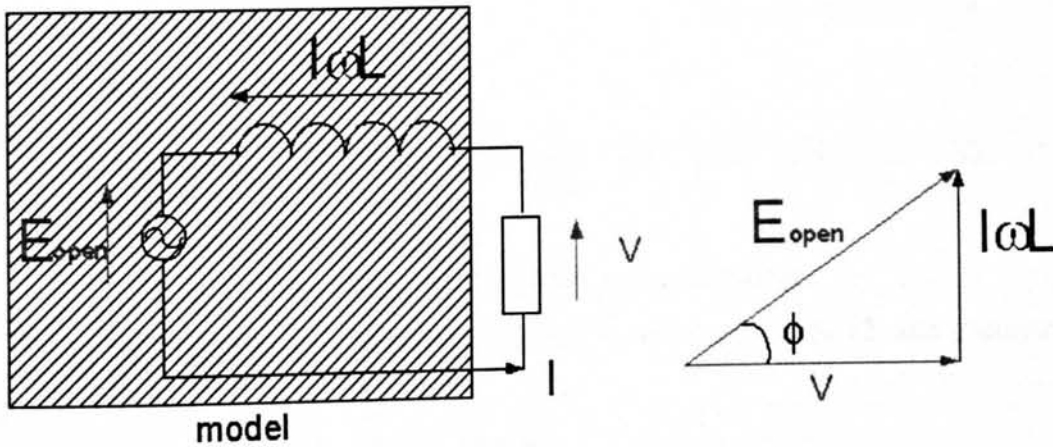


Figure 4.61: Equivalent circuit of VHM in short circuit

Figure 4.61 shows an equivalent circuit model of the VHM superimposed on the preferred model (*model E*, Section 4.3.2.6) connected in short circuit. Using the phasor diagram on the right hand side of the diagram it is possible to establish relationships between the three circuit elements. All the waveforms are assumed to be sinusoidal with the same angular velocity ω , which allows the maximum value of wave forms to be used to calculate relative phase differences. As such the elements shown in the

equivalent circuit and on the phasor diagram can be substituted with the flux linkages according to (4.32) to make a triangle of identical aspect ratio.

$$E_{open} \equiv \hat{\psi}_{PM}; I\omega L \equiv \hat{\psi}_1; IR \equiv \hat{\psi}_{tot} \quad (4.32)$$

Qualitatively, (4.32) states that E_{open} , which represents the open circuit emf, is a function of the flux driven by the magnets only, the voltage dropped across the series inductance is a function of the current driven flux whereas the voltage dropped across the resistor is a function of the net flux in the machine. Figure 4.62 shows the time-variation of these three elements at a constant speed of 0.8 m/s.

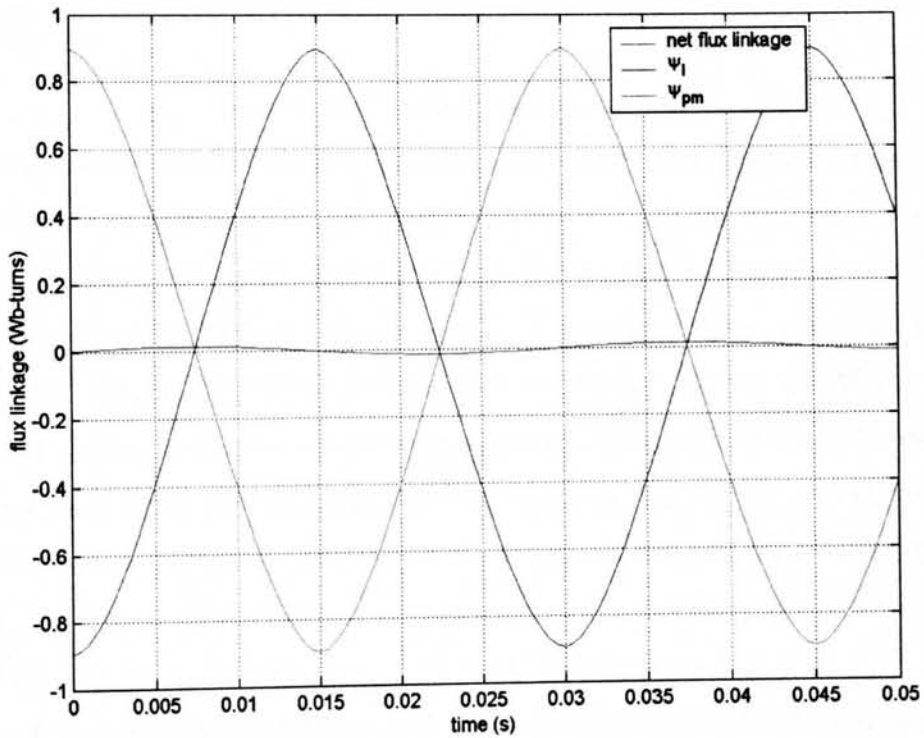


Figure 4.62: Flux flow in VHM during short circuit

The power factor can now be found using (4.33), incorporating (4.32) and geometry from Figure 4.61.

$$pf = \cos(\phi) = \frac{\hat{\psi}_{tot}}{\hat{\psi}_{PM}} = \frac{0.0146}{0.8976} = 0.0159 \quad (4.33)$$

It is clear from Figure 4.62 that the magnet driven flux and current driven flux are almost in anti-phase, giving a very small net flux flow. The collapse of the terminal voltage when current flows through the machine is thus explained. The very low power factor calculated in (4.33) confirms this.

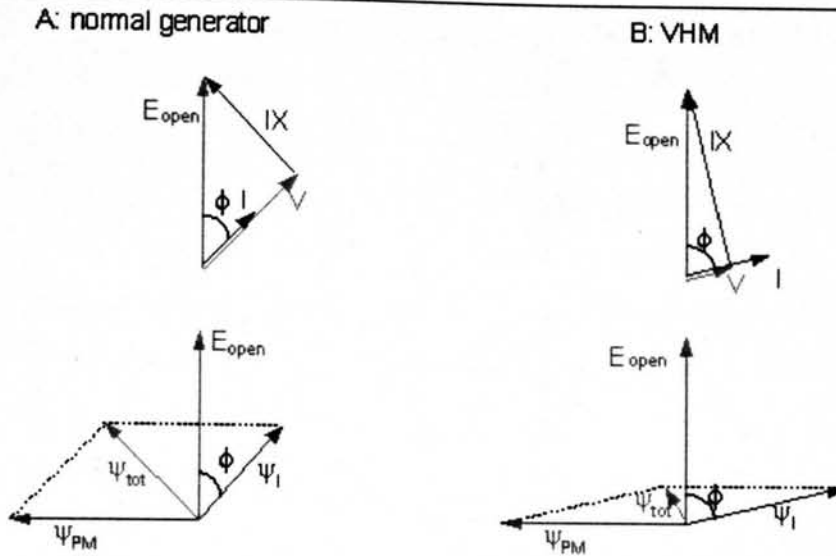


Figure 4.63: Phasor diagram of power factor

The relationship between the three flux components and the generator characteristics of the VHM can be illustrated by use of phasor diagrams. In Figure 4.63 voltage phasor diagrams are drawn above the equivalent airgap flux phasor diagrams. Figure 4.63A shows a typical pattern for an electrical machine. The magnetic flux, ψ_{PM} , leads and is pointing left. Lagging 90° behind this is the open circuit emf. Due to the inductance of the coil, the current, I , lags the voltage by an angle ϕ . The flux field driven by the coil current, ψ_I , is in phase with the current and the resultant flux, which defines terminal voltage V , is shown. Figure 4.63B shows the equivalent diagram for a VHM, with a larger lag in current. The magnitude of the ψ_{tot} phasor has considerably decreased by virtue of the flux due to the magnets and current almost opposing each other.

Figure 4.64 shows the phasor diagrams of the VHM with a corrected power factor and hence no phase difference between E_{open} and I . In order to achieve this, the terminals of the generator have been connected to a load which has a current leading the voltage by an angle ϕ . The resultant flux, and hence terminal voltage, of the machine is seen to be large. Operating in this manner, referred to as unity power factor, can thus be deduced to require ψ_I and ψ_{PM} to have a 90° phase difference. It is common practice to use a capacitor to perform this function.

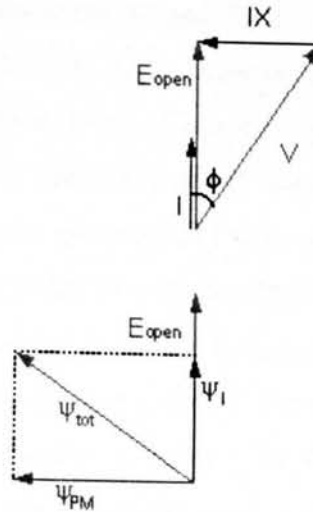


Figure 4.64: Phasor diagram of corrected power factor

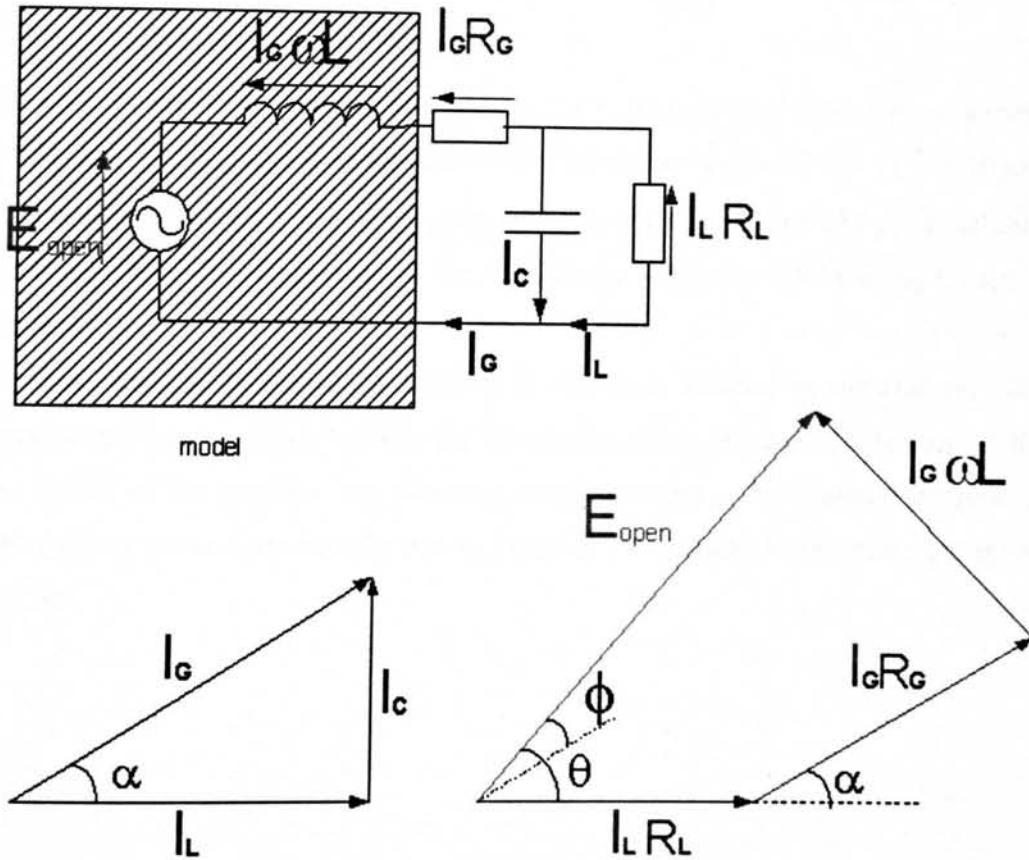


Figure 4.65: Capacitor assisted excitation of the VHM

Figure 4.65 shows the VHM model superimposed on a simple equivalent circuit for the case of capacitor assisted excitation. Also shown are two phasor diagrams, one corresponding to the circuit current and one to the voltage. The approximations used in (4.32) can again be used for E , $I_G \omega L_G$ and $I_G R_G$ in triangles where all sides have a

dependency on ω . In model E the terms 'E' and ' $I_G\omega L$ ' do not exist, with the output of the model being current, I_G . The term ' $I_L R_L$ ' is hence not related to any one group of flux linkage in the machine and so it is not possible to use an approximation of this form. Peak resultant voltages must instead be used in this geometric triangle. Appendix B shows how the vector geometry of Figure 4.65 can be used to calculate ϕ and hence power factor. It could also be used to calculate ideal values of R_L and C to give unity power factor ($\phi=0$). A simple method for selecting a capacitor approximately equal to this value states that the reactive power of the capacitor is intended to cancel out the reactive power of the inductor. In order to do this the reactance of these two elements must be forced to be equal in magnitude but in anti-phase, (4.34).

$$\begin{aligned} X_L &= -X_C \\ \therefore \omega L &= \frac{1}{\omega C} \end{aligned} \quad (4.34)$$

For a constant speed of 0.5 m/s, the 24 mm cyclic nature of the VHM gives ω a value of 130 rad/s. Assuming the inductance of the prototype is around 0.4 H, see Figure 4.27, and using available sizes of capacitor, (4.34) implies a value of 150 μF is suitable. Figure 4.66 shows the components of the flux linkage within the VHM being loaded in this manner.

The net flux linkage within the machine is clearly dominated by the current. The magnet driven flux and current driven flux are close to being 90° out of phase and so the power factor of the machine has effectively been reduced. The method detailed in Appendix B is used to calculate the power factor of the machine in this state and found to be 0.81.

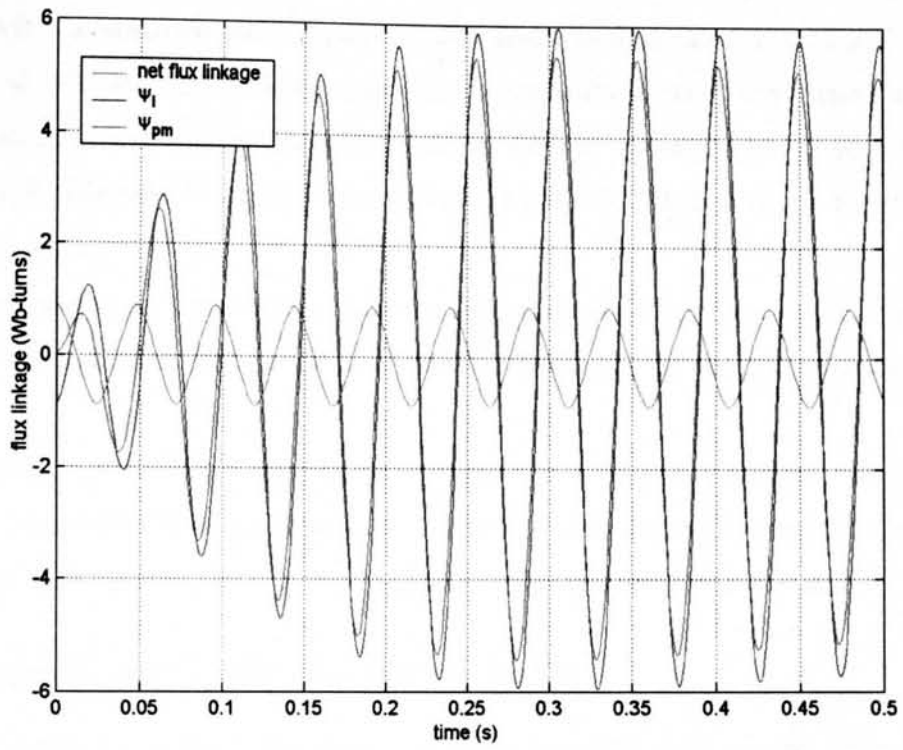


Figure 4.66: Flux linkages in the VHM with a capacitive load of 150 μF , resistive load of 630 Ω at a constant velocity of 0.5 m/s velocity

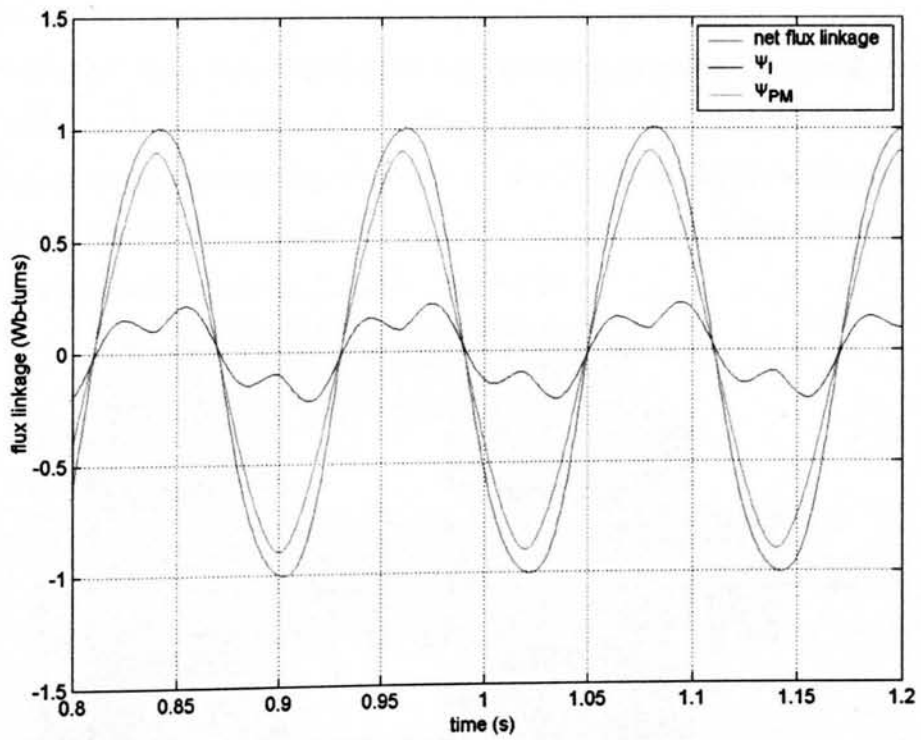


Figure 4.67: Flux linkages in the VHM with a capacitive load of 150 μF , resistive load of 630 Ω at a constant velocity of 0.8 m/s velocity

As the speed of machine moves away from 0.5 m/s the value of capacitance becomes further from the optimum and the power factor drops, with a value of 0.11 at 0.8 m/s and 0.38 at 0.2 m/s. In the latter example, the capacitor is now over-rated and the current can be seen to falter during the cycle as reactive power is transferred between inductor and capacitor. The pattern of flux linkage in the VHM is shown in Figure 4.67 for this situation.

Two superimposed frequency components are clearly visible in the ψ_1 trace of Figure 4.67, corresponding to the excited and resonant frequency of the capacitor-inductor circuit.

The advantages of capacitor assisted excitation as a way of controlling the power factor have been clearly demonstrated. The sensitivity of the capacitance to the angular velocity of the emf, or velocity of the translator, is clearly of prime importance.

4.7 Alternative Configurations of VHM

With confidence in the FEA, the design tools presented here can be extended to consider larger machines. It is likely that manufacturing constraints may prevent the use of airgaps as tight as 1 mm. Expansion of the airgap, say to 5 mm, has several effects. The shear stress and attractive forces are both reduced and the optimum magnet width, as calculated by (4.6) and shown in Figure 4.4, increases.

The configuration used throughout this Chapter has meant that the useful flux links all four coils in a phase, passing straight through the translator back iron. By altering the polarity of the magnets and the interconnection of the coils, it is possible to shift the flux pattern so that the flux linking the two stator cores are totally independent, having a return path through the centre of the rotor, Figure 4.68.

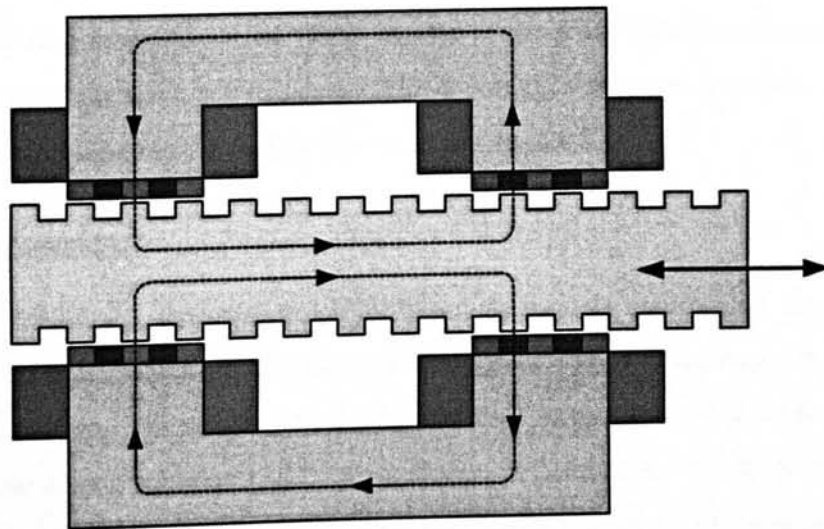


Figure 4.68: Alternative flux pattern

Electrically, this will have no effect on the machine, but several physical effects will become apparent. In this configuration, as all the flux no longer follows the same reluctance path, any deviation of the translator position towards one or other stator core will cause an imbalance in the coil driven-flux density in the two airgaps. The unfortunate side effect of this is a sharp increase in the resultant force on the translator, referring to Figure 4.19 the attraction to one side will move up the curves whilst the attraction to the other moves down. In the original flux pattern, the coil driven flux will be equal on either side of an unevenly spaced translator, and the unbalanced forces will be limited to those due to magnet excitation, the lowest curve of Figure 4.19.

If the return flux path is through the translator, a large back iron will be required and the structure will necessarily be large. However, a significant advantage of having a translator return flux path is that it allows for the possibility of a four sided electrical machine, all being magnetically independent. Figure 4.69 shows an end view of the configuration, with the translator oscillation into and out of the plain of paper.

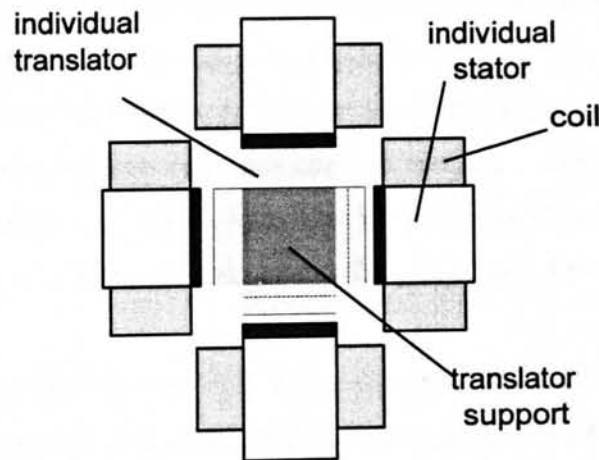


Figure 4.69: End view of four sided VHM

The resulting machine can be much shorter in the axial direction than a two sided machine having the same active airgap. This topology, which has an aspect ratio closer to that of a hydraulic ram, is further discussed in Chapter 7.

4.8 Discussion

A 3kW VHM was designed and built based on models assuming a simplified flux flow. A two dimensional FEA model was then presented to examine more closely the actual flux pattern. The simple approximations used in this and the previous chapter to predict shear stress, equation (3.12), were shown in Section 4.3.1.1 to give reasonable results and are hence a valid tool in terms of simple design procedures and machine sizing. The same analysis, however, when extended for emf prediction, as in equation

(4.5), was shown to be inadequate (Section 4.2.3.2) and appears to require FEA analysis. The interaction of the magnet and armature current flux resulted in a complex self inductance relationship with position and current. A variety of models for predicting the characteristics on load have been presented, with a favoured model selected. For open circuit and low current / short circuit predictions, the simple equivalent circuit of model A was shown to perform as well as the favoured model. For the purpose of future design work, this model, in combination with a simple equation such as (4.31) could be used to give an open circuit emf and short circuit current. The determination of the coefficients of that equation, however, require FEA.

The favoured model, which utilised a look up table relating the current and position to flux linkage, detailed in Section 4.3.2.6, used a Runge-Kutta integration routine at every time step and was hence computer intensive.

The airgap size has been demonstrated as crucial to the performance of this machine. Large attractive forces between translator and stator of around twice the magnitude of the useful axial force which pulsate with position have been identified. Much attention must therefore be paid to the lubrication and support structure of these linear machines.

For use as a generator, the VHM must be provided with reactive power. The benefits of this were demonstrated with capacitor assisted loading. The sensitivity of this method to emf frequency and hence translator velocity was demonstrated. For the reciprocating motion of a linear machine in an MEC, therefore, a more complex power inverter is required.

It has been demonstrated that the VHM is capable of airgap shear stresses above 100 kN/m^2 , several times greater than that found in more conventional topologies. For the slow speed applications of MECs a high shear stress such as this is crucial for a high power take off.

Chapter

5

The Air-Cored Tubular Machine

Equations governing the shear stress of an air-cored tubular machine were derived in Chapter 3. These equations are based on simplified flux flow assumptions in combination with the presence of an imaginary piece of steel at a distance tending to infinity from the magnetic translator. Within this chapter that simple analysis is extended to allow consideration of the emf induced within the coils and the resulting relationships are used to outline the design of a 3 kW prototype machine. Detailed FEA of this topology is then performed and compared with the results from an experimental rig. The aim of this chapter is therefore to present a design methodology similar to that developed for the VHM in the previous chapter.

5.1 Design of 3 kW Prototype

5.1.1 Flux density around translator

It is possible to formulate and analyse the equivalent magnetic circuit of the flux flow out of a single radial pole segment, width $d\theta$, into the adjacent pole, Figure 5.1. All the flow is assumed to emanate from the midpoint of the magnet and flow through the entire width of the magnet section into the steel spacer, thus ignoring leakage through the magnet air border. In combination with the concept of effective airgap introduced in Chapter 3, the flux density across the width of the steel / air border is assumed to be constant whilst that above the magnet / air border is assumed to be zero, Figure 5.2. All the steel is assumed to have an infinite permeability.

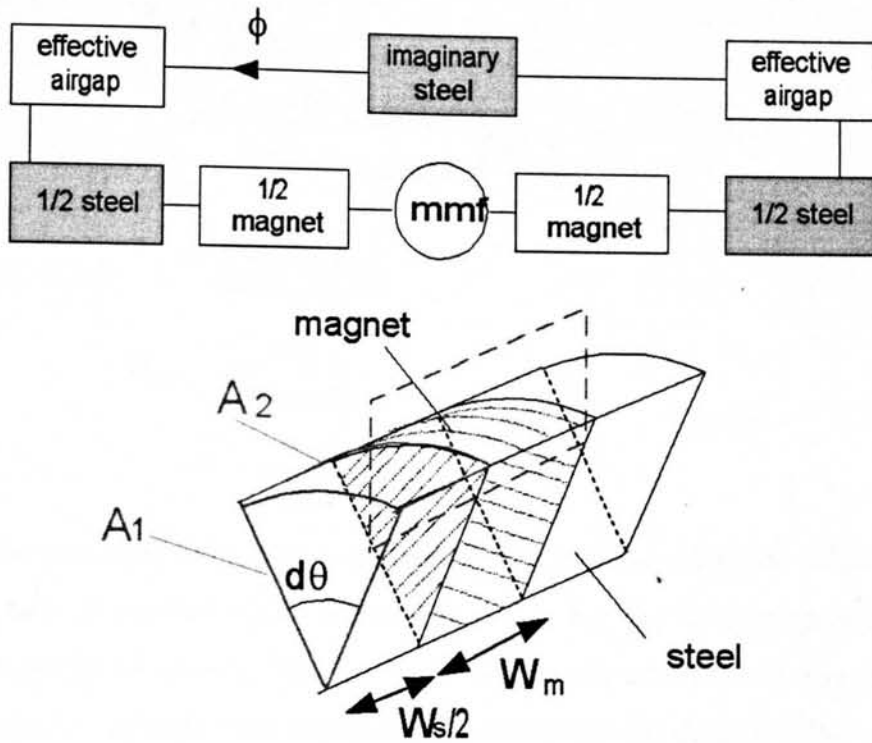


Figure 5.1: Equivalent circuit of radial segment

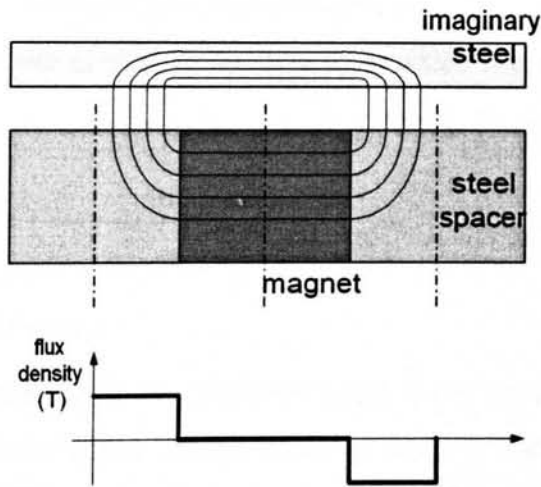


Figure 5.2: Assumed flux flow in air core machine

The reluctance of the two effective airgaps and each half of the magnet is given in (5.1) and (5.2) respectively.

$$\begin{aligned}
 S_g &= \frac{l_g}{\mu_0 d A_2} \\
 &= \frac{w_m + W_s}{\pi} \times \frac{1}{\mu_0 R_m d \theta \left(\frac{W_s}{2} \right)} \\
 &= \frac{2(w_m + W_s)}{\mu_0 \pi R_m W_s d \theta}
 \end{aligned} \tag{5.1}$$

$$\begin{aligned}
 S_{m/2} &= \frac{w_m}{2\mu_0 \mu_r d A_1} \\
 &= \frac{w_m}{\mu_0 \mu_r R_m^2 d \theta}
 \end{aligned} \tag{5.2}$$

The total reluctance of the flux path from each magnet may hence be calculated by summing two of each of these components (giving $S_m + 2S_g$) and integrating for θ between 0 and 2π , which will allow the flux flow from one pole to be as given in (5.3) when subjected to the mmf from the magnet with a remnant flux density of B_r .

$$\phi = \frac{\pi^2 B_r w_m W_s R_m^2}{2\mu_r R_m (w_m + W_s) + \pi w_m W_s} \tag{5.3}$$

The flux derived above divided by the area from which it emanates represents the value of flux density at the surface of the rotor, \hat{B}_g , given in (5.4).

$$\hat{B}_g = \frac{\pi B_r R_m w_m}{2\mu_r R_m (w_m + W_s) + \pi w_m W_s} \tag{5.4}$$

5.1.2 Selection of magnet

Due to a manufacturer enforced preferred upper limit on the diameter of each individual magnet piece, coupled with a desire to make a translator of comparable physical size to the VHM prototype, the magnets used for this machine have a diameter of 100 mm and a thickness of 25 mm.

5.1.3 Selection of Steel Spacer

For an increase in the width of steel spacer, the flux density at the translator will decrease in the approximately inverse relationship of equation (5.4), illustrated in Figure 5.3. In an attempt to exploit magnetic gearing, the entire translator pole width should be kept to a minimum, the lower limit being the maximum flux density permitted before the steel saturates.

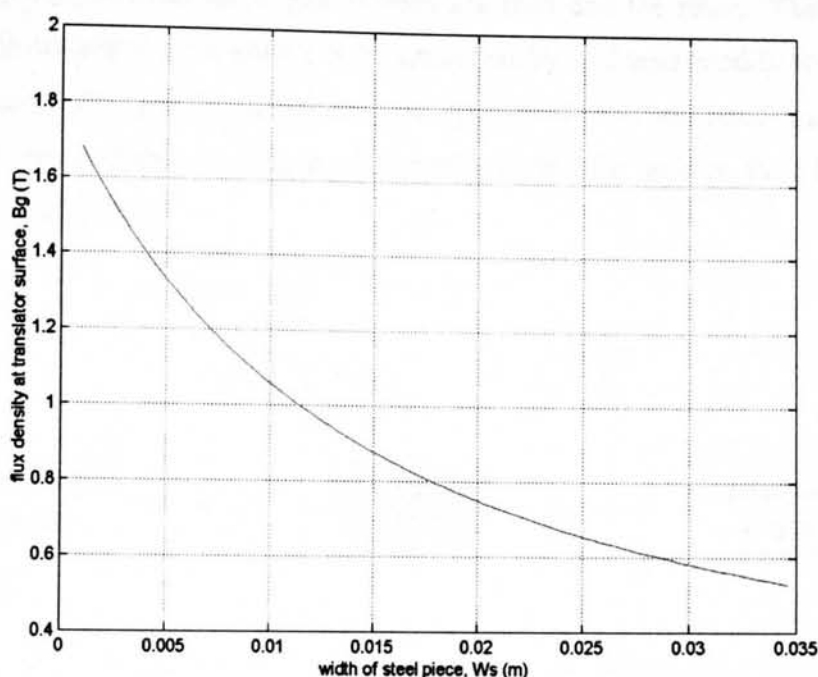


Figure 5.3: Variation of surface flux density with width of steel spacer

Figure 5.3 shows that a steel piece of width 25 mm corresponds to a surface flux density of 0.65 T, around half that at which steel starts to saturate. It can therefore be assumed that saturation will not occur until the mmf from the coils matches that of the magnets. Furthermore, selecting a steel width equal to that of the magnet piece has been previously recommended, [72] and section 3.4.2.1.

5.1.4 Coil support

In order to construct a machine whereby each individual coil has a surface to react force against, it is necessary to provide slots in the stator. Unlike an iron-core stator, where slots can be used to channel the flux, the presence of coil supports separating coils in this machine will decrease its performance. If there is a non magnetic keeper between each coil, then the area covered by each coil, and hence magnetic flux cutting it, will be reduced. In this simple analysis the performance of the machine will decline linearly with the width of spacer per coil. In order to minimise this effect, one support is provided every third coil which in a three phase winding corresponds to one spacer per translator pole. For a pole width of 50 mm, therefore, a 6 mm spacer can be expected to reduce the machine performance by 12 %.

5.1.5 Translator Support

In order to impart force and be supported, the cylindrical translator must either be enclosed in a non magnetic support tube or mounted on an axial shaft. The former of

these necessarily increases the airgap between the coils and the rotor. The effect of mounting the translator on a shaft can be simulated by a simple modification to the equivalent magnetic circuit. If the shaft is cylindrical, non magnetic and passing through the centre of the magnets, it will provide a path for leakage flux, S_L with a reluctance given by (5.5).

$$S = \frac{l}{\mu_0 A} \tag{5.5}$$

$$\therefore S_L = \frac{w_m}{\mu_0 \mu_r \pi r_h^2}$$

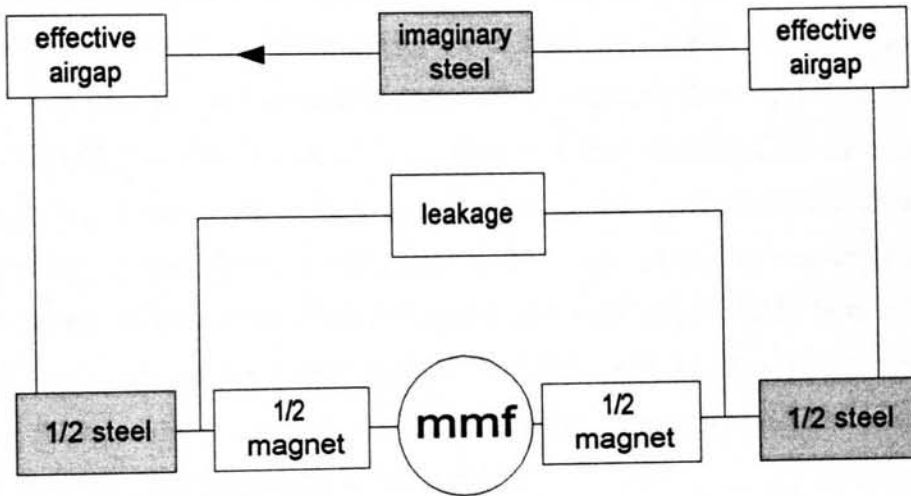


Figure 5.4: Equivalent circuit including leakage

The modified equivalent circuit is shown in Figure 5.4 and the effect of the shaft radius on the surface flux density using this equivalent circuit is shown in Figure 5.5.

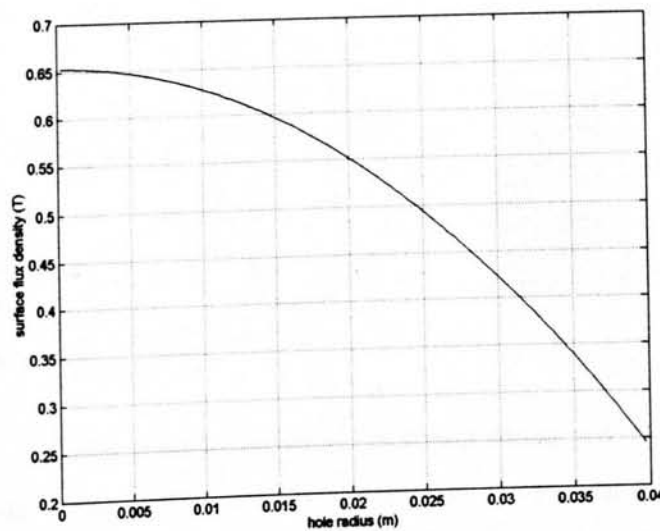


Figure 5.5: Effect of shaft size on surface flux density

The introduction of a 20 mm diameter hole hence only reduces the flux density at the magnet surface by less than 4% to 0.628 T.

5.1.6 Design of Stator Coils

5.1.6.1 Design

Unlike the VHM, the dimensions of the coils in the tubular topology are largely dictated by the size of other components within the machine. The available width has been predetermined by the translator pole width, the desire for a three phase output and the selection of coil support and is hence 14.7 mm. The inner diameter is a function of the magnet radius and minimum airgap technically achievable, whereas the outer diameter is limited by the exponential decay of the magnetic field. As such an outer diameter of 155 mm was chosen, corresponding to a flux density at the outer surface equal to 25 % of that at the surface, according to (3.16). The minimum airgap was assumed to be 2.5 mm, giving a coil height of 22.5 mm. Manually winding the coils around a bobbin of the correct internal diameter and width required 230 turns of 1 mm diameter wire to achieve the outer diameter – a fill factor of 0.54. For a peak current of 10 Amps, the equivalent current density for a single coil occupying the same space, J , is equal to $10 \times 230 / \text{coil area}$, or $6.9 \times 10^6 \text{ Am}^{-2}$.

5.1.7 Flux Cutting Coil

The total flux cutting a single coil can be calculated in order to investigate the force reacted and emf induced.

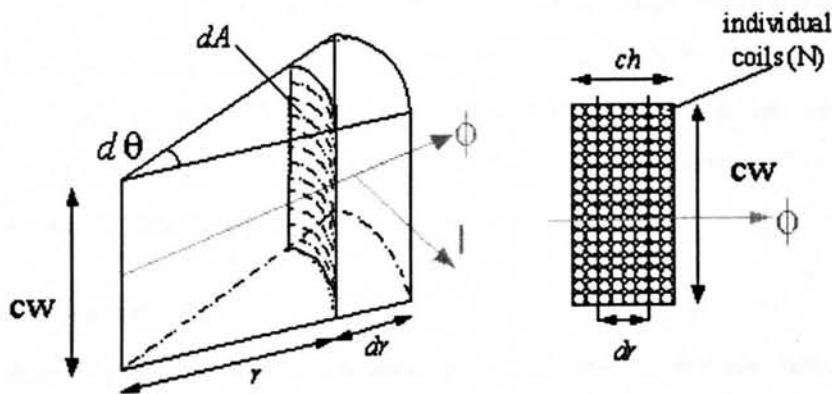


Figure 5.6: Derivation of flux linkage cutting coil

Referring to Figure 5.6, the flux linkage of a section dr of a coil is equal to the total flux, ϕ , multiplied by the number of turns contained in that section, $(dr/ch) \cdot N$. The flux linkage of a single coil will be an integral of this value in three dimensions, as shown in (5.6).

$$\begin{aligned}\psi_{coil} &= \frac{N}{ch} \int_0^{2\pi} \int_{R_i}^{R_o} \int_0^{cw} \hat{B}_g e^{-r/l_g} r dz dr d\theta \\ &= 2\pi(cw)\hat{B}_g(-l_g) \frac{N}{ch} e^{-g/l_g} \left[e^{-ch/l_g} (R_m + g + ch + l_g) - R_m - g - l_g \right]\end{aligned}\quad (5.6)$$

Where cw = coil width (m)

g = airgap (m)

ch = coil height (m)

See also Figure 3.13 for dimensions.

This value is assumed to be the peak value of a sinusoidal variation of flux linkage with coil position across the entire rotor pole

5.1.7.1 Force per coil

Restating equation (3.18) as an integral over the width of a coil in the z direction will give the peak force per coil, (5.7).

$$\begin{aligned}F_{coil} &= \int_0^{2\pi} \int_{R_i}^{R_o} \int_0^{cw} J\hat{B}_g e^{-r/l_g} r dz dr d\theta \\ &= 2\pi(cw)J\hat{B}_g(l_g) e^{-g/l_g} \left[R + g + l_g - e^{-ch/l_g} (R_m + g + ch + l_g) \right]\end{aligned}\quad (5.7)$$

As with flux linkage, the variation of force for a constant current density can be assumed to be sinusoidally varying with position. The net force reacted by all three phases over one translator pole can be used to calculate the number of poles required to constitute a 3 kW machine. To react the constant 6 kN force required to provide 3 kW at 0.5 ms^{-1} requires a peak force of 4 kN from each phase. Substituting the values described above into equation (5.7) yields 250 N per coil, implying that each phase must consist of at least 16 coils. For convenience, the stator will consist of two halves, each encompassing 8 translator poles.

5.1.7.2 Predicting emf

An expression for the peak emf induced in a coil can be derived according to equation (5.8). Using the peak value of flux linkage as given in (5.6) gives a peak emf of 12.5 Volts per coil, corresponding to 100 Volts per stator half.

$$\begin{aligned}
 E &= -\frac{d\psi_{\text{coil}}}{dt} \\
 &= -\frac{d\psi_{\text{coil}}}{dx} \cdot \frac{dx}{dt}; \\
 \psi_{\text{coil}} &= \hat{\psi}_{\text{coil}} \sin\left(2\pi \frac{x}{2(w_m + W_s)}\right) \\
 \therefore \frac{d\psi_{\text{coil}}}{dx} &= \hat{\psi}_{\text{coil}} \cos\left(\pi \frac{x}{(w_m + W_s)}\right) \cdot \frac{\pi}{w_m + W_s} \\
 \therefore E &= -\left(\frac{\pi}{w_m + W_s}\right) \hat{\psi}_{\text{coil}} \cos\left(\pi \frac{x}{w_m + W_s}\right) \cdot \frac{dx}{dt} \\
 \Rightarrow \hat{E} &= \hat{\psi}_{\text{coil}} \dot{x} \frac{\pi}{w_m + W_s}
 \end{aligned} \tag{5.8}$$

where x = displacement (m)

5.1.7.3 Predicting Inductance

The inductance L of a magnetic circuit may be expressed as (5.9).

$$L = \frac{\Psi}{I} = \frac{N\phi}{I} \tag{5.9}$$

The simplified flux flow assumption of Figure 5.2 is not valid when considering the current driven flux, as the derivation of the effective airgap specifically relied on the alternate nature of the poles of the translator. The reluctance network for flux driven from a coil above the translator now consists of several elements: the airgap between the coil and translator surface, the steel spacers, the magnetic regions and the return path. Although an analytical solution for the armature reaction field is possible in an axially magnetised iron cored machine, it is 'considerably more complex than for a radially magnetised machine' [71]. As such, a simplified method is presented here.

For a very thin coil attached to the surface of the translator, the mmf distribution becomes analogous to that of the translator magnets and so the concept of the effective airgap can be re-introduced. For a purely iron translator, the reluctance path of the flux is twice across the effective airgap, $2S_g$ as defined in (5.1). The flux at the translator becomes Equation (5.10).

$$\phi = \frac{NI\pi^2 \mu_0 W_s R_m}{2(w_m + W_s)} \tag{5.10}$$

The exponential decay used for the magnet driven flux is not applicable to the current induced flux and so the flux given in (5.10) is assumed to cut the entire coil. Substitution into (5.9) gives a value of inductance of 8.2 mH. This method is close to

the physical situation for machines with small airgap and thin coil / pole widths. A more accurate calculation requires a more complex method (e.g. the use of a Biot-Savart method or a full FEA program).

5.1.8 Prototype dimensions

Table 5-1 and Figure 5.7 show the final dimensions of the translator and loading conditions plus the nominal airgap, which in reality is not a design criteria but fixed by the manufacturing process.

Table 5-1: Dimensions of tubular prototype

Magnet width	0.025 m
Steel Width	0.025 m
Rotor diameter	0.1 m
Airgap	0.005 m
Velocity	0.5 m/s

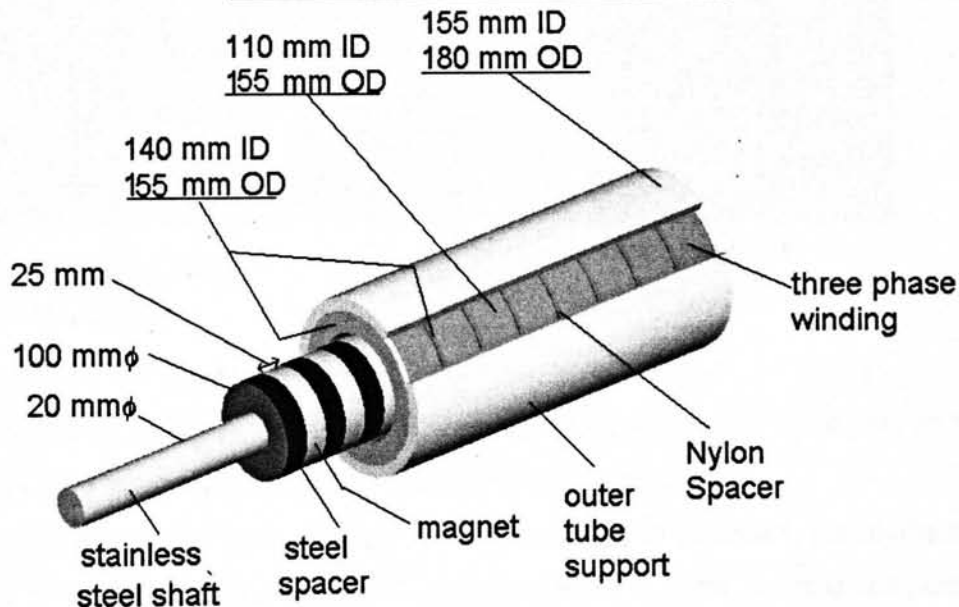


Figure 5.7: Dimensions of one half (8poles) of 3 kW tubular machine

5.2 Finite Element Analysis of Single Three Phase Coil in Ideal Machine

5.2.1 Details of the model

Although the tubular machine has a three dimensional flux pattern in Cartesian coordinates, its uniformity around the centre line ($x=0$) allows it to be modelled using two dimensional analysis in an axisymmetric coordinate system. The repetitive behaviour of the translator field could be investigated using a model consisting of one pole only,

but the use of a three phase winding means it is beneficial to have a wider scope model. The four magnet, four surface pole model of Figure 5.8 allows a three phase winding spanning a surface pitch to be modelled across two entire surface poles, leaving half a pole width clearance at each end. By terminating the model halfway through the stainless steel support, the boundary condition is set as a flux line, i.e. having zero normal flux. The same is true for terminating the model at the mid point of a translator steel spacer.

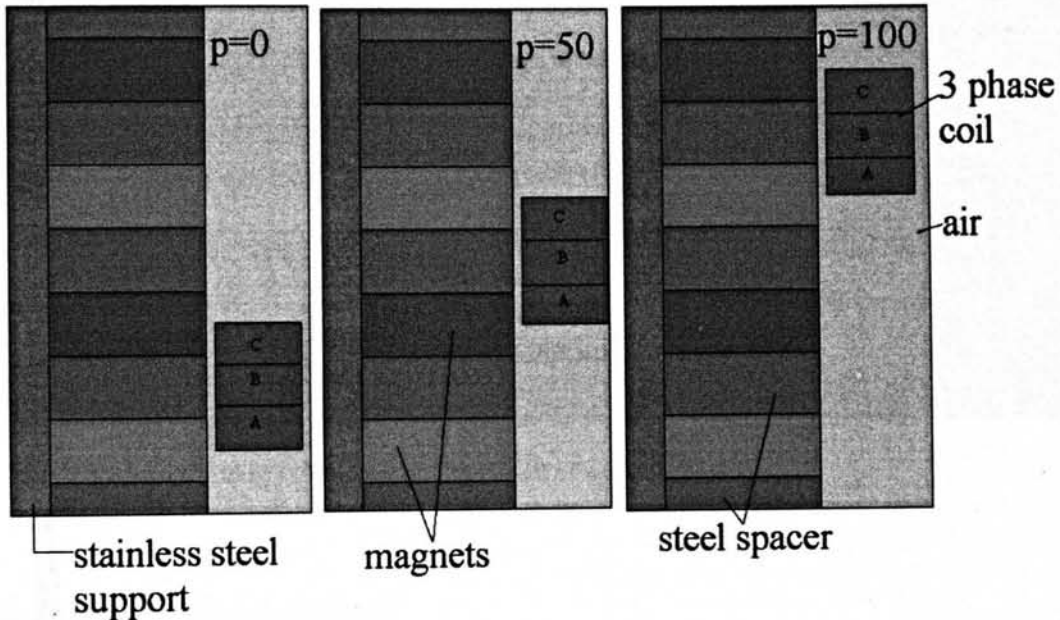


Figure 5.8: Position of coils

Also shown in Figure 5.8 is the definition used for coil position i.e. at $p=0$, $p=50$ and $p=100$ coil B is exactly aligned above a steel spacer / surface pole.

The model mesh is shown in Figure 5.9. As with the VHM model, the smallest mesh size is 1 mm and is located in the coil / airgap region. In order to avoid computational bias in the coil region, the mesh was made densely throughout the translator / air boundary. The general structure of the mesh remains unaltered as the coil changes position, but this comes at the expense of many more elements in the model than necessary.

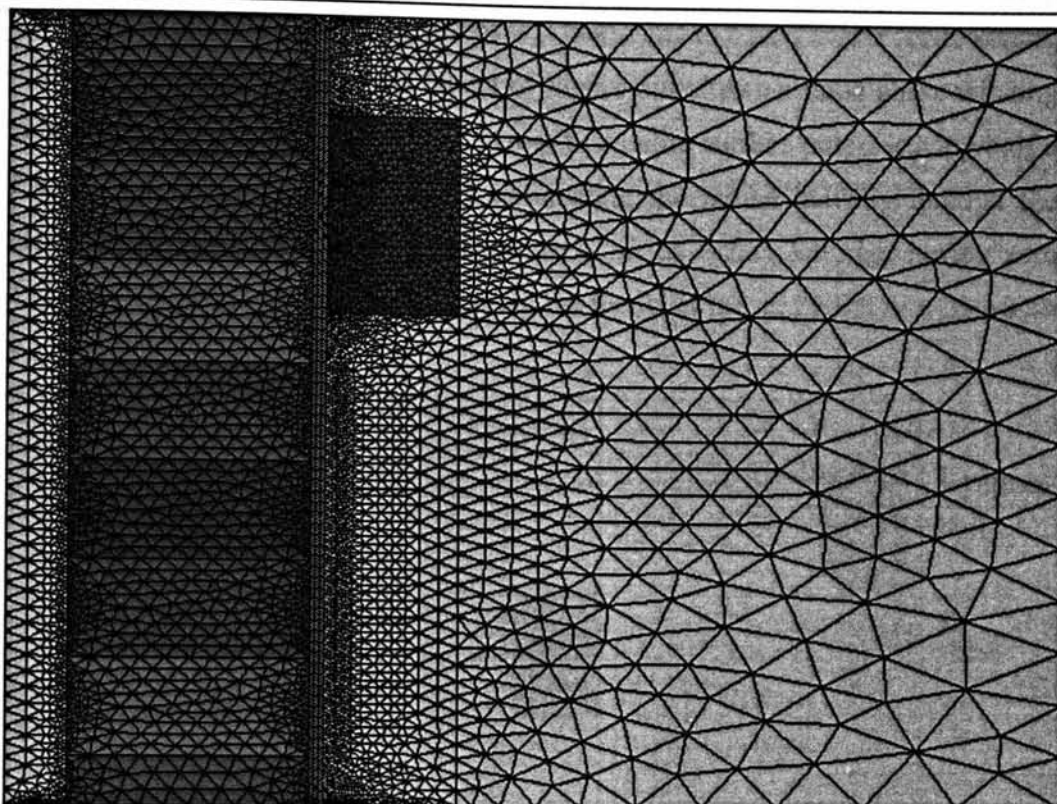


Figure 5.9: FEA mesh of tubular machine

5.2.2 Details of the Analysis

A line of length 'a' in the r direction in the r-z plane, as defined in Figure 5.10, represents a disc in a three dimensional coordinate system. The total flux linking such a disk in the z direction is equal to the flux density B_z multiplied by the area of that surface. Expressing this as a sum of elemental disks gives (5.11).

$$\begin{aligned}
 \phi &= \int_0^a B_z \cdot 2\pi r \cdot dr \\
 &= 2\pi \int_0^a B_z r dr \\
 &= 2\pi \int_0^a (\nabla \times \Omega_\theta) r dr \\
 &= 2\pi r \Omega_\theta(a)
 \end{aligned} \tag{ 5.11}$$

In order to fully account for the axisymmetric nature of the magnetic flux flow, the analysis software solves (5.11) in terms of a 'modified radial potential', which gives a value of $r \times A$ for each element. Calculation of flux is hence obtained by multiplying this value by 2π .

5.2.3 Details of Results

5.2.3.1 Translator

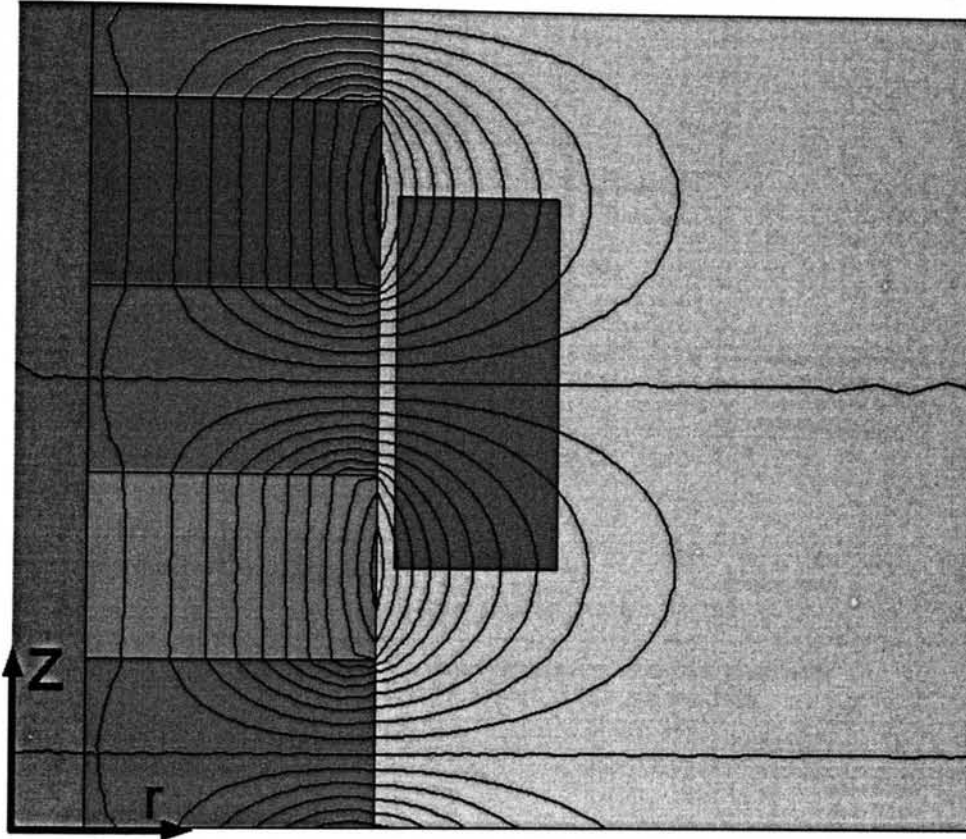


Figure 5.10: Flux lines of translator

Figure 5.10 shows the magnetic flux lines due to magnetic excitation only. The flux path through the magnets is primarily parallel to the axis. The leakage through the stainless steel central support is negligible compared to that on the translator surface.

The variation of both radial and axial flux density with position along the translator is shown in Figure 5.11. The flux density in the two directions follow a similar pattern but half a pole width out of phase with each other. At $p=25$, the surface above the centreline of a steel piece, there is no axial flux, which verifies the use of a zero normal flux condition at the boundary of the FEA model. The radial flux reaches a clear peak at the steel / magnet boundary, although the rapid decline of this value is less significant further away from the translator surface.

This data can be used to give some confidence in the simple model used to design the prototype. In Figure 5.11 the surface values of radial flux predicted in section 5.1 above were also included and show a reasonable first order approximation to those predicted by the FEA.

The graph of Figure 5.13 shows the average values of radial flux density over the steel and magnet sections of the translator, calculated by the FEA, plotted on the same axes as the flux density as calculated by the simple model using Equations (5.4), (3.16) and (5.5).

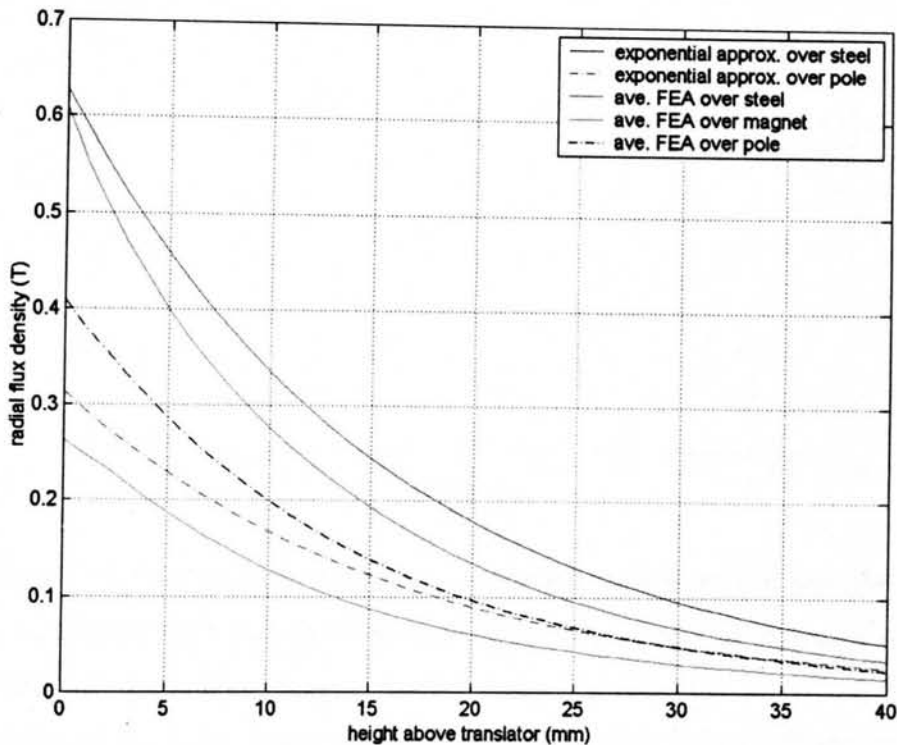


Figure 5.13: Comparison of model with 3D FEA averaged data

The simple model assumed that the flux density across a surface pole was constant, the limitations of this assumption have been demonstrated, Figure 5.11. Figure 5.13 shows that the average flux density at the surface of the steel segments calculated by the FEA is close to that predicted (over predicting by less than 5%). Over the magnet, however, the simple model assumed no leakage and hence zero flux density, whereas the FEA calculated a value just under half that above the steel. The exponential reduction of flux density with distance above the translator is a reasonable approximation when examining just the area above the steel segments. The two 'dashdot' lines of the graph correspond to the averaged values over an entire surface pole for the two methods. At positions close to the translator, the simplified method

over predicts drastically (23% at the surface) but the two methods converge at greater distances, 4% error at 25 mm and less than 1% at 30 mm. For machines with a small airgap there is therefore a need for the more detailed FEA analysis.

5.2.3.2 Coil Flux Linkage

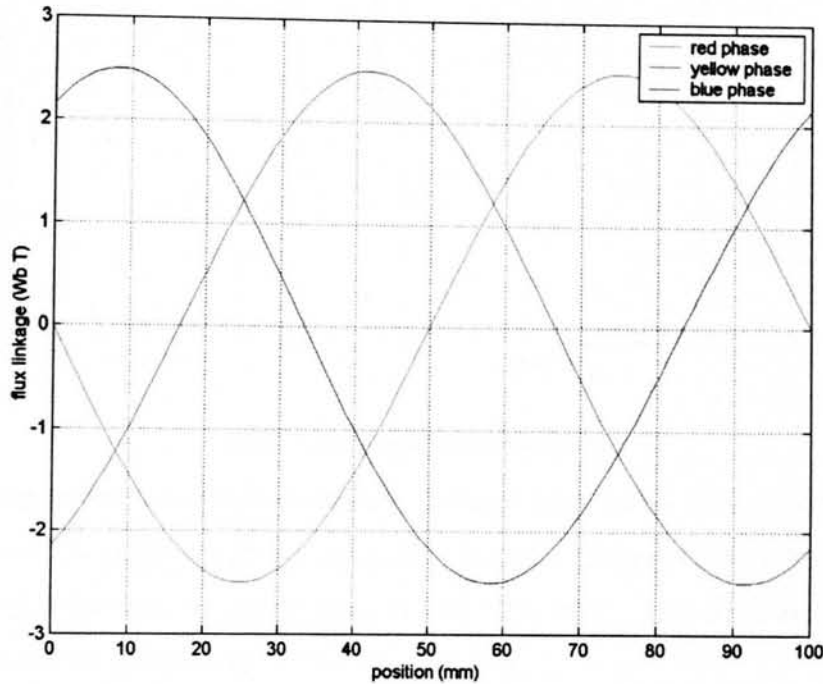


Figure 5.14: Variation of flux linkage with position for 8 coils for each of the 3 phases

Figure 5.14 shows the variation of flux cutting the three phases as the position of the coils is changed. Each half phase of the prototype consists of 8 individual 3 phase configurations of the type shown in Figure 5.8. The actual flux linkage is hence obtained by multiplying the value obtained in the FEA by eight. Three identical waveforms can be seen, each separated by 120° .

5.2.3.3 Armature Excitation

Replacing the magnetic regions of the simulation with air allows the inductances of the phases to be investigated. The single three phase coil inductance results for the simulation are presented Figure 5.15 and confirm the 50 mm cyclic nature.

Further confirmed in this diagram are the existence of three out of phase levels of inductance, namely the self inductance, mutual inductance of adjacent coils and the mutual inductance of non-adjacent coils. In this model, calculation of one of each of these values in combination with the known phase difference may be used to describe all three coils.

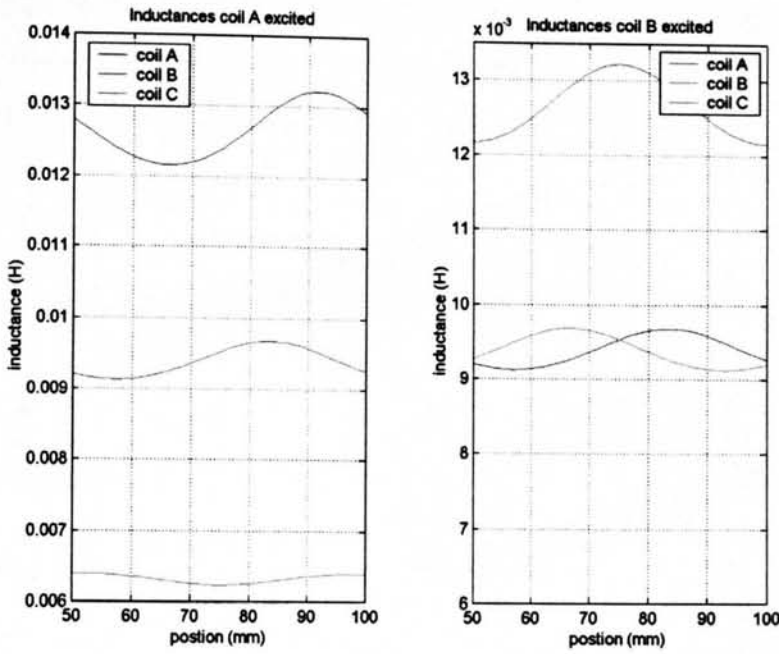


Figure 5.15: Single coil inductances

The validity of the inductance estimate of Section 5.1.7.3 may now be tested. The distributed mmf model gave a predicted value of 8.2 mH, whereas the results here show that the actual inductance varies between 12 and 13.5 mH. The error of the highly simplified method is of the order of 30-40% inaccurate.

5.2.3.4 On load

The flux linkage map of Figure 5.16 demonstrates the effect of coil position and current on flux linkage for a single phase. The graph shows a sinusoidal variation with position in combination with a linear relationship for current which is symmetrical about the origin. The linear relationship and symmetry about the zero current axis shows the inductance is independent of current.

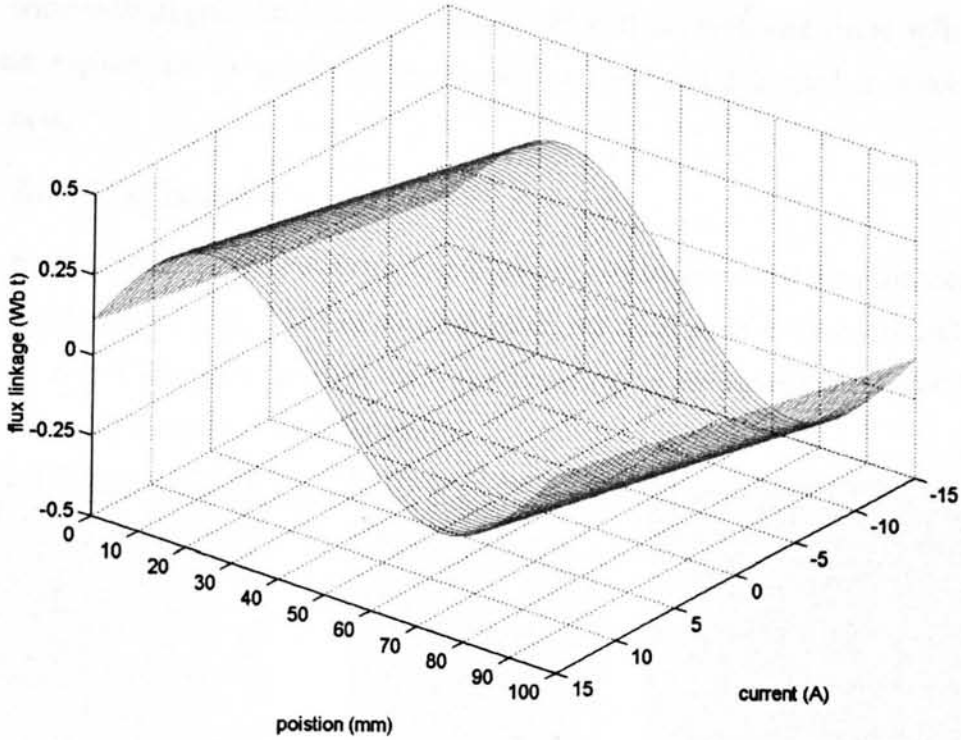


Figure 5.16: Flux linkage map of single coil (B)

5.3 Finite Element Analysis of Actual Three Phase Machine

5.3.1 Introduction

There are two reasons for extending the FEA model to include all eight poles present in each half of the stator. The first is a direct result of the topology of this family of machines, whereby the current driven flux emanating from one coil is not limited to influencing its adjacent neighbours, but several coils on each side, including those in the same phase. Considering a single phase, this effect manifests itself as the total phase inductance being less than the sum of the individual coil inductances.

Specific to the laboratory built prototype, the second reason for modelling several phases is the unbalanced nature of the three phases. To ease manufacture, the coils were grouped into three and supported in a single slot spanning a translator pole. The unfortunate side affect of this being that two of the phases are direct neighbours (red/yellow and yellow/blue) whereas the third (red/blue) is separated by a 6 mm plastic spacer, a significant distance when compared to the 14.7 mm coil width. The previous FEA assumed a coil width of $50/3$ or 16.7 mm.

By modelling all eight coils, constituting one of the two independent machine halves, both of the above effects are adequately accounted for. Furthermore, as demonstrated in

the preceding section, the simulation need only be run through all its positions three times: once with magnet excitation to calculate the emf induced, and twice with the magnetic regions set to air and either the red or blue phase excited to calculate inductances.

5.3.2 Details of model

The entire model, showing eight triple coil groups, coil supports and the definition of position is given in Figure 5.17. In this simulation, the coils remain stationary and the translator moves upwards, position zero corresponding to the magnet/steel interface being level with the edge of the outer spacer.

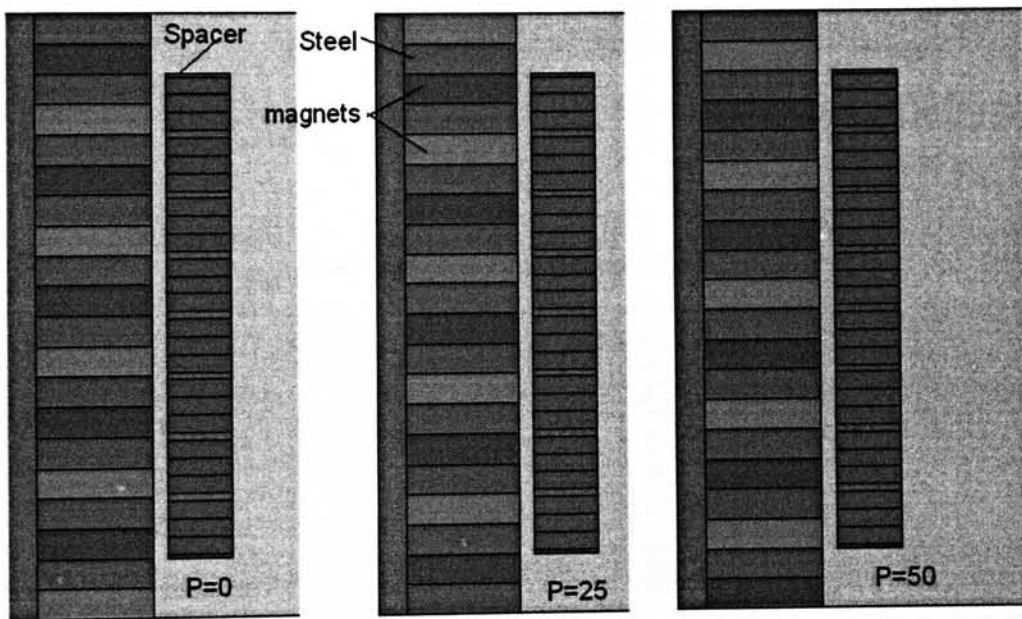


Figure 5.17: Position definition for large simulation

5.3.3 Details of Results

5.3.3.1 Phase flux linkage

Running the model over 100 mm, across two translator poles, gave the total flux linking each of the three phases as given in Figure 5.18. The vertical black lines cutting the peaks of the three phases can be used to indicate the phase differences. In a fully balanced system, all the peaks would coincide with the point at which the other two phases have equal values.

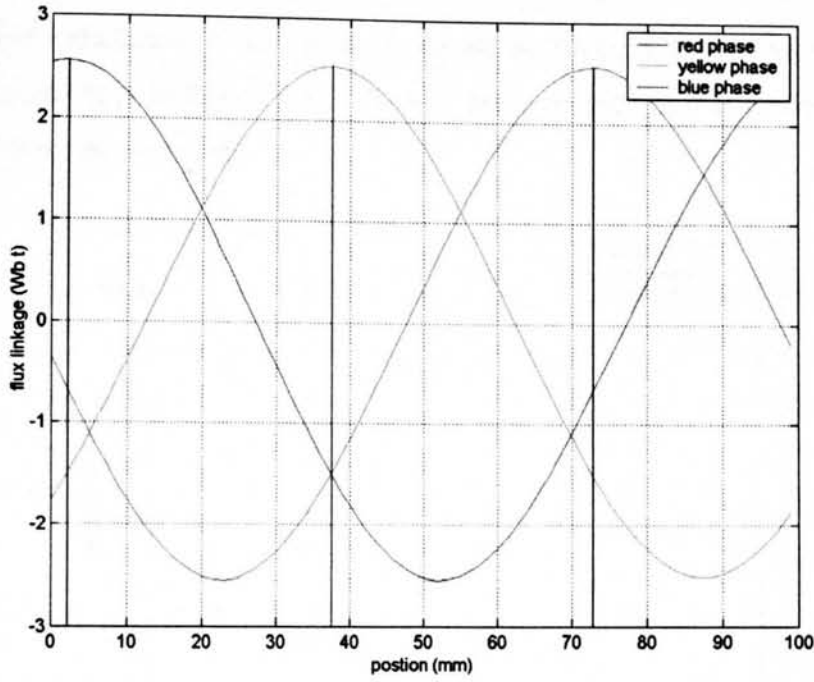


Figure 5.18: Flux cutting entire phases

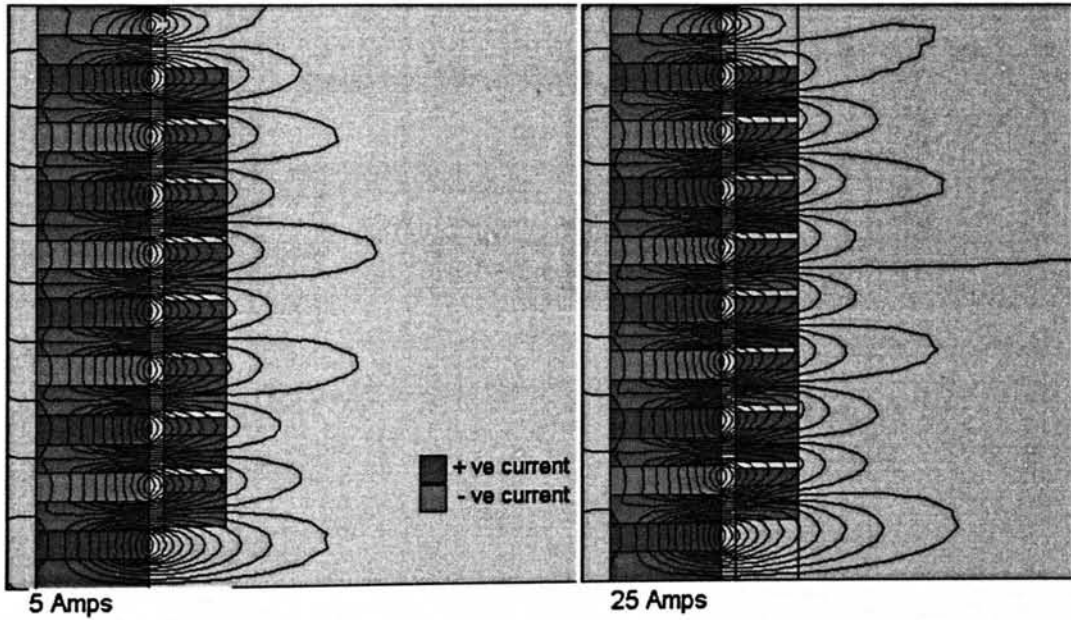


Figure 5.19: Flux plots of large FEA

Figure 5.19 shows the flux plots of the entire machine for a current of 5 and 25 Amps. Demonstrated here is the cyclic nature of the flux pattern and the dominance of magnet mmf even at high coil currents. The pattern is seen to alter only slightly in the two diagrams, and still significantly deviate from the expected flux pattern of a free standing coil.

5.3.3.2 Phase Inductances

The self inductance of each phase is shown in Figure 5.20 and the three sets of mutual inductances in Figure 5.21. Both of these provide further evidence of a non balanced three phase system.

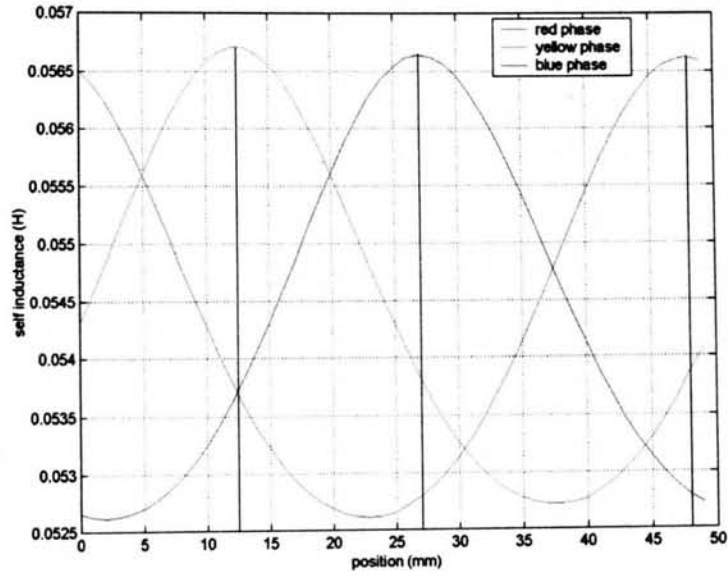


Figure 5.20: Self inductance of three phases

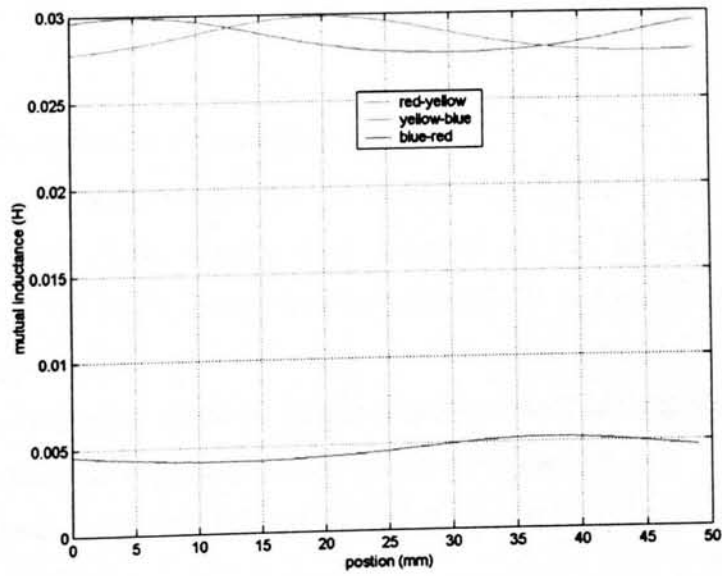


Figure 5.21: Mutual inductance between three phases

5.4 Utilisation of Finite Element Analysis

5.4.1 Force Calculations

5.4.1.1 Method

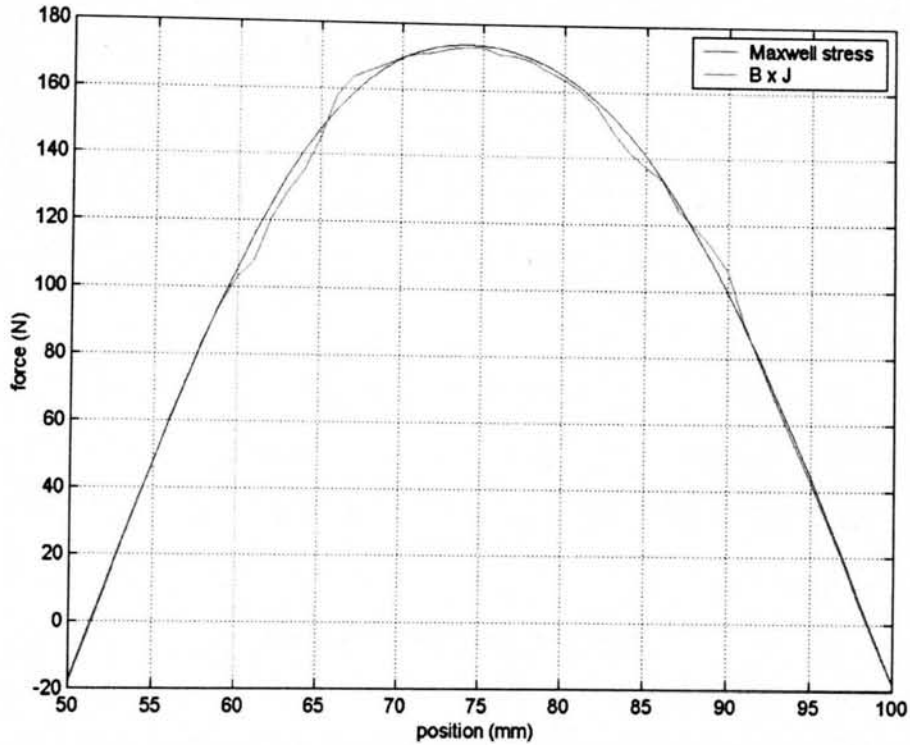


Figure 5.22: Comparison of force calculation method

There are two methods available for calculating forces in an axisymmetric simulation, the Maxwell stress tensor used in section 4.3.1 of the VHM Chapter and Lorenz's force, given in the first part of Equation (3.17) in Chapter 3. Figure 5.22 shows a comparison of the two methods for calculating the axial force. The Lorenz's force, whereby the product of current density and flux density is integrated over the coil area, gives the smoother result and is hence the preferred method.

In this section the single coil FEA simulation of Section 5.2 is used and all the forces are therefore per coil.

5.4.1.2 Normal / Radial Force

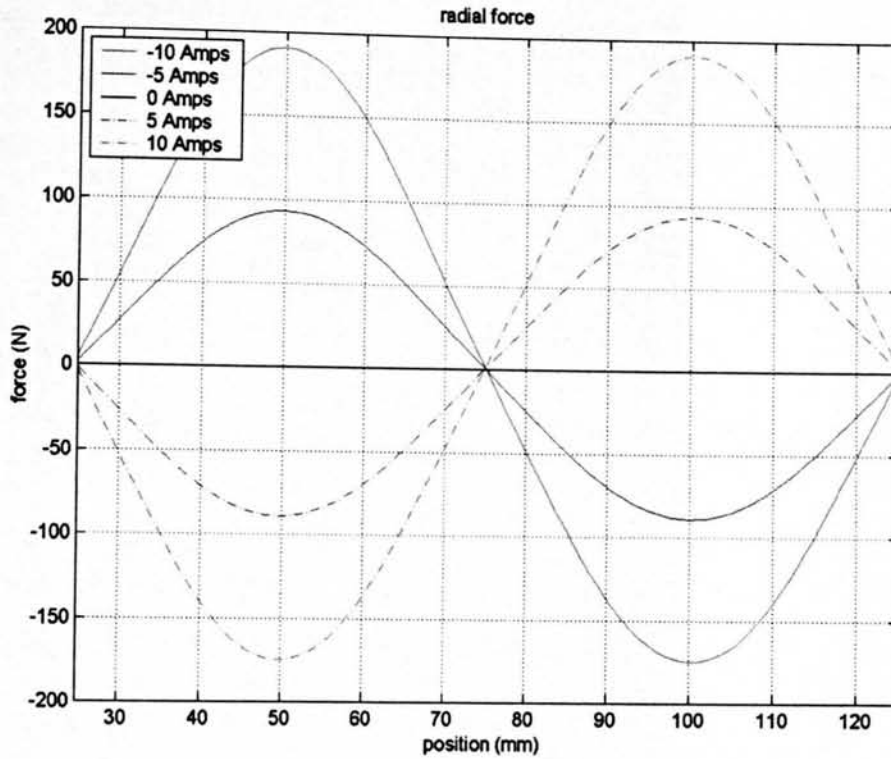


Figure 5.23: Calculated radial force

Figure 5.23 shows the variation of radial force over two pole pitches for a variety of coil currents. The maximum, which occurs as the coil passes above the centre point of the magnet, increases linearly with current with 10 Amps reacting 190 N. Inspection of the maxima demonstrate that its value is dependent on the current direction. This may be explained by inspection of flux plots.

Figure 5.24 shows the detailed flux plot of a coil above the centre line of a magnet section. In Figure 5.24A there is no current and the natural behaviour of the flux due to the presence of a magnet is observed. In Figure 5.24B a 20 Amp current is present in the coil, flowing in the direction that enforces the mmf of the magnet. In Figure 5.24C the current is in the opposite direction such that its mmf opposes that of the magnet. As the distance from the magnet surface increases, the major contributor of mmf switches from the magnet to the coil and the flux pattern alters accordingly. The radial force is a product of the current density and the axial flux density, the effect of current opposing the mmf of the magnets is to align the flux lines in the axial direction and so produce a greater force.

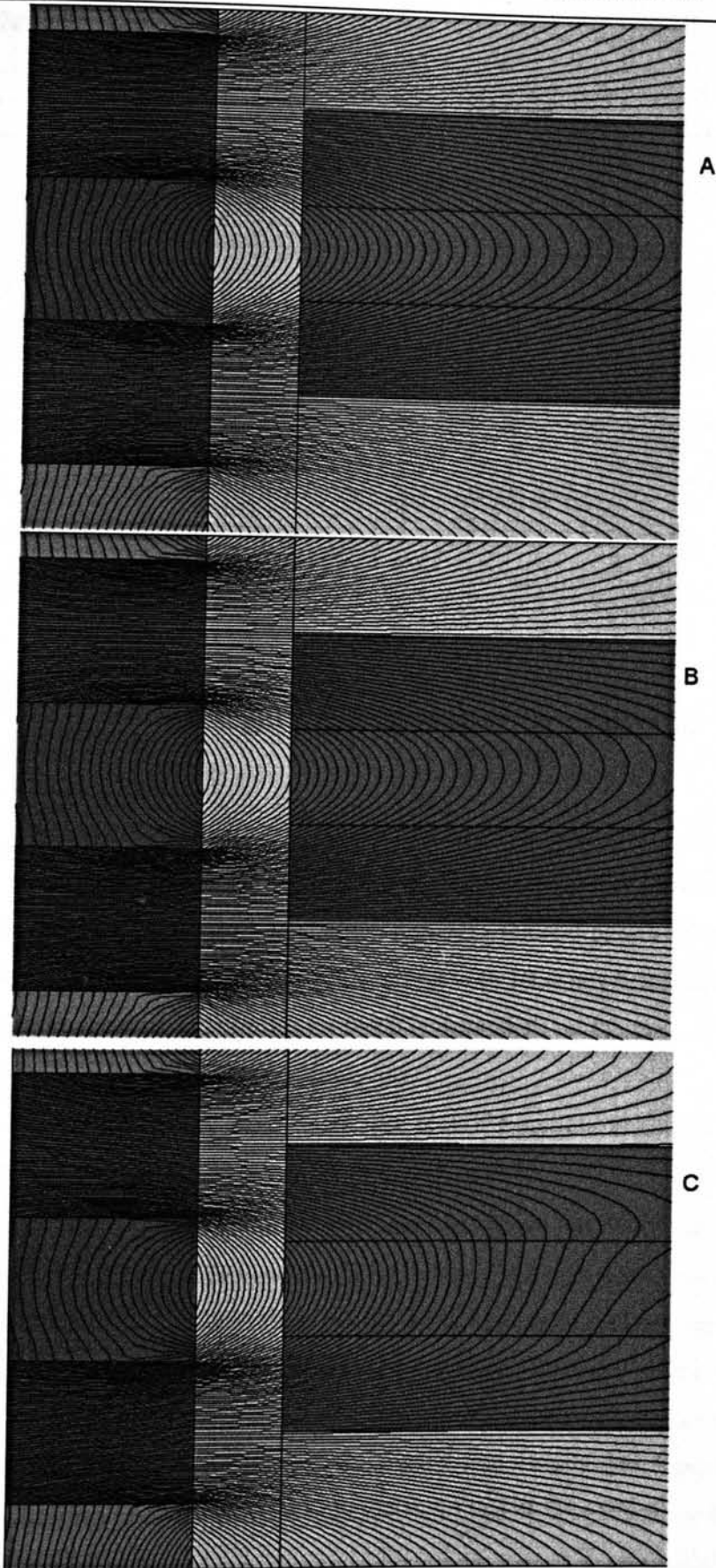


Figure 5.24: Flux plots for (A) 0, (B) +20 and (C)-20 Amp current aligned with centre of magnet

5.4.1.3 Axial Force

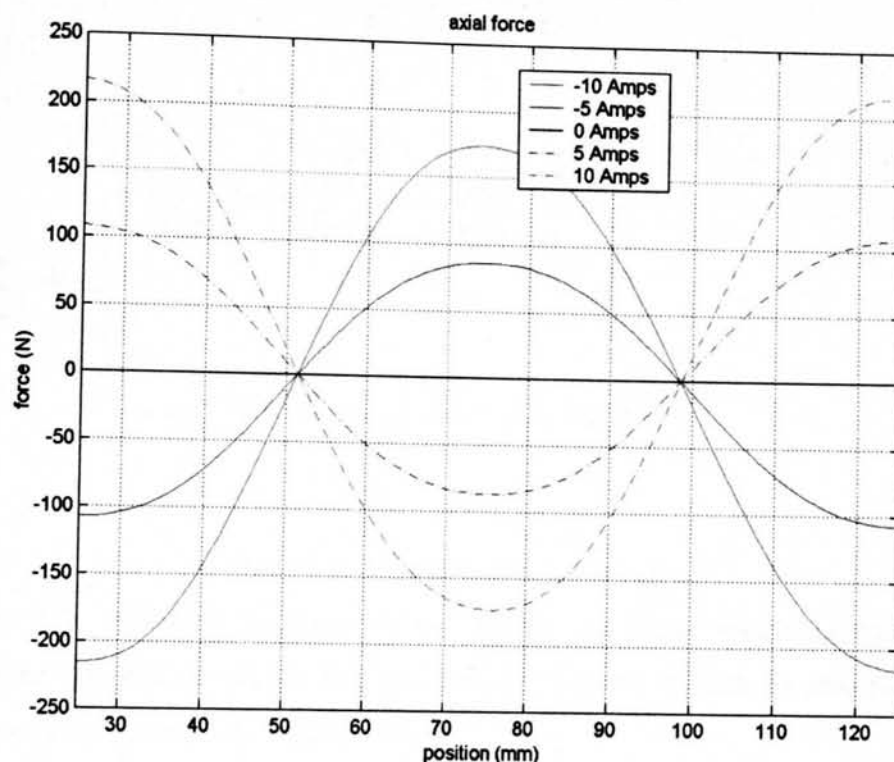


Figure 5.25: calculated axial force

The axial force of Figure 5.25 is a similar pattern to that of the radial, but half a pole out of phase, such that the maximum occurs as the coil passes over the centre of the steel. Again, the magnitude of the force is dependent on the direction of the current, with the maxima at 10 Amps being 216 N or 173 N.

5.4.2 Performance

5.4.2.1 Models for 1 phase

As demonstrated in the VHM Chapter, there are two alternative methods for predicting an electrical machine's behaviour. An equivalent circuit method, whereby the machine is split into contributing parts of magnet induced open circuit emf and a series inductance, or a look up table method, whereby exact flux-current-position reference tables are used at every time step. As the inductance is independent of current in the air cored tubular machine, the simple equivalent circuit model will suffice. When considering just one phase, this model is simple to implement as both the flux linking the coil and its inductance may be accurately modelled as sinusoidal functions.

The position dependant flux linkage is differentiated to make the emf a product of the velocity and a cosine function of position.

5.4.2.2 Simple Equivalent Circuit Model for 3 phases

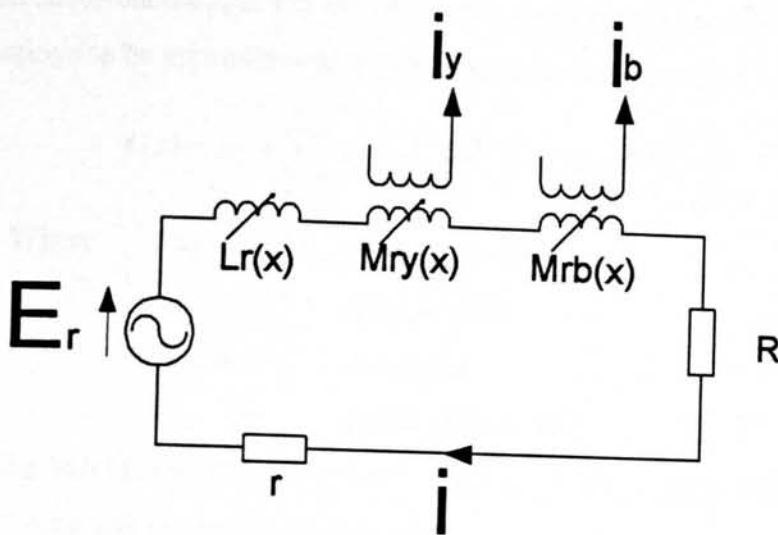


Figure 5.26: Equivalent circuit of red phase

Figure 5.26 shows the equivalent circuit for the red phase, including the mutual inductances (M), self inductance (L), the internal resistance (r) and the load (R). The voltage equation for this loop is given below (5.12).

$$E_r = L_r \frac{di_r}{dt} + i_r \frac{dL_r}{dt} + M_{ry} \frac{di_y}{dt} + i_y \frac{dM_{ry}}{dt} + M_{rb} \frac{di_b}{dt} + i_b \frac{dM_{rb}}{dt} + i_r(r + R) \quad (5.12)$$

If the machine were perfectly balanced then two simplifications could be employed, both given in (5.13).

$$\begin{aligned} M_{ry} &= M_{rb} = M_{by} \\ i_r + i_y + i_b &= 0 \end{aligned} \quad (5.13)$$

In an unbalanced machine, however, neither of these assumptions are valid and so the equations for the three currents must be re-stated as the differential equations of (5.14).

$$\begin{aligned} \frac{di_r}{dt} &= \left(E_r - M_{ry} \frac{di_y}{dt} - i_y \frac{dM_{ry}}{dt} - M_{rb} \frac{di_b}{dt} - i_b \frac{dM_{rb}}{dt} - i_r(r + R) \right) \\ \frac{di_b}{dt} &= \left(E_b - M_{rb} \frac{di_r}{dt} - i_r \frac{dM_{rb}}{dt} - M_{by} \frac{di_y}{dt} - i_y \frac{dM_{by}}{dt} - i_b(r + R) \right) \\ \frac{di_r}{dt} &= \left(E_y - M_{ry} \frac{di_r}{dt} - i_r \frac{dM_{ry}}{dt} - M_{by} \frac{di_y}{dt} - i_y \frac{dM_{by}}{dt} - i_y(r + R) \right) \end{aligned} \quad (5.14)$$

When considering the entire three phase machine and utilising the results from the larger FEA model, the inductances and magnet induced flux flow can no longer be simply approximated to a single sinusoidal function. The inductance waveforms are no longer pure sinusoids due to the imbalance caused by using coil support spacers only

every third coil. Furthermore, the importance of maintaining the correct phase differences encourages the use of Fourier series approximations, which allows periodic functions to be approximated to the form given in equation (5.15).

$$f(x) = a_0 + \sum_{n=1}^{\infty} \left(a_n \cos\left(\frac{2\pi nx}{l}\right) + b_n \sin\left(\frac{2\pi nx}{l}\right) \right) \quad (5.15)$$

Where $f(x)$ = periodic function

a_0 = average value

a_n & b_n = constants

l = period of function

The MATLAB [80] fast Fourier transform function (FFT) takes a discretely sampled set of data and returns its Fourier series.

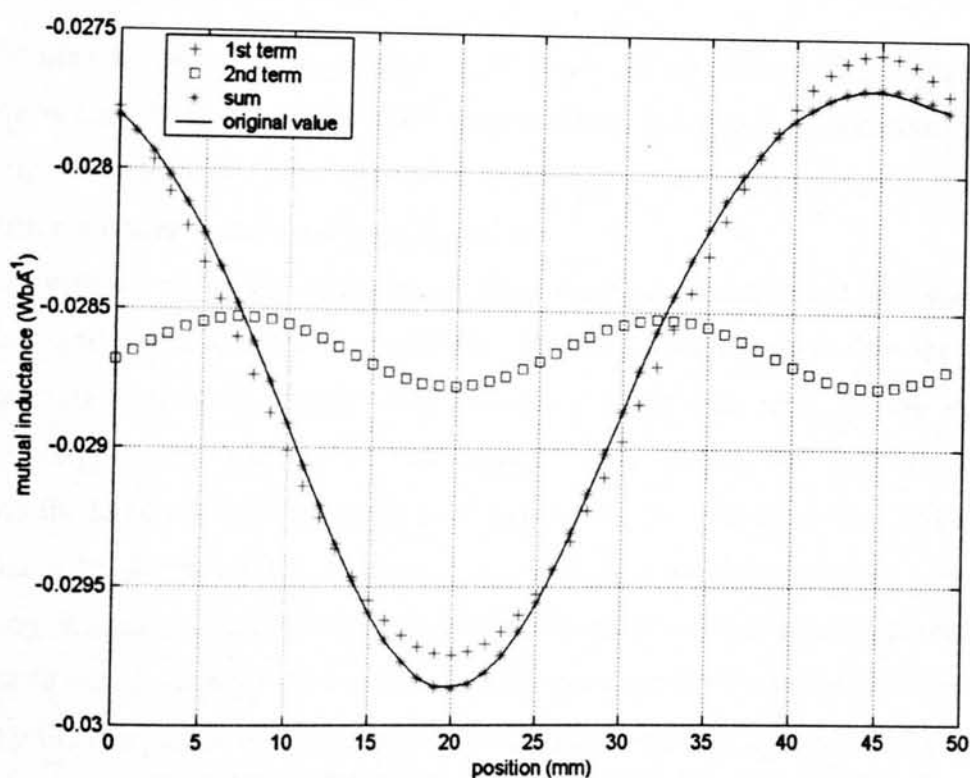


Figure 5.27: Fourier series approximation

Figure 5.27 shows the inductance relationship between the blue and yellow phases plotted on the same axis as the first two summations from (5.15). The close correlation between the sum of these terms and the original results makes further summation redundant. A similar effect was found for all the inductance relationships, whilst the magnet flux linkage required only the first terms, the second being 10^5 times smaller.

Each phase current must be solved simultaneously and numerically integrated over time. A SIMULINK [80] model was constructed within MATLAB to achieve this.

Equations (5.14) to (5.16) give the flux, emf, and self inductance for the red phase, with similar relationships existing for the other two phases. Coefficients of the equations governing all the phases are given in Appendix C.

$$\psi_r = b_1 \sin\left(\frac{2\pi x}{l}\right) + a_1 \cos\left(\frac{2\pi x}{l}\right) \quad (5.16)$$

$$E_r = \frac{2\pi}{l} \dot{x} \left(a_1 \sin\left(\frac{2\pi x}{l}\right) - b_1 \cos\left(\frac{2\pi x}{l}\right) \right) \quad (5.17)$$

$$L_r = a_0 + a_1 \cos\left(\frac{2\pi x}{l}\right) + b_1 \sin\left(\frac{2\pi x}{l}\right) + a_2 \cos\left(\frac{4\pi x}{l}\right) + b_2 \sin\left(\frac{4\pi x}{l}\right) \quad (5.18)$$

5.5 Verification of Models

5.5.1 Description of Testrig

The tubular machine was mounted horizontally and powered by a 225 mm length crank arm coupled to a 1:40 step down gearbox driven by a two pole induction machine. Varying the length of crank and motor speed allows the generator to be tested for different peak speeds and oscillation amplitudes.

The presence of exceptionally large strong magnets caused many problems when handling and manufacturing the translator. It was constructed in-situ on the 20 mm diameter stainless steel support rod, with the magnets and steel spacers mounted alternatively, Figure 5.28. Care was required when adding the steel components, because the large attractive magnetic force in combination with the brittle Nd-Fe-B was conducive to damaging the magnets. A metal jig was manufactured, capable of lowering the parts together, but again the brittle nature of the magnets prevented its successful use. A series of wooden spacers was settled on as the most reliable method of drawing the components close to each other whilst preventing a high speed collision.

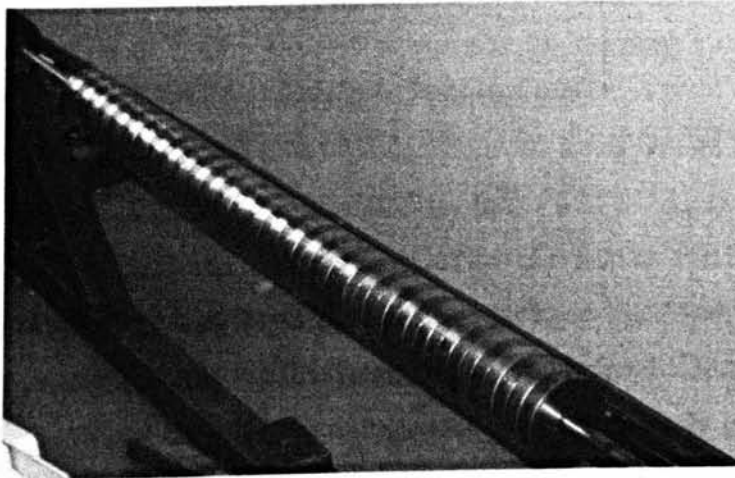


Figure 5.28: Tubular machine translator

An interesting effect was observed when the magnetic pieces were lowered onto the translator. At gaps of greater than 20 mm a strong repulsive force was observed, yet at a gap length of less than 20 mm this was rapidly replaced with a strong attractive force. At the larger gap lengths the new magnet was being repelled by the presence of like flux driven through the end mounted steel piece by the previously mounted magnet. At close proximity, however, the attractive force between the new magnet and the non saturated steel starts to dominate. This has a particularly significant consequence for disassembly.

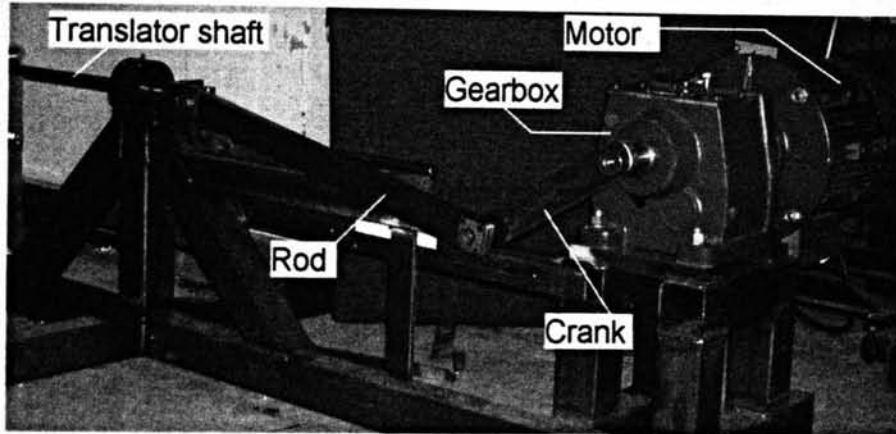


Figure 5.29: Mechanical excitation of translator

The stator body is a 15 mm wall thickness plastic tube with the stator coils suspended on the inside. Each individual coil consists of 230 turns of 1 mm diameter copper wire bound together by glass tape. Every third coil has a 6 mm nylon spacer mounted to the inside of the tube. The mounting points of the spacer serve to react force from the coils and ensure that the three coils represent exactly one translator pole width to ensure a three phase output. Great care was taken not to have any supporting metal closer to the translator than the coils. The tube was secured to an aluminium frame by in-house manufactured brass bolts, Figure 5.30.

The rigid connection between driving motor and driven translator, Figure 5.29, allows for the derivation of a simple model to describe the machine's motion. Figure 5.31 shows a schematic diagram of the crank rod arrangement.

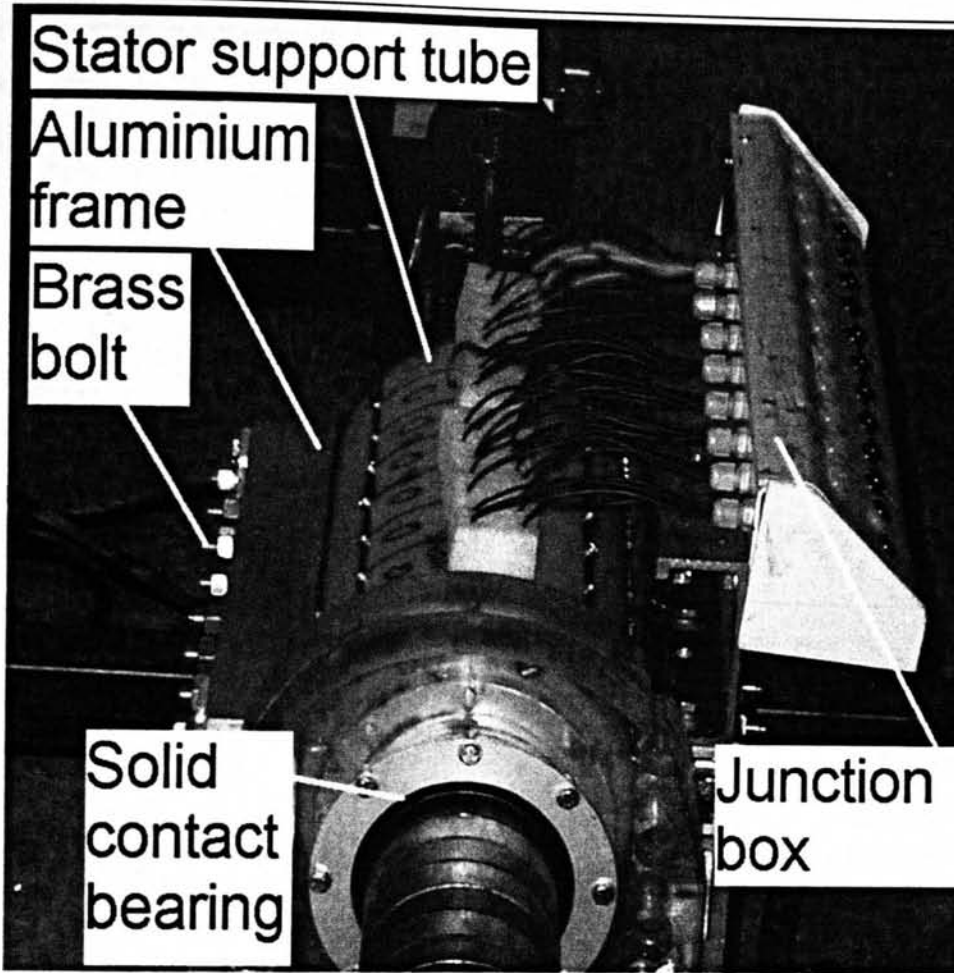


Figure 5.30: Photograph of prototype

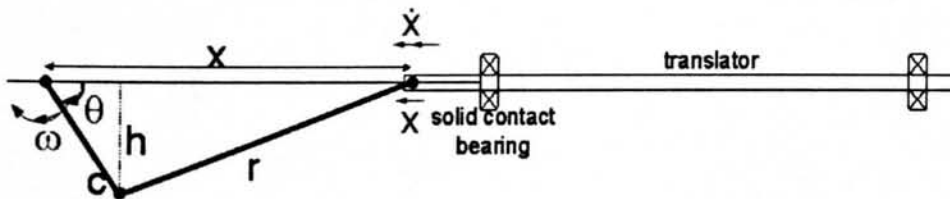


Figure 5.31: Geometric picture of crank arrangement

It is a simple geometric problem to describe the resulting motion, Equation (5.19). Analytical differentiation of this relationship gives a term for velocity, (5.23), thus avoiding the need for numerical differentiation routines in the performance model.

$$x = c \cos \theta + \sqrt{r^2 - c^2 \sin^2 \theta} \quad (5.19)$$

$$\dot{x} = c\omega \sin \omega t - \frac{\omega c^2 \sin(2\omega t)}{2\sqrt{r^2 - c^2 \sin^2 \omega t}} \quad (5.20)$$

5.5.2 Electrical Performance Models

5.5.2.1 Flux Density

The nature of this machine means that it is possible to measure the flux density at various points along the translator before the stator coils were mounted. A Hall probe

was used in order to validate the FEA work. Comparison between values predicted by the model given in Section 5.2 and experimental results for both radial and axial flux is given in Figure 5.32 and Figure 5.33. The correlation between the two is seen to be good.

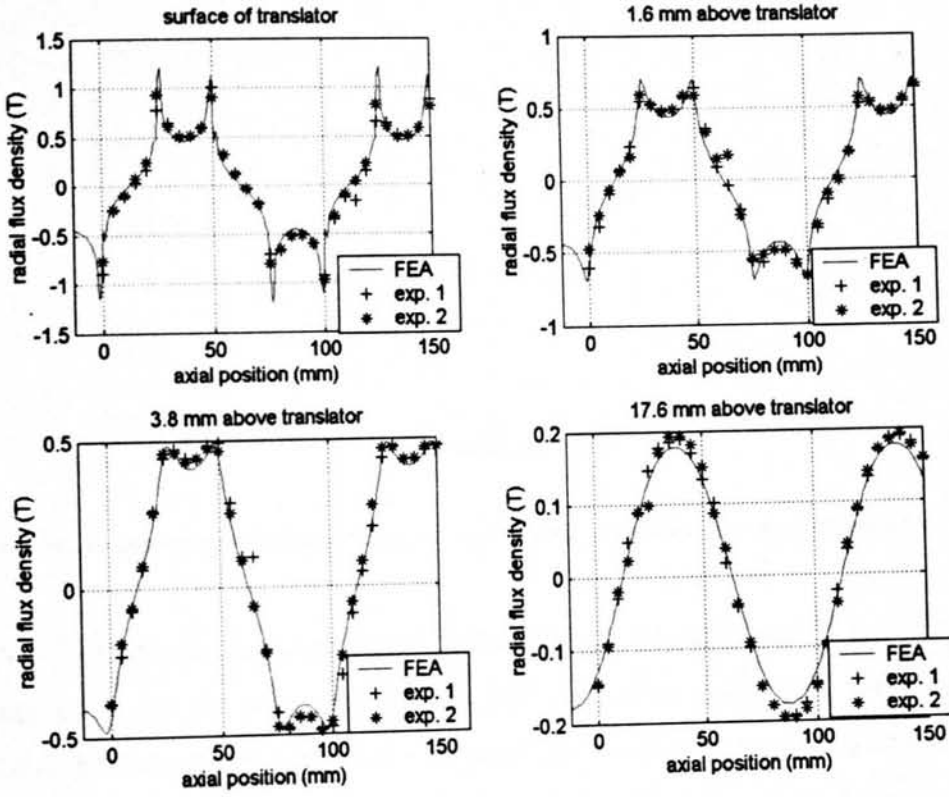


Figure 5.32: Comparison of actual and predicted radial flux density

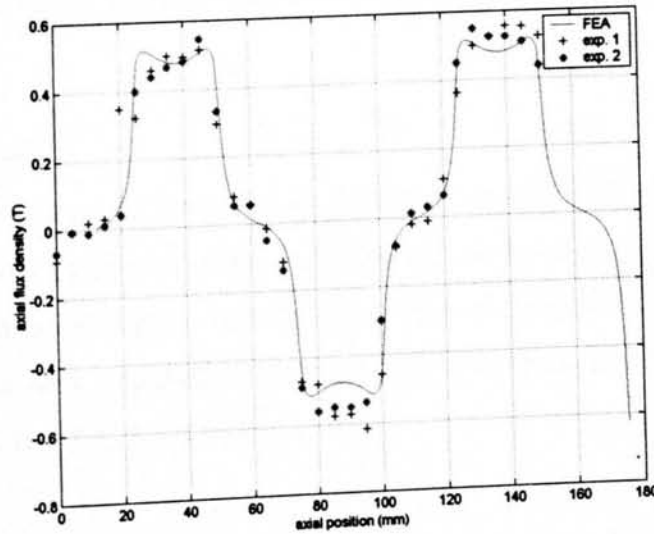


Figure 5.33: Comparison of measured and predicted axial flux

5.5.2.2 Inductance

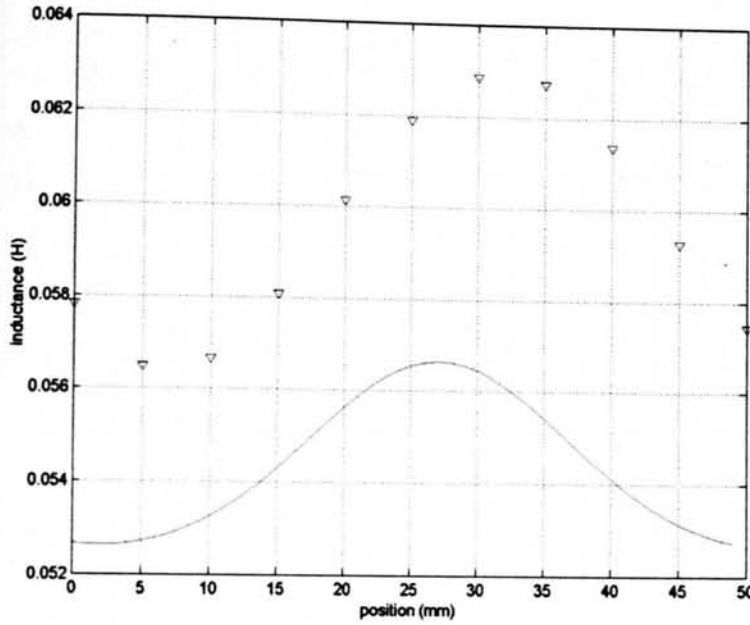


Figure 5.34: Comparison of experimental (▽) and FEA(-) predicted self inductance of an entire phase

Figure 5.34 shows a comparison of the phase inductance calculated in the FEA with that measured in the prototype using a laboratory inductance analyser. Ignoring the small phase difference between the two signals, due to the arbitrary definition of zero position in the laboratory, they have the same wave length but the values differ by 7% at the minima to 10% at the maxima. This difference is likely to be due to a combination of the non uniform nature of hand wound coils and a degree of uncertainty with the prototype airgap.

5.5.2.3 Open Circuit

The open circuit voltage for a single coil is shown in Figure 5.35, showing the model to give a 10 % under estimation of the experimental value. Also demonstrated is the inaccuracy of the constant angular velocity assumption of the model, accounting for the drift out of phase at peak amplitudes combined with the coincidence of the positions of zero linear velocity ($t = 2.5, 3.7, 4.9$ s).

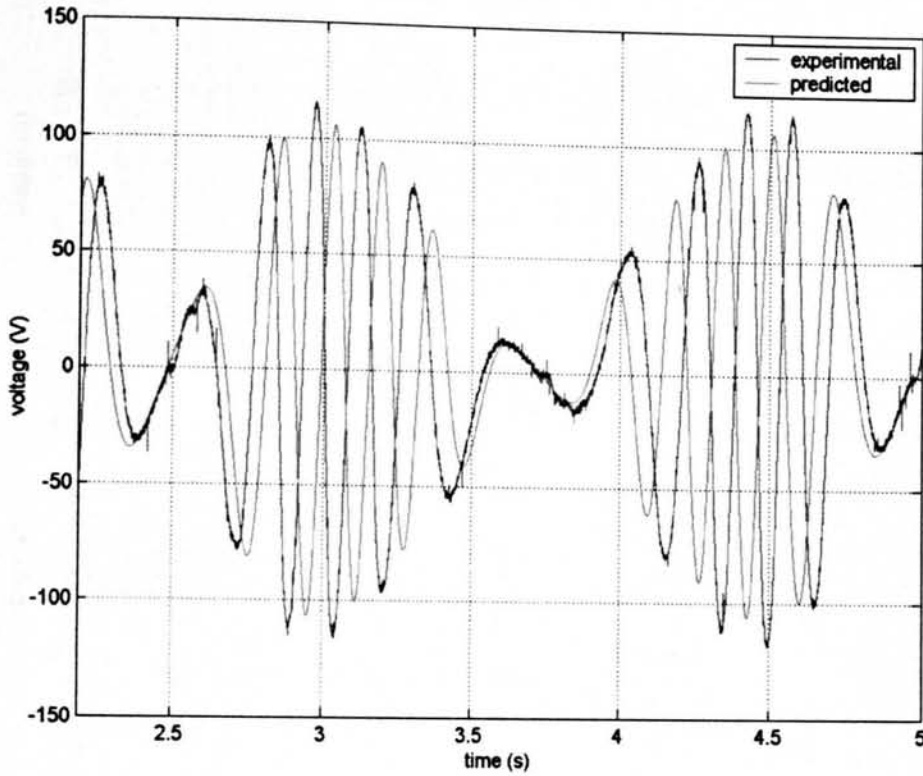


Figure 5.35: Open circuit results for a single phase

5.5.2.4 Resistive loading

In order to extract maximum power from an electrical machine it is necessary to make the external load resistance equal to the internal resistance. Because the inductance of this machine is comparatively low, this can be achieved by attaching a load equal to the coil resistance, just over 16 Ohms, to the phase terminals.

Figure 5.36 shows a comparison of the experimental and predicted voltages of all three phases when the machine is connected to three 17 Ohm resistors in a star configuration. The general correlation between the two plots is good, with the three phase shape being accurately predicted.

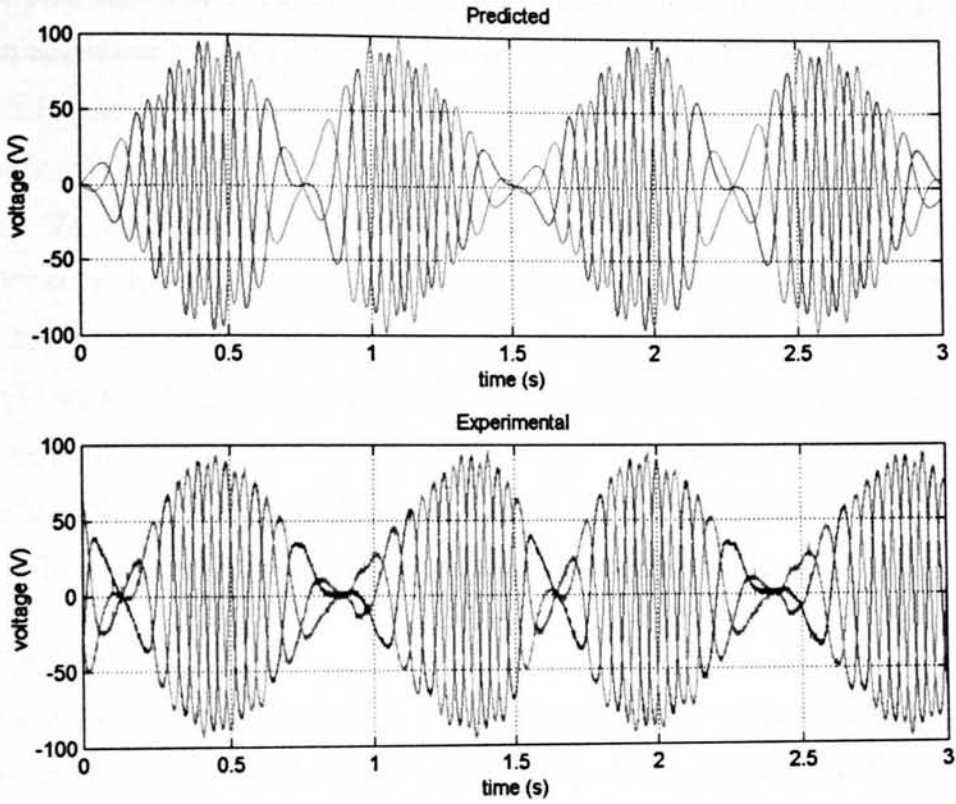


Figure 5.36: Comparison predicted and experimental voltages for a 17 Ohm load

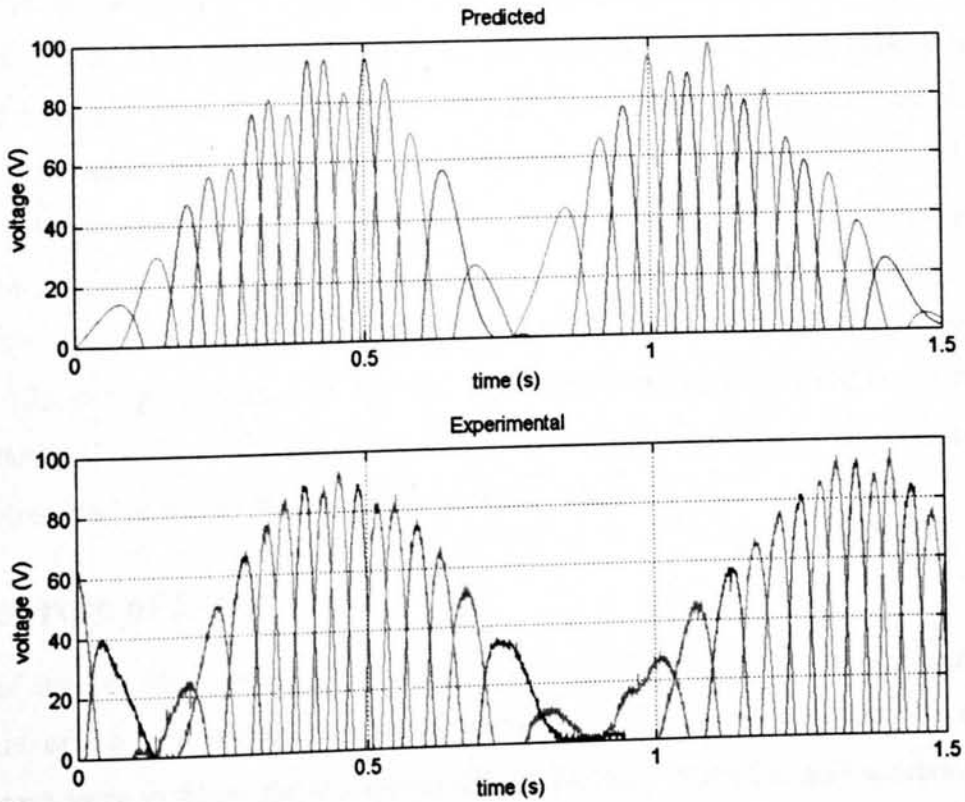


Figure 5.37: Varying voltage peaks

Figure 5.37 shows an enlarged section of the voltage waveforms and highlights the change in amplitude between the consecutive peaks of velocity. Consider the predicted waveform for the yellow phase (shown in \diamond). In the first cycle, between $t = 0$ and $t = 1.5$ s, the peak is only 80 Volts, yet in the second cycle, for t above 1.5, it reaches nearly 100 Volts. The blue and red phases, however, peak at around 95 Volts in the first cycle and 85 Volts in the second. Two effects are apparent: firstly all the phases alternate between higher and lower maximum values in consecutive cycles. Secondly the blue and red phases are closely related and have a larger maximum whilst the yellow phase has a lower peak. The effect is exaggerated in the predicted results, but also present in the experimental. It is a result of the unbalanced mutual inductances between the coils.

Comparison of the results gives an error on the prediction of $\pm 6\%$.

5.5.3 Concluding remarks

Details of the manufacture of one of the two planned stators to draw 3 kW at 0.5 m/s have been given. Some observations of handling large magnets were described and the testrig outlined. The flux density at and above the translator surface was shown to correlate well with that predicted using the FEA, whereas the phase inductance varied between 7-10% error.

For a translator speed of 0.5 ms^{-1} , section 5.1.7.2 predicted the emf for the prototype to be 100 Volts. For the same speed, the SIMULINK model, using FEA results, predicted an open circuit emf of 79 Volts. This 20 % error between the two predictions is quite reasonable considering the simplifications used. Similarly section 5.1.7.1 detailed a simple expression for the force developed per coil, equation (5.7), which gave a value of 250 N at 10 Amps. The FEA demonstrated that in the actual machine the peak value of force was dependant on the direction of current, with the two values of 216 and 173 giving an average of 194 N. The error in the simple model is therefore again around 20 %. The FEA simulation predicted the terminal voltage when connected to a resistive load to within 6% of the experimental value.

5.6 Sources of Error

One of the key observations when carrying out experimental work was the relative movement of the coils within their triplet groups. With a current flowing, the coils experience a force to follow the movement of the translator. With the rigid spacers only being present every third coil, there was some visible play in the coils, as they were compressed alternately against each spacer. In addition to this, a manufacturing defect

5.7 Real Time Response

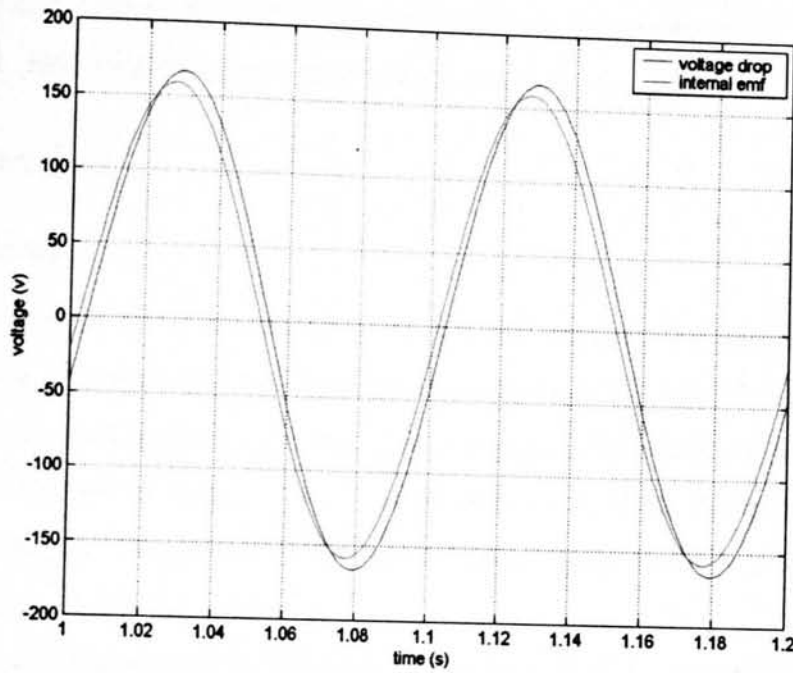


Figure 5.40: predicted internal emf and voltage drop at 1 m/s

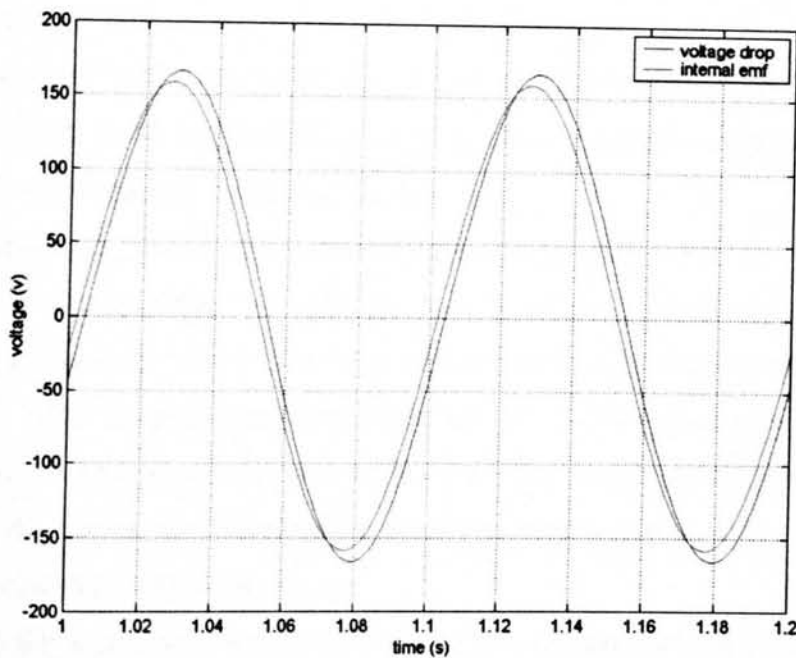


Figure 5.40 shows the single phase voltage results obtained from running the simulation at a constant velocity whilst connected to an external load of 16 Ohms. Illustrated is the total voltage dropped across the internal and external resistors plotted on the same axes as the theoretical internal emf used in the model. Comparison of the two traces allows the power factor of the tubular machine to be calculated in two ways.

Firstly, the phase difference between the two signals can be measured, the cosine of which will give the power factor, detailed in section 3.3.2.1. Secondly, relating the internal emf and voltage dropped across the machine's inductance to the power factor may be used. Both methods give a power factor of greater than 0.95.

5.8 Discussion

5.8.1 General

A 3kW prototype of the air-cored tubular machine based on the force reacted at 10 Amps has been presented. A two dimensional axisymmetric FEA model of the translator was created and used to predict the magnetic flux pattern above the translator and the behaviour of one set of coils. The nature of the manufactured prototype, however, required a separate FEA model of the entire 8 stator pole machine to calculate the unbalanced three phase set of inductances.

For the 8 pole prototype built, the maximum power taken out of a single phase was 540 Watts at a surface speed of 1 m/s, with a power factor of greater than 0.9. If both halves of the machine were manufactured, then all three phases would have produced a combined steady output power of 1.6 kW at this speed. An equal amount of energy would be dissipated by the unusually large internal resistance of the coils. The machine was designed for 3 kW using the simple magnetic circuit analysis, assuming no leakage at the magnet air border and no internal resistance.

At 10 Amps, each individual coil was capable of delivering a (calculated) maximum force of 216 N corresponding to a shear stress of 41 kN/m². The steady average three phase force per translator pole is 324 N, giving the average shear stress of the machine as 20 kN/m². The simplified analysis predicted the machine performance to within 20%, whereas the FEA simulation was within 6%. The simple model presented at the beginning of the chapter can therefore reasonably be used as a first stage tool to design tubular machines to an 80% accuracy.

As the tubular machine is scaled up, the internal resistance of the coils will likely decrease as the diameter of wire used increases. Furthermore, when designing larger scale machines, the quantity of magnetic material being used is likely to become an issue. To reduce the total material required the hole in the magnets could be enlarged, and the possibility of using radially magnetised or surface mounted PMs could be investigated.

5.8.2 Construction Issues

In retrospect it may prove more beneficial to mount the coils around a solid tubular surface, as this will provide an easy way of both supporting the coils at the base and manufacturing them to a consistent specification. The method used here was intended to leave the smallest possible gap between the inside diameter of the coil and the translator surface. The coils were wound around a removable bobbin which unfortunately resulted in a small variation in internal diameter between coils, depending on the tension in the coil etc. An airgap of 2.5 mm was strived for, yet as the coils settled the effective airgap was almost universally around 5 mm. The same airgap could have been achieved whilst using a 4 mm internal coil support, which would have ensured all the coils were uniform.

Furthermore, during the manufacture of the translator a plastic support was placed between every third coil to ensure that each single pole was exactly straddled by three coils. Unfortunately the uneven addition of the spacers had a significant impact on the mutual inductances between phases, resulting in an unbalanced three phase system. The advantage of mounting the spacers in this manner was a manufacturing and materials one. It is easier to mount one 6 mm sheet of Nylon than three individual 2 mm sheets. If there was an internal support for the coils, then the spacers would be supported on their internal and external circumferences, providing rigidity and allowing the utilisation of thinner material.

5.8.3 Radial Forces

The maximum radial force per coil was given in Section 5.4.1.2 as 190 N, which is the sum of forces around the entire circumference. The pressure exerted by the 155 mm outside diameter of the coil is therefore equivalent to 28 kNm^{-2} , at least two orders of magnitude below what a normal cylindrical vessel (e.g. a water pipe) might be expected to resist. Furthermore, these forces are much less than found in a normal electrical machine and less still than those present in the VHM. It is noteworthy that the radial forces are a maximum at the position where the tubular machine produces no axial force and hence does no useful work. When used as a generator, any current control strategy would likely have zero or little current flowing at this point, reducing the forces still further.

The resultant radial force on the translator will be zero as the system is symmetrical. In the event of a deviation from the central position a small net force will be reacted to it and so some form of lubrication is required. In this case the system is no longer

axisymmetric and so the calculation of flux paths and resultant forces becomes three dimensional, thus putting it outside the scope of the modelling presented here.

5.8.4 Use in Marine Energy Converters

The tubular machine, although having a low shear stress compared to the VHM, is suitable for direct drive marine energy converter power take off as its high power factor simplifies the electronics required for power conversion. Physically it requires very little structural support due to low radial forces and is ideally suited to the marine environment as a consequence of having the smooth cylindrical cross section preferred by conventional lubrication, protection and sealing methods.

5.9 Conclusion

This Chapter has investigated the behaviour of a prototype of the air-cored tubular machine and compared it to that predicted by FEA and a simplified magnetic circuit analysis. The peak shear stress of the machine was 41 kN/m^2 and the power factor was almost unity.

Chapter

6

Mechanical Integration

In the previous two Chapters the electrical aspects of linear generators have been investigated and models developed which are capable of predicting the behaviour of large machines. In this Chapter, the physical issues involved in integrating these machines into Marine Energy Converters (MECs) are explored. The aim of this Chapter is to help bridge the gap between laboratory 'dry run' prototypes and large-scale generators suitable for use in the marine environment. Some issues, such as corrosion, are equally applicable to both topologies of generator and dealt with together. The significant structural differences mean that much of this chapter is split into two sections: one for each generator investigated.

A detailed mechanical design is outside the scope of this thesis. The unique nature of using electrical generators in the marine environment, combined with linear generators being quite uncommon and design work being application specific, enforces the work presented here to be general and simplified. Emphasis has been on development of the topology of the electrical machines, with the mechanical design almost constituting a separate research programme. As such, some topics are basic observations, with other aspects covered in great detail. More work has been carried out on the VHM structure as the higher forces involved make it more critical to the topology performance as a whole.

6.1 General Considerations

Included in the design of electrical machine must be provision for survivability in large amplitude waves. In a hydraulic system this necessarily involves the use of an end stop device which will apply an extra force to the ram and prevent it from extending further than intended. With electrical power take off the same method can be utilised. However, in order to prevent possible damage to the MEC resulting from large forces applied by end stops, some forms of linear generator integration presented in this Chapter leave scope for alternative strategies. Unlike a hydraulic system, no permanent

damage will occur to a direct drive linear power take off system if it is subjected to oversized amplitude oscillation.

The generators need to be designed for long life in the marine environment. Based on the wave data used in Chapter 2, section 2.6.2 and reference [57], the actual surface of the sea can be expected to move in the region of 10×10^6 m or 10 000 km per year. Any design work should enable the device to operate over at least this distance uninterrupted, preferably many times greater.

6.2 Sealing

In order to operate a conventional dry electric machine in a marine environment where one part is moving relative to another necessarily requires the use of moving seals to protect the power conversion system from corrosion. A moving contact will wear over time and requires regular monitoring, maintenance or replacement. The dynamic performance of present day seal technology is limited. It was considered as one of the issues requiring further R&D highlighted in the Ove Arup report [3]. Consideration of this aspect is therefore vital to the integration of linear generators into the marine environment, particularly as it is an area which limits the speed and lifetime of hydraulic systems.

The alternative approach would be to avoid the use of a tight seal and allow some leakage into the generator, meaning the device would be run flooded. Any sealing mechanism would now only be required to prevent debris from entering and fouling the generator. Several issues must be considered in association with this idea. Having water in direct contact with the coils would provide improved cooling, allowing them to be run at a higher current and effectively increasing the shear stress of a given machine size. Equation (4.7) was used in Chapter 4 to describe the convection cooling of a VHM coil. The heat transfer coefficient for free convection can be expected to rise modestly when water replaces air as the cooling medium. With forced convection, however, the value can be several orders of magnitude greater when substituting water for air, e.g. [73]. Furthermore, a flooded machine can employ liquid lubrication, whereby pressurised sea water is used to maintain the required translator position without any direct contact between the moving surfaces. A maintenance free low friction method of lubrication with a theoretical infinite life is obtainable in this manner. Fluid bearings using oil have been used for many years in machine tools, where high precision and the ability to support large forces are required. The period of zero velocity necessary for reciprocating motion combined with the need for the bearing

surfaces to be parallel necessitates an external pressure source, i.e. a pump, for the use of fluid lubrication and hence hydrostatic, not hydrodynamic, lubrication must be considered.

6.3 Solid Bearings

6.3.1 Sliding Interface

The most basic type of bearing is a plain sliding bearing as it contains no extra moving parts, instead relying on solid to solid contact. Failure of this configuration of lubrication is non catastrophic, with a gradual wearing over time.

A sensible configuration would have one of the two surfaces, the part which is easier to replace, being made of a softer material and hence designed to wear faster. Using a set of soft replaceable pads mounted on the stator supporting the rotor, this system could be designed for annual replacement.

Oil impregnated self lubricating chemically inert plastics are available for dry applications. The wiping action cleans the shaft of soft particles, whilst harder particles become embedded in the liner, eliminating shaft damage.

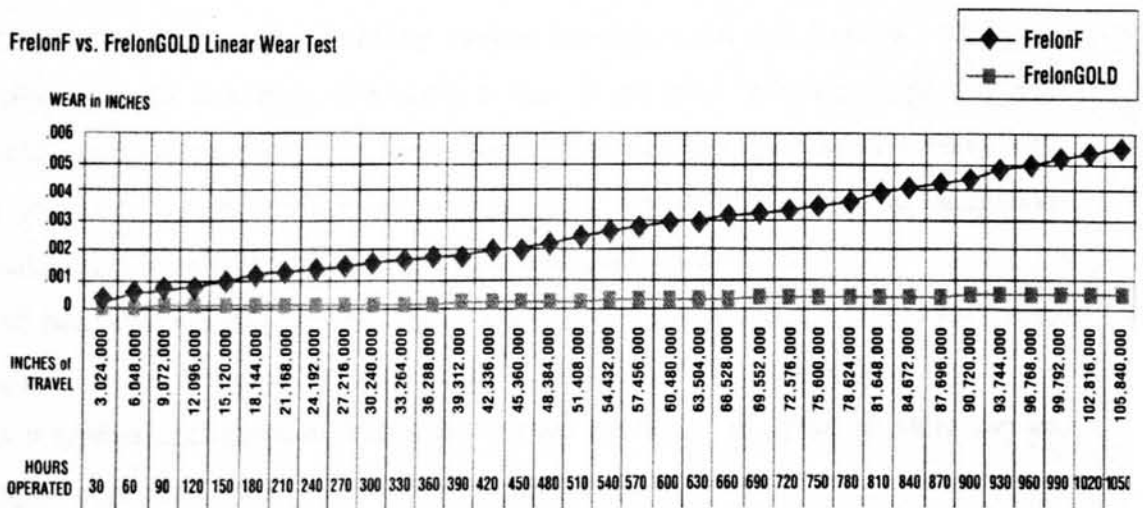


Figure 6.1: Manufacturers data on wear rate of solid contact bearings [83]

Figure 6.1 shows the results of a wear test on two commercially available solid contact bearings, carried out over 1050 hours (43 days) and a distance of 105 840 000 inches (2 600 km) [83]. The corresponding wear for the two materials is 0.0055 and 0.001 inches (0.14 and 0.025 mm). If the wear rate were linear then it could be assumed that it is possible to manufacture a bearing capable of travelling 10 000 km with a wear of just 0.1 mm.

Examining the least worn of the two, which is designed for use with hardened steel shafting and ceramic coated shafting, the maximum speed for intermittent load is given as 4.2 m/s, whereas the load capacity can be equal to a maximum pressure of 200 bar [83].

These chemically inert linings could clearly be suitable for use in this application, although some communication would be required with the manufacturer as to the effect of being permanently submerged in saline solution during their life time. They necessarily enforce regular maintenance of the device, but it appears to be possible to limit this to annually.

6.3.2 Rolling Contact

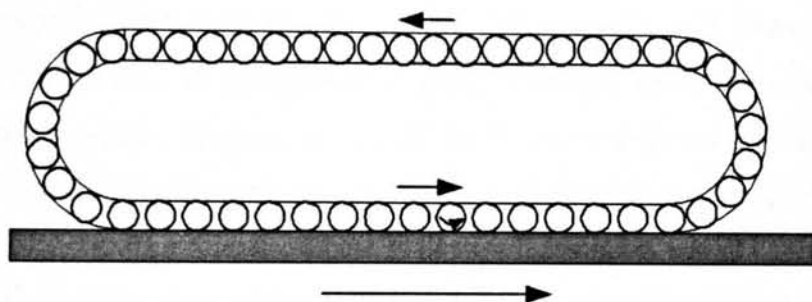


Figure 6.2 Roller bearing with return path

The most common sort of bearing used in industry is the ball bearing. They are typically mounted in a track concentric to that of the shaft they are supporting and follow the same rotary path. In a linear machine this would require either a return path to be provided, shown in Figure 6.2, or seriously reduce the amplitude of oscillation allowed, which is unlikely to be acceptable in this application.

Stud bearings, whereby a set of roller bearings is used to make a wheel and track type arrangement, are used widely in industry for heavy duty applications. Figure 6.3 shows a typical configuration with a flat contact surface. 'V' shape surfaces can be used up to a speed of 5 ms^{-1} if axial forces are present [84].

Track rollers can, theoretically, be designed for a life of 10^6 km if they are well lubricated and the load factor is kept very low, i.e. the expected load on each bearing is less than 10% of its rated maximum [84]. Totally unlubricated bearings, however will have a life time of the order of 10^4 km.

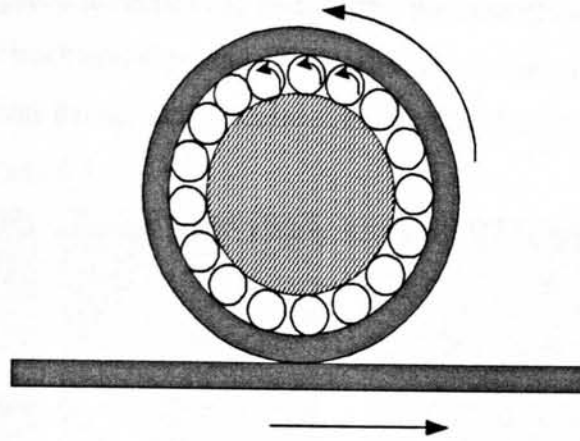


Figure 6.3: Stud bearing

A well designed track bearing can take the loads speeds and annual distances associated with this type of application if proper provision for lubrication is made. Rolling contact bearings, however, can suffer from catastrophic instant failure. It is customary to rate rolling elements in terms of total distance and average (L-50) and minimum (L-10) life. The former of these is the life that can be expected from 50% of the bearings whereas the latter is the minimum life expected from 90% of samples. The implication is that 10 % will not reach minimum life expectancy and could theoretically fail well anytime after installation.

6.4 Corrosion

Corrosion for the generator, as with the entire device, is an acute problem for marine energy converters. Each part of a device will either be constantly submerged, above sea level, or periodically submerged, the latter of which will suffer the most.

There is great opportunity for technology transfer from the oil and gas industries, both of which have experience in the manufacture of long lasting offshore structures. Selection of materials that have well understood behaviour in the offshore environment, for example steel and concrete, will simplify protection strategies. However, the two generators considered here contain two slightly more exotic materials: copper and Nd-Fe-B. The machine may hence be considered either as a whole, or with an alternative strategy for each component.

When two different metals are in electrical contact, the less noble of the two corrodes more than if they were isolated. This paves the way for attaching sacrificial components, anodes, to the outer surface of the generator, which would have to be periodically replenished but provide constant protection to the entire device.

The rare earth magnetic material is likely to suffer the most from corrosion due to its strongly negative electrochemical potential. The standard coating for Nd-Fe-B magnets is zinc based, which was thought to be suitable. Fundamental tests conducted prove this not to be the case, Figure 6.4.

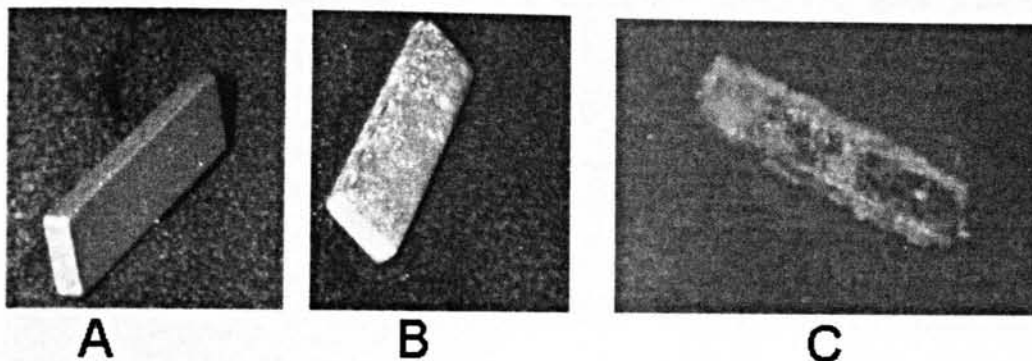


Figure 6.4: Standard coating for magnets (A) new, (B) after 6 weeks and (C) 2 years submersion in seawater.

The supply industry claims to offer suitable corrosion protection in the form of electro-painting, whereby a $15\mu\text{m}$ layer is applied to the material, giving it salt solution resistance up to 130°C [85], Figure 6.5B(i). Alternatively a $5\mu\text{m}$ aluminium yellow chromate coating may be applied, Figure 6.5A(i). Again fundamental tests demonstrated these coatings to be unsuitable, Figure 6.5A&B(ii).

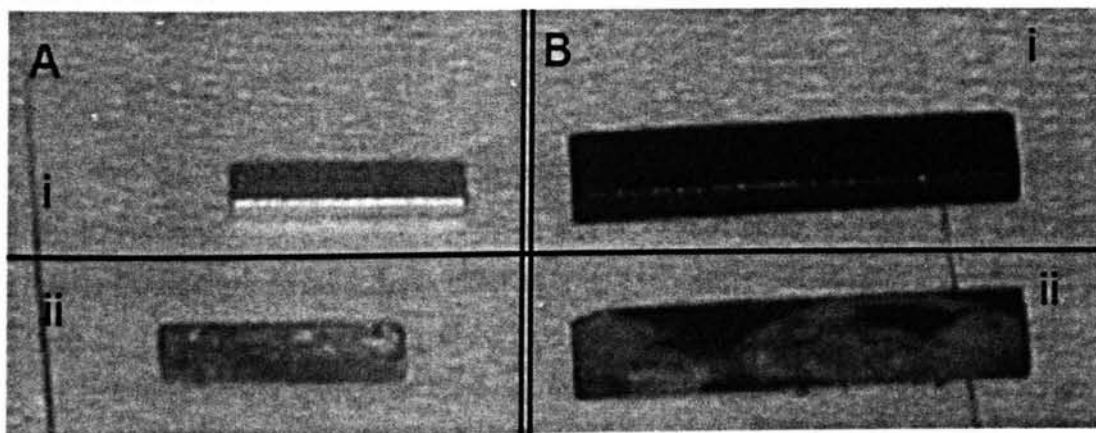


Figure 6.5: Alternative coatings for magnets, (i) as new, (ii) after 2 years submerged in seawater

Ceramic coatings are used by the hydraulics industry and have a proven reputation in the marine environment. For example, a $300\mu\text{m}$ layer of the commercial material Ceramax [86] would effectively seal the device from the surrounding environment. This material, on the market for over 10 years as a coating for offshore cylinder rods [87], is very hard (1000 Vickers) thus durable and abrasion proof. It is a non conducting inert material and at this thickness could be used to coat even the small airgap of the electrical machine. Unfortunately, there are concerns about its application to non-smooth surfaces [88] questioning its suitability for use on the VHM translator.

For the coils, insulation breakdown in a flooded environment is clearly a problem and may need separate investigation.

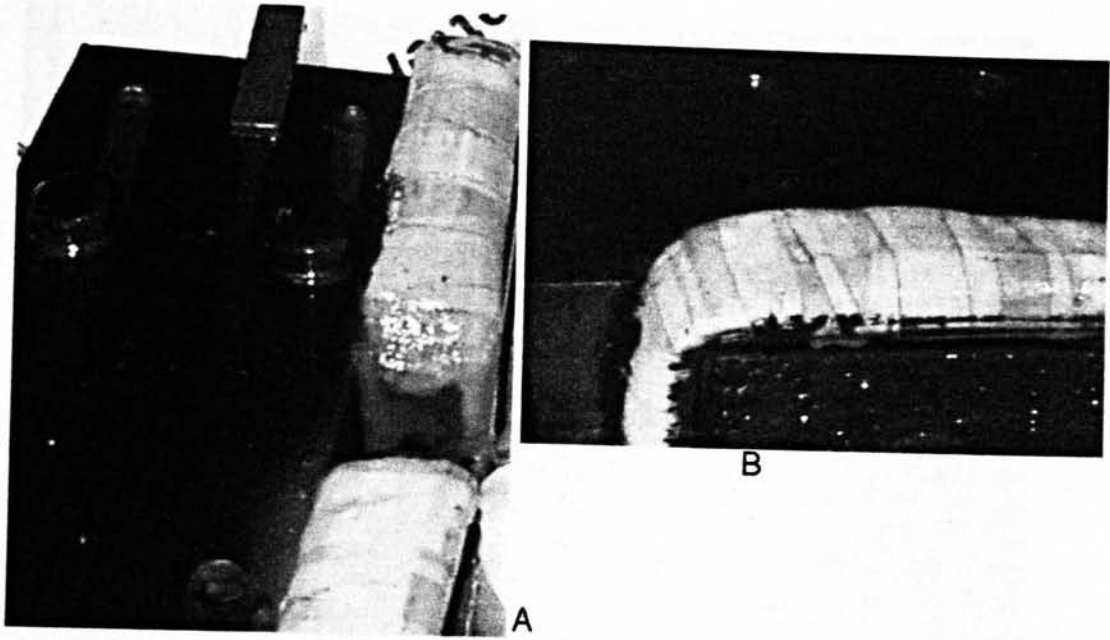


Figure 6.6: Coal Tar epoxy 6 weeks after submersion

Coal tar epoxy is used throughout the marine industry to protect large steel structures, such as docking gates. A small VHM stator coil was coated and submerged in seawater to investigate its behaviour for this application.

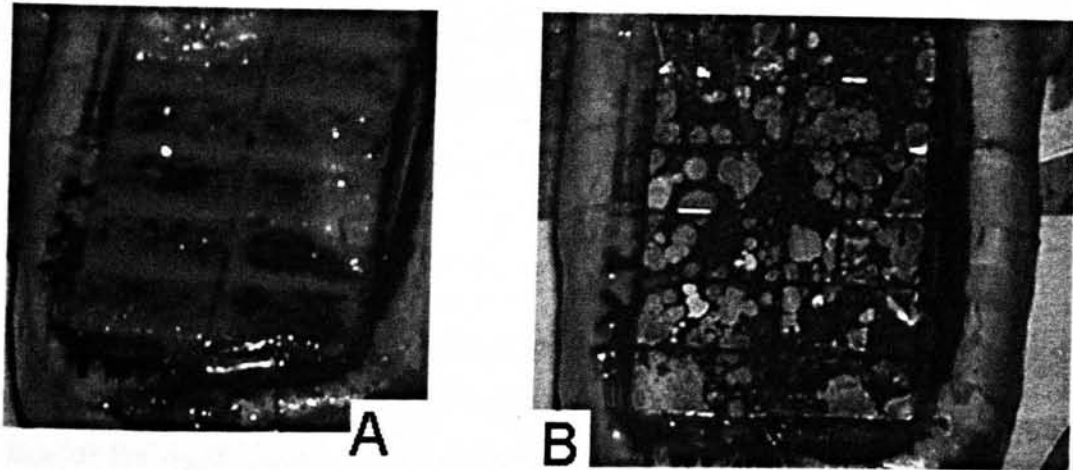


Figure 6.7: Coal Tar epoxy coating of magnets after 2 years submersion

Figure 6.6 shows sections of the stator shortly after it was submerged. The coils and surrounding cloth-tape were not covered as the tar does not adhere to a non-rigid surface. In Figure 6.6A, brown deposits can be seen covering the outside of the tar layer. This is likely to be deposits from the unprotected coils and magnet shown at the top of the picture. A close up of the magnet region in Figure 6.6B, however, shows significant corrosion. After two years submersion the corrosion in this area predictably deteriorated, Figure 6.7A, and the coating could be removed from the magnets with soft

abrasion Figure 6.7B. Furthermore, after this period most parts of the stator suffered slight corrosion Figure 6.8.

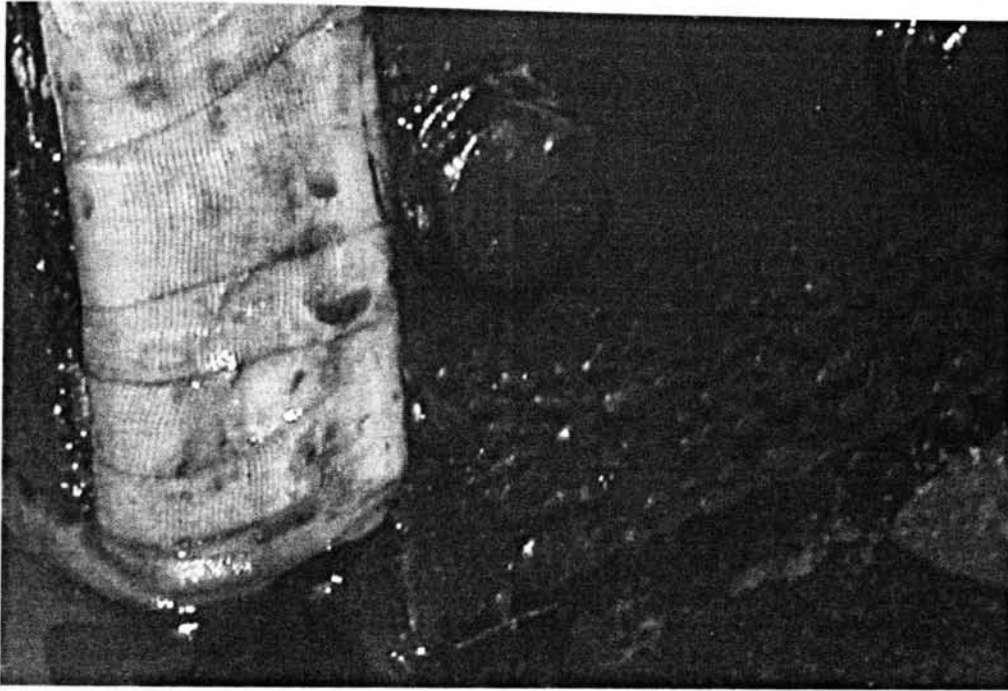


Figure 6.8: Coal tar epoxy coating of steel section after 2 years submersion

From these brief experiments of general observation, it is concluded that there is scope for more research into corrosion protection for all aspects of the generator design. Suggested coatings appear to be ineffective, whereas application of ceramic coatings is said to be troublesome. The issue is unresolved.

6.5 VHM

6.5.1 Introduction

For the VHM a non standard structure is required, capable of reacting against the high magnetic forces which, although varying with position, are always attractive.

Due to the rapid change of flux within the VHM, the main body of both the stator and the translator must be made of laminated steel, in order to minimise the formation of eddy currents. The support structure must compensate for the resulting weakness, particularly as the machine is likely to be quite large in a direction perpendicular to the plane of the laminations.

Figure 6.9 shows the VHM viewed along the axis of motion, so the translator moves in and out of the plain of the paper, with the simplified magnetic and structural forces included. In Figure 6.9A the translator is in the correct position: exactly in the middle of the two stator halves. The forces on the translator are equal and opposite, thus cancelling out, whereas the support structure still has to react against the closing force

of the airgap. In Figure 6.9B, the translator has moved slightly upwards, giving a smaller airgap and hence bigger attraction to the upper stator compared to that of the lower half. The net force difference must be provided by the translator support, shown here as a set of bearings, in order to prevent the airgap closing.

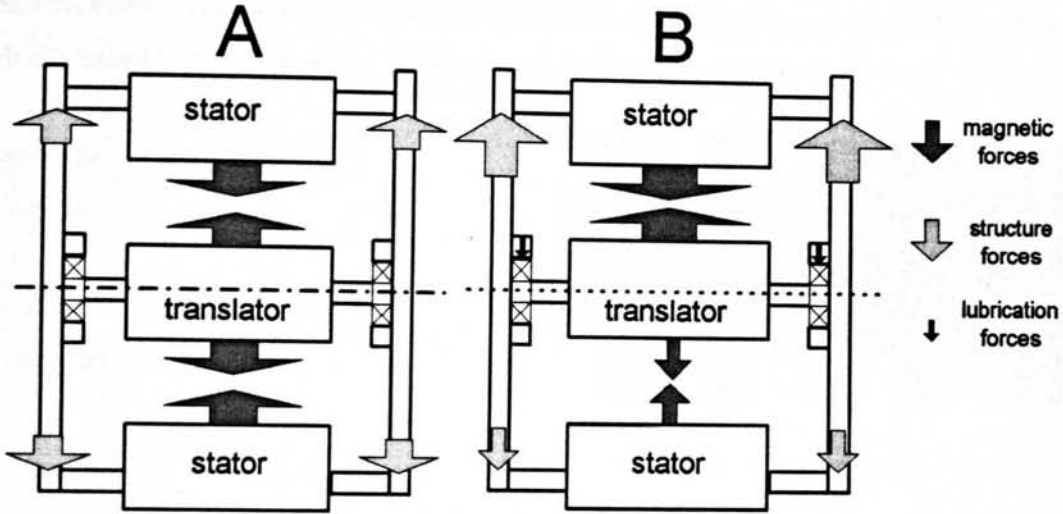


Figure 6.9: Forces on VHM. (A), with translator in centre & (B). with uneven airgap

6.5.2 Sealing

The sealing of the VHM translator is troublesome because of its toothed cross section. In order to use a conventional contact seal it is necessary to have a uniform cross section, which could be achieved by encasing the translator in a magnetically inert material as shown in Figure 6.10. The rotor slots would be filled to the same height as the teeth thus providing a flat surface for the seal to contact against, without influencing the overall magnetic properties.

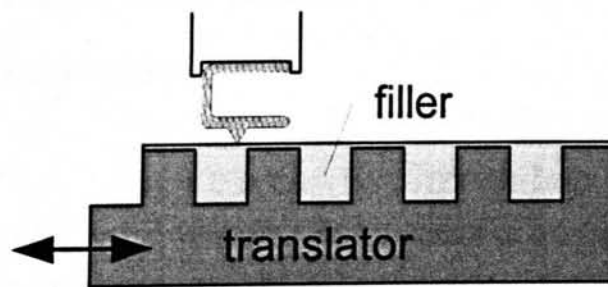


Figure 6.10: Filling the translator slots

As drawn, the translator has a rectangular cross section with sharp edges, still representing problems in terms of sealing. It may be possible to avoid this by giving the outer surface of the fill material a smooth profile. A ceramic material would have the correct magnetic properties whilst being sufficiently hard and smooth to be used as a sealing surface. In this configuration, there is scope for flexibility with the endstops as

large amplitude oscillation will break the seal of the stator case, but should not permanently damage the machine itself.

To avoid the use of a filler material, and utilise traditional cylindrical seals like those used in a hydraulic ram, it is necessary to transfer the motion of the translator to a cylindrical shaft. The electrical machine would need mounting in an oversized chamber which extended to the extremities of the motion, as shown in Figure 6.11.

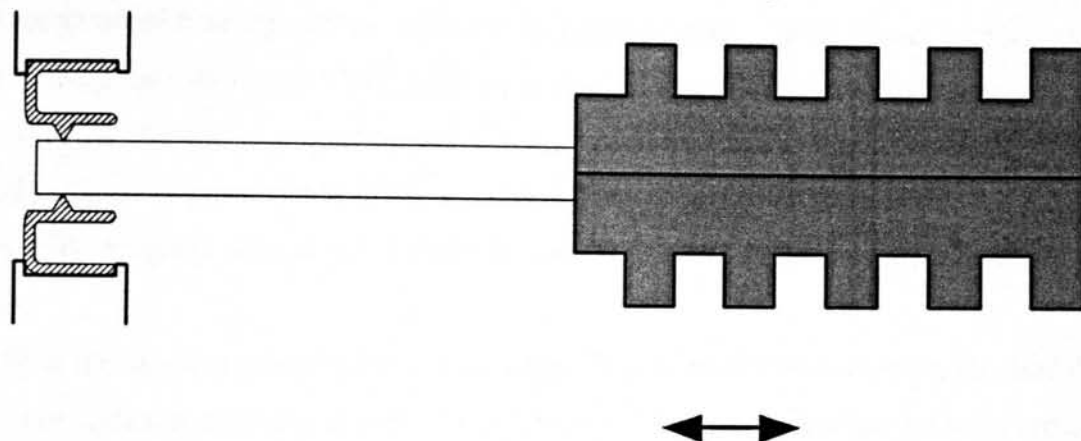


Figure 6.11: Cylindrical sealing for the VHM

An inherent feature of this design is the need for stringent endstops, as allowing the translator to extend too far would likely cause catastrophic damage to the outer case. Furthermore, the size of the entire stator must now be equal to that of the active area plus the maximum permissible amplitude. One possibility is that the entire air filled chamber incorporating the stator could be used to house the power electronic equipment necessary for VHM machines. Alternatively it could just be used for buoyancy and help offset the likely weight penalty of using direct drive.

6.5.3 Hydrostatic Lubrication

6.5.3.1 Introduction

Load relationships of a two dimensional hydrostatic bearing are given in (6.1), showing its dependence on viscosity and land clearance.

$$W \propto \frac{\mu Q}{H^3}; H_p \propto \frac{\mu Q^2}{H^3} \quad (6.1)$$

Where	W	=	load capacity of bearing
	μ	=	viscosity (kg/m/s)
	Q	=	flow rate (m ³ /s)
	H	=	clearance (m)

The use of sea water as the working fluid, with a viscosity much lower than that of normal lubricating oils, results in either the need for smaller land clearances or higher flow rates to achieve these high forces. It is hence necessary to develop expressions for the load capacity of the bearings, furthermore, the use of 3 dimensional analysis is required. This section details the logical process of hydrostatic bearing selection and explains simplifications and assumptions used as the basis for the final results. Although some bearings can be optimised for a general case, it is illuminating to design the bearing for a particular VHM, allowing numerical examples to compare topologies.

A VHM capable of producing 100 kW at a speed of 1 m/s is used, consisting of 3 single phase modules. Each of the 4 poles making up a module would have 12 X 12 mm wide magnets with an axial depth of 1m. One set of poles was modelled using FEA.

With the maximum rated current of 15 Amps flowing in the 240 turn coils, the model was run with the translator at various levels between the two fixed stator poles in order to calculate the resultant forces acting on it. The maximum axial force reacted was 18 kN for one pair of pole faces, implying 36 kN per module and a total of 108 kN for the 3 phases. The corresponding gap closure force between the translator and one side of the stator was 36 kN per face at the design airgap of 1mm, rising to 54 kN if the translator was allowed to deviate to within 0.05 mm of the translator.

When the translator sits in the mid point of the two stators there is no net force on it and hence no criteria with which to design a lubrication system. A small deviation from the midpoint, however, results in a large net force. The magnetic stiffness may hence be used. If the bearing system has a higher stiffness than the magnetic system, the implication is that for a given deviation from the midpoint of the airgap, the bearing forces will dominate and the translator will be centred. The stiffness at either side of the design clearance was calculated to be almost 25 MN/m, resulting in a 5kN force imbalance with a 0.2 mm deviation from the design clearance.

6.5.3.2 Flow assumptions

Much of the work in this section is based on laminar flow and hence relies on the Reynolds' number, Re , as given by (6.2), being sufficiently low, typically taken as less

$$\text{than 2000 [89]. } R_e = \frac{\rho}{\mu} \bar{v}H \quad (6.2)$$

Where ρ = density (kg/m^3)
 \bar{v} = average velocity (m/s)

Assuming the flow and dimensions of Figure 6.12, where the fluid flow lines are parallel and there is no leakage through the corners, the velocity of a fluid can be calculated for a particular square bearing and substituted into the Reynolds' equation, giving (6.3).

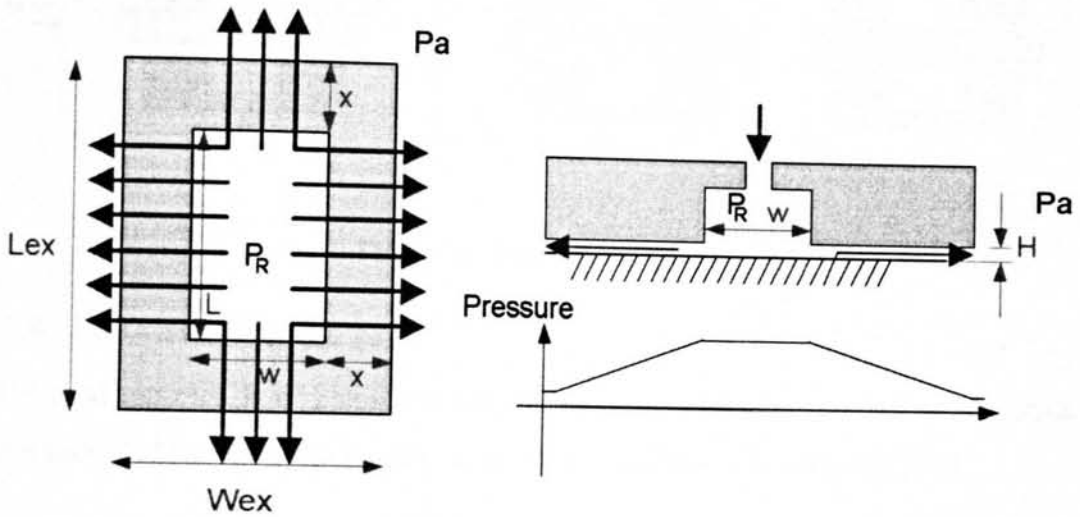


Figure 6.12: View from below bearing, showing assumed flow of fluid and dimensions

$$R_e = \frac{Q\rho}{2(w+L)\mu} \quad (6.3)$$

Where

w	=	recess width (m)
L	=	recess length (m)
x	=	land width (m)

6.5.3.3 Regulation

For a hydrostatic pad to work, there needs to be some sort of control over the fluid flow through it. If the bearing deviates from its design clearance, for example if the gap reduced, the pressure within the bearing recess needs to be increased in order to apply a greater force to the bearing and attempt to recover the design clearance. Figure 6.13 shows three possible configurations to achieve this of increasing mechanical complexity and effectiveness. In each one, the position of the translator is deduced from the recess pressure, which varies with bearing clearance.

In Figure 6.13A the pads are fed from a constant supply source through a fixed restrictor, typically a capillary or an orifice. The pressure drop across the restrictor allows for a variation in bearing recess pressure to compensate for deviation from the design condition. In Figure 6.13B the restrictors are variable, for example constant flow valves, which gives improved stiffness to the bearings. The ultimate system is given in Figure 6.13C, where each recess is fed from a separate constant flow pump, which,

assuming incompressible fluid, guarantees a fixed land width. Clearly the increasing effectiveness comes at the cost of increasing mechanical complexity.

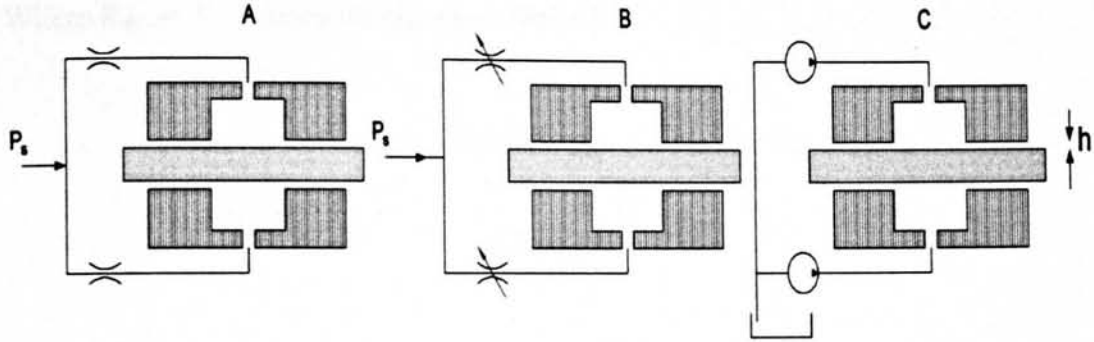


Figure 6.13: Flow control options

6.5.3.4 Stiffness of opposed pads

The load capacity, F , of a single rectangular pad hydrostatic bearing is a combination of that provided by the recess chamber and the bearing land. It is given by (6.4).

$$F = P_R wL + (w + L)x \frac{P_R}{2} 2 = P_R (wL + wx + Lx) \tag{6.4}$$

Where P_R = recess pressure (Pa)

Assuming laminar flow, the pressure drop across a flow between two parallel plates, of length L_{pp} , may be expressed by (6.5).

$$P_1 - P_2 = \left(\frac{12\mu x}{H^3 L_{pp}} \right) Q \tag{6.5}$$

Where P_1 & P_2 = pressures (Pa)

$$P_1 > P_2$$

If the exit pressure, P_2 , is the surrounding pressure, and P_1 is given as the relative pressure in the recess, from here on defined simply as P_R , then the hydraulic resistance, R_b , of the rectangular pad may be defined by (6.6).

$$R_b = \frac{P_R}{Q} = \frac{6\mu x}{(w + L)H^3} \tag{6.6}$$

Again, this is based on the assumption that the flow is as shown in Figure 6.12 and the corners are hence ignored.

Considering Figure 6.14, the diagram of an equivalent circuit comprising of a single pad bearing and a restrictor, the recess pressure, P_R , can be expressed as a function of the two hydraulic resistances and P_S , the supply pressure.(6.7)

$$P_R = P_S \frac{R_b}{R_b + R_R} \quad (6.7)$$

Where R_R = restrictor resistance (Pa/m^3)

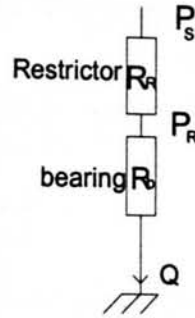


Figure 6.14: Equivalent circuit for a single pad

For maximum stiffness of a bearing operating at the intended clearance, P_R should equal half P_S . This is analogous to the maximum power transfer theory in electrical engineering, which states that internal and external resistances should be equal for maximum power transfer.

The resistance of the bearing, R_b , must therefore be equal to the restrictor resistance R_R at the design clearance. Defining this value at the reference pressure, R_{b0} , allows the value of the bearing resistance to be expressed non dimensionally, (6.8):

$$R'_b = \frac{R_b}{R_{b0}} \quad (6.8)$$

Equation (6.7) may now be expressed as below, (6.9).

$$P_R = P_S \frac{R'_b}{R'_b + 1} \quad (6.9)$$

Consider now the set of opposed pads shown in Figure 6.15, in which the translator has been offset by h .

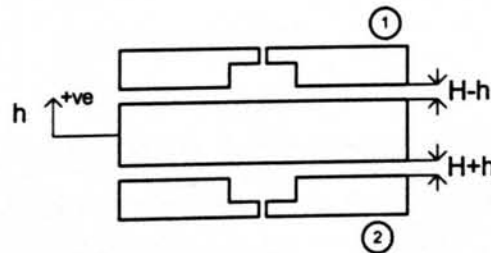


Figure 6.15: Opposed pads given a small displacement, h , from the design clearance, H

The reference resistance of the system is now given by (6.10).

$$R_{b0} = \frac{6\mu x}{(w+L)H^3} \quad (6.10)$$

The absolute hydraulic resistance of pad 1, and its non dimensional equivalent are given in(6.11) and (6.12) respectively. Similar relationships exist for pad 2.

$$R_{b1} = \frac{6\mu x}{(w+L)(H-h)^3} \quad (6.11)$$

$$R'_{b1} = \frac{H^3}{(H-h)^3} \quad (6.12)$$

Combining equations (6.4) to (6.12) and considering the resultant force on the pair of opposed pads when given the small displacement h shown in Figure 6.15 gives the net downward force as:

$$F_{net} = P_s(wL + wx + Lx) \left\{ \frac{H^3}{H^3 + (H-h)^3} - \frac{H^3}{H^3 + (H+h)^3} \right\} \quad (6.13)$$

Remembering that the stiffness is defined as the derivative of force with respect to displacement, and setting h to zero, allows the stiffness of the opposed bearings at the design clearance to be expressed, (6.14).

$$k_0 = \frac{3}{2} P_s (wL + wx + Lx) \frac{1}{H} \quad (6.14)$$

Where k_0 = stiffness of opposed pads at design clearance (N/m)

6.5.3.5 Pumping Power of Opposed Pads

The power required to pump fluid around a hydraulic circuit may be expressed as (6.15).

$$H_p = \frac{P^2}{R_{tot}} \quad (6.15)$$

Where H_p = pumping power (W)
 R_{tot} = total resistance of hydraulic circuit

At the design clearance the total power for the opposed pad bearing system, represented by the hydraulic circuit shown in Figure 6.16, can be expressed as (6.16), incorporating four resistances defined by (6.10).

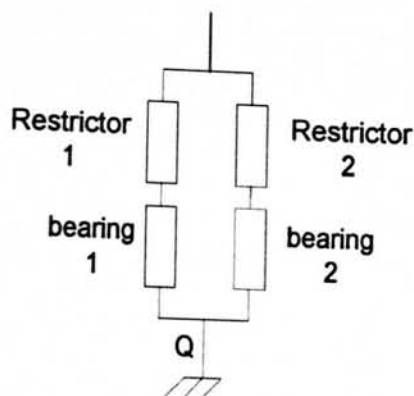


Figure 6.16: Equivalent circuit for opposed pad bearings

$$H_p = \frac{P_s^2 (w+L) H^3}{6\mu x} \quad (6.16)$$

Using a combination of (6.14) to (6.16), it is possible to express the pumping power required for a given set of opposed pads solely as a function of its dimensions and the required stiffness.

$$H_p = \frac{2}{27} \frac{k_0^2 H^5 (w+L)}{\mu x (wL + wx + Lx)^2} \quad (6.17)$$

6.5.3.6 Optimisation for stiffness

The size of the pads is made dimensionless by using the substitutions given in (6.18), thus allowing the power to be expressed in a dimensionless manner, (6.19).

$$L' = \frac{L}{w}; x' = \frac{x}{w}; H'_p = \frac{H_p}{H_{p0}} \quad (6.18)$$

$$H'_p = \frac{9}{2} \times \frac{(1+L')}{L'^2 + x'^2 + L'^2 x'^2 + 2L'x' + 2L'^2 x' + 2L'x'^2} \quad (6.19)$$

Where H_{p0} is the reference power, defined as that dissipated when L' and x' are equal to unity.

The graph of Figure 6.17 uses (6.19) and shows the relative pumping power required by bearings of different aspect ratios to achieve any equal stiffness. The width, w , of the bearing recess is the dimension which dictates the size of bearing.

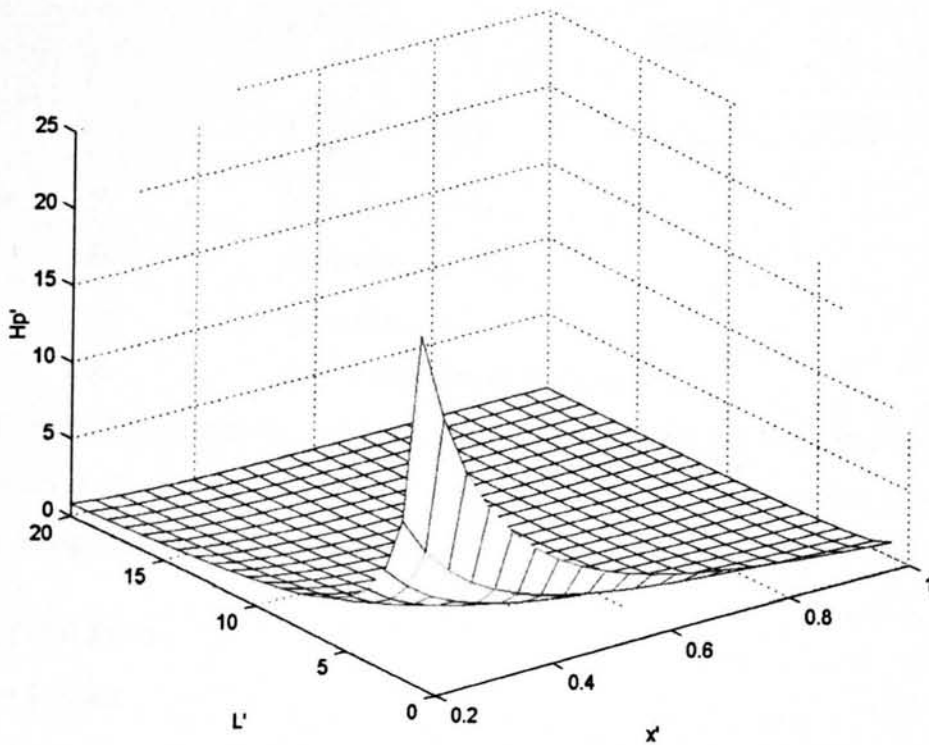


Figure 6.17: Dimensionless graph of relative pumping power versus relative pad size for any given stiffness

The total clearance, H , is assumed constant and is hence not a variable. From this it is clearly desirable to make L' , the ratio of length to width of the bearing recess, and x' , the ratio of land width to recess width, as large as possible in order to reduce power consumption. Physically this means that an increase in either the recess length or the land width reduces the pumping power required to obtain a specific stiffness. This simplified analysis hence implies that larger bearings are more desirable.

6.5.3.7 Friction Power

The frictional force of the bearing, i.e. the force required by the moving member to overcome the internal shear forces of the lubricant, acts in three distinct areas. These correspond to the two pairs of bearing lands, perpendicular and parallel to the plain of motion, and the bearing recess.

It is customary to ignore the power dissipated by shearing in the recess part of the pads when operated at low speeds. The friction force is hence approximated to that occurring over the bearing lands only, as given by (6.20).

$$\begin{aligned}
 H_f &= F_f \times v \\
 &= \frac{\mu v A}{H} \times v \\
 &= \frac{\mu v^2}{H} (L + w) 2x
 \end{aligned} \tag{6.20}$$

Where	F_f	=	friction force (N)
	H_f	=	friction power (W)
	v	=	velocity (m/s)
	A	=	area of two parallel surfaces (m^2)

Equation (6.20), contrary to that found in the stiffness section, 6.5.3.6, implies that a bearing with a short length, short land width and large value of clearance is a more desirable design for low power dissipation.

6.5.3.8 Total Power

Minimum Power

As a result of the two conflicting conditions outlined in the preceding sections, it is necessary to consider the total power dissipated by a given bearing. As the frictional power is dependent on the velocity of the bearing, whereas the pumping power is not, in order to allow a dimensionless comparison it is necessary to put some actual values into both equations. The values used are given in Table 6-1, where the stiffness is half that of the VHM because there will be one bearing on each side of the translator.

Table 6-1: Values used for total power comparison

Velocity	v	0.5 m/s
Dynamic viscosity	μ	0.0015 kg/ms
Stiffness at equilibrium position	k_0	12.5×10^6 N/m

Using these values, it is still possible to obtain the dimensionless value of total power, by dividing the calculated value of actual power by H_{t0} , the power dissipated when L' and H' are equal to unity. The actual and dimensionless total power are given in (6.21) and (6.22) respectively, with definitions given in (6.23).

$$H_t = \frac{0.75 \times 10^{-3} \times (L + x)x^2 (wL + wx + Lx)^2 + 7.72 \times 10^{15} \times H^6 (w + L)}{Hx(wL + wx + Lx)^2} \tag{6.21}$$

$$H_t' = \frac{0.75 \times 10^{-3} \times (L' + w')(w'L' + w' + L')^2 + [7.72 \times 10^{15} \times H'^6 (w' + L')]}{1.71 \times 10^{15} \times H'(w'L' + w' + L')^2} \tag{6.22}$$

$$H' = \frac{H}{x}; L' = \frac{L}{x}; w' = \frac{w}{x}; A = \frac{w}{L} \quad (6.23)$$

Inspection of the order of magnitude of the two parts of the numerator of equation (6.22) can be used to describe the behaviour of the bearing. The left hand term, which corresponds to the friction power, will be negligible unless either the clearance H' is very small, or L' is very large. At all other values, the right hand term, corresponding to the pumping power, will dominate.

The power dissipated by friction is therefore ignored in further analysis as it has been demonstrated to be negligible when compared with pumping power at realistic bearing dimensions.

6.5.3.9 Opposed Pads for 100 kW device

Ignoring the friction losses in the bearing allows the conclusions of the stiffness section, 6.5.3.6, to again be employed. It was stated there that the bearing should be large. The size of the bearings will be limited by the electrical machine design, in which case it is necessary to consider specific examples. In keeping with the concept of a modular VHM, i.e. one where the machine is essentially made up of independent phases the number of which dictates the overall power of the machine, the bearings may be designed such that there will be one pair of opposed pads for each pole. It will be assumed that one pad will run along the entire length of a stator pole.

Using the VHM outlined in 6.5.3.1 above, the total length of the bearing, consisting of recess and perpendicular lands, can therefore be up to 0.144 m. The total width of the bearing has no real constraint, and so is arbitrarily confined to 10% of that of the translator, i.e. 0.1 m, giving (6.24).

$$x = \frac{0.1 - w}{2} \quad (6.24)$$

$$L = 0.144 - 2x = 0.044 + w$$

The pumping power for these bearings, calculated using (6.17), is given in Figure 6.18. The values shown must be multiplied by 12 for the entire 100 kW machine, as the machine comprises of three modules, with two pole pairs per module and a bearing on each side of the stator.

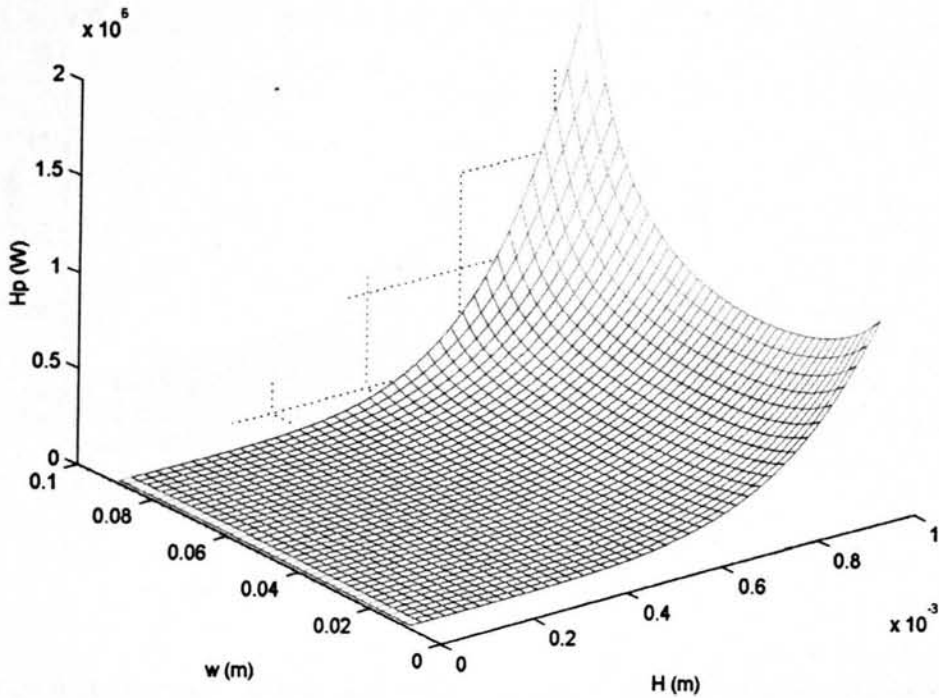


Figure 6.18: Pumping power for bearings designed for 100kW machine

At any design clearance, H , there is a value of width, w , which gives a minimum pumping power. This value of w is constant irrespective of the value of H and equal to 0.0427 m. The pumping power becomes very large as the land width and recess width become very large, tending towards 2 MW, clearly unsuitable for use as the lubrication system for a 100 kW generator. The limit of the validity of these equations must be remembered, which assumes laminar flow. Figure 6.19 shows the Reynolds' number, from (6.3), plotted against its accepted limit for laminar flow, 2000.

At any point above the 2000 mark, the flow must be assumed to be turbulent and the equations governing its flow become invalid. In order to maintain laminar flow it is necessary to limit the value of design clearance, H , for a given value of recess width, w . The equation of the upper limit is given in (6.25), derived by equating the Reynolds' number, (6.3), to the flow through one bearing and restrictor (obtained from (6.14) and (6.16)).

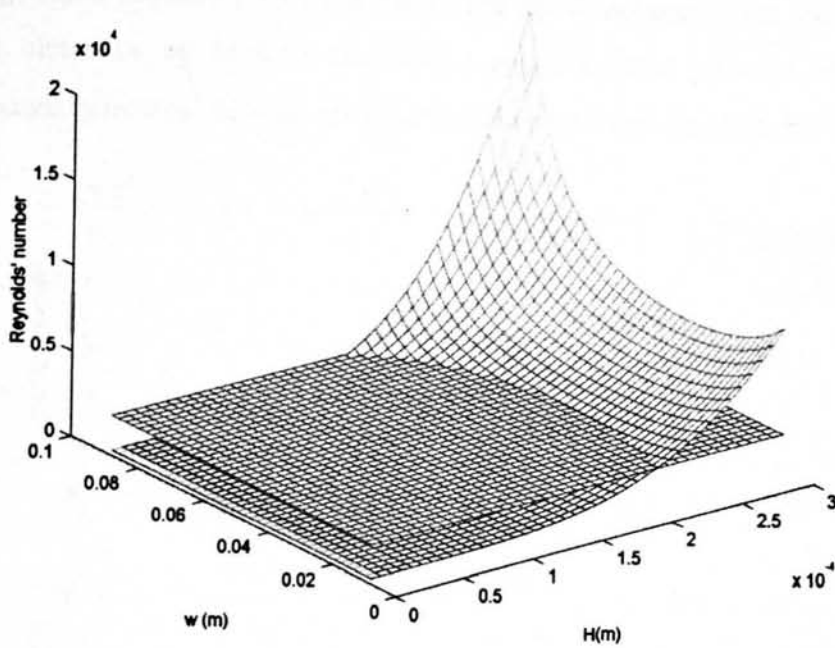


Figure 6.19: Reynolds' number for flow out of bearing compared with 2000, maximum to ensure laminar flow

$$H = \left(\frac{36R_e \mu^2 x (wL + wx + Lx)}{K_0 \rho} \right)^{1/4} \quad (6.25)$$

The maximum allowable clearance for condition of minimum power dissipation is obtained by substituting the value of 0.0427 into Equation (6.25), which yields 0.23 mm. The minimum value of pumping power for clearance values up to and including this value can be satisfactorily used to design a bearing using the assumption of laminar flow.

This methodology of finding the dimensions of minimum power dissipating recess width for a given external bearing dimension and then using Equation (6.25) to find the maximum allowable clearance, can equally be applied to any external dimension.

The external bearing length, L_{ex} in Figure 6.2, is chosen as half, equal to and double the 0.144 m VHM face width. The external width of bearing is then altered between a square and a rectangle of aspect ratio 10.

Figure 6.20 shows the pumping power and maximum clearance permitted for this range of bearings and demonstrates that by enlarging the external size of the bearings, the tolerance on the clearance can be relaxed and the overall pumping power required to achieve the desired stiffness is reduced. For a square bearing of total length 0.288 m, for example, it is possible to construct a bearing that can have a design clearance of almost 0.45 mm and requires around 4 kW. Unfortunately this bearing adds 60% onto

the width of the machine and is twice the length of one pole. A more realistic size bearing, which requires 5 kW, is a square bearing of external width 0.0728 m and can have a clearance up to 0.15 mm with a required input pressure of 5 bar. The corresponding internal dimensions for all possible bearings are given in Figure 6.21.

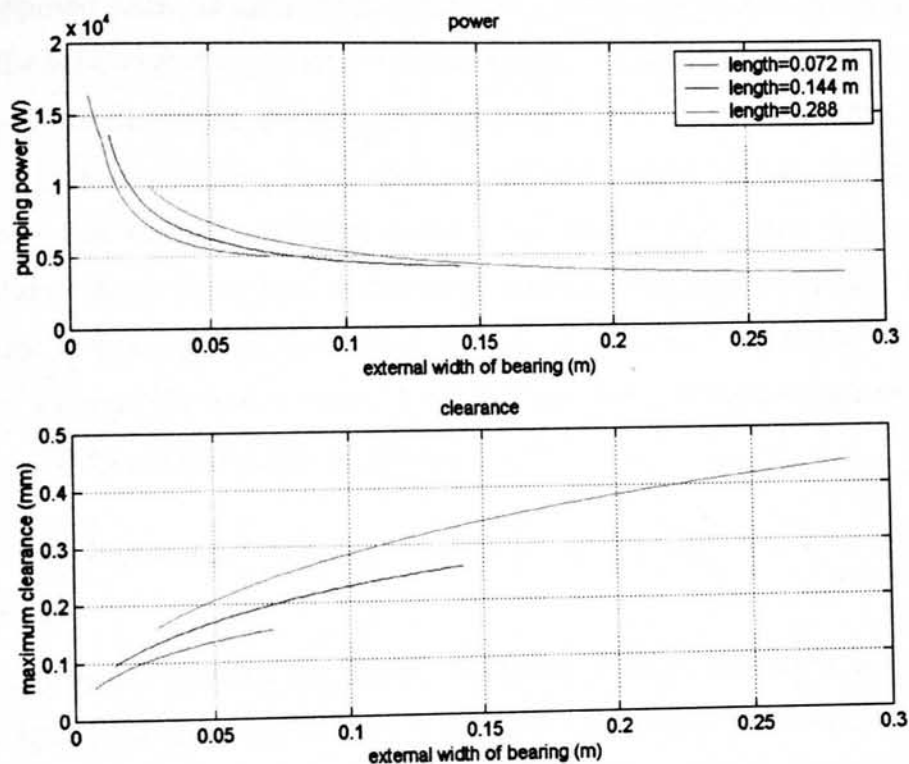


Figure 6.20: Minimum pumping power and maximum clearance of large bearings

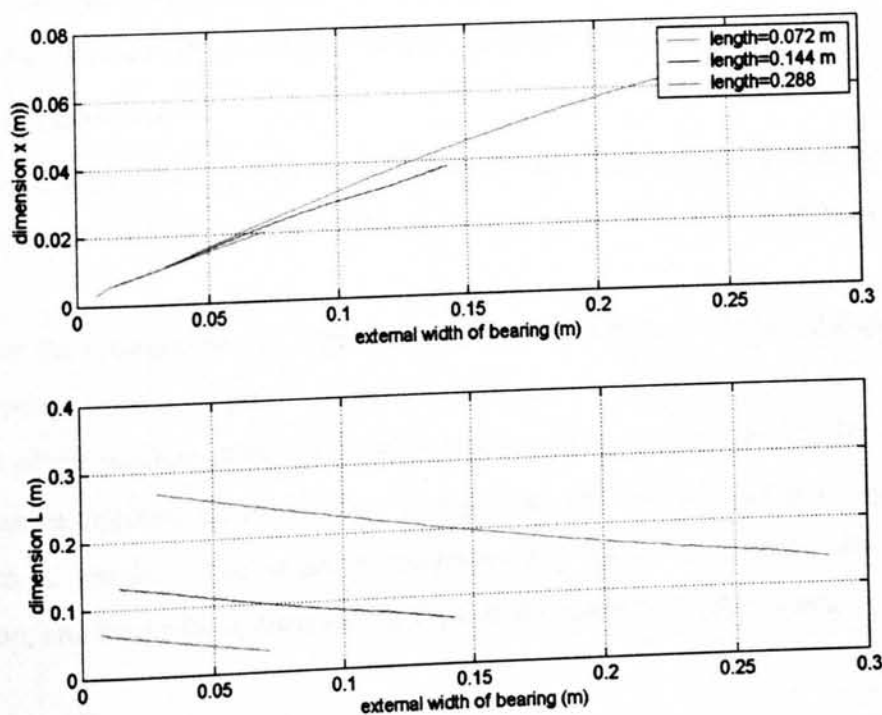


Figure 6.21: Dimensions of bearings in Figure 6.20

Concluding remarks

The behaviour of opposed pad bearings has been investigated using simple laminar fluid flow theory. The concept of hydrostatic lubrication and the need for flow regulation was introduced and used to derive a simple expression for the stiffness of a pair of opposed pads. Dimensionless optimisation techniques were then developed to explore the behaviour of aspect ratio and bearing size. The power dissipated by friction was deemed negligible compared with the pumping power. For particular external bearing dimensions, it was found that an optimum value existed for the recess dimensions that implied minimum power dissipation. This value was used, in combination with an upper limit on the design clearance that ensured laminar flow, to design sets of bearings capable of supporting the translator of a 100 kW VHM. A 0.0728 m external dimension square 5 kW bearing was proposed, which required a clearance of 0.15 mm and supply pressure of 5 bar.

6.5.3.10 Self-Regulating Bearings**Introduction**

The hydrostatic bearings introduced above require flow regulation between the pressure source and the actual bearing. This source of hydraulic resistance is necessary to regulate the recess pressure in response to loads applied to the bearing. By its very nature, then, there must be a pressure drop across it and hence power loss within it. In self regulating bearings, the design of the bearings is such that there is no need for this added resistance and so there is a potential for increased efficiency.

Principle of operation

It is crucial that the overall hydraulic resistance of a self regulating bearing remains constant regardless of the position of the land being supported, thus ensuring a constant flow rate.

Consider the rotating shaft of Figure 6.22. The fluid enters from the right and is split into two equal resistance paths. It is clear that these resistance paths will be equal regardless of the position of the shaft, due to the opposing sets of identical lands. If the input pressure remains constant, then so too does the pressure dropped across the bearing as a whole. The pressure diagram of Figure 6.23 shows the pressure distribution, and hence force distribution, for a small upwards displacement.

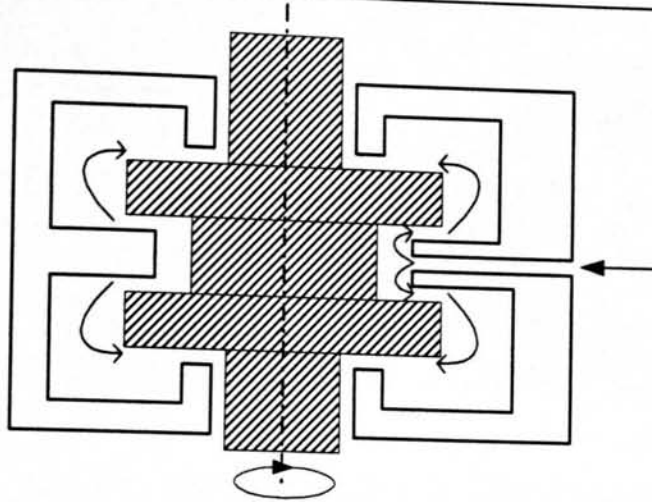


Figure 6.22: Self regulating bearing, flow path

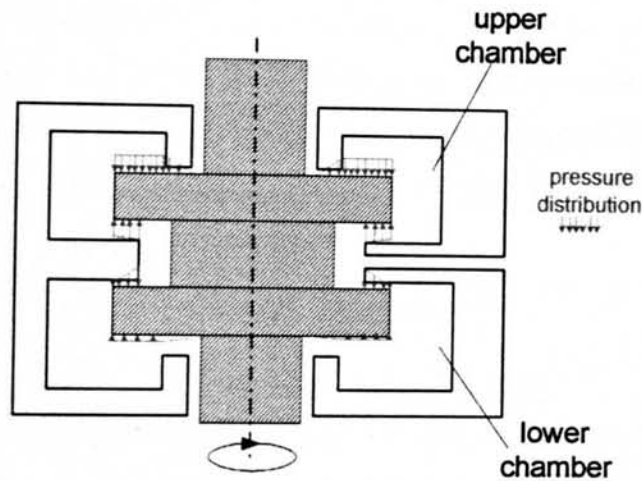


Figure 6.23: Self regulating bearing, pressure distribution

The upper chamber is at a greater pressure than the lower, and hence there is a net force downwards, opposing the initial force required for the displacement. As the total hydraulic resistance has not been altered, the lubricant supply source, and hence any other bearings connected to it, remains unaltered by this displacement.

The principle of self regulation is applicable to linear, as well as rotary, slideways. It has been proposed, by Bassani and Piccigallo [90], that the system shown in Figure 6.24 could be used as a hydrostatic slideway, which would be independently self regulating in two perpendicular directions.

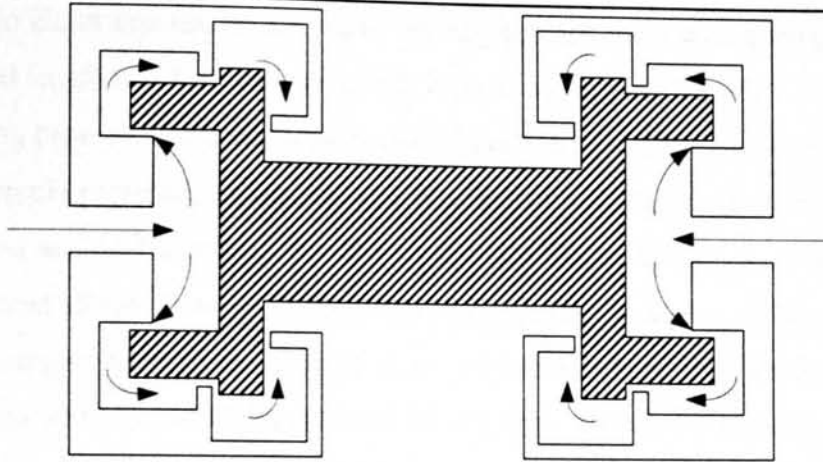


Figure 6.24: Self regulating opposed pad hydrostatic slideway

Two dimensional flow

For the case where axial flow can be ignored, and the flow is purely two dimensional as shown in Figure 6.24, Bassani and Piccigallo have presented a very extensive theoretical analysis linking the parameters of the bearing together. For example, (6.26) links the vertical stiffness of the arrangement to the geometry and flow rate.

$$K = \frac{9}{2} \mu Q (B_1^2 - b_1^2) \left\{ \frac{1}{h_1^4} + \frac{1}{(2h_{10} - h_1)^4} \right\} \quad (6.26)$$

Where B_1 & B_2 are pad sizes in orthogonal directions

In order to achieve two dimensional flow, Bassani and Piccigallo suggested the use of lateral seals. Referring to the logic behind the use of hydrostatic bearings in wave energy devices, it is clear that if lateral seals are to be used, then the advantage of their use, i.e. near infinite life, would be seriously diminished. The only way to investigate the bearing with unsealed ends would be to consider the case of an infinite, or near infinite length bearing. It is conceivable that this would leave the end effects as negligible in the overall bearing behaviour.

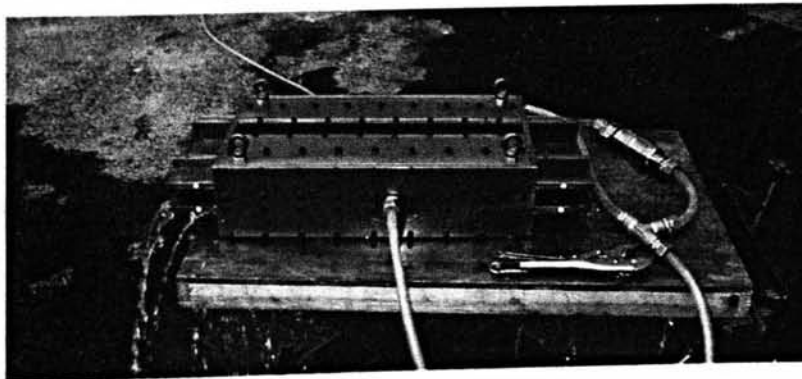


Figure 6.25: End effects of hydrostatic slide way

Experimental work by the author demonstrated that three dimensional effects were both apparent and significant in the case of a long bearing and it was evidently not

acceptable to claim that end effects would be insignificant, even in scenarios where the bearing axial length was long compared with its land width, Figure 6.25.

The testrig presented here was built with the intention of verifying a two dimensional stiffness formula presented by Bassani and Piccigallo [90]. The clearances were set to the minimum achievable tolerance in the workshop. When connected to mains water pressure almost all the flow was leakage flow through the end plates, with a very small flow rate emerging through the intended upper clearance. Increasing the flow rate was technically possible, but would have clearly resulted in a very power intensive bearing.

For continued investigation of self regulating hydrostatic bearings, therefore, it is necessary to consider flow in three dimensions and investigate alternative end configurations.

Concluding remarks

Self regulating bearings have the theoretical advantage of removing the power loss associated with flow restrictors required by other hydrostatic bearings. Although their use in three dimensions has been documented, to achieve this requires the use of lateral seals. Initial simple three dimensional analysis, not presented here, revealed that the true flow pattern through a self regulating bearing is too complex to be adequately accounted for using the intuitive simplifications suitable for opposed pad bearings. To design a true self regulating bearing with constant hydraulic resistance would require three dimensional fluid analysis, possibly using an FEA program such as FLUENT [91]. Verification would involve measuring a variety of pressures and flows, constituting an almost independent research project from the body of this thesis.

6.5.3.11 Conclusions

The concept of hydrostatic lubrication using sea water as the medium to withstand the high airgap closing forces of a 100 kW VHM has been investigated. Using an assumption of laminar flow, a relationship between pad size and required stiffness was derived for a set of opposed bearings. The most satisfactory design, which dissipated 5 kW of pumping power, required a bearing clearance of 0.15 mm, which may cause manufacturing problems. If the analysis were extended to turbulent flow, i.e. one where all the load was taken by the bearing recesses and not by the bearing lands, smaller bearings or bearings with greater land clearances would probably be possible.

Further work would be desirable into turbulent flow bearings and possibly more detailed analysis of self regulating bearings.

6.5.4 Support Structure

The VHM has stringent demands for its structure, due to the high attractive magnetic forces present, the need to maintain a small airgap and the necessity of the steel sections to be laminated. The main body of the VHM thus consists of laser cut 1 mm thick steel sheets bound together. Figure 6.26 shows the relationship between manufacturing tolerance levels and lamination thickness, demonstrating the desire for sheets of less than 3 mm thickness.

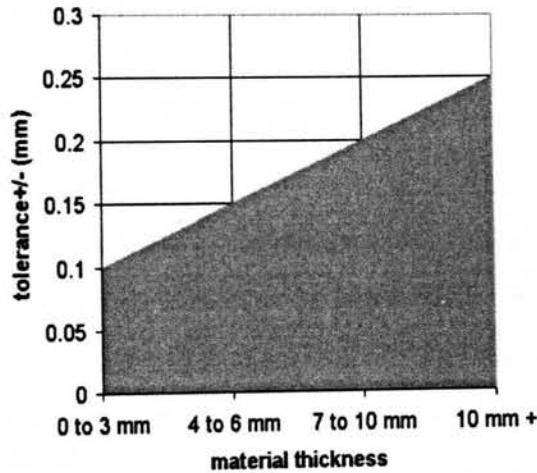


Figure 6.26: Lamination tolerances [92]

A wide machine, one which is large in a plane perpendicular to its rotor motion, results in a magnetic force acting over the stator in such a way that the system becomes a beam with a distributed load. The bending moment of this load will tend to separate the laminations of the structure, which the support structure is designed to prevent. In the laboratory prototype, the laminations were welded to ensure they did not splay apart Figure 6.27. Electrically joining the individual laminations in this manner would not be acceptable in a larger machine, as it allows the formation of power consuming eddy currents and hinders the effectiveness of the laminations.

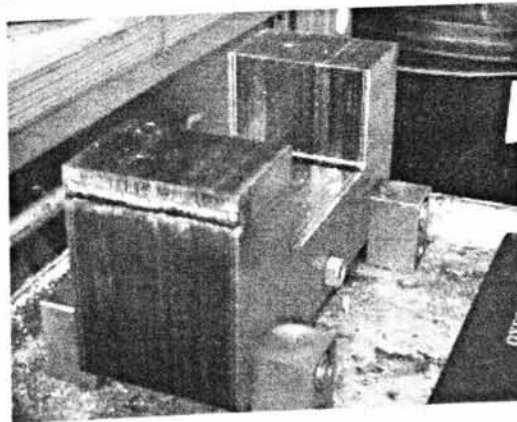


Figure 6.27: Welding of laboratory laminations

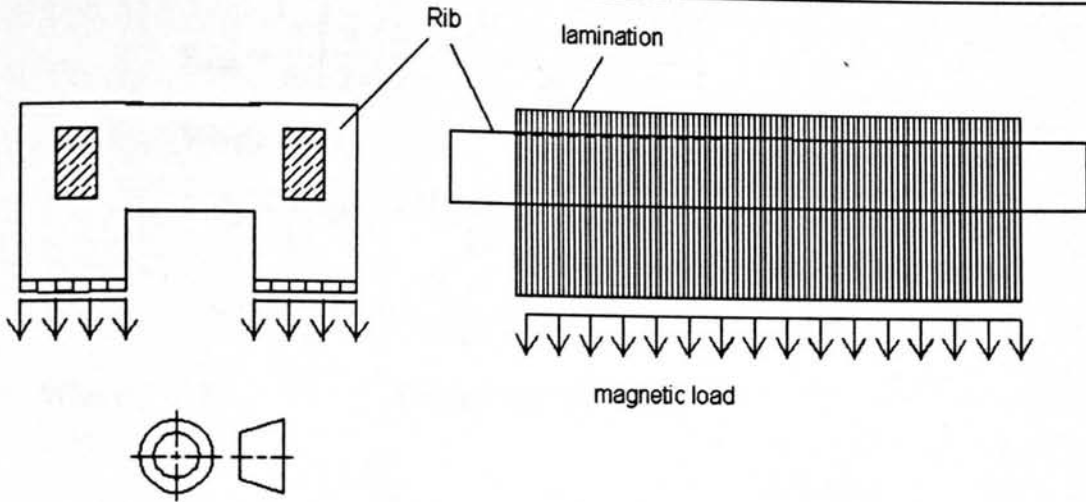


Figure 6.28: Skeletal Structure

The stator laminations may be supported by an external framework of fins and ribs. In this way the laminated structure is relieved of the bending moment, and each lamination only has to resist pure tensile force, Figure 6.28 shows the layout if each pole has its own rib. This section hence assumes that the skeletal structure has to react against the whole bending force, and can be designed independently of the electrical machine.

The problem can be simplified to the built in beam of Figure 6.29. Equation (6.27) describes the maximum deflection of the centre of the beam (as derived in Appendix D) in terms of its dimensions. For a maximum specified deflection, the second moment of area I , defined in (6.28), can be used to determine the required cross section of beam.

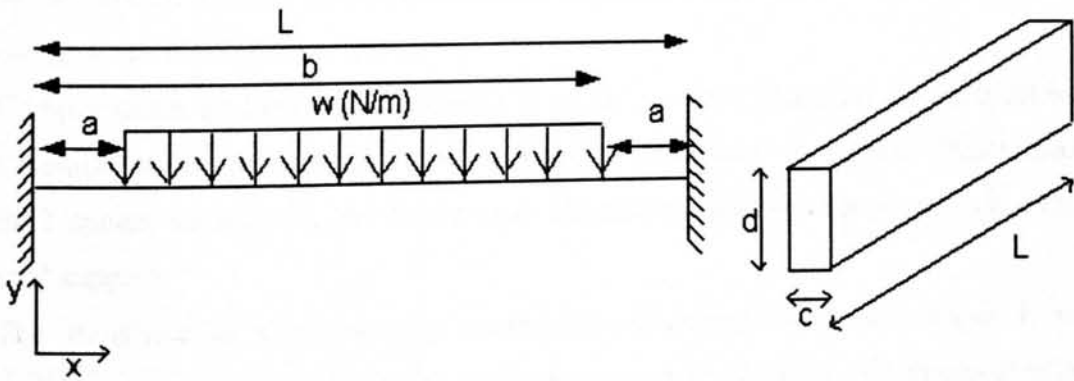


Figure 6.29: Equivalent beam for a VHM

$$y_{\max} = \frac{1}{EI} \left(\frac{w}{24} \left(\frac{L}{2} - b \right)^4 + \frac{C_1 L^3}{48} + \frac{C_2 L^2}{8} \right)$$

Where :

$$C_1 = \frac{w}{L^2} (b^3 - a^3) - \frac{w}{2L^4} (b^4 - a^4) \quad (6.27)$$

$$C_2 = \frac{w}{6L} (b^4 - a^4) \left(\frac{1}{2L} + \frac{1}{L^2} \right) - \frac{w}{3L} (b^3 - a^3)$$

Where E = Young's Modulus (Pa)

$$I = \frac{cd^3}{12} \quad (6.28)$$

If the magnetic compressive force from each pole is transferred onto a single beam in pure compression, the beam will shrink by δ m, as given in (6.29).

$$\delta = \frac{FL}{EA} \quad (6.29)$$

It is now possible to design a simplified support structure for the VHM.

6.6 Tubular

6.6.1 Introduction

Integration of the tubular machine into marine energy converters is likely to be less problematical than for the VHM. The cylindrical translator cross-section eases sealing whilst the reduced forces between the translator and stator place less demands on the lubrication and support structures.

Complications are likely to arise mainly from the choice of materials, which must be non metallic within the vicinity of the coils and non magnetic elsewhere. Plastic and Tufnell appear suitable for the former and aluminium, stainless steel and brass for general support.

The translator is a permanently magnetised structure, which will mean it is susceptible to trapping metallic debris from the marine environment. Provision should be made for removal of such debris in combination with an investigation into likely quantities.

6.6.2 Sealing

The smooth regular cross sectional area of the translator lends itself favourably to ceramic coating. The resulting structure could then be either sealed using technology

transfer directly from hydraulic rams, or the copper coils alone could be sealed in the plastic stator support structure by use of end plates.

6.6.3 Hydrostatic bearings

The lack of large forces in the air cored tubular machine make the demands on a hydrostatic lubrication system much less stringent than for the VHM. No analysis is presented here as two dimensional FEA has not allowed the variation of magnetic force with concentricity of translator to be quantified. In Chapter 5 the magnetic force between the translator and stator was expressed as an equivalent pressure of less than 1 Bar. Hydrostatic pads operating at medium pressures to react a force against the translator would be governed by similar equations to those presented for the VHM above and likely require only low pumping power.

6.6.4 Support structure

As much of the tubular machine stator support has to be non magnetic, plastic is an obvious choice. This was used for the coil support in the prototype device and proved perfectly feasible. In this respect, the support structure is likely to be very light in comparison to the solid metal translator. No detailed structural work has been undertaken.

6.7 Comparison of Machine Topologies

6.7.1.1 Introduction

When selecting an electrical machine for this application, the key criteria will be either the performance per kg, m³ or pound sterling. Using the relationships derived in previous Chapters and, for the VHM only, the lubrication system, it is possible to compare the two available topologies of machine for a given application. Nominally, the case study machine is required to extract 100 kW when travelling at 1ms⁻¹ with a current density of 1×10^6 A m⁻².

The cost estimate is very crude and based on the price of materials as bought for the prototypes. There would clearly be economies of scale associated with larger material orders, but the relative price between the two machines would likely remain the same. For example, at the time of writing, as a raw material copper is worth \$1.6 US per kg, around a third the value used here. Furthermore, no attempt has been made to gauge the relative manufacturing costs, nor has any account been made for external load on translator.

Table 6-2: Material prices used in cost analysis

Steel bar (£/kg)	0.7
Nd-Fe-B magnets (£/kg)	27
Stainless steel bar (£/kg)	4.4
Copper (£/kg)	2.6
Laminated Steel (£/kg)	2.6
Plastics (£/kg)	0.7

6.7.1.2 VHM

Using the six module 100 kW machine described earlier in Section 6.5.3.1, combined with the 0.0728 m square hydrostatic bearings recommended in section 6.5.3.9 and the support method of section 6.5.4, the parameters of an entire VHM can be calculated. The proceeding paragraphs give details of the selection and calculation of the machine dimensions.

The stator back iron is equated to the height of the rib ('d' in Figure 6.29) above the pole face and 5 cm between pole faces where no force is felt and its only purpose is to carry magnetic flux. A 1 cm gap is assumed between the upward support and the laminations, dimension 'a' in Figure 6.29, which is substituted into Equation (6.27) to reveal that a bar of 0.05 m width and 0.14 m height will have a maximum deflection of 0.05 mm when subjected to a distributed load summing to the 36 kN of magnetic force felt by the stator. The deflection of a bar of these dimensions is hence such that the 1 mm airgap will close to 0.95 mm in the centre of the machine. The upward support will have a compression of an order of magnitude below this, as calculated by (6.29) and thus these values are appropriate to maintain the airgap.

The hydrostatic bearings are modelled as solid steel 2 cm high blocks, and the track is a 0.072 m wide 0.01 m thick steel bar clamped on each side of the translator.

For a 2 m peak to peak stroke, the translator requires a length of 5.7 m with the other dimensions given in Table 6-4 below. The parameters of the resulting machine are given in Table 6-4 and Table 6-5.

Table 6-3: Mass of 100 kW VHM

Magnets	Copper	Stator and translator laminations	Total VHM unsupported	Support/lubrication steel	Total
67 kg	780 kg	5.6 tonnes	6.4 tonnes	0.9 tonnes	7.3 tonnes

Table 6-4: Size of 100 kW VHM

Stator length	Stator width	Stator breadth	Stator volume
1.72 m	1.2 m	0.4 m	0.8 m ³

Table 6-5: Cost of 100kw VHM

Magnets	Copper	Steel	Laminated steel	Total
£1 800	£2 100	£630	£14 600	£19 100

6.7.1.3 Tubular machine

For the tubular machine, no relationships have been defined for the size of the support and lubrication systems. The mass is likely to be dominated by the translator and coils, however, which have been defined. A tubular translator has been designed consisting of 0.2 m diameter 50 mm thickness magnets mounted alternately with steel pieces of the same dimensions on a stainless steel shaft of 80 mm diameter. The stator consists of a 4 mm thick internal support for the coils mounted concentric to the translator with an airgap of a 1 mm. The magnetic gap of the machine is hence 5 mm. The external support of the coil is a tube of 20 mm wall thickness and the inter-coil spacers are nominally set to 10 % of the copper volume. All the plastic components are assumed to have a density of 3600 kg/m³. Table 6-6-Table 6-8 describe the resulting machine.

Table 6-6: Mass of 100 kW tubular machine

Magnets	Copper	Steel	Stainless Steel	Plastics	Total
1.7 tonnes	1.1 tonnes	1.6 tonnes	130 kg	240 kg	4.6 tonnes

Table 6-7: Size of 100 kW tubular machine

Stator height	Stator diameter	Stator volume
1.4 m	0.58 m	0.4 m ³

Table 6-8: Cost of 100 kW tubular machine

Magnets	Copper	Steel	Stainless Steel	Plastics	Total
£45 900	£2 900	£1 600	£565	£170	£50 200

6.7.1.4 Comparison

Table 6-9: Comparison of VHM and tubular machines

	Force			Power		
	kN/kg	kN/m ³	N/£	kW/kg	kW/m ³	£/W
VHM	13.7	125	5.2	13.7	125	190
Tubular	21.7	250	2	21.7	250	502

Table 6-9 allows a direct comparison of the two 100 kW machines in terms of performance. The VHM is less than half the price of the tubular machine, yet requires twice the volume to house the stator. The VHM machine is likely to be the heavier of the two machines. Figure 6.30 and Figure 6.31 show a comparison of the dimensions of the two machines.

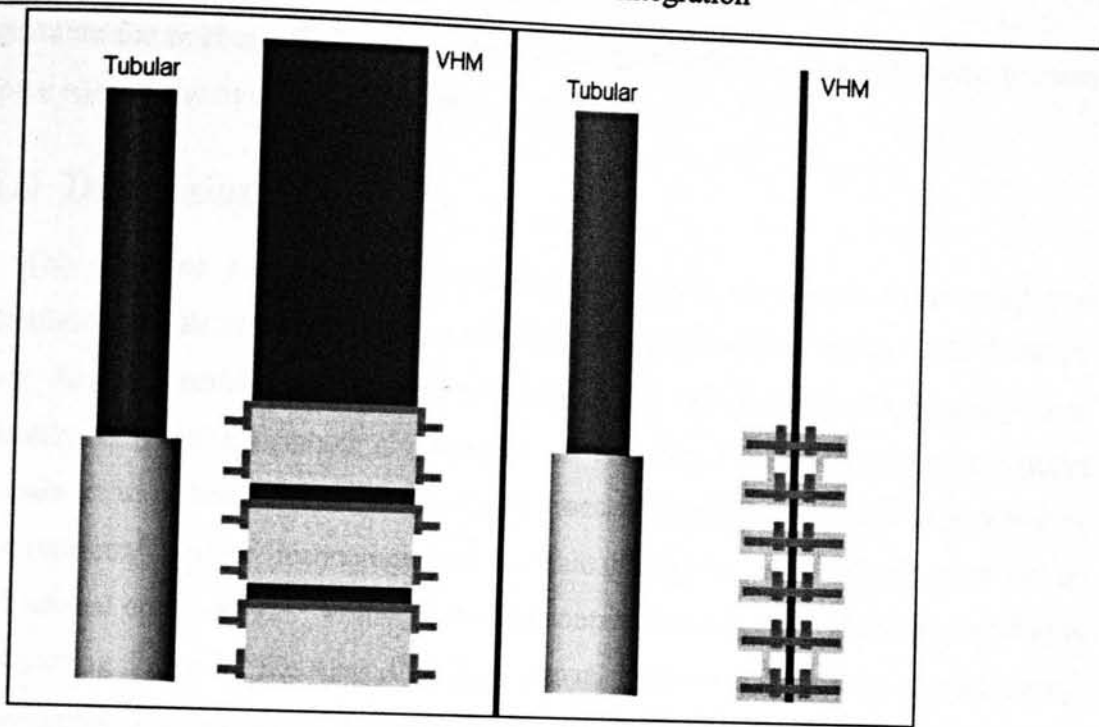


Figure 6.30: Side view comparisons of both 100 kW machines

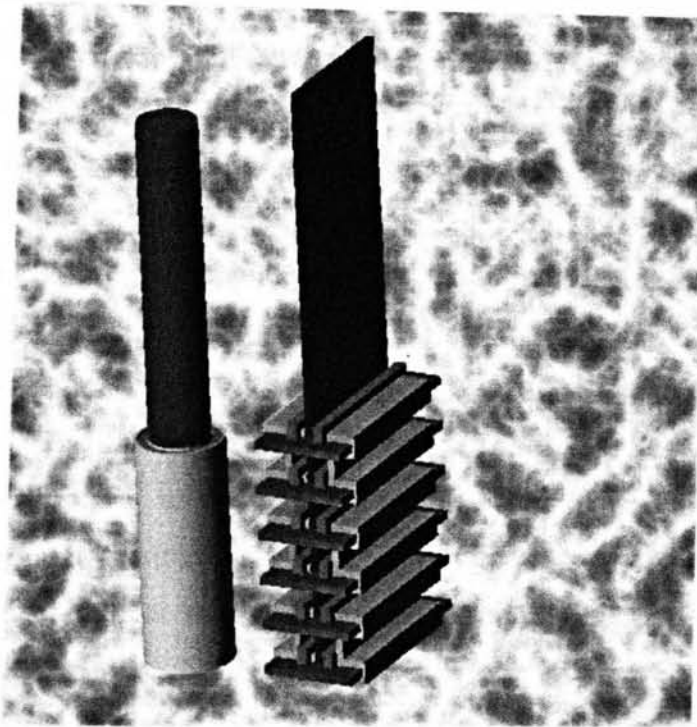


Figure 6.31: Rendered view of both 100 kW machines

Whilst the conclusions regarding total mass and cost should be taken only as guidelines, comparison of the mass of copper and magnet material used in each machines is more credible. The tubular machine requires about 25 times the mass of magnet material and 50 % more copper.

The total mass of the VHM is based on simplified theory of both lubrication and structural support to counteract the strong magnetic forces, whereas the tubular machine

accounts for neither. Both machines will require additional support in order to react force against the translator in the direction of its motion.

6.8 Discussion

This Chapter has investigated the physical issues associated with using two alternative topologies in direct drive marine energy converters. For the VHM there are two distinct sealing methods, either encasing the translator in magnetically inert material to provide a smooth cross section, or enclosing the linear machine and entire translator in a sealed case. The tubular translator lends itself more favourably to conventional sealing technology and ceramic protection as a consequence of its cylindrical cross section. Rolling and solid contact bearings exist which are capable of supporting linear motion over the likely annual distance travelled by marine energy converters, the former of which requires the device to be sealed to allow good lubrication. The opportunity exists for the development of hydrostatic bearings to support the translator in either machine, with an associated increase in maintenance intervals as a consequence of their non contact / zero wear characteristic. A 5 kW lubrication system was proposed, capable of supporting the translator of a 100 kW VHM, utilising a bearing clearance of 0.15 mm along the 1.7 m stator length. Self regulating bearings were briefly discussed by merit of their possible increase in efficiency, due to the lack of requirement for flow regulators. The likely three dimensional flow pattern implied that more detailed analysis would be necessary to verify their use. The tubular machine is anticipated to be less troublesome for hydrostatic lubrication due to the reduced magnetic forces present and increased translator surface area. Further work in the area of three dimensional flux pattern analysis is desirable in order to obtain an expression for the net force on a non-concentric translator.

Several corrosion strategies were investigated and subsequently discredited. Ceramic material Ceramax appears hopeful for the tubular machine, but currently is only used to coat smooth structures and so may not be suitable for the VHM.

The two topologies of machine were compared for a rated power of 100 kW at 1 m/s and found to be of similar dimensions. The heavier VHM appears to be cheaper than the tubular machine, implying that it would be more suited to a sea bed mounted device. A floating device, where mass and volume may be of more significance than cost is recommended to utilise a tubular machine. The power factor of this machine was found to be almost unity in Chapter 5, in stark contrast to the power electronic support

equipment that is necessary to realise the potential of a VHM. The cost of an active rectifier to achieve unity power factor for the VHM has not been accounted for.

6.9 Conclusion

Issues surrounding the use of linear machines in MECs have been discussed. The two machines have been found to be of similar overall size, with the VHM using a much smaller amount of magnetic material to react the same force. Furthermore, the tubular machine is more suited to suitable corrosion and sealing techniques, but will place less demands on the support structure. A simplified support and lubrication structure for a 100 kW VHM was presented.

Chapter

7

Proposed VHM Design for a 150 kW Tidal Energy Device

In this Chapter a linear generator is proposed as the power take off mechanism for a direct drive Stingray tidal stream generator, a description and picture of which was given in section 1.2.2 and [42]. The dimensions and behaviour of the current power take off are used as the input parameters for a design study of a direct drive version. The Chapter is intended to demonstrate the effect of electrical machine location within an MEC on generator characteristics.

The topology chosen is the VHM, as this was shown to use less magnetic material and develop a higher shear stress when compared to the air cored tubular machine in Chapter 6.

7.1 150 kW Stingray

In 2002 a 150 kW demonstrator device was designed, built and installed at Yell Sound in Shetland by the Engineering Business Ltd. The power take off mechanism consisted of four opposing hydraulic rams used to drive oil around a hydraulic circuit, via a hydraulic motor coupled to a rotary generator. It is possible to apply a variety of different control strategies in an attempt to maximise the power taken from the channel. For example, two features which may be controlled are the hydroplane angle of attack and the phase, shape and magnitude of the power take off force. The upper limit of extracted power will be dictated by the 59% Betz limit when considering the entire area swept by the hydroplane. Currently it is primarily the concept of tidal stream generation that is being investigated and there is no research programme in altering the present hydraulic take off mechanism. The direct drive concept is likely to be considered later in the Engineering Business development programme, in the region of 5-10 years from now [93].

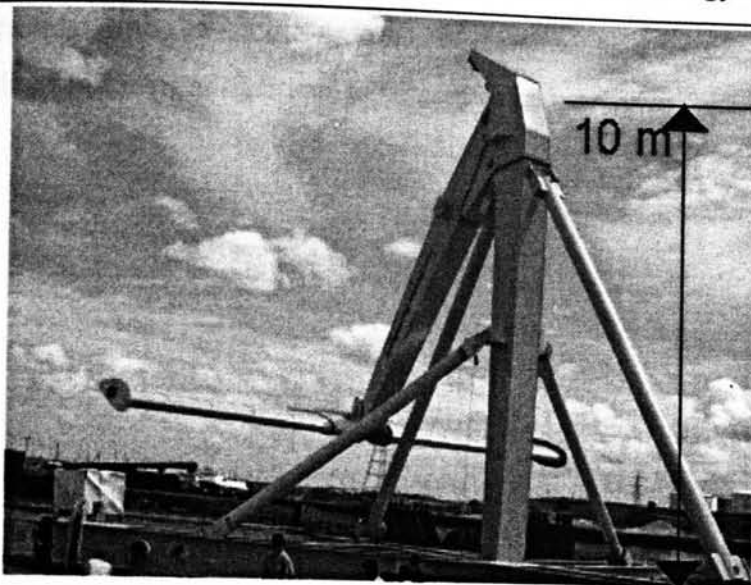


Figure 7.1: Photograph of 150 kW prototype shortly before deployment

Figure 7.1 shows a photograph of the prototype as it was being assembled in Summer 2002. For this investigation the movement of the arm is assumed to extend 30° above and below the horizontal in a purely sinusoidal manner with a period of 21 seconds. The hydrofoils will oscillate between 5 and 17 m above the seabed, which is a typical cycle for a water velocity of 1.5 m/s. The speed and motion may be controlled to maximise the power captured by the device.

7.2 Power Take off Mechanism

The current Stingray power take off uses hydraulic rams to force high pressure oil through a hydraulic pump connected to a conventional rotary electrical machine. The simple nature of the hydraulic circuit, which contains no accumulators to smooth flow, means the electrical machine experiences bi-directional rotary motion of variable velocity.

The power take off configuration consists of four hydraulic cylinders, two mounted in antipose on each side of the device as shown in Figure 7.2. One end of each of the cylinders is fixed to the post whilst the other is allowed to follow the movement of the pivotal arm. The configuration is such that the net moment arm for each opposed pair, i.e. the perpendicular distance between the action of the rams and the pivotal point, remains roughly unaltered throughout the oscillation cycle of the device. Its actual variation is shown in Figure 7.3. In combination with the hydraulic configuration of the cylinders, namely the coupling of a full bore to the opposing piston's partial bore (the effective area in push connected to the effective area in pull), then nominally the

pressure in the hydraulic system always represents a specific torque applied to the arm, allowing for simplifications to be used when specifying the hydraulic system.

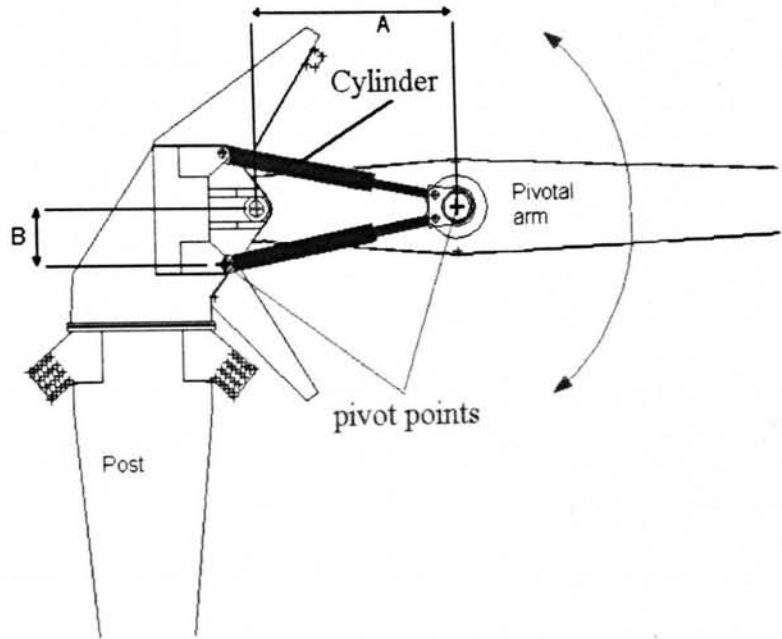


Figure 7.2: Configuration of hydraulic cylinders

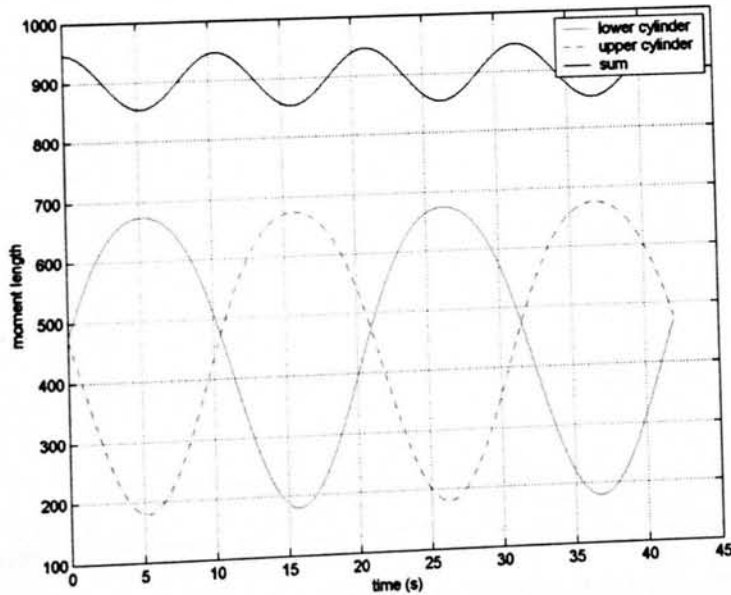


Figure 7.3: Moment length cylinders have on pivot arm over 2 cycles

The variation in total length of one set of cylinders, the distance between its mounting points, is shown in Figure 7.4 and demonstrates that the topology proposed results in a slightly unsymmetrical waveform. Also shown in this figure is the cylinder velocity, which has a peak of just 0.1 m/s.

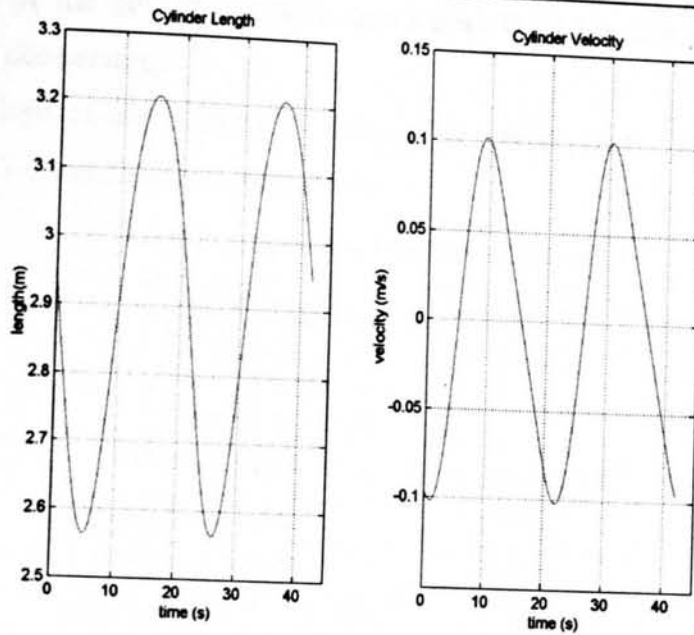


Figure 7.4: Characteristics of cylinder cycle

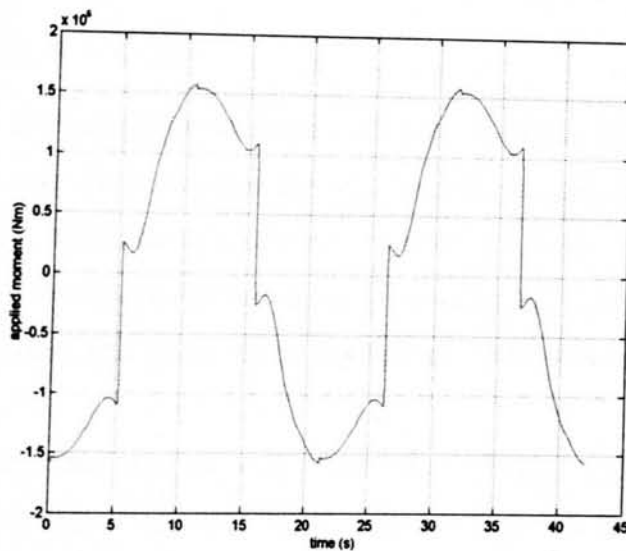


Figure 7.5: Moment exerted by power take off

Using hydraulic pump torque vs. speed data from the Stingray device [94] operating in an optimised cycle, the equivalent force applied to the arm by the entire hydraulic system can be obtained. The use of this data, converted into a look up table, allows the linear generators to deliver the exact same response as the current power take off system. The total moment applied to the arm by all four cylinders is given in Figure 7.5. It should be noted that the discontinuities shown here and throughout this Chapter result from the assumption of instantaneous switching of hydroplane angle of attack. This affects the results at positions of direction change, 5.25, 15.75, 26.25 and 36.75 seconds. At the maxima of the curves there is a slight discontinuity, not present in the physical situation, resulting from the use of a look up table for the load speed

characteristics of the current hydraulic drive, evident as the motion changes from accelerating to decelerating.

The dimensions of one cylinder and mass of the entire power take off system are given in Table 7-1 and Table 7-2 respectively

Table 7-1: Approximate dimensions of cylinder

Push area (m ²)	0.0374
Pull area (m ²)	0.0279
Outer diameter (m)	0.25
Cylinder length (m)	2

Table 7-2: Estimated mass of hydraulic system

Cylinder (1 of 4)	120 kg
Hydraulic motor	100 kg
Electric Machine (300kW)	500 kg
Hydraulic oil (0.2 m ³)	140 kg
Piping	25 kg
Total	1.2 tonnes

7.3 Specifying a VHM

Using the flux flow along the translator back iron, as proposed in Section 4.7, and thus proposing a four sided machine around a central support, the stator length of machine is kept to a minimum at the expense of making a wider machine for a given active airgap area. The topology is inherently closer to that of a hydraulic cylinder than the two sided machine and hence more appropriate when investigating their direct replacement.

A single machine with 6 magnets on each stator face will give a 15 kN peak force per unit axial length at a constant rated current of 15 Amps. This data can be used to dictate the required axial length of the machine.

The constant current force is cyclic over twice the magnet pitch of the machine. In reality, when the generator is connected to a load the current would constantly vary such that the force was always opposed to the direction of travel. Three similar modules are positioned with respect to one another in the direction of motion such that they are separated by 120 electrical degrees to form a 3-phase single sided machine. In total there will be four such machines around a single square translator, making up a three phase module with a combined average force of 47 kN per metre axial length. The number of these three phase configurations is dictated by the space available on the Stingray.

7.4 Direct Replacement of Cylinders

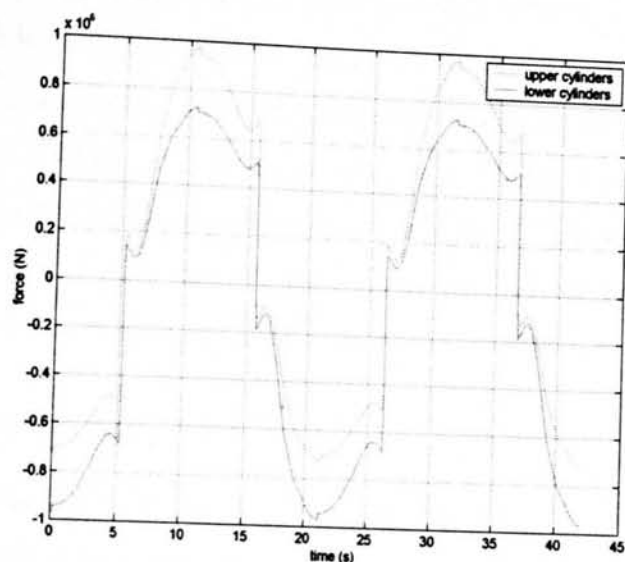


Figure 7.6: Force provided by individual cylinders

During a typical cycle in a 4 knot tidal stream the force reacted by one of each of the upper and lower cylinders will be of the form shown in Figure 7.6. Each curve consists of two maxima, occurring at the same time as the maximum velocity of the cylinders. The nature of a hydraulic cylinder is such that it is capable of delivering a greater force in its full bore direction than when it is retracting. The electrical machine need not be capable of delivering the largest force demanded of the hydraulic system, around 970 kN, therefore, but a slightly smaller force, distributed evenly between the four opposing generators, which matches the total applied moment, 850 kN.

Table 7-3: Linear generator for direct replacement of cylinders

Axial length of phase (m)	2.26
Outer width (m)	2.63
Mass rotor (tonnes)	13
Mass magnets (tonnes)	0.48
Mass copper (tonnes)	6.2
Total mass (tonnes)	43

As shown in Figure 7.4, the total length of the cylinder remains above 2.56 m and oscillates between this value and 0.64 m longer. The minimum total length may be used as the active length of the machine whereas the maximum extension will give the required length of translator. A square machine capable of delivering the required peak force consisting of four three phase modules is detailed in Table 7-3. When compared to the outer diameter of the cylinders, which is approximately one tenth of this value, direct drive by simple replacement of the cylinders is somewhat cumbersome, and adds

68 tonnes to the mass of the machine. This large mass is a direct result of the translator speed being just 0.1 m/s and demanding a very high reactive force.

Electrically and in terms of total mass, there is no difference between having four of these generators or one set of opposed generators occupying the same space, each capable of reacting 1.7 MN. It is likely, however, that the latter option, consisting of two 4.9 m wide 85 tonne machines, would fit more conveniently into the machine.

As a substitute to hydraulic rams, direct drive power take off mounted here is not very attractive due to the extra mass and alternative locations must be investigated.

7.5 Enlarged Moment Arm

The position of the hydraulic rams and the magnitude of the moment arm dictates the velocity, pressure and stroke length of the power cycle. Clearly, when replacing the power take off for a direct drive system, there are different priorities involved in locating the system parts. Electrical machines benefit from positions of higher velocity as the required reactive force is lower, whilst still extracting the same power from the body. Hydraulic systems can operate at pressures of several hundred bar (10^7 Pa) and are hence able to react huge forces. They also have a seal-enforced upper limit on permitted velocity. Furthermore, if an electrical machine can be made longer in the direction of travel, the required width will decrease for the same active area and hence rated force. The active chamber of a hydraulic ram, however, should be kept as small as possible to reduce weight and volume of fluid.

These conflicting factors imply that the best place for a hydraulic power take off system is the worst place to consider a direct drive system. The latter would benefit from locating the generators in a position on the Stingray with a larger moment arm and active length.

Referring again to Figure 7.2, the two dimensions which can be most conveniently altered are marked as A and B. The former mainly alters the minimum (active) length whereas the latter greatly affects the moment arm length. For demonstration purposes, both of these dimensions are doubled. The required moment can now be applied by two opposed generators with have an active length of 4.66 metres each reacting a maximum force of 680 kN over a 1.44 m amplitude of oscillation. Two generators of the type detailed in Table 7-4 could provide this function. The total mass added by the direct drive system is now 69 tonnes. To gauge a feeling of how this would sit in the device, Figure 7.7 shows a scale diagram allowing comparison of the linear generator to both an original cylinder and the device itself.

Table 7-4: Linear generator suitable for use with enlarged moment arm

Axial length of phase (m)	1.03
Outer width (m)	1.40
Mass rotor (tonnes)	11
Mass magnets (tonnes)	0.39
Mass copper (tonnes)	5.1
Total mass (tonnes)	35

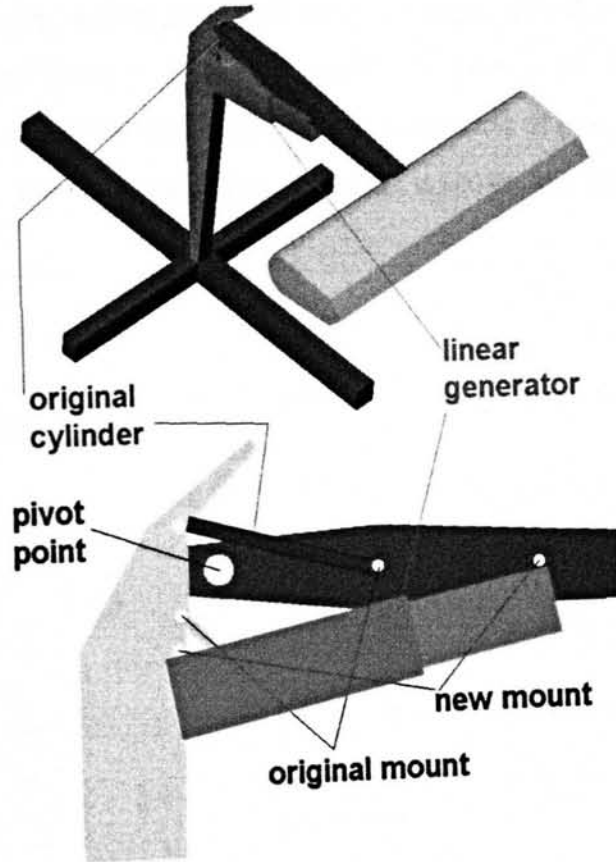


Figure 7.7: Comparison of proposed generator and existing cylinder

Although the generator is clearly larger than its hydraulic equivalent, when compared with the scale of the machine it is not a cumbersome alternative. If the pivot arm, dimension B, could again be doubled, then the total width of the generator would be comparable to the combined width of the two cylinders it would be replacing. Demonstrated is the importance of the location of the generators, with 8 tonnes being saved on the direct drive concept by altering its position.

7.6 Alternative Location

Following the preference for high speed and low forces to its limit would result in the electric machine being driven at the same amplitude as the hydrofoils. This would effectively bypass the influence of the pivot arm altogether and result in the linear

generator being coupled between the hydrofoil and the foundations directly. An example design study can be used to find the ultimate position of a single linear generator coupling the pivot arm to the base. The maximum permissible active length is now dictated by the clearance between the pivot arm at its lowest position and the base, which varies according to the distance from the post. To provide the pivot arm with the same total moment from a single linear generator, the force which that generator is expected to react will clearly decline as distance from the post increases. Using the generator data as above, and dictating that the active length of the machine must be a whole number of three phase modules, it is possible to examine the relative features of generators placed at all points along the arm. The extremities of position are 0.5 m and 10 m from the post. The force required for this range is shown in Figure 7.8

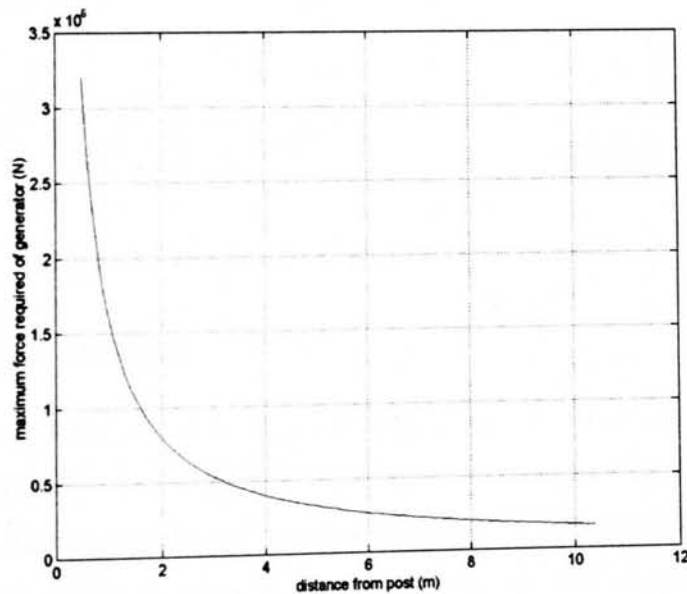


Figure 7.8: Force required to exert moment at different generator positions

If the minimum is taken as 2 metres from the post, the total force is kept well below 1 MN and the design study becomes more illuminating. Figure 7.9 shows some possible design criteria on which an appropriate generator could be chosen.

The smallest and lightest machine has an overall width of 0.6 m and a mass of 10 tonnes. If the linear generator were situated here it would follow the 12 m vertical oscillations of the hydroplanes, which pivot around the top of the post some 11 m away. The resulting motion is hence no longer linear but traces a circular arc. To account for this, the translator and stator of the generator could also be made to have the same curvature.

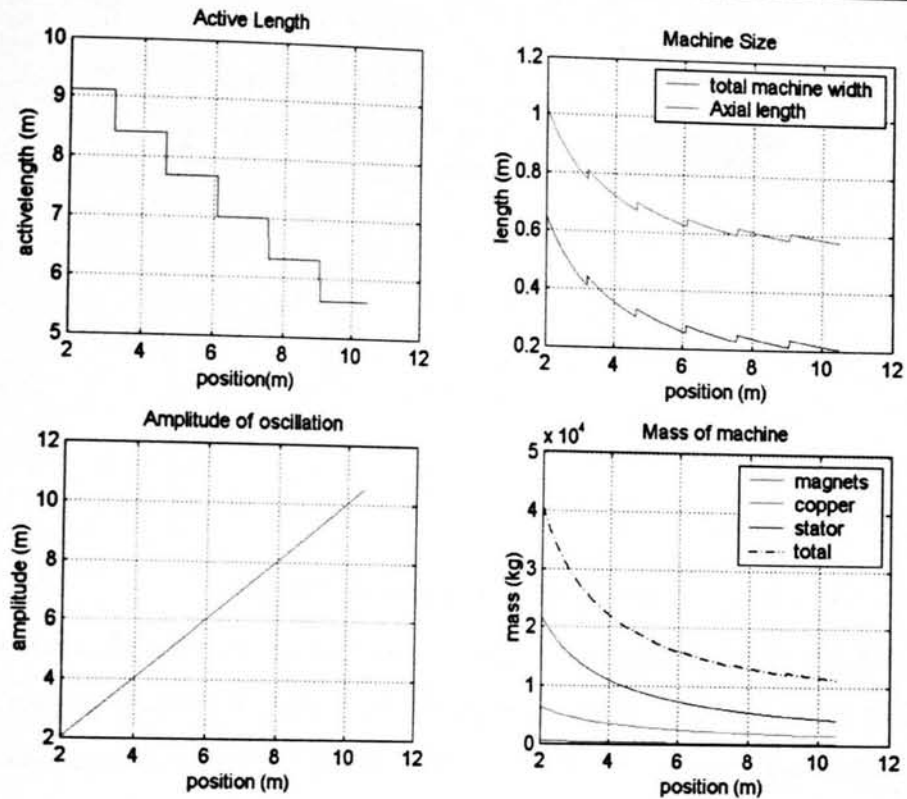


Figure 7.9: Design study of generator distance from post

7.7 Integrated Design

The design work so far has combined the Stingray device, which has been designed and optimised for hydraulic power take off, with the semi optimised four sided linear VHM machine. The dependency on position of the electrical machine size has hence been demonstrated. The next logical stage is to integrate the VHM and the Stingray at a much earlier stage in the design process and optimise them both simultaneously. Two examples of this are given below.

Figure 7.10 shows the curved stator of a possible linear generator mounted on the Stingray arm interacting with the stationary translator, mounted on the post. The machine will behave in an identical manner as the previous VHM, yet the curved nature of its locus has eliminated the need for a hinged stator.

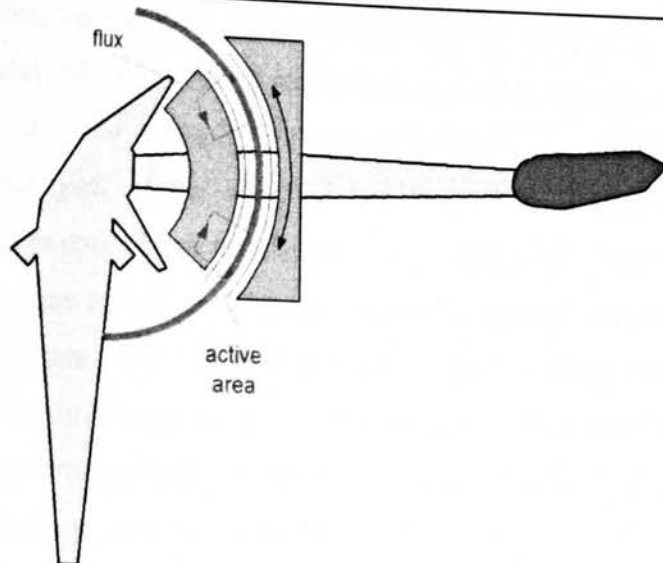


Figure 7.10: hemispherical flux machine

Alternatively, following the integration through to its natural conclusion, the linear generator can be attached directly to the hydroplane and the arm part of the Stingray could be abandoned altogether. The device, however, would no longer be the Stingray.

7.8 Discussion

Simple substitution of hydraulic cylinders for linear generators would imply that a direct drive system is not a suitable power take off mechanism for the Stingray device. This is not a valid comparison, however, as the positioning of the rams has been influenced by their performance parameters. The positioning of alternative methods of power take off should therefore also take into account their associated characteristics. To extract an equal amount of power as a set of hydraulic rams, which are renowned for reacting high forces but are limited to low velocities, an electrical machine is more suited to a position offering higher velocities and smaller forces over a longer stroke. There is no theoretical limit to the velocity of an electrical machine.

Although the direct drive option will likely always be a more mass intensive option, it has been demonstrated that careful positioning of the electrical machine can reduce this effect from an additional 168 tonnes when considering direct replacement to 9 tonnes. It should be borne in mind that the present design of Stingray requires a large amount of ballast to maintain stability against the moment of the vertical forces on the hydrofoils. Further detailed designing for direct drive may be able to use the mass of the generators as ballast and thus keep the overall weight of the Stingray close to its present value.

If the direct drive option were to be investigated more fully, it is likely that there would be some play off between the requirements of such a power take off and the Stingray device itself. For example, the optimum position suggested in this Chapter totally prevents the yaw of the hydrofoil, which may form part of the Stingray performance at a later date. Likewise, the generator could be more incorporated into the pivot arm to save space or weight. The numerical investigation has been limited to flat reciprocating generators with a two dimensional flux flow only. Semi-cylindrical machines along the axis of rotation, in combination with axial or three dimensional flux flows, could offer performance improvements and should form part of any serious direct drive tidal stream energy converter of this type.

7.9 Conclusion

Various integration options have been presented for the integration of a linear VHM into a direct drive version of the Stingray tidal stream energy device. No technical barriers to this were encountered although an increase in mass appears to be inevitable as long as the Stingray and electrical machine design are kept separate.

The influence of generator position on system mass has been demonstrated.

Chapter

8

Direct Drive Wave Energy Converter

In this chapter, the models developed describing the behaviour of electrical machines are expanded to a size suitable for use in a Wave Energy Converter (WEC). The performance of a real WEC is analysed to specify the likely requirements of an electrical machine suitable for direct drive power take off. The energy converter considered is the Archimedes Wave Swing (AWS), as described in Chapter 1 and [29].

8.1 Principle of Power Extraction

The vertical position, y , of the oscillating part of the AWS, known as the floater, is described by the force equation (8.1).

$$(M_{fl} + M_a) \frac{d^2 y}{dt^2} + (\beta_h + \beta_g) \frac{dy}{dt} + C_{AWS} y = F_w \quad (8.1)$$

Where	M_{fl}	=	mass of floater (kg)
	M_a	=	added mass (mass of water above floater) (kg)
	β_h	=	hydrodynamic damping coefficient of AWS (f (wave period)) (Ns/m)
	β_g	=	damping coefficient of generator (Ns/m)
	C_{AWS}	=	spring constant of AWS (N/m)
	F_w	=	diffraction force of the wave acting on AWS (N)

According to this equation, the generator acts as a pure damper, giving a reactive force proportional to the velocity of the device. Resonance of the device occurs when the spring force and the inertia force cancel each other out, i.e. :

$$(M_{fl} + M_a) \frac{d^2 y}{dt^2} + C_{AWS} y = 0 \quad (8.2)$$

Varying the spring constant, C_{AWS} , provides a mechanism for tuning the device depending on the incoming waves and is achieved by varying the air pressure within the floater. The force equation at resonance is now reduced to (8.3).

$$(\beta_h + \beta_g) \frac{dy}{dt} = F_w \quad (8.3)$$

The energy extracted from the waves in this state will be lost to hydrodynamic damping as well as transferred to the electrical generator. Analogous to the maximum power transfer theory for electrical systems, whereby it is desirable for the internal resistance of an appliance to equal its external resistance, the maximum power obtainable for the electrical machine is achieved when the two damping terms are equal, (8.4).

$$\beta_g = \beta_h \quad (8.4)$$

The required velocity of the floater can now be expressed as (8.5).

$$\dot{y} = \frac{F_w}{2\beta_h} \quad (8.5)$$

By assuming the generator to be a purely damping element and using air pressure to control the floater allows the electrical machine for the AWS to be designed without developing a complex current control strategy. In other WECs the power take off mechanism may be required to act as an inertia, spring or negative spring element, requiring strict control of the reactive force.

8.2 Prototype

8.2.1 Introduction

A pilot scheme has been built [95] which includes a permanent magnet linear generator. Performance data of both the AWS and the linear generator may hence be used to evaluate the characteristics of either of the electrical machine topologies proposed in this thesis. The pilot device has a rated stroke length of 7 m and a maximum of 9 m for the 9 m diameter floater. Figure 8.1 shows the prototype device as it is prepared for deployment.

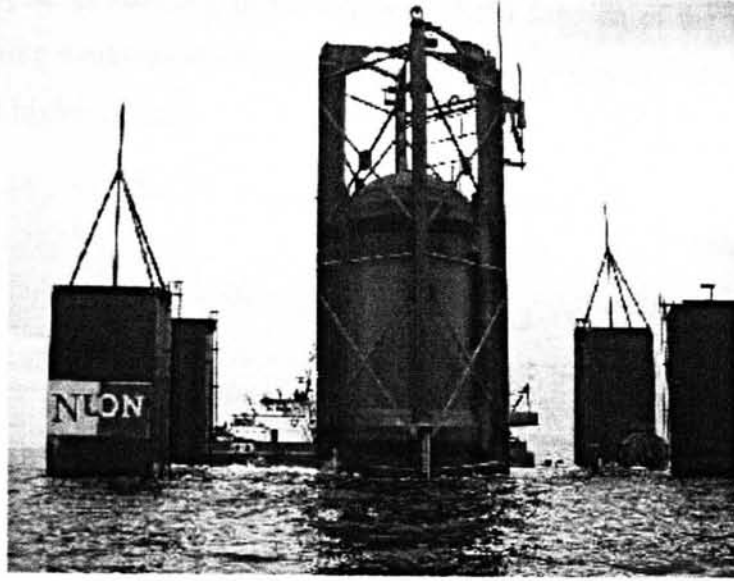


Figure 8.1: AWS during a (failed) attempt at launching

The large forces a vessel of this size can exert, in combination with the generally low shear stress of electric machines, have led the designers to place water dampers in parallel with the linear generator. These are intended to provide additional thrust during periods of high force, allowing both overload protection for the generator and also decoupling the relationship between device size and required power take off.

8.2.2 Device Characteristics

The force felt by the device, F_w , as waves pass over it varies linearly with amplitude and non linearly with wave period, the latter relationship is shown in Figure 8.2. These values are obtained by locking the floater position and measuring the resultant force in expected sea states. The force rises with the wave amplitude and appears to tend towards $7.5 \times 10^5 \text{ Nm}^{-1}$ at large wave periods.

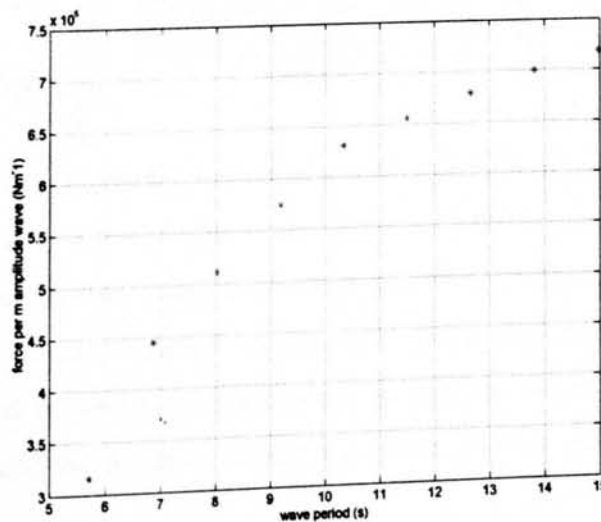


Figure 8.2: F_w per m wave amplitude vs. wave period

The hydrodynamic damping of the device is also a function of the wave period, Figure 8.3, having a maximum value of $7.8 \times 10^4 \text{Ns}^{-1}$ at a period of 7 seconds and then dropping off at higher periods.

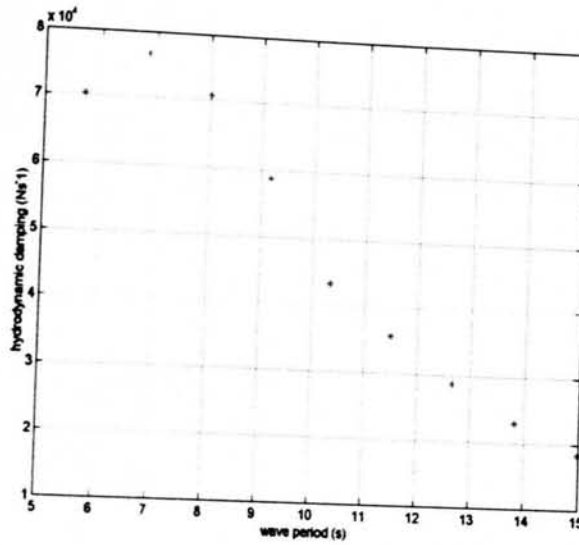


Figure 8.3: Variation of hydrodynamic damping

8.2.3 Present Power Take off

The power take off for the prototype is a double sided linear permanent magnet synchronous machine, a cross section of which is given in Figure 8.4 [95].

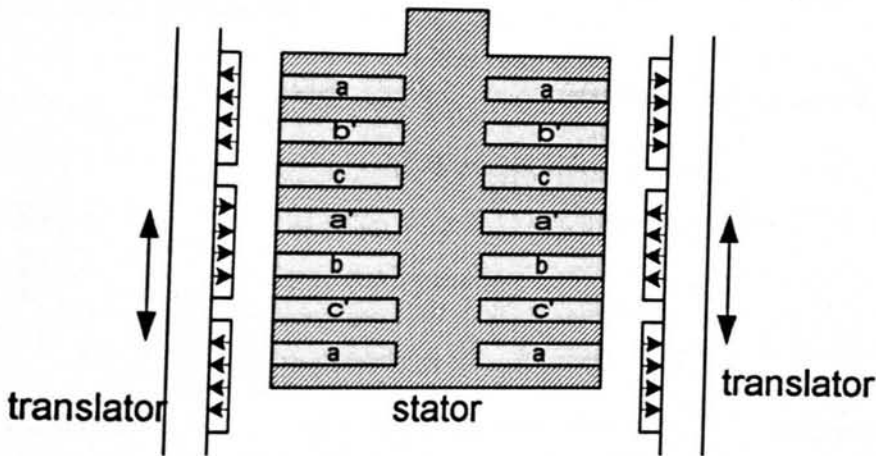


Figure 8.4: Segment of present power take off

The translator is only a few metres longer than the stator and therefore towards the extremities of oscillation there is not a full overlap between the two. Open circuit emf of this machine is hence reduced at the end points and not truly sinusoidal. Furthermore, in order to react a specific force as part of the power take off strategy it has to be borne in mind that a greater current is required at either end of the cycle.

8.2.4 Energy Yield

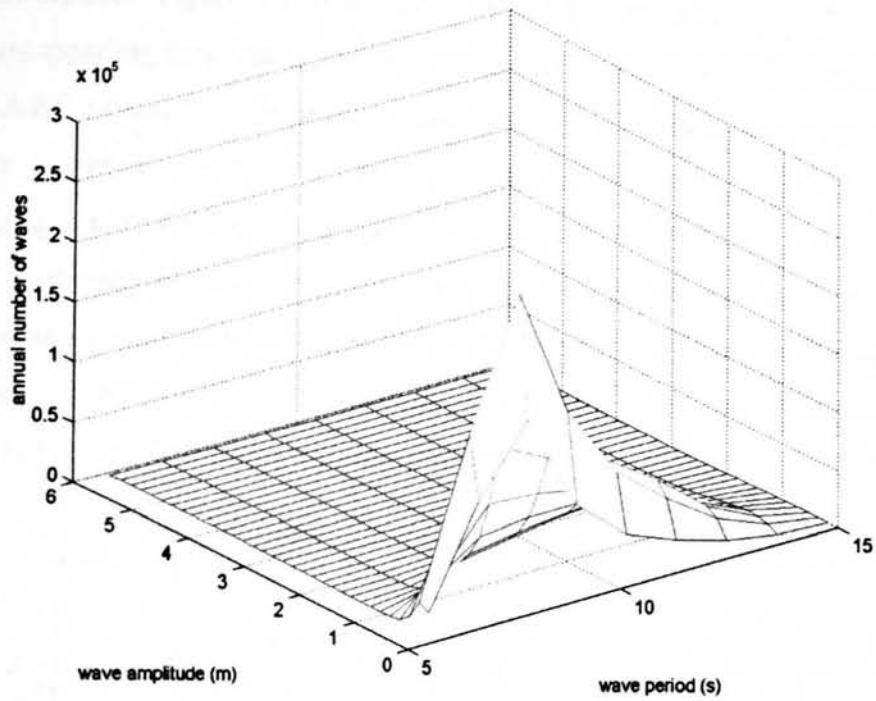


Figure 8.5: Annual wave distribution of test site

Controlling the AWS as described in Section 8.1 for the sea state of Figure 8.5 [96] results in the device characteristics shown in Figure 8.6.

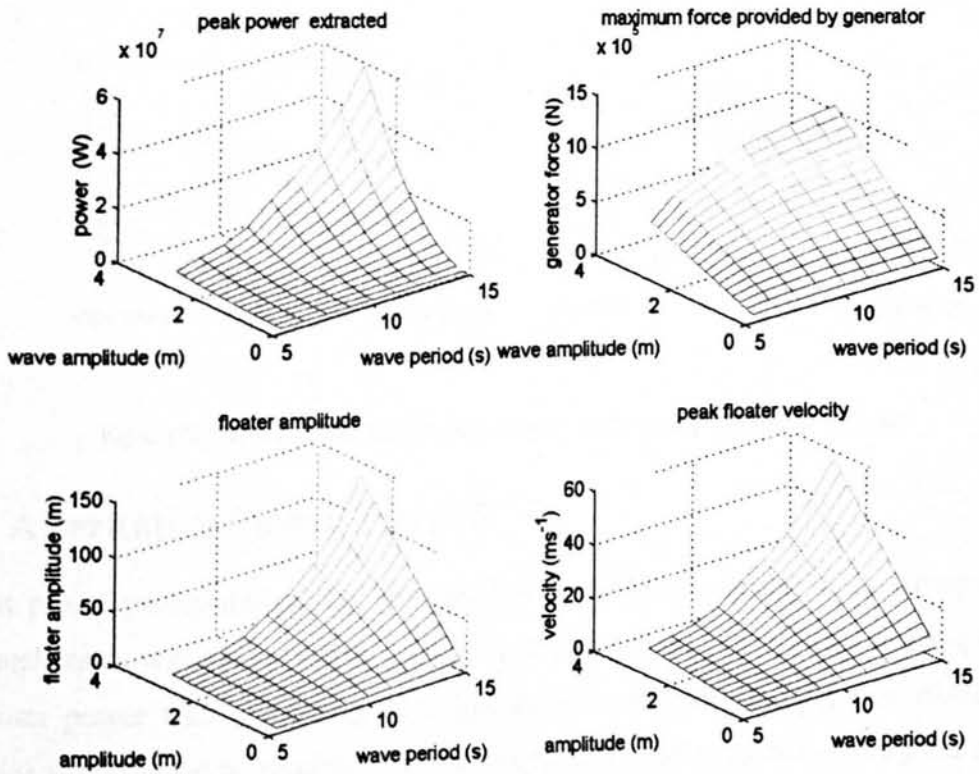


Figure 8.6: Characteristics of unrestricted AWS

as design criteria in this section, which for the present power take off correspond to a current of 200 Amps and voltage of 2 kV.

An equilibrium of air and water pressure around the lip of the floater allows the AWS to operate without any moving seals and a non flooded environment within the device is assured. The present electrical machine uses wheel type bearings for lubrication, which have a rated life of approximately one year and are the limiting factor for maintenance of the device [96]. As the AWS is mounted on the sea bed, maintenance will most likely involve retrieval to the surface and subsequent re-deployment; both expensive weather dependent operations ideally kept to a minimum. As such the tubular machine is chosen as the electrical machine topology, on the assumption that the low magnetic forces are likely to reduce bearing wear and hence increase maintenance intervals.

8.4 Design of tubular machine

In this section air cored tubular machines are designed using Equation (5.7) and the same methodology as used in the topology comparison of Section 6.7.1.3. The airgap is specified as 5 mm.

In brief, the main features of this design methodology have the coil height set to twice the theoretical equivalent airgap length, l_g , as given in Equation (3.13), the magnet width equal to the steel width and the coils are assumed to have a 40% fill factor and carry a current density of 2 A/mm^2 .

8.4.1 Single machine

In order for a single machine whose length is limited to 10 m to react 1.8 MN requires a very large active area and hence translator radius. These designs can only be discussed if it is assumed there are no limits on the manufacture and handling of PMs.

Figure 8.8 shows the parameters of suitable machines with radii varying from 0.4 to 1.5 m and magnet width varying from 0.3-0.8 m.

For the wider magnet geometries there is a point of minimal total mass corresponding to a magnet radius of around 0.5 m. The magnet mass is consistently lower with a reduction in translator radius and utilisation of the maximum available translator length. Reduction of magnet width, however, has a smaller effect as the volume of magnetic material remains roughly constant, simply consisting of more pole pieces to make up the same active area.

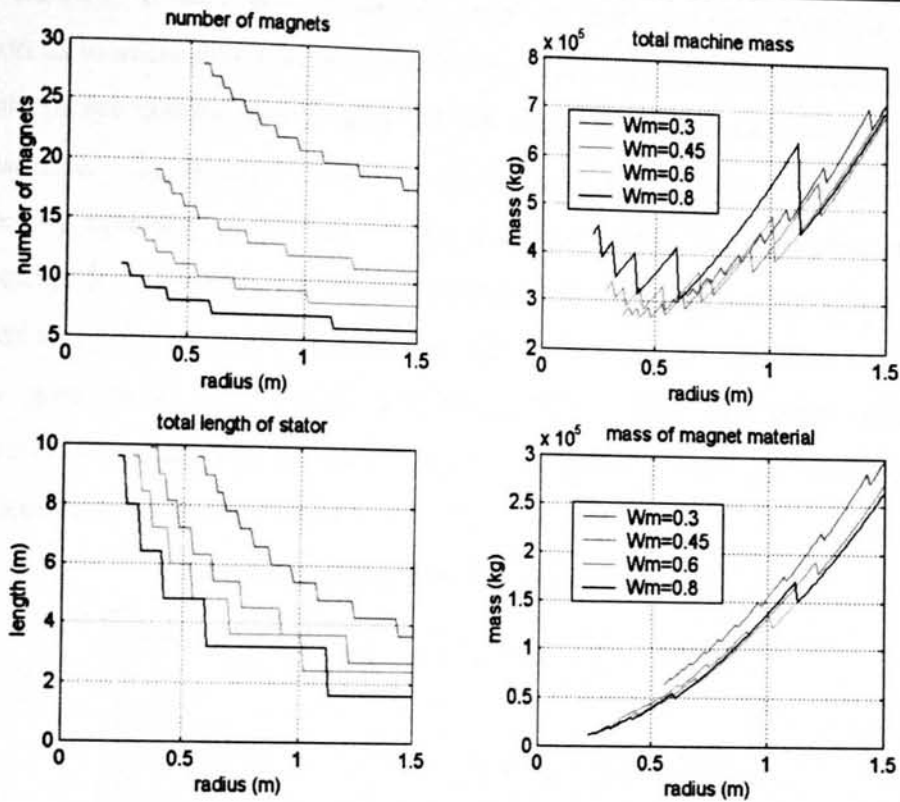


Figure 8.8: Many designs of tubular machine

Two alternative examples are highlighted for discussion, corresponding to the minimum radii for magnet widths of 0.8 m and 0.3 m. The former consists of eleven 0.22 m radius magnets weighing 948 kg each and the latter has 28 larger magnets of 0.55 m radius each weighing 2.2 tonnes. These appear to be the smallest magnets which can be used to make a single machine of 10 m stator length capable of reacting the required force.

Handling of these enormous magnets is likely to be troublesome and possibly dangerous. It is hence necessary to investigate using multiple machines of a lower rating.

8.4.2 Multiple machines

For the air cored tubular machine it is likely that a number of identical smaller machines will be mounted in parallel within the AWS to provide an equivalent reactive force to the one large machine proposed. Stipulating the length of the stator to be equal to 10 m, a variety of magnet radii and widths can be investigated to give dimensions of alternative machines.

Table 8-1 shows 5 alternative machines and the number which would be required to provide comparable power take off to the present system. The magnet radius and width is varied from 0.1-0.2 m and the required number of machines varies from 15 to 4. The

assumed current, voltage and number of turns per coil are also given to allow speculation as to alternative wiring configurations. The total mass of all but one of the configurations are approximately equal and less than the minimum achievable with a single machine. Explained by merit of the shear stress of these machines being approximately inversely proportional to R_m , Equation (3.19), yet the active area is proportional to R_m^2 , implying that a larger machine will react a greater force, but at the expense of using the magnetic material less efficiently. Smaller machines are hence likely to give better performance per magnet kg. The two most attractive configurations represent the extremes in terms of required number of machines and magnet piece size: machines A and D.

Table 8-1: Selection of tubular machines for AWS

Machine	A	B	C	D	E
Wire diameter (mm)	5	5	5	5	10
Current(Amp)	39	39	39	39	157
R_m (m)	0.1	0.1	0.2	0.2	0.15
W_m (m)	0.1	0.2	0.1	0.2	0.15
No. stator poles	50	25	50	25	33
Turns /coil	216	865	216	865	122
Voltage per coil at 2.2m/s (V)	95	360	203	781	82
F / machine (N)	122	230	260	500	277
Required no. of machines	15	8	7	4	7
Total mass (tonnes)	250	300	255	260	255

Machine E is included to demonstrate that the choice of wire diameter limits the number of turns available per coil, yet increases the current flowing through them. The overall characteristics of the machine are not significantly altered.

8.4.3 Power Conversion

Although the small-scale tubular machine has better generating characteristics than the VHM in terms of power factor, some consideration must be given to the effect of inductance at larger scale tubular machines. For an accurate design of air cored tubular machine, FEA of actual topologies is recommended. For the purpose of demonstration, however, the inductance approximation given in Section 5.1.7.3 is used to examine the power characteristics of the generators proposed in the preceding section. It was demonstrated in Chapter 5, Section 5.4.2.1, that the tubular machine could be modelled as a pure emf source with a series reactance like that of Figure 8.9, which allows the simple phasor diagram, also shown in Figure 8.9, to be used to analyse the voltage.

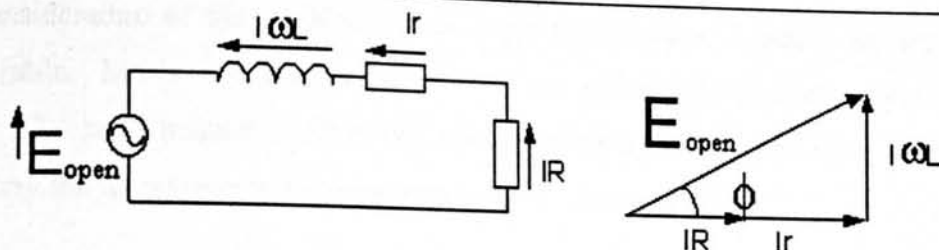


Figure 8.9: Phasor diagram of tubular machine with resistive load

The electrical machines were designed for a rated current and maximum speed, the value of a purely resistive load that ensures the rated current flows at the maximum speed can thus be chosen using geometric relationships derived from Figure 8.9.

Table 8-2: Generator characteristics of tubular machines

Model	A	B	C	D	E
Internal resistance (Ohm)	0.2	1.1	0.37	1.6	0.042
Load (Ohm)	2.18	7.13	4.75	16.6	0.455
Inductance (mH)	14.5	232	28.9	464	6.9
Power/coil (kW)	3.36	11.0	7.32	25.6	11.2
Power factor	0.98	0.90	0.98	0.92	0.95

Table 8-2 shows the resistor values necessary for individual coils and the power dissipated within them at the rated current. As the airgap for all the machines is equal to 5 mm, it is always less than 5% the value of the radius, a close approximation to the coils being surface mounted. It is likely that the value of inductance, based on a method which ignores the airgap and treats the coils as point current sources, is reasonably accurate. The resulting power factor is consistently above 0.9. These values are used in Table 8-3, which gives the peak phase power as the product of coil power and number of poles, the average machine power as 1.5 times this value, and the total configuration power as the sum of all the generators.

Table 8-3: Power delivered to load for alternative generators

	A	B	C	D	E
Peak phase (kW)	167	275	366	641	370
Total machine(kW)	250	412	549	962	555
Total (MW)	3.8	3.3	3.8	3.8	3.9

The power removed from the AWS, equal to the product of velocity and force, is 3.96 MW for all the machines. Table 8-3 shows the power delivered to a simple load resistor and is a function of the internal resistance and coil inductance. The efficiency of alternative configurations may hence be investigated and varies from 83 to 98 % for alternative configurations.

Consideration of the machine masses imply that machine A and E are the most favourable. Machine B has the largest mass and delivers the smallest power to the load. The large magnet width in this machine requires a large coil pitch, adversely affecting the inductance and internal resistance of the machine.

8.5 Discussion

The AWS is a good machine to speculate about tubular machines for direct drive power take off because it decouples the spring constant of the device from the damping, allowing the electrical machine design to be solely based on the peak thrust required. By designing a tubular machine for such a device the order of magnitude of its size is demonstrated. Unfortunately, it is not possible to compare the present electrical generator to the one proposed in terms of mass as that information is not available. However, this concept is already direct drive and so the main purpose of this Chapter has been to investigate alternative configurations of tubular machine.

There is a choice between one large machine and several small ones in parallel. In terms of manufacture and handling, it is very likely that smaller magnets will be more attractive. It has also been shown that smaller radii translators exhibit a higher shear stress and there is hence no weight penalty for using many small machines in parallel when compared to one large machine. The tubular machine is hence likely to be more suitable for machines either with sufficient space for several generators mounted in parallel, or for long thin machines, which allows the use of many small radii magnets.

Five alternative configurations of air cored tubular machines were presented utilising what is likely to be the largest PMs that can be easily handled. As the tubular machine is well represented by simple equivalent circuit analysis it is possible to specify equivalent resistance of power conversion equipment. All machines specified gave power take off with a power factor of greater than 0.9.

8.6 Conclusion

Several configurations of tubular machine have been presented capable of reacting the maximum force required by a prototype version of the Archimedes Wave Swing wave energy converter. The likely size of machines used in MECs has been outlined, with the concept of several smaller machines used in parallel demonstrated as a way of avoiding the use of large PMs.

The consistently low inductance of air cored machines demonstrates their suitability for use as a generator in this application.

Chapter

9

Discussion, Conclusion and Recommendations

The key points made in this thesis are summarised in chronological order followed by a general discussion of the results with reference to Marine Energy Converters (MECs) and novel topology electrical machines. Several areas of further research are suggested to complete and progress the work presented in this thesis, a final conclusion to which is then provided.

9.1 Chapter / Results Summary

In Chapter 1 the concept, desire and history of harnessing energy from the marine resource was introduced. The two possible sources of energy identified were wave energy and tidal stream energy. The principles and devices suitable for capturing this energy were discussed. The concept of resonance and the subsequent need for control over the behaviour of wave energy devices in order to increase capture efficiency was demonstrated.

In Chapter 2 the choice of power take off mechanism for MECs was demonstrated to play a major role in their design and the quantity of energy which they can subsequently be expected to capture. A variety of methods commonly proposed to match the physical motion within the devices to the high speed rotary motion traditionally required by electrical machines for conversion into electrical energy were then presented. All of these methods were shown to introduce additional mechanical components, complexity and maintenance requirements apart from the direct drive option. In the latter the moving element of the capture device is coupled directly to that of the electrical machine for conversion into electrical energy. Traditional topology electrical machines require large active areas to react the large forces inherent in direct drive systems. The opportunity to explore novel and modern electrical machine topologies for this application was thus highlighted.

In Chapter 3 the general layout of linear generators was explained. Details of conventional field wound machines, permanent magnet excited machines, Variable Reluctance Permanent Magnet (VRPM) machines and an air cored tubular machine were given. The mathematical development of simple expressions giving the predicted shear force developed in the air gap was given for each topology. These expressions, in combination with some general comments regarding the structure of each machine and its suitability for use in an MEC, were used to select two suitable machines for further development: the Vernier Hybrid Machine (VHM) and the air cored tubular machine. These two machines were modelled in great detail in Chapters 4 and 5 respectively.

The VHM was analysed in two dimensional Finite Element Analysis (FEA), the results of which were used to develop a variety of performance and force models capable of describing the behaviour of a 3 kW laboratory built prototype. A detailed description of the design process of the prototype and development of the models was given. The chosen performance model, which utilised a look up table for the current, position and flux data of the machine in combination with a Runge-Kutta-Nyström integration routine, was found to describe the machine's loaded behaviour satisfactorily. Several points were noted in relation to the VHM's suitability for use as a linear generator. Most significantly, the experimental prototype verified the high thrust forces predicted, showing a shear stress of greater than 100 kN/m^2 , many times larger than that expected in field wound machines. However, two disadvantages with the VHM became apparent. Firstly, the magnetic closing force in the airgap was found to be large, around twice that of the useful force produced by the machine. The resulting structural demands are further compounded by the pulsation of these attractive forces over a translator pitch. The net force on an accurately positioned translator in a double-sided machine, however, should be zero. The second disadvantage is that of the power factor being very poor, giving it bad characteristics as a generator. The power factor was demonstrated to be significantly improved at constant velocity by the use of capacitor assisted excitation. Using simplified analysis, a value of capacitance was chosen and a power factor of over 0.8 was achieved, as compared with less than 0.1 for short circuit or purely resistive loading. The sensitivity of capacitor assisted excitation to emf frequency was highlighted, implying an alternative strategy is required for the variable velocity applications considered here. Both these disadvantages appear to be inherent in this topology due to the highly effective magnetic circuit necessary for high shear stresses.

The air cored tubular machine detailed in Chapter 5 was described by a basic model, applicable because of its simple magnetic circuit and low inductance. Two two-dimensional axisymmetric FEA models were presented, one encompassing just a single rotor pole, giving high resolution predictions of the translator flux pattern. The second, encompassing an entire 8 pole half of the prototype, was necessary to model the phase and interphase inductances. An unfortunate side effect of the uneven stator coil support structure of the prototype was highlighted in the latter model, which correctly predicted an unbalanced three phase system. Intercoil supports should therefore be placed between every coil to give a balanced three phase machine, and not every third coil as used here. The methodology presented approximated the FEA generated flux linkage and inductance results to Fourier series', allowing analytical differentiation to be used in the ensuing performance models. Fundamentally, the circuit model was a simple open circuit emf source in series with a position dependant ideal variable inductor. This model demonstrated the excellent generator characteristics of the air cored tubular machine, with a power factor of greater than 0.9 when connected to a purely resistive load. The peak shear stress in the machine was 40 kN/m^2 .

In Chapter 6 some physical aspects associated with mounting these two machine topologies within an MEC were discussed. Several appropriate lubrication methods were identified as being capable of surviving the likely annual distances associated with MECs. The VHM translator was demonstrated to be troublesome with respect to sealing, although two alternative strategies were proposed. The tubular machine could benefit from sealing experience and technology transfer from the hydraulic industry. Hydrostatic lubrication of the VHM translator was examined in detail with a 5 kW system of opposed pads based on laminar flow proposed, capable of supporting the forces associated with a 100 kW generator. A simplified support system for the laminated VHM core was outlined. The magnetic forces were said to be almost absent from the air cored stator of the tubular machine and so no support structure was examined. A size comparison of the two machine topologies was presented for 100 kW generators and showed the external dimensions of the stators to be comparable.

In Chapter 7 a variety of VHM machines were proposed as the power take off for the Stingray™ tidal stream generator. The important effects of generator position on its size and mass were established. Importantly, the ideal place for positioning a hydraulic power take off system was demonstrated as being the least suitable location of a direct drive power take off system. The need to integrate the device and power take off systems early in the design process was hence noted.

In Chapter 8 the use of an air cored tubular machine as the power take off for an Archimedes Wave Swing (AWS) prototype was examined. Although single machines capable of providing suitable power take off are theoretically possible, the large magnet diameter involved will likely make them difficult or even dangerous to assemble. Furthermore, the shear stress of the tubular machine decreases as the translator radius increases, so although a greater force is reacted from wider machines, less efficient use of the magnet material is made. Several alternative configurations were proposed, whereby smaller generators were placed in parallel to share the load. Finally, the excellent qualities of tubular machines for use as generators were further demonstrated.

9.2 Discussion

The work presented in this thesis may be discussed in four categories: general, selection of machine topology, a favoured direct drive proposal for MECs and finally electrical machine research.

9.2.1 General

The topology of successful MECs has yet to be finalised, with the two prototype examples used here still being developed. The Stingray was deployed in the summer of 2002 and the AWS has yet to be submerged, after failed attempts in both 2001 and 2002. The VHM was first proposed in 1999 [97] and journal papers have yet to be published, whereas no previous literature was available on the tubular air cored generator. With two areas of infant technology being combined in this research it is hard to draw firm conclusions and recommendations. Furthermore, there is a feeling within the wave energy community of the need to avoid making high profile failures, which are likely to discredit the marine renewable energy industry as a whole. As such progress in this area is often slow and cautious, implying a suitability for a small number of reliable conclusions in preference to many sweeping optimistic statements of the potential savings and benefits of direct drive power take off.

Within this thesis it was demonstrated that electrical machines capable of reacting the large forces required at the velocities associated with most MECs exist. The decision to use direct drive must be taken in conjunction with the device design, with the knowledge that it offers the most direct method of converting the physical motion into electrical power. Once that decision has been made, the two topologies presented here represent advantages over conventional topologies.

9.2.2 Choice of topology

The choice of machine topology is linked to the specific demands of the device. Compact devices would favour a four-sided high current VHM, assuming sufficient provision could be made for the support structure. A tubular machine is more suitable for devices where there is potential for either a long stator, or several generators to be used in parallel. In devices where resonance control is provided by a system separate from the power take off, e.g. device angle, buoyancy force, water dampers or an additional hydraulic system, either generator could be recommended. Where the power take off and control mechanism are inherently linked, however, at this stage the tubular machine must be recommended by merit of the more basic current control mechanism. There is still uncertainty as to integrating a current control strategy with the unity power factor inverter necessary to use the VHM as a generator.

In Chapter 8 the translator of the present AWS electrical machine was stated as being 'only a few metres longer than the stator'. For a topology with translator mounted magnetic material, the length of the translator will have a significant impact on the device cost. The tubular translator is likely to be manufactured from 50 % magnetic material, which makes the cost verses allowable amplitude ratio much steeper. The purely steel structure of the VHM translator implies the economics of enlarging the translator will likely be insignificant. Furthermore, whereas the translator of the tubular machine is by its nature broad, the VHM translator can, in some flux pattern configurations, be made slender and thus light, ensuring the added mass of extending its length is also insignificant.

In short, a tubular machine is preferable for devices allowing long stators and oscillating with small amplitudes. For all other devices, using the VHM under the prerequisite of suitable current control strategies being developed should be considered.

9.2.3 Direct drive prototype

In the author's opinion, the most attractive Wave Energy Converter (WEC) suitable for a direct drive demonstration project is the Interproject Sweden (IPS) buoy. This deep water device, which can act as a point absorber, has two features which will allow it to pave the way for a first generation direct drive electrical generator power take off system. Firstly, the unique method of decoupling from the inertia of the surrounding water inherently limits the amplitude of the power take off device, eliminating the need for endstops and simplifying decision of translator length. Secondly, the concept of tilting the device to change its point of resonance and widen its frequency bandwidth

eliminates the need to develop a control system for the power take off mechanism. Prototypes of the device itself are presently commercially sensitive, being owned by Aquaenergy, an American company [34], but the present power take off is known to involve elastomeric hose and a seawater pump. The sloping concept is still in the development stage at the University of Edinburgh [98]. As such, information suitable for a design study was unavailable and thus the more developed and accessible AWS and Stingray devices were used in this thesis. The commercial IPS is tubular and long relative to its diameter, making it suitable for an air cored tubular machine. The Edinburgh version of the device, however, is a paddled shape device, being quite wide in the direction of the wave front and more naturally suited to the VHM.

9.2.4 Electrical Machines

The majority of the work in this thesis has been based on the development of two novel topology electrical machines and so this must form the main area of conclusions drawn.

The performance of the VHM acting as a generator has never previously been analysed except by the author [99], although an initial force analysis has been published for this [65, 97] and similar [68] topologies. The interaction of flux driven by the magnets and current was explored. A complex inductance relationship with current was discovered which means accurate modelling, particularly at high current / second order capacitive loading scenarios requires the use of flux-current-position look up table method utilising the Runge-Kutta-Nystrom integrating technique. The cogging torque modelling method of permanent magnet stored co-energy, previously only applied to single-magnet-per-pole flux reversal machines, was developed here for VRPM machines with multi-magnet poles. It was concluded that the co-energy of adjacent magnet pairs must be considered. The influence of end effects on cogging torque was shown to cause uneven peaks on the cogging-force displacement curves. Furthermore, leakage between adjacent magnets is significant for the VHM, which makes it difficult to predict emf using the same simple techniques that appear adequate for shear stress prediction.

The air cored tubular machine was shown to be capable of exerting large forces, despite the lack of flux return path in the stator. It was further demonstrated to be a desirable generator due to its almost negligible coil inductance, which gave a low power factor and allowed the use of a simple open circuit emf-series reactance equivalent circuit model. When considering the construction of such a topology, the problem of

having uneven stator slots was highlighted as were the difficulties of using externally supported coils.

The success of the VHM as a generator for use at non constant velocities is dependent on the outcome of a sister project at the University of Durham, which is exploring the possibility of building an active rectifier to remove the power from the VHM at unity power factor. Initial results were good and the second stage of testing is about to commence. In this respect, the tubular machine is the only topology that can be recommended for this application at this stage as it already has a power factor in line with that of wind turbines (>0.9).

A further aspect of research at the University of Durham is using the current to control the force of a generator in a WEC to bring the entire device into resonance. This method, being developed for the VHM, is equally applicable to the tubular device. If the outcome of the project is successful, the direct drive concept will not only be suitable for power take off for WECs with buoyancy / bandwidth control, but for all other non pneumatic WECs.

9.3 Suggestions for further work

The constraint of time and the desire to deliver meaningful conclusions has led to many avenues of research being curtailed to keep the main thread of work focused. In particular a self regulating bearing was designed and built, but gave disappointing results. A three dimensional method for predicting its behaviour was developed, the results of which were inconclusive and so not included here. Further work in this area and on the effect of turbulent high-pressure flow in opposed pad bearings could prove beneficial. The use of magnetic bearings may also prove a viable way of providing non-contact / infinite life lubrication to linear generators.

Optimisation of VHM topology, in terms of magnet and tooth width, number of magnets per stator pole and larger airgaps may represent a method for reducing the machine mass. Two-dimensional FEA has been demonstrated here as a suitable tool with which to do this. Further mass reduction can be expected with a more detailed structural analysis. The proposed support structure involved the construction of a skeletal beam structure to resist the magnetic forces and was based on the assumption that the laminated VHM stator itself could take no load. In reality this will not be the case, and the structure could be pre-tensioned in such a way as to act as a solid bar. Work on the behaviour of long laminated beams subjected to a distributed magnetic load could thus be undertaken.

Modelling of an air cored tubular machine in three dimensional FEA would allow non-concentric radial forces to be quantified and hence aid the design of both the lubrication system and support structure. Further, a more detailed method of predicting inductance would be beneficial and allow accurate performance predictions of large machines to be developed. Work into the optimisation of the proportion of magnet to steel in the translator using FEA for an air cored stator is also desirable.

A comprehensive research programme into corrosion protection for electrical machines in the marine environment is required. In particular, the use of the Ceramax ceramic coating on both the cylindrical translator of the tubular machine and the rectangular translator of the VHM would allow their further development for flooded operation.

Ultimately, either directly proceeding or concurrent with the research suggested above, a small-scale prototype direct drive device is the next logical step. The author's recommendation for that device to be an IPS buoy was given above, Section 9.2.4. The rated power of the device should be in the range of 10-100 kW, large enough to net some useful power yet small enough to allow its manufacture, deployment and behaviour to reveal further research topics without excessive financial risk.

9.4 Conclusion

Within this thesis, principles and devices for extraction of energy from the marine resource have been identified. The possibility of integrating linear generators in these designs was outlined, allowing the manufacture of direct drive marine energy converters. In order to do this a variety of possible machine topologies were described. Two of these topologies were identified as being particularly suitable and modelled extensively. These topologies represented extremes in terms of shear force, quantity of magnetic material used, power factor and inherent magnetic forces.

The development of marine energy converters from hydraulic power take off systems to direct drive systems incorporating PM linear generators would represent an important step towards overall device simplification and reliability improvement. This thesis provides much information to aid that development and found no fundamental technical barriers.

Appendix A: DERIVATION OF EQUIVALENT AIRGAP

Laplace's equation of a scalar magnetic potential in an airgap is given in (A.1).

$$\frac{\partial^2 \Omega}{\partial x^2} + \frac{\partial^2 \Omega}{\partial y^2} = 0 \quad (\text{A.1})$$

Where Ω = magnetic scalar potential

The equivalent current sheet and mmf distribution of the rotor is shown in Figure A.

1

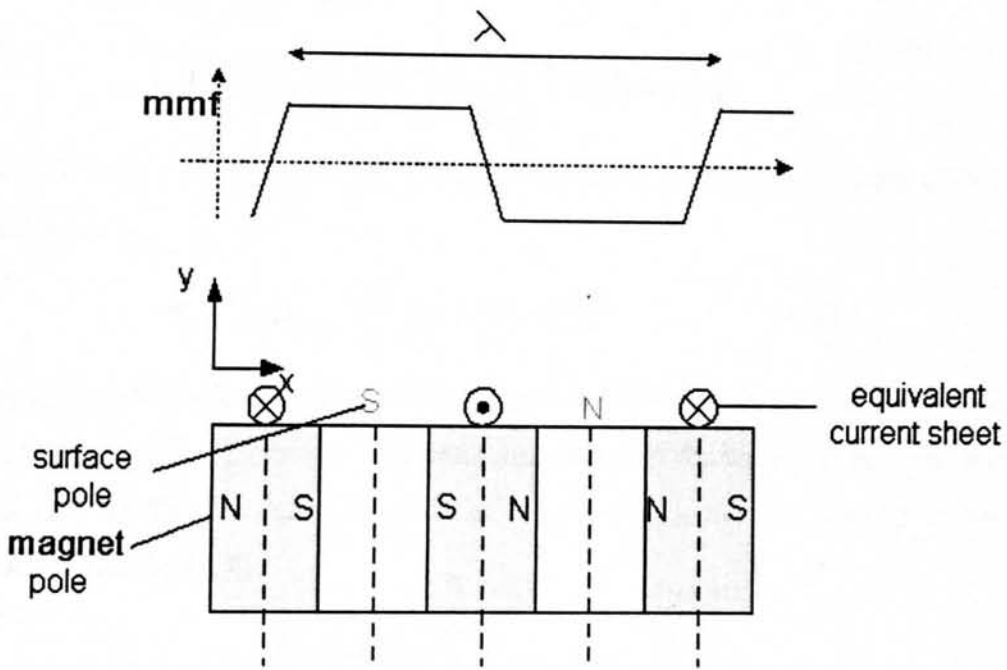


Figure A. 1: mmf distribution of rotor

The mmf distribution can be broken down into sinusoidal harmonics of the form given in (A.2)

$$\Omega(x) = \Omega_m \sin\left(\frac{2\pi mx}{\lambda}\right) \quad (\text{A.2})$$

Where λ = wavelength (m)
 m = harmonic number

The general solution of (A.1) will therefore be of the form (A.3)

$$\begin{aligned} \Omega(x, y) &= \Omega(x)\Omega(y) \\ &= \Omega(y) \sin\left(\frac{2\pi mx}{\lambda}\right) \end{aligned} \quad (\text{A.3})$$

The boundary conditions for Ω in the (y) direction are:

$\Omega(0) = \Omega_m$; mmf has a value at the rotor surface

$\Omega(g)=0$; the mmf is zero at the extremity of the airgap (when $x=g$)

From [100] the solution of an equation of this form with exactly these boundary conditions is

$$\Omega(x, y) = \Omega_m \frac{\sinh(2\pi mn(g-y)/\lambda) \sin(2\pi mx/\lambda)}{\sinh(2\pi mn/\lambda)} \quad (\text{A.4})$$

From Maxwell's equation, (A.5), the flux density in the y-direction can be found using (A.6).

$$H = -\nabla\Omega \quad (\text{A.5})$$

$$\begin{aligned} B_y &= -\mu_0 \left(\frac{\partial\Omega}{\partial y} \right) \\ &= \mu_0 \Omega_m \left(\frac{2\pi m}{\lambda} \right) \frac{\cosh(2\pi m(g-y)/\lambda)}{\sinh(2\pi mg/\lambda)} \sin(2\pi mx/\lambda) \end{aligned} \quad (\text{A.6})$$

This will be at a maximum at the surface of the rotor, $y=0$ and peak when $x/\lambda = 1/4$, as given in (A.7).

$$\hat{B}_y = \mu_0 \Omega_m \left(\frac{2\pi m}{\lambda} \right) (\coth(2\pi mg/\lambda)) \quad (\text{A.7})$$

As g approaches infinity and the machine effectively becomes an ironless machine, the hyperbolic function tends to 1. Remembering that m is the harmonic number, it can be seen that for the first harmonic with an infinite airgap the flux density in the y direction is given by (A.8).

$$\hat{B}_y = \mu_0 \Omega_1 \left(\frac{2\pi}{\lambda} \right) \quad (\text{A.8})$$

Assuming that the flux flows in straight lines and that the iron is infinitely permeable, all the mmf for the fundamental harmonic is dropped across the imaginary airgap.

$$mmf = A_1 = \hat{\phi} S_g = \hat{\phi} \frac{l_g}{\mu_0 A} = \frac{\hat{\phi} l_g}{A \mu_0} = \hat{B}_y \frac{l_g}{\mu_0} \quad (\text{A.9})$$

Where l_g is the length of an effective airgap which gives the same reluctance. Combining (A.8) and (A.9) shows that this effective airgap is (A.10).

$$l_g = \frac{\lambda}{2\pi} \quad (\text{A.10})$$

From Figure A.1 it can be seen that $\lambda=2(W_m+W_s)$, so the effective airgap becomes (A.11).

$$l_g = \frac{w_m + w_s}{\pi} \quad (\text{A.11})$$

Appendix B: DERIVATION OF POWER FACTOR FOR VHM IN CAPACITOR ASSISTED EXCITATION

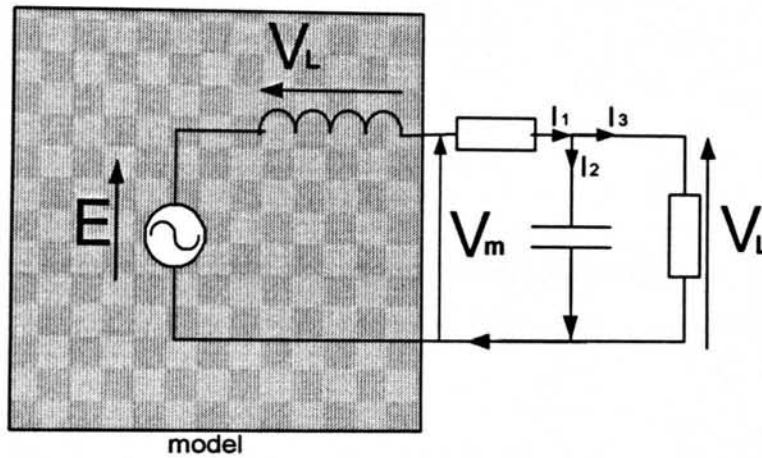


Figure B. 1: Capacitor loaded model of VHM

Figure B. 1 shows the equivalent circuit of a VHM connected to a resistive load and parallel capacitor. Labelled are the open circuit emf, E , the voltage at the output of the prediction model, V_m , the voltage dropped across the imaginary inductor, V_L , and the load voltage V_{LD} . The phasor representation of these voltages is given in Figure B. 2.

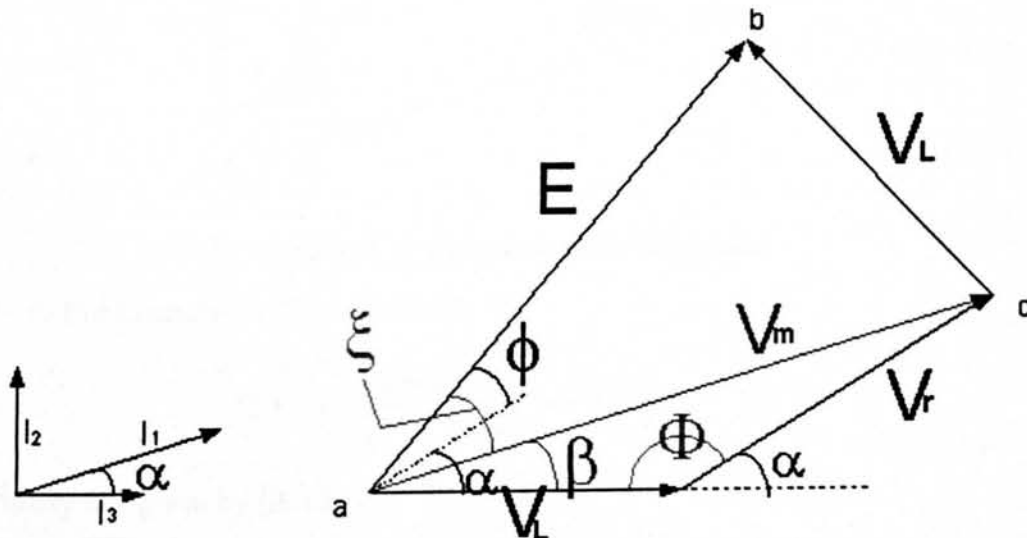


Figure B. 2: Voltage phasor representation of circuit

The cosine rule for triangles is given in its usual form in Equation (B.1) and rearranged in (B.2).

$$a^2 = b^2 + c^2 - 2bc \cos A \quad (B.1)$$

$$A = \cos^{-1} \left(\frac{b^2 + c^2 - a^2}{2bc} \right) \quad (B.2)$$

The resulting equations for angles for β and Φ are given in (B.3) and (B.4) respectively.

$$\beta = \cos^{-1} \left(\frac{V_m^2 + V_{LD}^2 - V_r^2}{2V_m V_{LD}} \right) \quad (B.3)$$

$$\Phi = \cos^{-1} \left(\frac{V_r^2 + V_{LD}^2 - V_m^2}{2V_r V_{LD}} \right) \quad (B.4)$$

α is deduced to be $\pi - \Phi$. Figure B. 3 shows the similar triangle 'abc' from Figure B. 2 re-drawn in terms of the flux linkage cutting the VHM coils, using the equivalence of (4.32).

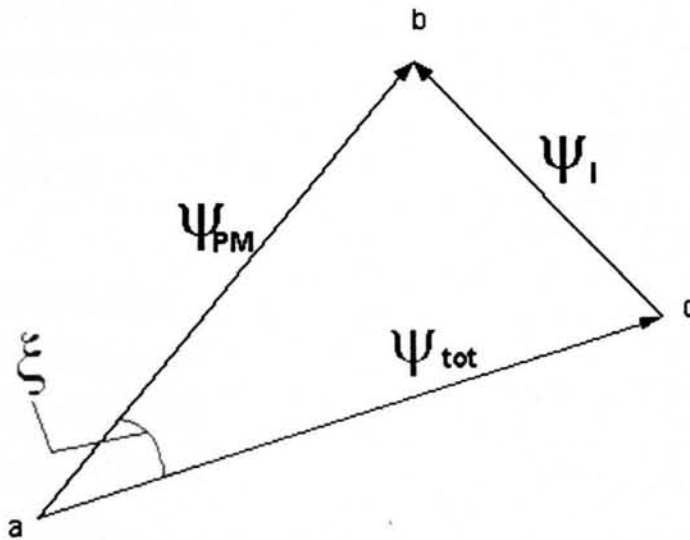


Figure B. 3: Equivalent flux linkage phasor

From this diagram ξ is found to be (B. 5).

$$\xi = \cos^{-1} \left(\frac{\hat{\psi}_{PM}^2 + \hat{\psi}_{tot}^2 - \psi_I^2}{2\hat{\psi}_{PM}\hat{\psi}_{tot}} \right) \quad (B. 5)$$

Finally ϕ is given by (B. 6).

$$\phi = \beta + \xi - \alpha \quad (B. 6)$$

Appendix C: COEFFICIENTS FOR FOURIER SERIES APPROXIMATION OF TUBULAR MACHINE

Mutual Inductances

Equation (C.1) gives the form of expression used to describe phase to phase inductances of tubular machine.

$$L_r = a_0 + a_1 \cos\left(\frac{2\pi x}{l}\right) + b_1 \sin\left(\frac{2\pi x}{l}\right) + a_2 \cos\left(\frac{4\pi x}{l}\right) + b_2 \sin\left(\frac{4\pi x}{l}\right) \quad (C.1)$$

Yellow-red phase

$$a_1 = 8.757486892880896e-004;$$

$$a_2 = 3.485567918524493e-005;$$

$$b_1 = 6.546706143142572e-004;$$

$$b_2 = 1.177364560423544e-004;$$

$$a_0 = 0.02866243434295;$$

Blue-red phase

$$a_1 = 9.851290941783335e-007;$$

$$a_2 = -5.194064119103531e-005;$$

$$b_1 = -5.299096273297722e-004;$$

$$b_2 = 1.177984768182401e-006;$$

$$a_0 = 0.00466592030858;$$

Blue-yellow phase

$$a_1 = 8.742741812641955e-004;$$

$$a_2 = -3.125658827707702e-005;$$

$$b_1 = -6.598842241096796e-004;$$

$$b_2 = 1.208454718103388e-004;$$

$$a_0 = -0.02865275836229;$$

Self inductances

Yellow

$$a_1 = 1.389330932581548e-005;$$

$$a_2 = -2.069553637097679e-004;$$

$b_1=0.00198763147882;$
 $b_2=-1.208038877114054e-006;$
 $a_0=0.05450809679009;$

Blue

$a_1=-0.00192899399826;$
 $a_2=1.783044970892694e-004;$
 $b_1=-5.297686319134646e-004;$
 $b_2=1.055508587005971e-004;$
 $a_0=0.05442662607694;$

red

$a_1=0.00191959351483;$
 $a_2=1.753672996884767e-004;$
 $b_1=-5.493123490834898e-004;$
 $b_2=-1.070830168626756e-004;$
 $a_0=0.05441391231691;$

Magnet Flux Linkage

Equation (C.2)) gives the form of expression used to represent the magnetic flux linkage.

$$\psi_r = b_1 \sin\left(\frac{2\pi x}{l}\right) + a_1 \cos\left(\frac{2\pi x}{l}\right) \quad (C.2)$$

red phase

$a_1=-0.36194134084122$
 $b_1=-2.50328026627131;$

yellow phase

$a_1=-1.76893885530924;$
 $b_1=1.77637986444189;$

blue phase

$a_1=2.50474201142485;$
 $b_1=0.35165387931590;$

Appendix D: DEFLECTION OF DISTRIBUTED BEAM

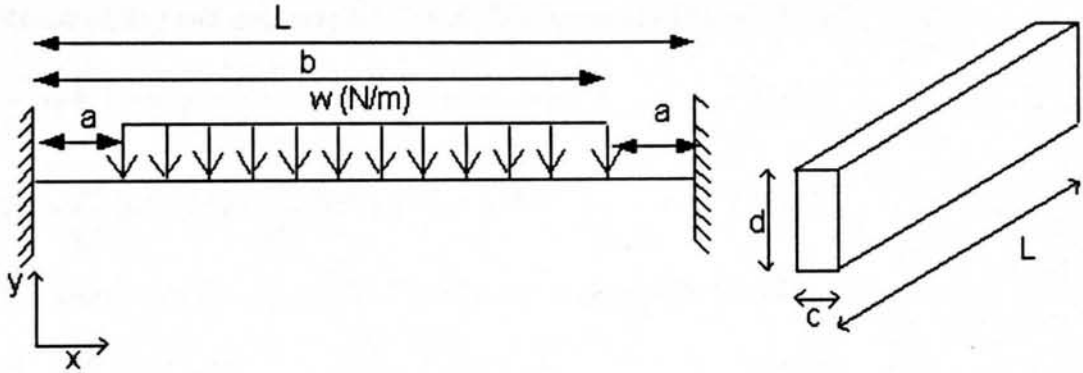


Figure D. 1: Beam with distributed load

The distributed beam of Figure D. 1 can be described using the loading equation of (C.1), where q is the load intensity.

$$q = -w\langle x-a \rangle^0 + w\langle x-b \rangle^0 \quad (D.1)$$

Integrating this 4 times give Equations (D.2) – (D.5), introducing the shear stress v , bending moment m , the slope equation dy/dx and the deflection curve y respectively

$$v = \int q = -w\langle x-a \rangle^1 + w\langle x-b \rangle^1 + C_1 \quad (D.2)$$

$$m = \int v = -\frac{w}{2}\langle x-a \rangle^2 + \frac{w}{2}\langle x-b \rangle^2 + C_1x + C_2 \quad (D.3)$$

$$EI \frac{dy}{dx} = \int M = -\frac{w}{6}\langle x-a \rangle^3 + \frac{w}{6}\langle x-b \rangle^3 + C_1 \frac{x^2}{2} + C_2x + C_3 \quad (D.4)$$

$$EIy = -\frac{w}{24}\langle x-a \rangle^4 + \frac{w}{24}\langle x-b \rangle^4 + C_1 \frac{x^3}{6} + C_2 \frac{x^2}{2} + C_3x + C_4 \quad (D.5)$$

Where E = Young's modulus of material
 I = second moment of area of the beam

Inserting the boundary condition that $y=0$ at $x=0$ and $x=L$ into (D.5) gives (D.6) and (D.7) respectively.

$$C_4 = 0 \quad (D.6)$$

$$0 = \frac{-w}{24}(b)^4 + \frac{w}{24}(a)^4 + \frac{C_1L^3}{6} + \frac{C_2L^2}{2} + C_3L = 0 \quad (D.7)$$

Using the zero bending condition at the built in ends gives the boundary conditions of $dy/dx=0$ at $x=0$ and $x=L$, substituted into (D.4) gives (D.8) and (D.9) respectively.

$$C_3 = 0 \quad (D.8)$$

$$-\frac{w}{6}(b)^3 + \frac{w}{6}(a)^3 + \frac{C_1 L^2}{2} + C_2 L = 0 \quad (D.9)$$

Re-arranging and equating (D.7) and (D.9) gives (D.10), resulting in (D.11)

$$\frac{w}{12L^3}(b^4 - a^4) - \frac{2C_1 L}{6} = \frac{w}{6L}(b^3 - a^3) - \frac{3C_1 L}{6} \quad (D.10)$$

$$C_1 = \frac{w}{L^2}(b^3 - a^3) - \frac{w}{2L^4}(b^4 - a^4) \quad (D.11)$$

Substitution of (D.11) into (D.7) and re-arranging gives (D.12)

$$C_2 = \frac{w}{6L}(b^4 - a^4) \left(\frac{1}{2L} + \frac{1}{L^2} \right) - \frac{w}{3L}(b^3 - a^3) \quad (D.12)$$

Maximum extension will be in the centre, $x=L/2$, substituted into (D.5) gives (D.13)

$$EIy_{\max} = \frac{w}{24} \left(\frac{L}{2} - b \right)^4 + \frac{C_1 L^3}{48} + \frac{C_2 L^2}{8} \quad (D.13)$$

REFERENCES

- 1 European Thematic Network, <http://www.wave-energy.net/>
- 2 ROSS, D., 'Power from the Waves', Oxford University Press, 1995, ISBN 0 19 856511 9
- 3 OVE ARUP & PARTNERS, 'Wave Energy: Technology Transfer & R&D Recommendations', Report for the DTI, 2000
- 4 THORPE, T. W. 'An assessment of the ART OSPREY wave energy device', ETSU report R-90, prepared for the UK DTI
- 5 'The Energy Review', Performance and Innovation Unit Report, 2002, UK Government, available at: <http://www.cabinet-office.gov.uk/innovation/2002/energy/report/index.htm>
- 6 THORPE, T.W.: 'A Review of Wave Energy', ETSU Report R72, 1992, UK DTI
- 7 THORPE, T.W.: 'A Brief Review of Wave Energy', ETSU Report R120, 1999, available at <http://www.dti.gov.uk/renewable/pdf/r120w97.pdf>
- 8 EVANS, D.V.: 'A theory for Wave-Power absorption by oscillating bodies', Journal of Fluid Mechanics, 77, 1976, pp1-23
- 9 FALNES, J.: 'Principles for capture of energy from ocean waves. Phase control and optimum oscillation Control Strategies' Department of Physics, NTNU, Trondheim, Norway, available at: <http://www.phys.ntnu.no/instdef/grupper/miljofysikk/bolgeforsk/phcontrl.pdf>
- 10 NEBEL,P.: 'Maximising the Efficiency of wave-Energy Plant Using Complex Conjugate Control', Proceedings of the Institution of Mechanical Engineers, vol.206,pp225-
- 11 NEBEL, P. and WOODEHEAD, P.L.: 'Optimum Control of a Duck at Full scale', Proceedings of the European Wave Energy Symposium, Edinburgh, Scotland, 1993, pp40-428
- 12 GREENHOW, M. and WHITE, S.P.: 'Optimal Heave of Some Axisymmetric Wave Energy Devices in Sinusoidal Waves', Applied Ocean Research 19, 1997, pp141-159
- 13 EIDSMOEN, E.: 'Simulation of a Tight Moored Heaving-Buoy Wave-Energy Converter with Phase Control', Division of Physics, Norwegian University of Science and Technology, N7034, Trondhiem, Norway
- 14 EIDSMOEN, E.: 'Simulation of a Slack Moored Heaving-Buoy Wave-Energy Converter with Phase Control', Division of Physics, Norwegian University of

- science and Technology, N7034, Trondhiem, Norway.
- 15 FALNES, J.: 'Optimum control of Oscillation of Wave Energy Converters', annex "Wave Energy Converters: Generic Technical Evaluation Study"
 - 16 Ocean power Delivery Ltd. 2 Commercial St, Edinburgh, EH6 6JA, Scotland, UK <http://www.oceanpd.com>
 - 17 YEMM, R.W., HENDERSON, R. M., and TAYLOR, C. A. E. , 'The OPD Pelamis WEC: Current Status and onward Programme', Proceedings of the fourth European Wave Energy Conference, Aalborg, Denmark, 2000, ISBN 87-90074-09-2
 - 18 SALTER, S.H., : 'Wave Power', Nature Vol 249, 1974, pp720-724
 - 19 PIZER, D.J, RETZLER, C.H and YEMM, R.W.: 'The OPD Pelamis: Experimental and Numerical results from the hydrodynamic work programme' Proceedings of the fourth European Wave Energy Conference, Aalborg, Denmark, 2000, ISBN 87-90074-09-2
 - 20 BRACEWELL, R.H. : 'Frog and PS Frog: a study of two reaction less wave energy converters', PhD thesis, Lancaster university, 1990, available at <http://edclinux.eng.cam.ac.uk/~rhb24/rhbthes.pdf>
 - 21 CHAPLIN, R.V., FENCH, M.J. and BRACEWELL R.H. : 'An Improved Version of PS Frog Converter', Proceedings of the Second European Wave Power Conference, 1993, Lisbon, pp345-350
 - 22 THOMAS, G.P. and GALLAGHER, B.P., : 'An Assessment of Design Parameters for the Bristol Cylinder', Proceedings of the 1993 European Wave Energy Symposium, Edinburgh, pp 139-144
 - 23 LONG, A.E. and WHITTAKER, T.J.T. : 'Wave Power-a challenge to engineers', Proceedings of the Institution of Civil Engineers, part 1 vol 84, 1988, pp355-374
 - 24 THORPE, T.W., : 'An Overview of Wave Energy Technologies', summary of presentation given to the UK Marine Foresight Panel, 13 May 1998
 - 25 YU, Z. and FALNES, J., : 'State-Space Modelling of a Vertical Cylinder in Heave', Applied Ocean Research 17, 1995, pp265-275
 - 26 SJÖSTRÖM, B.O. : 'The Past, Present and Future of the Hose-Pump Wave Energy Converter', Proceedings of the 1993 European Wave Energy Symposium, 1993, Edinburgh pp311-316
 - 27 BERGGREN, L. and JOHANSSON, M.,: 'Hydrodynamic coefficients of a Wave energy device Consisting of a Buoy and a Submerged Plate', Applied Ocean Research (14), 1992, pp51-58
 - 28 EIDSMOEN, E.,: 'Hydrodynamic Parameters for a two-body Axisymmetric

- System'. Applied Ocean Research (17), 1995
- 29 POLINDER, H., GARDNER, F. and VRIESEMA, B. 'Linear PM generator for wave energy conversion in the AWS'. proc. of the International Conference on Electrical Machines, pp309-313, August 2000, Epsoo, Finland.
- 30 De Weel 20,1736 KB, Zijdewind, The Netherlands, <http://www.waveswing.com>
- 31 Interproject Service AB, Gripensnäs, S-640 33, Bettna, Sweden
<http://www.ips-ab.com>
- 32 SALTER, S.H. and CHIAO-PO LINN, : 'The Sloped IPS Wave Energy Converter' Proceedings of the second European Wave Power Conference, 1995, Lisbon pp337-44
- 33 SALTER, S.H. and CHIAO-PO LINN, : 'Wide Tank Efficiency Measurements on a model of the Sloped IPS Buoy', Proceedings. Of the 3rd European Wave Energy Conference, p 200-206, Patras, 1998
- 34 AquaEnergy Group, Ltd, P.O. Box 1276, Mercer Island, WA 98040. USA
<http://www.aquaenergygroup.com>
- 35 TAYLOR, J.R.M., and MACKAY, I.: 'The Design of an eddy current dynamometer for a free-floating sloped IPS buoy', Proceedings of Marine Renewable Energy Conference, MAREC. Newcastle, March 2001, ISBN 1-90253-43-6, pp 67-74
- 36 HAWS, E. T., 'Tidal Power – a major prospect for the 21st century (Royal Society Parsons Memorial Lecture)', Proc Instn of Civ Engrs, Marit. & Energy, Vol (124) March 1997, pp1-24
- 37 'Tidal stream energy review', ETSU report for the DTI, publication number T/05/00155, 1993
- 38 'The commercial prospects for tidal power', ETSU report T/06/00209/REP or DTI publication URN 01/1011, 2001
- 39 EUROPEAN COMMISSION report, 'The exploitation of tidal marine currents' EUR 16683
- 40 RUDKIN, E. J. and LOUGHNAN, H. G. H., 'Vortec – the marine energy solution', Proceedings of Marine Renewable Energy Conference, MAREC. Newcastle, March 2001, ISBN 1-90253-43-6,pp151-159
- 41 FRAENKEL, P.L., 'Power from Marine Currents', Proceedings of the ImechE Part –A, Journal of Power and Energy, 2002, Vol 216, pp1-14
- 42 TRAPP, A.D., WATCHCORN, M.; 'EB development of tidal stream energy', Proceedings of Marine Renewable Energy Conference, MAREC. Newcastle, March 2001, ISBN 1-90253-43-6,

- 43 CHALMERS B. J., WU, W. , SPOONER, E. 'An axial-flux permanent-magnet generator for a gearless wind energy system', IEEE Trans. on Energy Conv. Vol 14, June 1999 pp251-257
- 44 FISH, P. R., 'From prototype to large scale – preparations for the new offshore wind farm market', Proceedings of Marine Renewable Energy Conference, MAREC. Newcastle, March 2001, ISBN 1-90253-43-6
- 45 HEIER S., 'Grid integration of Wind Energy Conversion Systems', John Wiley & Sons, ISBN 0-471-97143 X
- 46 MØLLER, T. 'A Man of Clear Signals, Wind Power Monthly, Vol 15, No. 11 November 1999 pp34-37
- 47 KIM, T. H., TAKAO, M., SETOGUCHI T, KANEKO, K, INOUE, M, 'Performance comparison of turbines for wave power conversion', Int. Journal of Thermal Sciences, (40), 2001, pp681-689
- 48 SALTER, S. H., "Variable Pitch Air Turbines", Proc. 1993 European Wave Energy Symposium, July 1993, Edinburgh, UK, p435
- 49 KIMT, T. H., SETOGUCHI, TAKAO, M. KANEKO, K., SANTHAKUMAR, S, 'Study of turbine with self-pitch-controlled blades for wave energy conversion', Int.Journal of Thermal Sciences, Vol. 41, Jan 2002 pp 101-107
- 50 RAMPEN, W.H.S., ALMOND, J.P., TAYLOR, J.R.M, EHSAN Md, SALTER, S.H., 'Progress on the development of the wedding-cake hydraulic pump/motor', Proceedings 2nd European Wave Power Conference, Lisbon, Portugal, Nov.1995 pp289-296. EUR 16932 EN
- 51 McCONNEL, J. Comparative Fatigue Tests on 3-core 22 kV A.C. Submarine Cable for Floating Wave Energy Converters. Pirelli Report 8526. WESC(80) GT 125 (from ETSU)
- 52 BAZ, A. and MORCOS, S.: "Development of Direct and Indirect Wave energy Converter", presented at The International Symposium on Wave and Tidal Energy, September 1978, University of Kent, UK
- 53 KORDE, U.A.: 'Control Strategies for Oscillating Water Column Devices', Proceedings of the Second European Wave Power Conference, 1993, Lisbon pp260-267
- 54 KELLY, H.P.: 'The Direct Energy Conversion Method: The use of Linear Generators to Capture and Convert Sea Directly to Electrical Power', poster Presentation at I Mech E International one day seminar : 'Wave Power; Moving Towards Commercial Viability', London, November 1999
- 55 BROOKING, P.R.M., MUELLER, M.A., BAKER, N. J., HAYDOCK, L. & BROWN, N, 'Power conversion in a low speed reciprocating electrical generator', International Conference on Electrical Machines, Brugge, Belgium, August 2002

- KROGSTAD, H.E.: 'Statistikk over bølgeparametre. 'Haltenbanken' (64° 10.5' N, 9° 10.0' E)' Continental Shelf Institute (IKU), Trondheim, Norway, 1978 (cited in [60])
- 57 EIDSMOEN, H, 'Simulation of a slack moored heaving buoy wave-energy converter with phase control'. Technical Report, Institutt fo fysikk, NTNU, May 1996, <http://www.phys.ntnu.no/instdef/grupper/miljofysikk/bolgeforsk/inexe.html>
- 58 ARZEL, T., BJARTE-LARSSON, T. and FALNES, J. 'Hydrodynamic parameters for a floating WEC force reacting against a submerged body', Proceedings 4th European Wave Energy Conference 2000, Dec. 2000, Aalborg, Denmark, ISBN 87-90074-09-2
- 59 "Enerpac Hydraulics", Sales literature, ENERPA Ltd, Unit 3m Colemeadow Road, North Moons Moar, Redditch, Worcester, B98 9BP, UK- specifically RR-15032 model
- 60 WATADA, M, YANASHIMA, K, OISHI, Y & EBIHARA, D, 'Improvement on characteristics of linear oscillatory actuator for artificial hearts', IEEE Trans. on magnetics, Vol.29, No.6, Nov 1993
- 61 SEN, P.C, 'Principles of Electrical Machines and Power Electronics' J Wiley & sons inc. ISBN 0-471-02295-0, p292, 1997
- 62 BALCHIN MJ, EASTHAM JF & COLES PC, 'Effects of pole flux distribution in a homopolar linear synchronous machine', Journal of Applied Physics 75 (10): pp6987-6989 Part 2B May 1994
- 63 WEH H, HOFFMAN H & LANDRATH J, "New Permanent Magnet Excited Synchronous Machine with High Efficiency at Low Speeds.", Proc. Int. Conf. Elec. Machines, Pisa, Italy, Sept. 1988, pp35-40.
- 64 HUSBAND, M, 'Developing the transverse flux motor TFM', One day seminar, 'New topologies for electrical machines', UK Magnetics Society, Leicester, September 2002
- 65 SPOONER E. & HAYDOCK, L., 'Vernier Hybrid Machines', to be published, IEE Proceedings Part B, Electric Power Applications.
- 66 MECROW, B. C. & JACK, A. G. 'A new high torque density permanent magnet machine configuration', Proc. of the Int. Elec. Machines Conf., Cambridge Mass. USA, Sept 1990
- 67 HARRIS, M. R. & MECROW, B. C., 'Variable Reluctance Permanent Magnet Motors for High Specific Output', Proc. IEE International Conference in Electrical Machines and Drives, Oxford, UK, 1993
- 68 IWABUCHI, N, KAWAHARA, A, KUME, T, KABASHIMA, T & NAGASKA, N, 'A novel High-Torque Reluctance Motor with Rare Earth

- Magnet', IEEE Trans on Ind. App., Vol. 30, No.3, June 1994, pp609-613
- 69 HARRIS, M. R., PAJROOMAN, G. H. & ABU SHARKH, S. M. 'The problem of power factor in VRPM (Transverse Flux Machines', Int. Conf. On Electrical Machines and Drives, Cambridge 1997, IEE publication 444, ISBN 0 85296 6962
- 70 CHEN Z., SPOONER E., NORRIS W.T. & WILLIAMSON A.C., "Capacitor-assisted excitation of permanent magnet generators", IEE Proc. Electr. Power Appl., Vol. 145, No. 6, November 1998.
- 71 WANG, J., JEWELL, G.W. and HWE, D.: 'A general Framework for the Analysis and Design of Tubular Linear Permanent Magnet Machines', IEE Trans. on Magnetics, Vol.35, No. 3, May1999, pp1986-1999
- 72 WANG, J., JEWELL, G.W. and HWE, D.: 'Design optimisation and comparison of tubular permanent magnet machine topologies', IEE proc. Electrical power Applications, Vol148, No.5, Sept 2001, pp456-464
- 73 BURGHARDT, M. D. : 'Engineering Thermodynamics with Applications', Third Edition, Harper & Row, New York, ISBN 0 06 0410434, 1986, pp 489-490
- 74 PC-OPERA User Guide, Vector Fields Ltd., 24 Bankside, Kidlington, Oxford, OX5 1JE UK, 1999
- 75 RIZK, J. NAGRIAL, M.: ' Computation of Cogging Torque in Permanent magnet Machines', IEE International Conference in Electrical Machines and Drives, ICEM, 1998, p1123-1127
- 76 MILLER, T.J.E., 'Switched Reluctance Motors and their Control', Clarendon Press; ISBN: 0 198593872, Oxford, U. K., 1993
- 77 CHENG, M. ,CHAU, K. T. ,CHAN, C. C., 'Static Characteristics of a new doubly salient permanent motor', IEEE Trans. on Energy Conv., Vol. 16 No.1 March 2001, pp20-25
- 78 DEODHAR, R.P. et al: 'Prediction of Cogging Torque Using the Flux-MMF Diagram Technique', IEEE Trans. of Ind. App. Vol 32, May 1996, pp569-575.
- 79 CAMPBELL, P.: 'Comments on Energy Stored in Permanent Magnets', IEEE Trans. on Magn, vol.36, Jan 2000, pp402-403
- 80 MATLAB 6, release 12, The MathWorks, Inc, 3 Apple Hill Drive, Natick, MA, USA
- 81 KREYSZIG, E, 'Advanced Engineering Mathematics', J Wiley & sons, Singapore 1993, ISBN 0 471 3328-X pp1051
- 82 Load cell. Wegtstone bridge, data sheet available at <http://www.tedea-huntleigh.com>, Tedea-Huntleigh, 37 Portmanmoor Road,

Cardiff. CF24 5HE

- 83 HEPSCO slide systems Ltd, Lower Moor Business Park, Tiverton, Devon, U.K., EX16 6TG. 'Simplicity. Self-Lubricated Bearings', company literature.
- 84 HEPSCO slide systems Ltd, Lower Moor Business Park, Tiverton, Devon, U.K., EX16 6TG. 'Heavy Duty Slide Systems', company literature.
- 85 Company Literature. VACUUMSCHMELZE GMBH & Co. KG, Gruener Weg 37, D-63450 Hanau, Germany <http://www.vacuumschmelze.de>
- 86 Hydraudyne Cylinders B.V., Kuisbroeksestraat 1, 5281 AA Boxtel, P.O.Box 32, 5280, The Netherlands, <http://www.hydraudyne.nl> . Subsidiary of Mannesmann Rexroth
- 87 Rexroth Hydraulics company literature, Hydraudyne Cylinders B.V. Kruisbroeksestraat 1, 5281 RV Boxtel, P.O.Box 32, 5280 AA Boxtel, The Netherlands. Specifically: <http://www.rexroth.com/riq/1999/riq.1999-3/en/article8.pdf>,
- 88 CLAYBER, J. : personal communication, Rexroth sales representative UK, 2001
- 89 MASSEY, B. S., 'Mechanics of Fluids', Chapman and Hall, London, ISBN 0 412 34280 4, 1989, p145
- 90 BASSANI, R. & PICCIGALLO, B. 'Hydrostatic Lubrication' Elsevier, London, 1992 ISBN0 4444 88498 X
- 91 FLUENT Europe Ltd, Holmwood House, Cortworth Road, Sheffield, S11 9LP, UK
- 92 N G Bailey Manufacturing, Company literature, NG Bailey & Co Ltd, Heathcote, Ilkley, West Yorkshire, UK, LS29 9AS <http://www.ngbailey.co.uk>
- 93 TRAPP, T., personal communication, The Engineering Business Ltd, Broomhaugh House, Riding Mill, Northumberland, NE44 6EG
- 94 SLEE, D., personal correspondence, The Engineering Business Ltd, Broomhaugh House, Riding Mill, Northumberland, NE44 6EG, June 2002
- 95 POLINDER, H., DAMEN, M.E.C., GARDNER, F., 'Modelling and test results of the AWS linear PM generator system', proc. of the International Conference on Electrical Machines, August 2002, Brugge, Belgium
- 96 POLINDER, H., Personal correspondence about position of AWS prototype, September 2002
- 97 SPOONER, E. : 'High Torque Machines', Digest of the Manchester Machines Research Group Seminar, 1999
- 98 PAYNE, G, 'Preliminary numerical simulations of the Sloped IPS Buoy',

Proceedings of the Marine Renewable Energy Conference, MAREC 2002,
Newcastle pp79-89

- 99 MUELLER, M. A., BAKER, N.J. 'Modelling the Performance of the Vernier Hybrid Machine', Submitted for publication, IEE Part B Proceedings, 14/10/02.
- 100 CHALMERS, B.J., GREEN, A.M, REECE, A.B.J and AL-BADI, A.H. 'Modelling and simulation of the Torus generator', IEE proc.-Electr. Power Appl, Vol 144, No.6, November 1997, pp446-452

